

Improvements to Two Viscometers
Based on a Magnetic Suspension Coupling and
Measurements on Carbon Dioxide

Dissertation
zur Erlangung
des Grades

Doktor-Ingenieur

der

Fakultät für Maschinenbau
der Ruhr-Universität Bochum

von

Michael Schäfer
aus Essen

Bochum 2015

Dissertation eingereicht am: 21. Oktober 2015
Tag der mündlichen Prüfung: 23. November 2015

Erster Referent: Prof. Dr.-Ing. R. Span
Zweiter Referent: Dr.-Ing. M. Richter (Emmy Noether-Gruppenleiter)

Diese Arbeit entstand während meiner Tätigkeit als wissenschaftlicher Mitarbeiter am Lehrstuhl für Thermodynamik der Ruhr-Universität Bochum unter der Leitung von Herrn Prof. Dr.-Ing. R. Span.

An erster Stelle danke ich Herrn Prof. Dr.-Ing. R. Span, da er diese Arbeit anregte und ihre Durchführung ermöglichte. Durch seine kritische Sichtweise wurde diese Arbeit wesentlich bereichert, und sie profitierte von seiner fundierten wissenschaftlichen Erfahrung.

Mein besonderer Dank gilt Herrn Dr.-Ing. M. Richter für die Übernahme des Korreferats. Er verfolgte diese Arbeit mit sehr viel Interesse. Ich bedanke mich für die gute Zusammenarbeit und das große Vertrauen, das er mir entgegenbrachte, besonders wenn es erforderlich war, neue Wege zu gehen und Probleme auf unvoreingenommene Art und Weise zu lösen.

Mit ein Grund für den erfolgreichen Abschluss meiner Promotion war das gute Arbeitsklima am Lehrstuhl, das von Freundlichkeit und Hilfsbereitschaft geprägt war. Allen jetzigen und ehemaligen Mitarbeitern des Lehrstuhls und insbesondere der HESF-Arbeitsgruppe danke ich herzlich dafür. Ich danke den Mitarbeitern der Elektronikwerkstatt und der mechanischen Werkstatt.

Bedanken möchte ich mich auch bei Herrn Dr.-Ing. R. Kleinrahm, der immer ein offenes Ohr für jegliche Art von Anliegen hatte, bei Herrn Dr.-Ing. A. Laesecke für sein motivierendes Interesse an meiner Arbeit und bei Herrn Dr.-Ing. N. Kurzeja, von dem ich viel über experimentelles, wissenschaftliches Arbeiten lernte.

Ich bedanke mich bei Herrn M.-A. Herrndorf und Herrn K. Humberg, da sie durch ihre selbstständige und engagierte Mitarbeit als studentische Hilfskräfte wesentlich zum Gelingen dieser Arbeit beitrugen. Dasselbe gilt für die vielen Studierenden, die bei mir ihre Semester-, Bachelor- und Masterarbeiten schrieben.

Mit Herrn A. Jäger und Frau G. Tsankova habe ich viel Zeit verbracht, da ich mit ihnen das Büro teilte. Für die schöne Zeit bedanke ich mich. Ein persönliches Dankeschön geht außerdem an Frau J. Deutscher für viele inspirierende Gespräche und das konstruktive Feedback im Rahmen der Korrektur der Dissertation.

Bei meiner Familie möchte ich mich herzlich für den Rückhalt während der letzten Jahre bedanken.

Bochum, im Dezember 2015



(Michael Schäfer)

Table of Contents

Table of Symbols	VI
1 Introduction	1
2 Apparatuses and Measurement Principles	4
2.1 Description of the Low-Pressure Viscometer	4
2.2 Description of the Viscometer-Densimeter	12
3 Improvements to the Apparatuses	17
3.1 A System for Time-Measurement and Automation of the Viscosity Sequence	18
3.2 A Temperature-Controlled Gas-Dosing System	21
3.3 Overhaul of the Vacuum System	26
3.4 Equipment to Measure the Rotating Body's Suspension Height and the Temperature	28
3.5 Enhancements of the Low-Pressure Viscometer	29
3.5.1 Improvement of the Device for Aligning the Cylinder System . .	30
3.5.2 Rebuild of the Rotating Body of the Low-Pressure Viscometer . .	31
3.6 Improvements to the Viscometer-Densimeter	32
3.6.1 Evaluation of the Former Viscosity-Density Measurement System	32
3.6.2 A New Viscosity-Density Measurement System	35
3.6.3 Improved Positioning System of the Viscometer-Densimeter . . .	39
3.6.4 Evaluation of the Improved Measurement System	41
4 Evaluation of the Viscosity Measurement	43
4.1 Effects Interfering with the Viscosity Measurement	43
4.1.1 Hysteresis	43
4.1.2 Effects Generated by Sorption and Vibrations	44
4.2 Compensation of a Viscosity Dependent Offset	46
4.2.1 Determination of the Residual Damping by Vacuum Measurements	48
4.2.2 Multi-Fluid Calibration Method to Determine the Residual Damping	50
4.2.3 Evaluation of Measuring and Calibrating the Residual Damping	51

4.3	Compensation of a Systematic Viscosity Offset	54
4.3.1	Determination of the Geometries of the Cylinder Systems	54
4.3.2	Mass and Volume Determinations	59
4.3.3	The Axial Moment of Inertia of the Rotating Body	61
4.3.4	Uncertainty Analysis of the Absolute Measurement Principle for the Low-Pressure Viscometer	66
4.3.5	Evaluation of the Fluid-Dynamic Model	69
4.3.6	Measuring the Viscosity Relative to Helium	78
4.4	Evaluation of the Extended Model Function	79
5	Measurement of the Viscosity of Carbon Dioxide at Low Pressures	82
5.1	Experimental Procedures	82
5.2	Uncertainty Analysis	84
5.3	Results of the Measurements on Carbon Dioxide	88
6	A Simple Apparatus for the Gravimetric Preparation of Gaseous Mixtures	95
6.1	Theory of the Gas-Mixture Preparation System	96
6.2	Description of the Gas-Mixture Preparation System	97
6.3	Experimental Procedures	100
6.4	Uncertainty Analysis, Results and their Validation	103
7	Summary and Conclusion	106
8	References	109
A	Technical Drawings	117
A.1	Angle Plate to Fix the Manual Positioner of the Low-Pressure Viscometer	117
A.2	Draft Shield of the Viscometer-Densimeter's Balance	119
A.3	Modifications to the Stand for the Viscometer-Densimeter's Balance . . .	123
A.4	The Viscometer-Densimeter's Flow-Guide Tube	125
B	Experimental Carbon Dioxide Data	138

Table of Symbols

C	apparatus coefficient
c	viscous coefficient
D	damping
f	frequency
h	height
J	axial moment of inertia
k	coverage factor
L	length
M	molar mass
m	mass
n	number of revolutions
p	pressure
r	radius
Re	Reynolds number
T	Kelvin temperature (ITS-90)
t	time
u	standard uncertainty
U	expanded uncertainty
V	volume
W	weight
x	composition
z	non-stationary parameter
α	thermal expansion coefficient
η	dynamic viscosity
Δ	difference
τ	period
ρ	density

Subscripts

0	zero density or standard state at $T = 293.15\text{ K}$
a; air	air
ave	average
bal	balance
c	combined
cal	calibrated
calc	calculated

corr	corrected
cyl	cylinder
disc	disc
ecc	eccentricity
exp	experimental
ext	extrapolated
hys	hysteresis
i	inner
init	initial
max	maximal
mix	mixture
o	outer
ref	reference
reg	regression
res	residual
R	residual
s	sinker
scat	scatter
sorp	sorption
vis	viscous
w	water
∞	infinity

Abbreviations

AC	alternating current
CG	combustion gas
CMM	coordinate-measuring machine
DMM	digital multimeter
EOS	equation of state
PEEK	Polyether ether ketone
PTFE	polytetrafluoroethylene
ITS-90	international temperature scale of 1990
PID	Proportional-Integral-Differential
rpm	rounds per minute
SRG	Spinning Rotor Gauge
TTL	transistor-transistor logic

1 Introduction

A major objective in process engineering is efficiency. An efficient process saves energy and resources and is therefore economic. On the one hand, to achieve a high efficiency, the properties of the substances involved have to be known with high accuracy, especially during the design phase of the process. On the other hand, many processes have two things in common: (1) there is a fluid flow of substances, and (2) the substances are fluid mixtures. The viscosity of the substances is a fundamental property to describe the fluid flow. Thus, the accurate knowledge of the viscosity of mixtures is a key to an economic design.

Currently, the recommended approach to obtain accurate viscosities is to use a correlation, which is based on experimental data (*Millat et al., 1996*). A common type of correlation is the residual concept (*Nieto de Castro and Wakeham, 1996*). It is widely applied for pure gases, but it is also applicable for the viscosity of mixtures in a wide temperature and pressure range (*Friend, 1990*). According to the residual concept, the viscosity is calculated as the sum of two terms:

$$\eta(\rho, T, x) = \eta_0(T, x) + \Delta\eta_{\text{res}}(\rho, T, x). \quad (1.1)$$

The first term $\eta_0(T, x)$ is called viscosity at zero density. It is dependent on temperature T and mixture composition x . The second term $\Delta\eta_{\text{res}}(\rho, T, x)$ is the residual part, which depends on density ρ , temperature T , and mixture composition x . Ideally, two kinds of experimental data should be available to set up a correlation according to eq. (1.1) for a specific mixture: experimental mixture viscosities of the low-pressure region and experimental viscosity data of the mixture, which are measured at elevated density in dependence of the density.

The viscosity of mixtures at elevated density is commonly measured only in dependence of temperature and pressure, although the density of the mixture is required to set up the residual part of eq. (1.1). When the density of the mixture is not part of the experimental data, the density of the mixture has to be calculated with pressure, temperature, and the composition of the mixture as input parameters. Thus, the uncertainty of the calculation of the mixture's density affects the uncertainty of the viscosity correlation of the mixture. For most mixtures, the relative expanded uncertainty of the calculated density is larger than 0.1 % (*Gernert and Span, 2015*). However, an uncertainty in density of less than 0.1 % is desired, otherwise the uncertainty of the viscosity correlation is significantly increased (*Docter et al., 1997*).

Considering this background, *Docter et al. (1997)* developed a viscometer-densimeter to measure the viscosity of gases in dependence of density. The viscosity was determined on the basis of the decay rate of a slender cylindrical body, which rotated inside the

measuring cell and was held by a magnetic suspension coupling utilized as a nearly frictionless bearing. The density was measured according to the single-sinker method (*Brachthäuser et al.*, 1993). This apparatus was improved by *Evers et al.* (2002) to determine the viscosity in an absolute way. *Evers et al.* (2002) measured the viscosity in dependence of the density for several pure fluids (Ar, CH₄, He, Ne, Kr). Thereafter, *Wöll* (2005) investigated the viscosity and density of humid and moist air. Finally, *El Hawary* (2009) used the viscometer-densimeter to measure the viscosity of gaseous CH₄-N₂ mixtures. The temperatures of *El Hawary*'s measurements ranged from (253.15 to 473.15) K with pressures up to 20 MPa. The relative expanded combined uncertainty ($k = 2$) in viscosity was reported by *El Hawary* (2009) to be 0.25 %. *El Hawary* (2009) measured the corresponding density of the mixtures in an absolute way. The relative expanded combined uncertainty ($k = 2$) in density was reported to be 0.02 % at elevated densities. In summary, the viscometer-densimeter is suitable to provide experimental data for setting up the residual part of eq. (1.1). Beyond this purpose, the data measured with the viscometer-densimeter can provide data for validating or improving theoretical models describing the viscosity of mixtures at elevated densities.

In addition to the viscometer-densimeter, a prototype of a second apparatus was developed by *Evers et al.* (2002). The prototype was designed for measuring the viscosity in the low-density region in an absolute way. This apparatus is now known as the low-pressure viscometer. Like the viscometer-densimeter, the low-pressure viscometer measures the viscosity using a magnetic suspension coupling as a nearly frictionless bearing for a rotating body. In contrast to the viscometer-densimeter, a lower uncertainty was achieved by enlarging the width of the annulus of the cylinder system and by omitting the density measurement. This simplification was reasonable, as the viscosity depends only to a small extent on the density with pressures up to ≈ 2.4 MPa. *El Hawary* (2009) improved *Evers*' prototype and measured the viscosity of gaseous CH₄-N₂ mixtures at temperatures from (253.15 to 473.15) K with pressures up to 2.4 MPa. A relative expanded combined uncertainty ($k = 2$) in viscosity of 0.06 % was reported by *El Hawary* (2009).

Although initially the low-pressure viscometer was developed to validate the results of the viscometer-densimeter, its capabilities are more comprehensive. It can provide very accurate data to determine the viscosity at zero density. Therefore, the data have to be extrapolated to zero density. As can be seen in eq. (1.1), the viscosity at zero density is a fundamental part of the residual concept. Thus, the accuracy of viscosity correlations can be improved significantly in the low density region by taking into account the measurements of the low-pressure viscometer. Furthermore, the data are valuable to validate calculated viscosities at zero density. Recently, this approach was applied for mixtures; see *Hellmann et al.* (2014). In addition, the initial density dependence of

mixtures, i.e., the second transport virial coefficient (*Rainwater and Friend, 1987*) can be investigated.

In general, there is a lack of accurate experimental viscosity data, especially in case of mixtures (*Millat et al., 1996*). Therefore, an objective of this work was to prepare the low-pressure viscometer and the viscometer-densimeter at the chair of thermodynamics at Ruhr-Universität Bochum for the measurement of gaseous mixtures. One future goal is the viscosity measurement of binary gaseous mixtures containing carbon dioxide and nitrogen, as these mixtures are relevant in the context of carbon capture and storage.

However, gaseous carbon dioxide-rich mixtures have to be handled elaborately to avoid condensation. Condensation changes the composition of the gaseous phase of the mixture. Consequently, a temperature-controlled gas-dosing system was needed. Furthermore, carbon dioxide is a strong solvent. Therefore, the use of non-metal parts within the gas-dosing system had to be minimal. The development of a suitable temperature-controlled gas-dosing system is described in chapter 3 of the present work.

Only one system for automating the viscosity measurement was available for both apparatuses. In consequence, a time-efficient simultaneous operation of the apparatuses was hindered. In addition, the existing automation system was unreliable due to an age-related deterioration of its electronic components. Thus, another objective of this work was to develop a new automation system for the viscosity measurement so that both apparatuses can be operated reliably at the same time. This matter is part of chapter 3 as well.

A large scatter of more than 2 % in viscosity was observed in the data of the viscometer-densimeter. Thus, the measurement principle of the viscometer-densimeter had to be refined, which is also described in chapter 3.

Two different offsets of the measured viscosities were observed in comparison to reference viscosities: (1) a systematic offset in viscosity, and (2) a viscosity dependent offset. Therefore, the measurement principle had to be evaluated. The evaluation of the measurement principle and how the offsets were compensated by an extended model function is discussed in chapter 4. The extended model function was applied to measure the viscosity of gaseous carbon dioxide using the low-pressure viscometer. These measurements are presented in chapter 5.

To investigate the dependence of the viscosity on the composition of a mixture, several mixtures of different composition have to be measured. However, commercially available mixtures do not fulfill the requirements concerning filling pressure or uncertainty in composition. Therefore, an apparatus for the gravimetric preparation of gaseous mixtures was developed. This apparatus is described in chapter 6.

At the beginning of this work – chapter 2 – the low-pressure viscometer and the viscometer-densimeter are presented. This presentation includes the measurement principles and the technical realization of the apparatuses.

2 Apparatuses and Measurement Principles

Two apparatuses are described in this chapter: the viscometer-densimeter and the low-pressure viscometer. The descriptions are based on the level of development presented in the dissertation of *El Hawary (2009)*, as this level of development was the starting point for this work.

In this chapter, first, the viscosity-measurement principle is explained using the low-pressure viscometer as an example. Thereafter, the technical realization of the low-pressure viscometer is described. The second part of this chapter deals with the description of the viscometer-densimeter. For completeness the viscosity-measurement principle is explained shortly with the viscometer-densimeter as an example. Furthermore, the density-measurement principle and the technical realization of the viscometer-densimeter are described.

The descriptions within this chapter were based on the publications of *Docter et al. (1997)*, *Docter et al. (1999)*, *Evers (2001)*, *Evers et al. (2002)*, *Wöll (2005)*, *El Hawary (2009)* and *Schäfer et al. (2015)*, in which also more details about the apparatuses can be found.

A piping and instrumentation diagram of the apparatuses depicting the level of development reported by *El Hawary (2009)* is shown in figure 2.1. From left to right, the electronics of the low-pressure viscometer, the low-pressure viscometer, the gas-dosing system, the viscometer-densimeter, and electronics of both apparatuses can be seen. See figure 3.1 for a photo of both apparatuses in the laboratory. However, figure 3.1 depicts the setup of the apparatuses after they were enhanced and moved to a new laboratory.

2.1 Description of the Low-Pressure Viscometer

The measurement principle of the rotating-body viscometer was originally developed by *Docter et al. (1997)*, who initially built the viscometer-densimeter. With this apparatus the viscosity and the density can be measured simultaneously; the viscosity-measurement principle was combined with a single-sinker densimeter. *Evers (2001)* simplified the viscometer-densimeter's measurement principle and developed a prototype of a rotating-body viscometer, which was specifically designed for the low-pressure region. The low-pressure viscometer did not incorporate a density measurement system. Furthermore, the annulus of the cylinder system was enlarged whereby the measuring range was limited to low pressures. However, thereby, the measurement uncertainty was reduced considerably.

El Hawary (2009) developed Evers' prototype further in the context of his dissertation. The apparatus was set on an own shock absorbing frame, the temperature range was extended and a second sample inlet/outlet was installed at the measuring cell. The second fluid inlet/outlet enabled flushing the measuring cell with the sample gas.

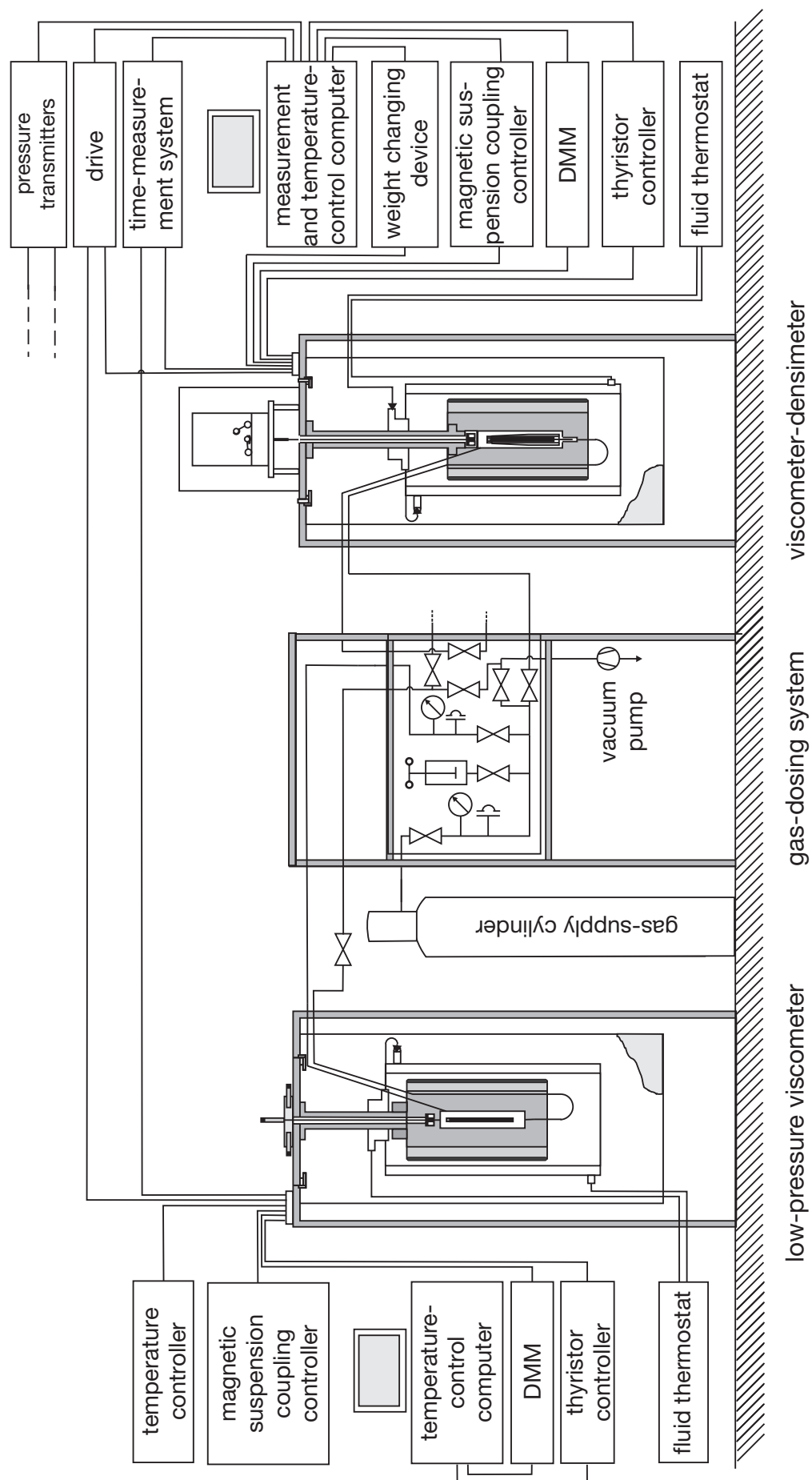


Figure 2.1 Piping and instrumentation diagram of both viscometers. The level of development reported by *El Hawary (2009)* is shown.

Theory of Viscosity Measurement

In the following, first the principal set up of the viscosity system is described. Therefore, a simplified drawing of the measuring cell of the viscosity system is depicted in figure 2.2. As can be seen, a slender cylindrical body, called rotating body, was vertically suspended by a magnetic suspension coupling, consisting of an electromagnet, a permanent magnet, a position sensor, and a control system. A detailed description of the magnetic suspension coupling in conjunction with a viscometer is given by *Docter et al. (1997)* and *Evers (2001)*. This coupling served as an almost frictionless bearing for the rotation of the rotating body around its symmetry axis.

The viscosity measurement sequence is divided into three parts: acceleration, flow formation, and data acquisition. These parts are depicted in figure 2.3. There, the rotational frequency during the course of a viscosity measurement is plotted versus time. As can be seen in figure 2.2, four drive coils were positioned around the measuring cell. By inducing a magnetic field rotating with time, the rotating body was set into rotation around its vertical axis. The resulting increase in rotational frequency (acceleration) is shown between points (1) and (2). The drive was deactivated after reaching the maximal frequency f_{\max} . The data acquisition between point (3) and (4) was not started until the rotational frequency was below a starting frequency f_{start} . Thereby, the formation of the

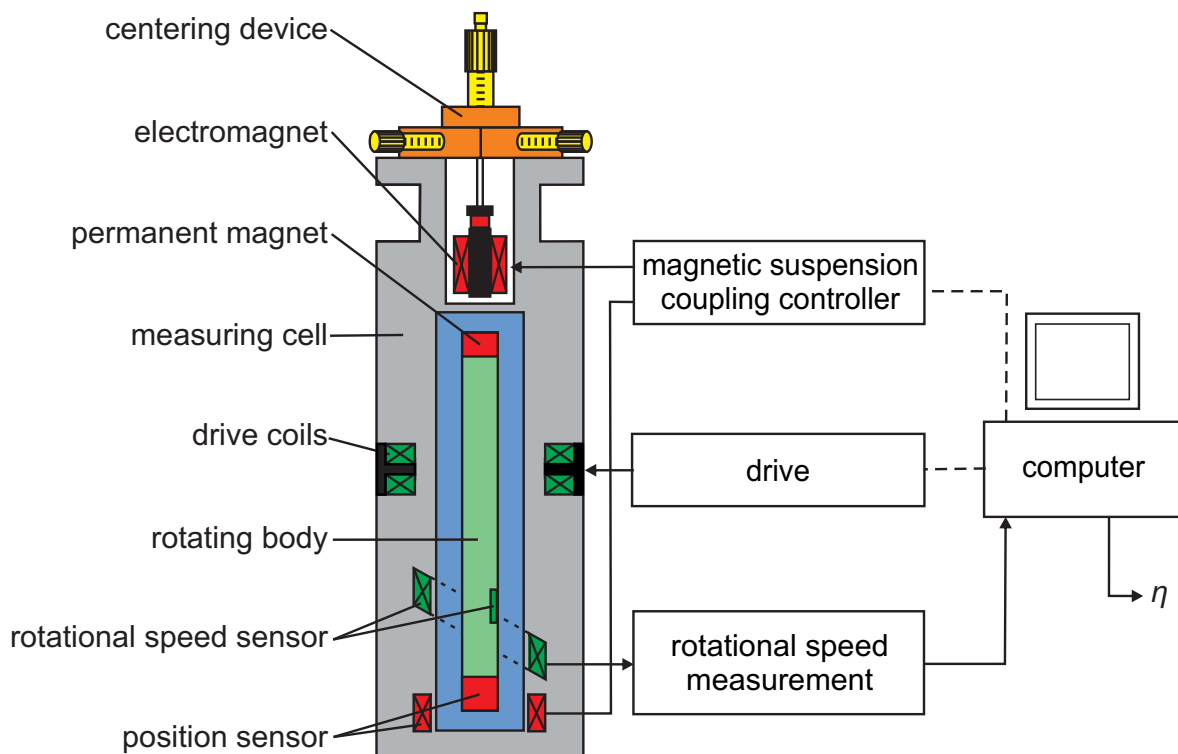


Figure 2.2 Basic principle of the low-pressure viscometer. This illustration is based on a figure of *Evers et al. (2002)*.

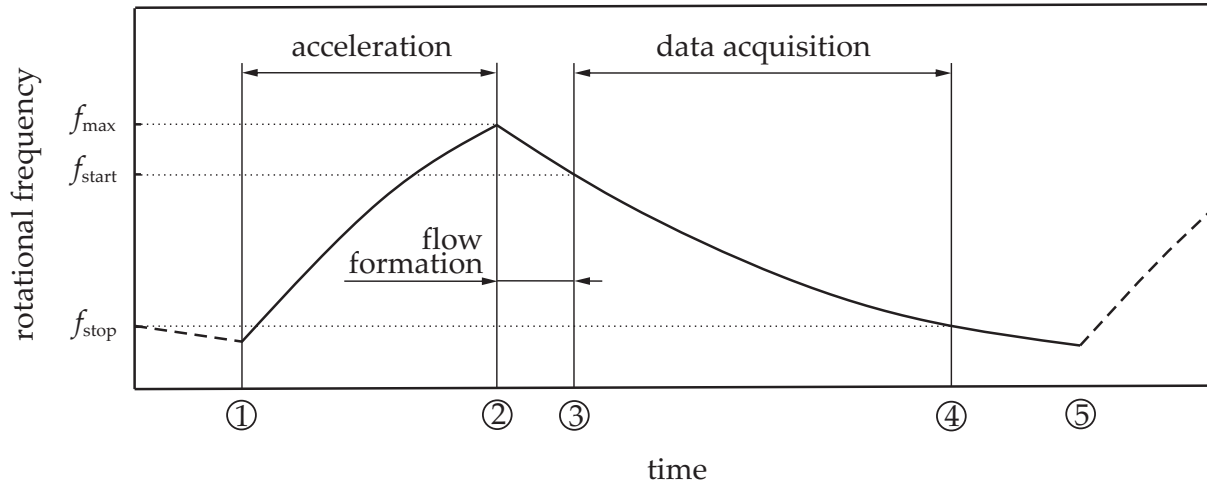


Figure 2.3 Schematic of the viscosity-measurement sequence.

flow was ensured. During the data acquisition, the rotational frequency was decelerated due to the viscous drag of the fluid surrounding the rotating body. At the stopping frequency f_{stop} , a single measurement was completed. After point (4), e.g., at point (5), a new measurement sequence could be started.

During the viscosity-measurement sequence, the speed of rotation was measured with a rotational speed sensor. This sensor consisted of an induction coil and a small magnetic core being incorporated into the rotating body and built-in about 4.75 mm out of the center of rotation. The axis of the coil was inclined to about 45° with regard to the rotational axis of the cylinder. As soon as the rotating body was accelerated, the magnetic core changed the inductance of the coil depending on the angle of rotation. The angle dependent inductance of the sensor was converted into a voltage signal, which was low-pass filtered, offset, and amplified in order to analyze it. In the upper part of figure 2.4, an example for the processed voltage signal of the rotational speed sensor U_D is plotted vs. time t .

The revolution times τ_i of the rotating body can be determined from this signal utilizing a time-measurement system. The absolute time t_i is calculated by adding up the periods τ_i . The graph resulting from plotting the number of revolutions n vs. the absolute time t is shown in the lower part of figure 2.4. As can be seen, the number of revolutions of the cylinder $n(t)$ varies exponentially with time t to an asymptotic value n_∞ :

$$n(t) = n_\infty [1 - \exp(-Dt)] . \quad (2.1)$$

The two parameters, n_∞ and D , are calculated by fitting eq. (2.1) to the measured (n, t) points, whereas the damping value D is characteristic for the curvature of the bottom graph in figure 2.4. Eq. (2.1) is the connection between the measured input parameters n_i and t_i and the physical model of the measurement principle.

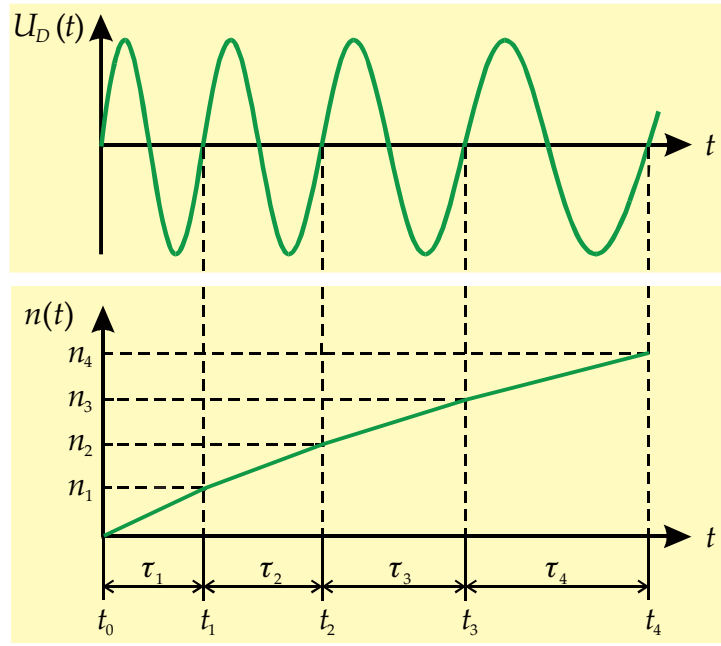


Figure 2.4 Top: voltage signal U_D of the rotational speed sensor plotted vs. time t . Bottom: number of revolutions n plotted vs. time t , which is the sum of the measured revolution times τ_i . (Figure taken from *Docter, 1997.*)

The physical model is based on the equilibrium of the two moments acting upon the rotating body: (1) the viscous moment, which slows the rotating body down and (2) the axial moment of inertia, which keeps the rotating body in rotation. The viscous moment depends on the dynamic viscosity, thus the viscosity is part of the rotating body's equation of motion. This equation was elaborately discussed by *Evers (2001)* and only the outcomes are presented here.

An outcome of the physical model is that the damping D depends on the dynamic viscosity. Solving the equation of motion for the viscosity yields to the model function of the measurement principle:

$$\eta = \frac{D(J + z\rho) - D_R \cdot J}{c_{\text{vis}}}. \quad (2.2)$$

The different input parameters of eq. (2.2) are discussed in the following, starting with the viscous coefficient c_{vis} . This parameter accounts for the viscous drag of the fluid. However, technically speaking, it is only applicable if the fluid flow is laminar and stationary. Consequently, the application of eq. (2.2) is strictly restricted to a laminar flow regime induced by the rotating body when measuring the viscosity inside the measuring cell. The viscous coefficient depends on the dimensions of the cylinder system.

For though, the rotation of the rotating body is mainly slowed down due to the viscous drag of the surrounding fluid, there are further influences decelerating the rotating body.

One of the main influences in addition to the fluid damping are eddy currents. When the rotating body is in rotation, the magnetic field of the permanent magnet rotates with it. Thus, an inhomogeneity of the permanent magnet induces eddy currents in the electrical conductive material of the measuring cell. Also the position sensor, the rotating speed sensor or the deactivated drive coils could have an influence. These influences in their entirety are named residual damping D_R . Thus, the measured damping D can be seen as the sum of the fluid damping D_{fluid} and the residual damping D_R . Consequently, the damping D has to be corrected for the residual damping, as given in the numerator of eq. (2.2). To determine the residual damping, the damping is measured while evacuating the measuring cell. However, the influence of the fluid, i.e., the residual molecules, is very low but significant even at the lowest vacuum pressures achievable. Therefore, the residual damping is determined by extrapolating the damping values to zero density.

In addition to the residual damping, the rotating body's axial moment of inertia J is an important input parameter of the model function, as the model function is very sensitive to it. J depends on the distribution of the rotating body's mass around its rotation axis. It is dependent of the geometries and the densities of the rotating body. A further parameter of the model function is the non-stationary parameter z . It is used to compensate for the non-stationary characteristic of the cylinder flow while measuring. The fluid itself is rotating during the measurement. Thus, it also has a moment of inertia. The product of the non-stationary parameter z and the fluid density ρ accounts for this increase in the axial moment of inertia. The non-stationary parameter z depends on the dimensions of the cylinder system.

Physically, the model function in form of eq. (2.2) is more suitable to explain the different input parameters. However, the model function can be represented in a shorter form introduced by *Evers (2001)*. By defining an extended apparatus coefficient

$$C^* = \frac{c_{\text{vis}}}{J} \quad (2.3)$$

and an extended non-stationary parameter

$$z^* = \left(1 + \frac{z\rho}{J}\right) \quad (2.4)$$

the model function reads

$$\eta = \frac{z^*D - D_R}{C^*}, \quad (2.5)$$

which is the formulation used in *Evers et al. (2002)* and *Schäfer et al. (2015)*.

Technical Realization of the Low-Pressure Viscometer

In figure 2.5, a schematic drawing of the viscometer is shown. The core apparatus was accommodated in a shock-absorbing frame to prevent the measuring cell from disturbing vibrations. The thermostatted measuring cell was installed underneath the base plate. Four screws were installed at each corner of the base plate and these screws rested on the frame. With these screws the angle of the instrument was adjusted with a resolution of 0.003° (arcdegree). Furthermore, a positioning device for centering the cylindrical system was placed upon the base plate. With this device the rotating body was moved inside the measuring cell. The diameter of the rotating body was 11 mm, the width of the annulus between the rotating body and the measuring cell was 4.5 mm, and the length of the rotating body was 116 mm.

The measuring cell was made of a titanium alloy ($\text{Ti}_6\text{Al}_4\text{V}$). This alloy has a very low electrical conductivity, so eddy currents induced by the inhomogeneity of the magnetic field of the rotating permanent magnet are very weak. In consequence, the residual damping measured in the evacuated measuring cell was minimized. Thus, the influence of the measured residual damping on the damping value was in general less than 3 %.

A two-stage thermostat and a thermal insulation cover surrounded the measuring cell. The outer thermostat stage was a double-wall stainless-steel container, and heat exchanging fluid was circulated through, employing a closed dynamic temperature-control system (Julabo, Germany, type: LH85). The temperature of the outer thermostat stage was maintained about 1 K below the measuring cell temperature so that the thermostat was working as a heat sink in the thermostating system. To minimize the heat loss at high temperatures, an electrical heater was linked to the tube connecting the measuring cell with the base plate. The inner thermostat stage, which contained an electrical heating device, was firmly attached to the measuring cell and was almost completely shielded isothermally by the outer thermostat stage. The temperature of the inner thermostat stage was controlled using a Pt-100 Ω sensor (Merz, Germany, type: P 100/2528) with ITS-90 calibration. The temperature of the measuring cell was measured utilizing an AC resistance thermometry bridge (ASL, UK, type: F250 MKII) and a second Pt-100 Ω sensor (Isotech, USA, type: 909/100) with ITS-90 calibration, which was in direct contact with the measuring cell on a level with the rotating body. The pressure was measured with a vibrating-quartz-crystal-type pressure transmitter with a range of 3.45 MPa (Paroscientific, USA, type: 1500A-01).

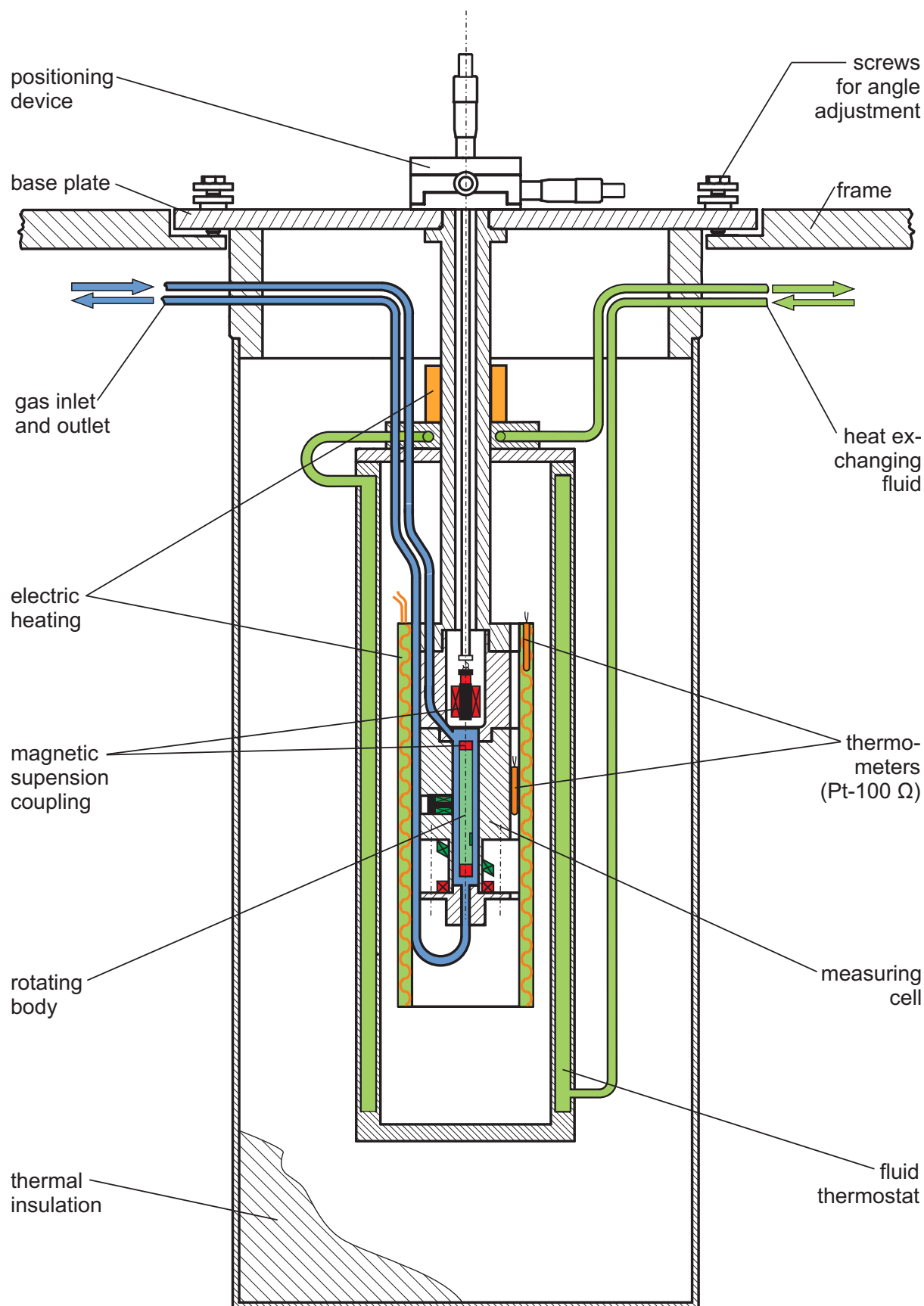


Figure 2.5 Schematic of the low-pressure viscometer. The figure represents the level of development achieved by *El Hawary (2009)*.

2.2 Description of the Viscometer-Densimeter

As mentioned before, the viscometer-densimeter was developed by *Docter et al. (1997)*. *Evers (2001)* simplified the geometry of the measuring cell significantly. Therefore, since then, it was considered possible to measure the viscosity in an absolute way more accurate than it was done by *Docter et al. (1997)*, who measured the viscosity in a relative way, using nitrogen as reference fluid. During the work of *Wöll (2005)*, a new software to automate the measurements was set up. Unfortunately, the apparatus was damaged while measuring moist air during the work of *Wöll (2005)*. *El Hawary (2009)* had to rebuild and replace many parts of the apparatus, including the rotating body, the sinker, parts of the measuring cell, the drive coils, and the balance. Thus, the apparatus was overhauled at the end of the work of *El Hawary (2009)*.

The following section is divided into three parts: in the first part the principle of the single-sinker densimeter and thereafter, in the second part, the principle of the viscosity-measurement principle are explained. In the final part, the technical realization of the viscometer-densimeter is presented.

Theory of the Density Measurement

The single-sinker densimeter and its compact version were developed by *Brachthäuser et al. (1993)* and *Docter et al. (1997)* at the chair of thermodynamics at Ruhr-Universität Bochum headed by Prof. Wagner (*Wagner and Kleinrahm, 2004*). To explain the density measurement principle, a simplified drawing of the measuring cell of the viscometer-densimeter is shown in figure 2.6.

Inside the measuring cell, the rotating body is suspended by a magnetic suspension coupling. As above-mentioned, this coupling consists of an electromagnet, a permanent magnet, a position sensor and a control system. The electromagnet is attached to the underpan weighing hook of the balance. Thus, forces acting upon the permanent magnet inside the measuring cell can be measured with the balance. The vertical position of the rotating body is stabilized and controlled utilizing the control system. Controlled upward and downward movements of the rotating body inside the measuring cell are possible. Two positions are shown in figure 2.6: the tare position (left) and the density measuring position (right).

In the tare position, only the rotating body is magnetically suspended. Thus, the sinker rests on the bottom of the measuring cell and the balance can be tared to zero. To achieve the measuring position (right part of figure 2.6), the rotating body is lifted. In the measuring position, the the sinker is coupled to rotating body and the sinker can be weighed in fluid.

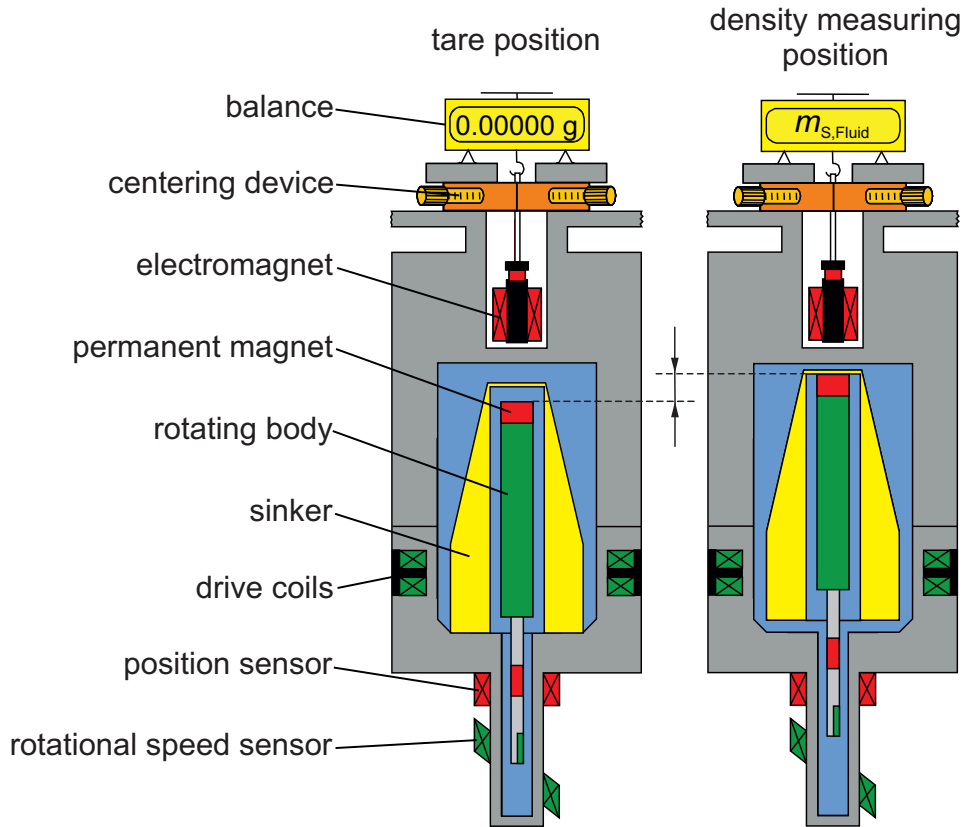


Figure 2.6 Schematic of the measuring cell of the viscometer-densimeter.
(Figure taken from *El Hawary, 2009.*)

Physically, the densimeter is based on Archimedes' buoyancy principle. In the closed measuring cell, the sinker is surrounded by the fluid of unknown density. An upward buoyancy force is exerted on the sinker. This force depends on the density of the fluid and the volume of the fluid displaced by the sinker. The buoyancy force can be determined by comparing the weight of the sinker in vacuum to the weight of the sinker in fluid. The density can be calculated by

$$\rho = \frac{m_{s,vac}^* - m_{s,fluid}^*}{V(T,p)}, \quad (2.6)$$

where $m_{s,vac}^*$ is the result of weighing the sinker by means of a balance in combination with the magnetic suspension coupling inside the evacuated measuring cell, $m_{s,fluid}^*$ is the result of weighing the sinker immersed in fluid, and $V(T,p)$ is the temperature and pressure dependent volume of the sinker. A load compensation mechanism ensures that the balance is operated near its tare position. Systematic deviations aroused by a change in the slope of the characteristic curve over the weighing range of the balance are thereby minimized. For further detail about the current state of the art of the compact single sinker densimeter, see *Richter et al. (2015)*.

Theory of Viscosity Measurement

The principle of viscosity measurement of the viscometer-densimeter is similar to the one of the low-pressure viscometer described in section 2.1. A schematic of the viscometer-densimeter can be seen in figure 2.7 a). In analogy to the low-pressure viscometer, a magnetic suspension coupling serves as an almost frictionless bearing for the rotating body. The rotating body can be accelerated with four drive coils. When the drive is switched off, the rotating body rotates freely and is mainly slowed down due to the viscous drag of the fluid surrounding it. The ferromagnetic cores of the position sensor and the rotational speed sensor are incorporated into a cylindrical sensor rod, located below the main cylinder. Thus, in contrast to the rotating body of the low-pressure viscometer, the rotating body of the viscometer-densimeter is composed of two cylinders with different diameters. Consequently, both the axial moment of inertia J and the viscous coefficient c_{vis} are calculated in a different way for each apparatus, due to the differences in the design of the rotating bodies and the cylinder systems. However, the theory how the signal of the rotational speed sensor is transferred to yield the number of revolutions depending on time is the same as for the low-pressure viscometer (see figure 2.4). This is, therefore, not explained again.

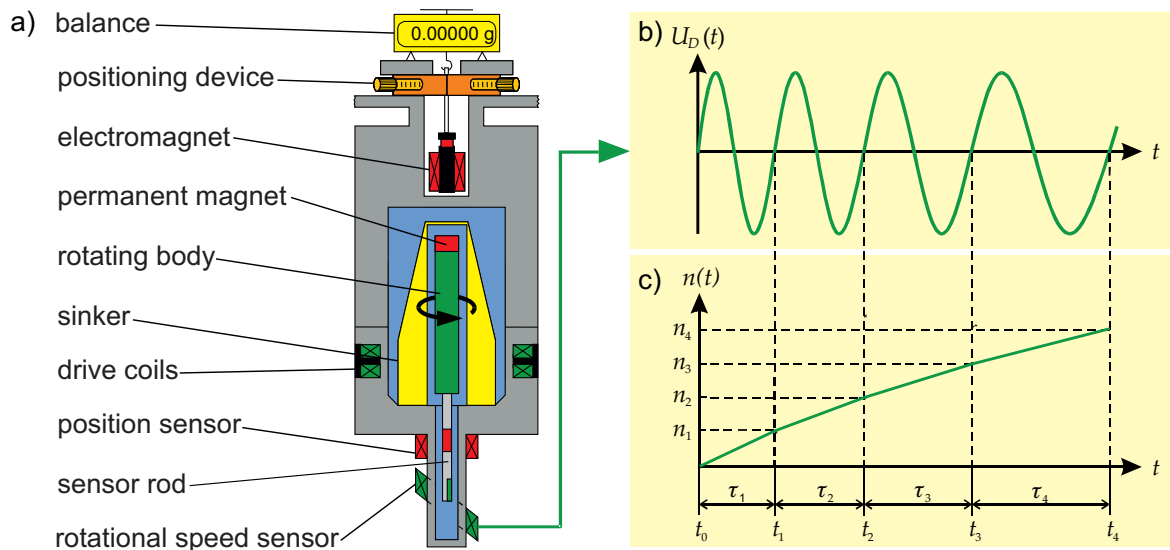


Figure 2.7 Schematic of the viscometer-densimeter presenting the signal for the determination of the viscosity. (Figure taken from *El Hawary, 2009*.)

Technical Realization of the Viscometer-Densimeter

A schematic of the viscometer-densimeter is shown in figure 2.8. As can be seen, the design of the viscometer-densimeter is similar to the low-pressure viscometer's design. The core apparatus was also accommodated in a shock-absorbing frame to prevent

the measuring cell from disturbing vibrations. The thermostatted measuring cell was installed underneath the base plate, which was mounted to the frame using four screws. These screws were used to adjust the angle of the base plate – and the instrument – with a resolution of 0.003° (arc degree). The essential difference to the low-pressure viscometer was the electronic balance, which was placed above the base plate. A device for changing the compensation weights was integrated into the balance. As the electromagnet is connected to the balance the entire balance has to be moved to align the cylinder system. Therefore, the balance sits on a positioning device. The resolution of the micrometer screws were $10\text{ }\mu\text{m}$; their sensitivity was $1\text{ }\mu\text{m}$.

The cylinder system consisted of the rotating body, the sinker, and, of the sensor rod, which was surrounded by a tube. The diameters of the rotating body were 10.6 mm and 3 mm for the main part of the rotating body and the sensor rod, respectively; their lengths were 118 mm and 60 mm, respectively. The width of the annulus between the main cylinder and the sinker was 1.45 mm; 1 mm was the annulus around the sensor rod.

Different materials were used within the viscometer-densimeter. The main part of the rotating body was made of aluminum (AlMg_3). The sinker (mass of 60 g) was made of beryllium copper and titanium. The upper part of the measuring cell was made of beryllium copper (CuBe_2), and the lower part of Inconel.

Thermostating the viscometer-densimeter was almost identical to the low-pressure viscometer. A two-stage thermostat and a thermal insulation cover surrounded the measuring cell. The outer thermostat stage was a double-wall stainless-steel container, and heat exchanging fluid was circulated through, employing a closed dynamic temperature-control system (Julabo, Germany, type: LH85). The temperature of the outer thermostat stage was maintained about 1 K below the measuring cell temperature so that the thermostat was working as a heat sink in the thermostating system. The inner thermostat stage, which contained an electrical heating device, was firmly attached to the measuring cell and was almost completely shielded isothermally by the outer thermostat stage. The temperature of the inner thermostat stage was controlled using a Pt-100 Ω sensor (Merz, Germany, type: P 100/2528) with ITS-90 calibration. The temperature of the measuring cell was measured utilizing an AC resistance thermometry bridge (ASL, UK, type: F17) and a second Pt-100 Ω sensor (Isotech, USA, type: 909/100) with ITS-90 calibration, which was in direct contact with the measuring cell on a level with the rotating body. The pressure was measured with a vibrating-quartz-crystal-type pressure transmitter with a range of 41.68 MPa (Paroscientific, USA, type: 1006 K-01).

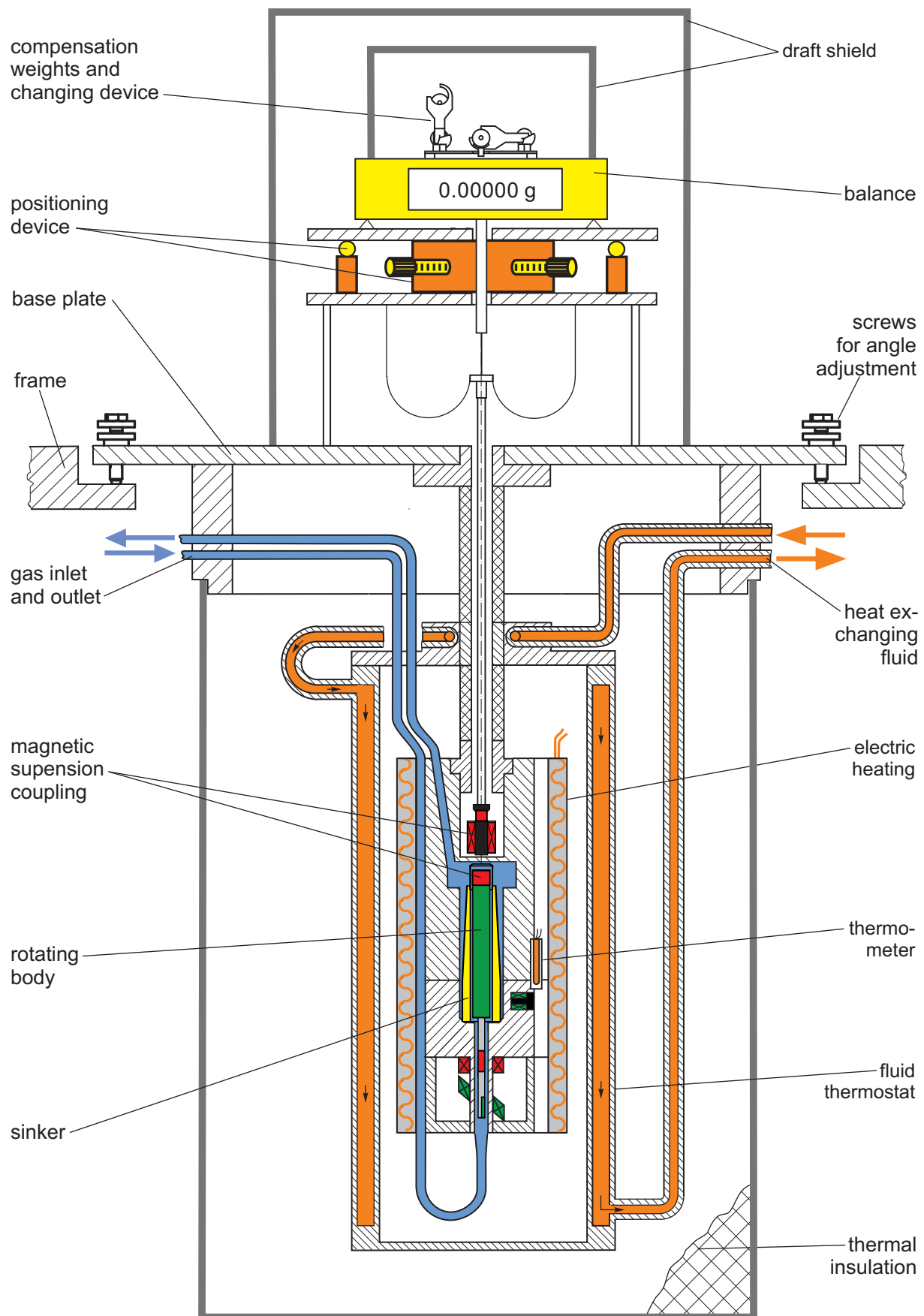


Figure 2.8 Schematic of the viscometer-densimeter, representing the level of development achieved by *El Hawary (2009)*.

3 Improvements to the Apparatuses

The following chapter deals with the technical enhancements, which were realized during this work. The first four sections focus on the enhancements relevant for both apparatuses. Section 3.1 is about a new system for measuring the revolution time and controlling the viscosity-measurement sequence. Thereafter, in section 3.2, a temperature-controlled gas dosing system is presented. Furthermore, improvements considering the vacuum system (section 3.3), and new equipment to measure the suspension height and the temperature (section 3.4) are described. The last two sections deal with apparatus specific enhancements. In section 3.5 it is explained, how the low-pressure viscometer was improved by modifying the positioning device and replacing the rotating body. Changes in the design of the viscometer-densimeter, i.e., the redesign of the measuring cell, are presented in the end of this chapter, in section 3.6.

Both apparatuses were moved into a new laboratory. A photo of the apparatuses in the new laboratory is shown in figure 3.1. From left to right, the temperature-controlled gas-dosing system, the low-pressure viscometer, the viscometer-densimeter and the racks containing the electronics of both apparatuses can be seen.



Figure 3.1 Photo of the low-pressure viscometer and the viscometer-densimeter in the new laboratory.

3.1 A System for Time-Measurement and Automation of the Viscosity Sequence

At the beginning of this work, the low-pressure viscometer was not a stand-alone apparatus, as most of the equipment for measuring the viscosity was used by both apparatuses. When both apparatuses were in operation, the user had to switch between the viscometer-densimeter and the low-pressure viscometer; measurements could not be carried out simultaneously. This hindered a time efficient operation and demanded an elaborate organization of the measurement plans. As can be seen in figure 2.1, both apparatuses shared the time-measurement system, the measurement computer, and special electronics for accelerating the respective rotating body. The combination of these three parts of equipment is called viscosity-measurement system in the following. The special electronics for accelerating the respective rotating body are called drive.

In addition to a missing second viscosity-measurement system, the existing viscosity measurement system was very unreliable. Errors in the time measurement – i.e., errors in the revolution time – occurred on a regular basis. The accelerating process was often aborted due to false revolution times. Therefore, many measurements had to be restarted. If the rotating body was accelerated successfully, errors within the revolution time resulted in wrong damping values, or again in the abortion of the measurement. Damping measurements over a long time span of up to 60 min, as required to determine the residual damping in case of the low-pressure viscometer, were practically not possible (*Schäfer, 2009*). Furthermore, the deterioration of electronic components yielded to multiple downtimes of the time-measurement system. The frequent repair of the time-measurement system was time-consuming because the documentation of the circuitry was incomplete. When the system was out of service, both apparatuses were affected.

Therefore, a new viscosity-measurement system was developed in the term paper of *Humberg (2013a)*. A schematic of the new viscosity-measurement system is shown in figure 3.2. As illustrated in figure 3.2, the new viscosity-measurement system consists of a 19 inch-industry computer (Plug-In Electronic, Germany), two measuring boards (bmcm, Germany, type: PCIBase II MADDA 16), a drive (self-made), a relay box (self-made) and a signal-preparation unit (self-made). In the signal-preparation unit, the signal from the rotational speed sensor is offset, low-pass filtered, then amplified and split into two. Thereafter, the prepared signal is scanned with the two measuring boards. To operate the viscosity-measurement sequence (accelerating the rotating body, starting, and ending the data acquisition) the rotational frequency – i.e., the revolution time – has to be measured in real time. Therefore, a measuring board measures the signal continuously and the rotational frequency is determined using the computer's system time as reference. The system time has an uncertainty of up to 0.5 s, which is, however, sufficient to control the measurement sequence. If the rotating body has to be accelerated, the drive is activated automatically utilizing the relay box incorporating a RS232 port.

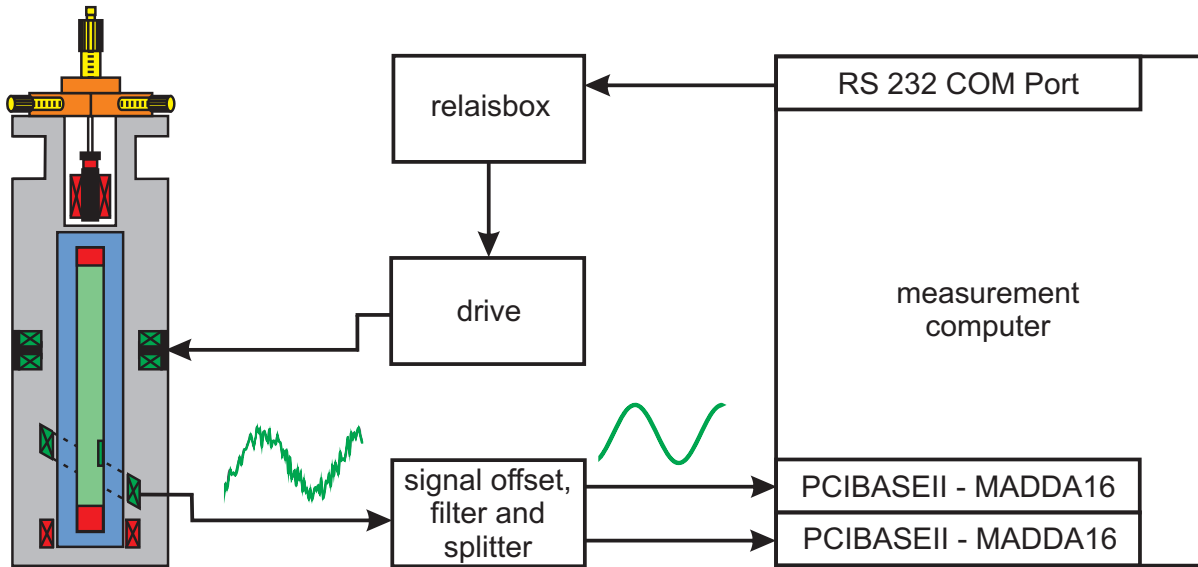


Figure 3.2 Schematic of the system controlling the viscosity-measurement sequence.

When the data acquisition sequence is started, the prepared signal is scanned additionally with the second measuring board very accurately. For this scan a software tool was written (*Humberg, 2013a*), which is run simultaneously and independently of the main measurement software. Thus, the process of controlling the sequence of the viscosity measurement and the accurate data acquisition of the prepared signal are separated. Therefore, this system works very reliable.

The prepared signal of the rotational speed sensor is scanned with a frequency of 100 Hz (100 voltage measurements per second) for a defined time of, e.g., 9 min. After finishing a measurement, the stored signal is analyzed to determine the revolution times. In the first place, the stored signal is slightly averaged. Thereafter, all points are identified, at which the voltage value passes a certain voltage level of, e.g., 1 mV in positive direction. To determine the time of a revolution, it is sufficient to sum up the number of measurements between two following points. Due to the scanning frequency of 100 Hz, the time between two single voltage measurements is 10 ms. Thus, a number of 100 measurements between two points yields to a revolution time of 1 s. In practice, the exact time is calculated by linear interpolation. To determine all revolution times, this procedure is applied for all found points.

The new time-measurement system was validated using the DCF77 reference time signal, which is provided by the German Federal Institute of Physics and Metrology (Physikalisch technische Bundesanstalt). Therefore, the frequency of this signal (77.5 kHz) was scaled down to 100 mHz, which equals a time period of 10 s. This scaled signal was measured using the new time-measurement system over a time span of one hour. The same procedure was applied with the signal scaled down to a frequency of 1 Hz. Within the time span of one hour, the deviation in absolute time was up

to 90 ms. The influence of this deviation to the damping was investigated by adding the observed time deviations to experimentally determined revolution times. Thereafter, the damping was calculated on the basis of the modified revolution times. For a typical measurement of argon (measuring time: 9 min, start frequency: 200 mHz, $D = 1028.568 \mu\text{s}^{-1}$), the damping calculated from the modified revolution times was set off by $\Delta D = +0.03 \mu\text{s}^{-1}$. This equals an offset in viscosity of 0.003 %, taking helium at $T = 298.15 \text{ K}$ and $p = 0.1 \text{ MPa}$ as example. The same test was done for a vacuum measurement (measuring time: 60 min, starting frequency: 200 mHz, $D = 13.255 \mu\text{s}^{-1}$). A deviation of $\Delta D = +0.0003 \mu\text{s}^{-1}$ was observed, although the offset in absolute time was 90 ms. The reason for the little difference is most likely that eq. (2.1) reproduces the number of revolutions in vacuum with a relatively high uncertainty (see appendix of *Humberg (2015)* for deviation plots). Therefore, deviations in time do not affect the measured vacuum damping that significantly.

As a further validation, the damping was simultaneously measured using the previous time-measurement system developed by *Docter et al. (1997)* and the new time-measurement system. For the validation the damping of helium at $T = 333.15 \text{ K}$ and $p = 0.2 \text{ MPa}$ was chosen. All parameters (e.g., measurement time, start and stop frequencies) were kept equal. The results of this test are shown in figure 3.3, in which the damping values determined with Docter's time-measurement system and the damping values determined on the basis of measurements with the new time-measurement system are compared. As can be seen, the average of the damping values is very similar. Furthermore, the scatter of the new system's damping values is lower than the scatter of Docter's system.

With regard to figure 3.3, the new time-measurement system is considered to be as accurate as the previously used one. The accuracy in time can be improved by

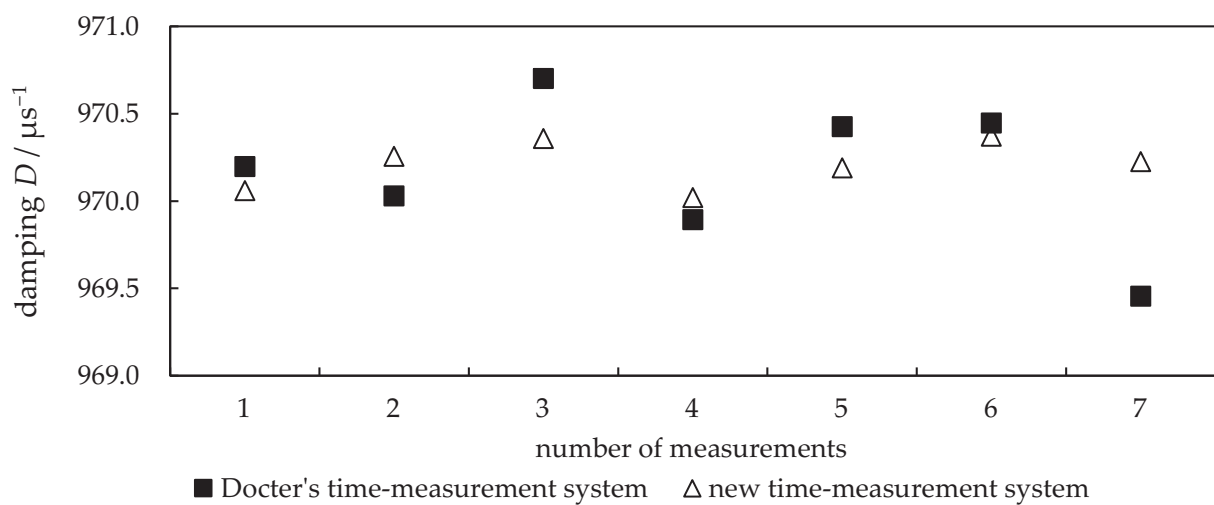


Figure 3.3 Comparison of the damping values calculated using Docter's and the new time-measurement system. (*Humberg, 2013a*)

integrating a better measuring card, or by simultaneously measuring the DCF77 signal. The second approach is difficult, as the reception of the signal is hindered by the location of the apparatuses in the building. The first approach is technically feasible, however, the observed deviations are almost negligible. The accuracy of the time measurement is not the main source of the uncertainty in viscosity, as it is discussed in chapter 4. Therefore, from an experimental point of view, the new time-measurement system fulfills all requirements.

In conclusion, the development of the new system for controlling the viscosity-measurement sequence and measuring the revolution time is a major improvement to both apparatuses. The apparatuses can now be operated independently, which saves a significant amount of time. Docter's system was successfully replaced.

3.2 A Temperature-Controlled Gas-Dosing System

The elaborate handling of gaseous mixtures is fundamental to ensure that the composition of the mixture is not changed during the transfer from the sample cylinder to the apparatus. A reason for a shift in composition can be the condensation of one mixture component. Condensation could likely occur, when carbon dioxide-rich mixtures are handled, as is explained in the following.

A gas-dosing system which is not temperature-controlled has a temperature close to the ambient temperature of about 294.15 K. Taking a $\text{CO}_2\text{-N}_2$ mixture with $x_{\text{CO}_2} = 75 \text{ mol-}\%$ (and $x_{\text{N}_2} = 25 \text{ mol-}\%$) at pressures of 12 MPa as an example, the state of the sample fluid inside the gas-dosing system is close the mixture's dew line. Hence, a temperature decrease of only 10 K within the gas-dosing system, e.g., while expanding a $\text{CO}_2\text{-N}_2$ mixture down to $p = 10 \text{ MPa}$, leads to condensation. However, condensation can be avoided by heating the gas-dosing system to a temperature of 323.15 K, which is higher than the critical temperature of carbon dioxide.

Initially, the most time efficient approach to fulfill this requirement was first considered to be the modification of the gas-dosing system of *El Hawary (2009)*, which was not temperature-controlled. El Hawary's gas-dosing system was very spacious. Consequently, a relatively large temperature-control system would have been necessary. Furthermore, the valves were mounted directly onto the metal frame of the gas-dosing system. This hindered an energy efficient temperature-control, as a great heat loss to the frame was expected. In addition, the valves were worn out and the entire system was contaminated with lubricant. Against this background, it was decided to develop a new temperature-controlled gas-dosing system. This new system was set up during the term paper of *Herrndorf (2012a)*.

An overview of the new temperature-controlled gas-dosing system is given in figure 3.4. The functionality of the system is described in the following on the basis of this

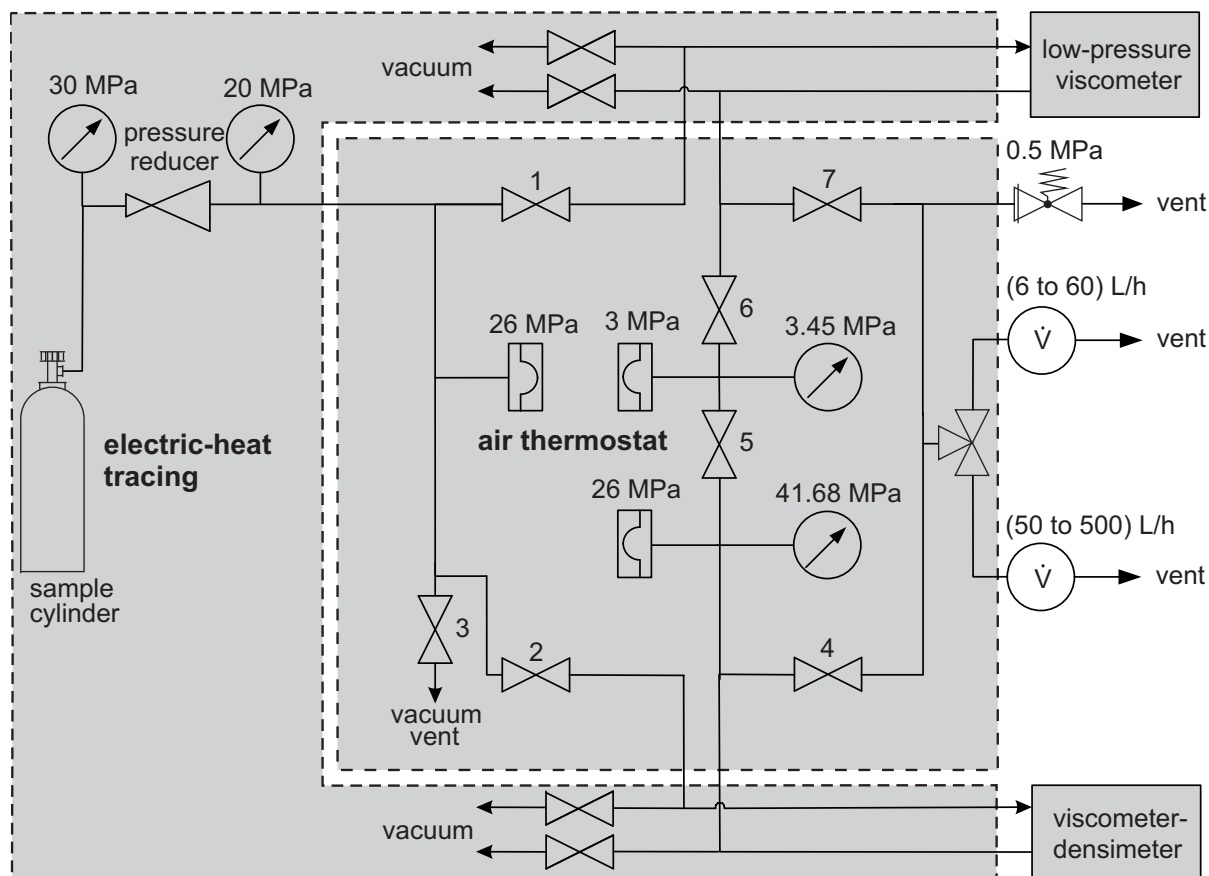


Figure 3.4 Schematic of the piping and instrumentation of the new temperature-controlled gas-dosing system. The vacuum system is not shown.

schematic. The sample cylinder is found on the left side of figure 3.4. In order to fill the apparatuses with the sample fluid, first the sample fluid is expanded with a pressure reducer. The low-pressure viscometer is filled via valve 1; the viscometer-densimeter with valve 2. The sample fluid can be released from the left part of the piping using valve 3. Furthermore, the outlet of valve 3 is suitable to evacuate the piping. When filling, the sample fluid reaches the pressure transmitters after it has passed the apparatuses. In this way, a possible contamination of the sample fluid can be avoided. The two pressure transmitters are separated by valve 5. However, valve 5 can be opened to connect both pressure transmitters. With valve 6 being closed and valve 5 being open, the pressure transmitter of the low-pressure viscometer can be used for measuring the pressure of the viscometer-densimeter. This is advantageous, as the pressure transmitter of the low-pressure viscometer has a lower uncertainty as the pressure transmitter utilized for the viscometer-densimeter. After filling the apparatuses, the sample fluid can be released from the low-pressure viscometer using valve 7; for the viscometer-densimeter using valve 4. Two different volume-flow meters are available to observe the volume flow of the sample fluid being vented. Thereby, a wide volume-flow range of (6 to 500) L/h is covered. As the outlet of both apparatuses is combined, both volume-flow meters

can be used separately for each apparatus. The volume-flow meters of the gas-dosing system are protected against overpressure by a safety valve.

Concept and Equipment for Controlling the Temperature

As it is indicated in figure 3.4, two concepts were used to control the temperature: (1) The pipes, the sample cylinder and the pressure reducer of the gas-dosing system are temperature-controlled by electric-heat tracing. (2) The rest is temperature-controlled using an air thermostat, which includes the valves, the pressure transmitters and the bursting discs. In the following, the set-up of the air thermostat is described. The technical drawings of the air thermostat can be found in *Herrndorf (2012a)*.

Four photos of the air thermostat are shown in figure 3.5. As visible in figure 3.5 a), the basis for fixing the valves is a perforated plate mounted to a base plate. The valves are installed on the front side of the perforated plate. The two pressure transmitters are mounted on the back side. The perforated plate is surrounded by the two housings; the base plate is the bottom of the inner housing. The outer housing is depicted in figure 3.5 b). Both housings can be seen in figure 3.5 c), where a top view of the system is shown. The top plates of both housings are removed in figure 3.5 c). When the tops are installed, the sole opening of the inner housing is at the front, in opposition to a fan heater. The fan heater (RO/SE Blechverarbeitung, Germany, type: HH400), is a fan, which incorporates electric heating. Its temperature is controlled using a Pt-100 Ω temperature sensor and a multi-channel temperature-controller (Horst, Germany, type: HT60). The fan heater rests on two supports visible in the back of figure 3.5 b). The inner housing rests on the four other supports. Thus, a distance of 10 cm between the inner and the outer housing is observed for all six sides. As can be seen in figure 3.5 c), the valves are incorporated in the inner housing. To enable the operation of the valves, their handles were replaced by octagonal rods (wrench size 13 mm). The end of the rods is visible in figure 3.5 d). A torque of 2.5 Nm was found to be sufficient for closing the valves. It is recommended to utilize a torque wrench to observe this torque to prevent the wear out of the valves.

When the air thermostat is in operation, the fan heater circulates and heats the air inside the housings. As the sole opening of the inner housing is at its front, the heated air is forced to flow around the inner housing's outer side before entering it. In this way, the components mounted on the perforated plate are thermostatted evenly. Four simple temperature sensors are displaying the temperatures of the valves for filling the apparatuses and venting sample gas (valves 1, 2, 4 and 7). Thus, temperature changes due to the expansion of the gases can be observed.

As mentioned before, the pipes are thermostatted utilizing electrical heat tracing. A photo of this system is shown in figure 3.6. As can be seen, two pipes (Swagelok, USA, type: SS-T2-S-028-6ME) (fluid inlet and fluid outlet) are in direct contact to the electrical-

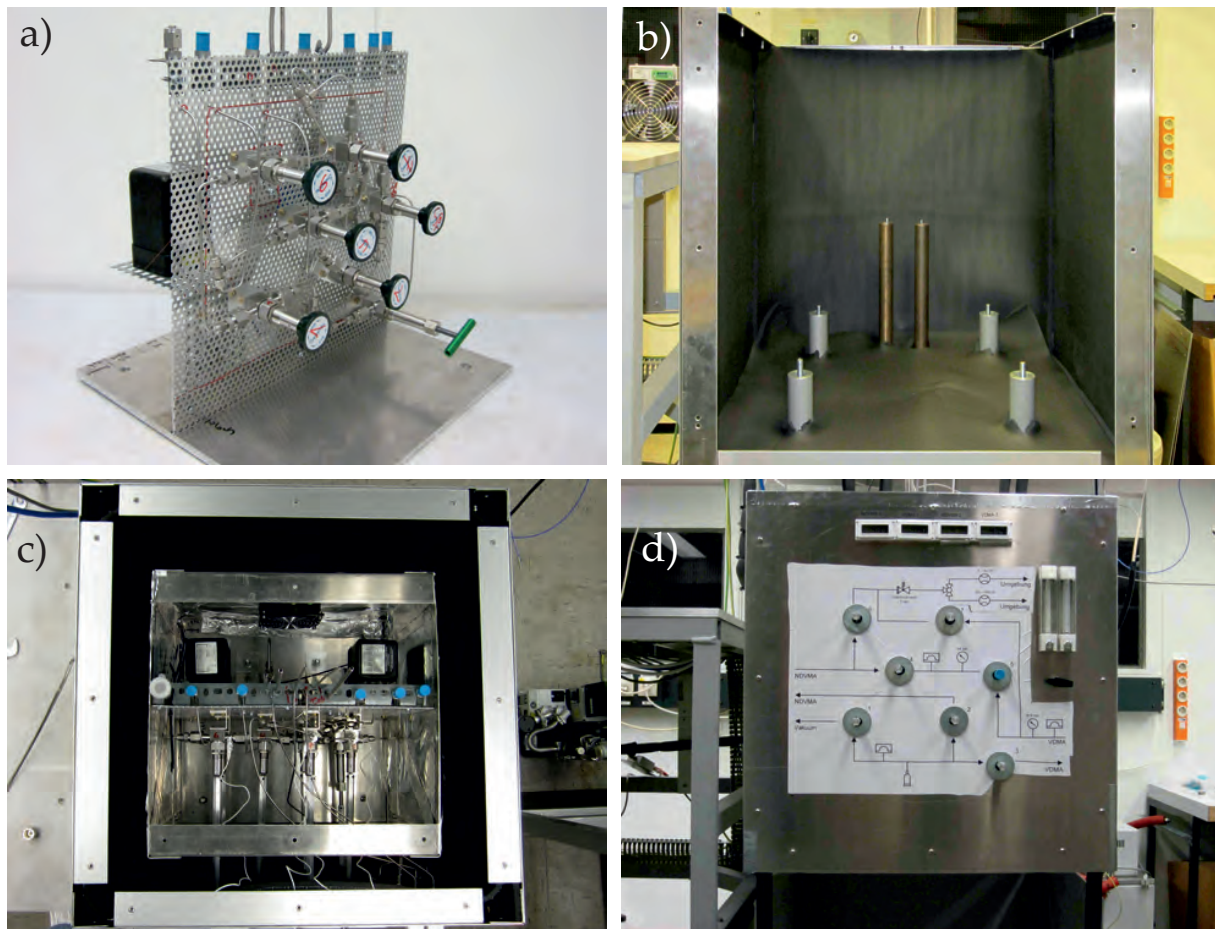


Figure 3.5 Four photos of the temperature-controlled gas-dosing system developed by Herrndorf (2012a). Shown is:
 a) the perforated plate with the valves and pressure sensors installed,
 b) a view into the outer box,
 c) an insight of the interior with removed top,
 d) the front view without insulation.

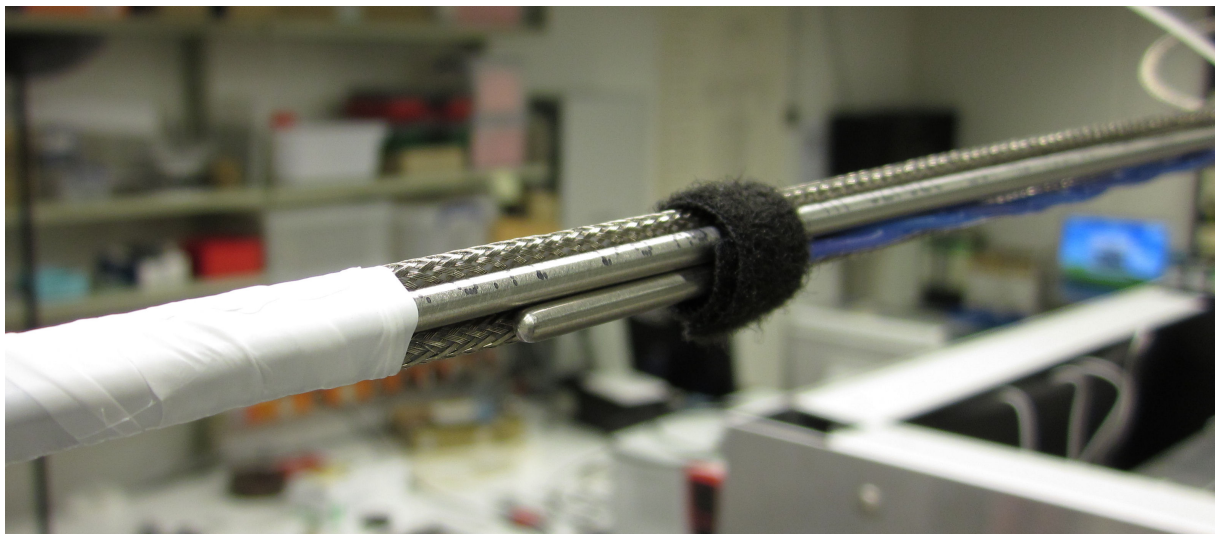


Figure 3.6 Photo of the electrical heating system for the pipes. A platinum resistance thermometer for controlling the temperature is visible.

heat tracing (Horst, Germany, type: HS-450°C). To improve the heat transfer, the bundle is wrapped in Teflon tape. The temperature is measured with a Pt-100 Ω platinum resistance thermometer (Horst, Germany, type: Pt100/250°C), which is wrapped into the bundle, as shown in figure 3.6. Therefore, this thermometer is in direct contact with both the pipes and the heating element. To control the temperature inside the bundle, the same the multi-channel controller (Horst, Germany, type: HT60) is used, which controls the temperature of the fan heater. The thermostatted piping is insulated (Armacell, Luxemburg, type: Armaflex).

Further Equipment of the Gas-Dosing System

The gas-dosing system consists of commercially available standard parts to a great extend. These parts are presented in the following. First it is explained, how suitable valves were chosen. It was observed that the valves used by *El Hawary (2009)* (Swagelok, USA, type: SS-3NRS6MM-PK) had two unfavorable features: (1) The tip of the stem was rotating when actuating the valve; (2) The valves incorporated a lubricated packing made of polymer (polyetheretherketone). These two features resulted in severe problems. As the tip of the valves was rotating when actuating the valve, the stem of the valves was worn out and leaking; swarf did separate from the stem. Especially the lubricated packing was an unfavorable choice. When the gas-dosing system was evacuated, the lubricant diffused into the tubes and contaminated the entire apparatus, including the measuring cell. In addition to this, packings are not fully leak tight. Therefore, a packing has to be re-tightened to minimize the leakage (*Docter, 1992*). If this is not done elaborately, the packing can be destroyed; in the worst case, the entire apparatus is contaminated with particles of a destroyed packing; see *El Hawary (2003)*. Furthermore, the sample fluid can diffuse into the packing. Thereby, the packing can be destroyed, e.g., in case of carbon dioxide as sample fluid. Furthermore, a packing (e.g. made of PEEK) acts like a “sponge” for the sample fluid. Thus, a newly filled-in sample fluid can be contaminated by residuals in the packing. In general, any surface not made of metal endorses sorption effects whereby the composition of a mixture can be changed. Thus, metal surfaces should be preferred. In summary, the previously utilized valves were not suitable. Against this background, the following demands for an appropriate valve were stated: a non-rotating stem, which is made of metal, and a full-metal sealing instead of a packing. Further demands concerning the valves were a working pressure of 20 MPa with temperatures up to 333.15 K, an easy-to-handle fitting for connecting the valve to the tube system, and a room-saving design.

Two types of valves (Swagelok, USA, type: SS-4BRG-V51 and SS-4URG-V51) fulfilled most requirements. These valves are bellows sealed to atmosphere, the VCR-fitting is easy to handle and the valves are small. Unfortunately, the operating pressure of these

valves was limited to $p = 7$ MPa and $p = 17.2$ MPa for the types SS-4BRG-V51 and SS-4URG-V51, respectively (Swagelok, 2011). However, a safety factor of 4 was stated for both valve types (Böcker, 2011). According to this specification, the bursting pressures for the SS-4BRG-V51 and the SS-4URG-V51 are 28 MPa and 68.8 MPa, respectively. To investigate the valves' robustness, in-house hydraulic pressure tests were undertaken (Daun, 2012). A pressure of 20 MPa was applied to the bellows 40 times. The valves passed this pressure-cycling test and were not destroyed up to pressures of 25 MPa with the pressure applied to the bellows. If the pressure is applied to the stem, the bursting pressure is higher than 30 MPa. Thus, both types of valve passed these tests. Therefore, these valves were chosen for the application in the gas-dosing system.

In addition to the valves, further equipment was integrated into the gas-dosing system. As can be seen in figure 3.5 d), two volume-flow meters (Krohne, Germany, type: DK800/R) were installed on the front plate of the air thermostat in the upper right region. These meters cover a flow rate of (6 to 60) L/h and (50 to 500) L/h, respectively. Although the flow rate is only valid for air at $T = 293.15$ K, the reading is a valuable measure for the volume flow. The outlet of the measuring cells of both apparatuses is combined in one pipe. Thereafter, the fluid flow is directed to a ball valve. It is possible to switch between the two volume-flow meters using the ball valve. The volume-flow meters are protected against overpressure with a safety valve (Swagelok, USA, type: SS-RL3M4-F4-MO, spring type: 177-13K-RL3).

The pressure sensors are also protected against overpressure. For the low-pressure viscometer's pressure sensor a bursting disc with a bursting pressure of 3 MPa (Schlesinger, Germany, type: B12,5rn30-031) was chosen. The pressure sensor of the viscometer-densimeter is protected by a bursting disc (Schlesinger, Germany, type B12,5r260-03L) with a bursting pressure of 26 MPa. The same bursting disc is applied to limit the pressure in the piping between the sample cylinder and the valves 1, 2 and 3.

In summary, a new gas-dosing system was designed and set up. Full metal sealed bellows valves with a non-rotating stem were chosen. Thereby, the valves are expected to be durable, effects caused by sorption and diffusion are minimized, and the valves can be evacuated to high vacuum. Purging of the apparatuses can be controlled with two volume-flow meters. To avoid condensation, the entire system is temperature-controlled utilizing electric heat tracing and an air thermostat.

3.3 Overhaul of the Vacuum System

The vacuum system is essential for the operation of both apparatuses: The gas-dosing system and the measuring cell have to be evacuated multiple times during every fluid exchange; the vacuum weight of the viscometer-densimeter's sinker and the residual damping of both apparatuses are measured in vacuum. There are two requirements

for the vacuum system: (1) realization of vacuum pressures $\leq 5 \cdot 10^{-5}$ hPa, and (2) the vacuum pressure has to be measured accurately, as the vacuum pressure is needed to extrapolate the damping measured in vacuum to the limit of zero density for the determination of the residual damping.

The vacuum system of *Evers (2001)* fulfilled these requirements and was therefore not changed by *Wöll (2005)* or *El Hawary (2009)*. It consisted of a turbo-molecular pump, a rotary-vane pump and two vacuum sensors. A turbo-molecular pump can achieve very low vacuum pressures of 10^{-10} mbar (*Frank, 1982*). Using a turbo-molecular pump avoids the diffusion of oil from the vacuum pump into the gas-dosing system and the measuring cell.

However, due to its age, the vacuum system needed to be overhauled. The improvements concerning the vacuum system are summarized in the following. A new rotary-vane pump (oerlikon leybold vacuum, Germany, type: TRIVAC D 2,5 E) is now used to provide the fore-vacuum for the turbo-molecular vacuum pump. In addition, a leaking vacuum valve located between the two pumps was replaced. This valve is used to vent both pumps after usage. These improvements made the vacuum system considerably more efficient, almost reducing evacuation times by half.

Furthermore, both vacuum sensors were broken. Thus, the vacuum system was equipped with two new vacuum sensors (Pfeiffer Vacuum, Germany, type: PKR 261). The new sensors have a measuring range from ambient pressure down to $5 \cdot 10^{-9}$ hPa. The manufacturer states a relative expanded uncertainty ($k = \sqrt{3}$) of 30 %.

Both apparatuses were equipped with two additional bellows valves (Swagelok, USA, type: SS-4BRG-V51) located in the gas-supply tubes close to the thermal insulation of the apparatuses. Thereby, the vacuum pump can be connected to the tubing close to the measuring cell. Low vacuum pressures can be achieved in this way. The new sensors can be connected up- and downstream of the measuring cell. This is advantageous to determine the vacuum pressure inside the measuring cell, as the vacuum pressure increases with distance to the vacuum pump. A good estimate of the vacuum pressure inside the measuring cell can now be made by averaging the two readings.

Further improvement was made to the sealing of the vacuum equipment. Now, all connections are sealed by metal, i.e., aluminum gaskets are used for the vacuum flanges; otherwise VCR-gaskets (Swagelok, USA) are used. However, the vacuum is limited in case of the low-pressure viscometer. There, the measuring cell is sealed by two non-metal O-ring gaskets.

When setting up the vacuum system, a distance of at least 0.5 m between the vacuum sensors and the thermal insulation hood has to be observed, as the vacuum sensors incorporate strong permanent magnets. To enable this distance, vacuum tubes with a nominal diameter of KF25 and a length of 1.5 m are used.

3.4 Equipment to Measure the Rotating Body's Suspension Height and the Temperature

New equipment to measure the suspension height of the rotating body and to control and measure the temperature of the measuring cell and the inner thermostat stage was integrated into the apparatuses. The following section describes this new equipment and the replacements to point out the improvements and to document the changes.

Measurement of the Position Sensor's Voltage Signal

During the commissioning of the low-pressure viscometer, the cylinder system has to be aligned in vertical direction. Therefore, the vertical distance of the electromagnet to the pressure separating wall of the measuring cell is changed in small steps and the damping is measured at each position. The damping depends on the distance of the electromagnet to the pressure separating wall of the measuring cell; a parabolic function is observed. The minimum in the damping values is the best estimate for the concentric position of the cylinder system in vertical direction.

It is possible that the viscous coefficient of the disc flow c_{disc} (eq. (4.8)) depends on the free space above the disc. This is discussed in section 4.3.5. Furthermore, possible changes of the suspension height depending on temperature have to be investigated. Therefore, the knowledge of the suspension height matters.

A voltage signal, which comes from the position sensor, can be taken as a measure for the suspension height. Thus, a digital multimeter (Keithley, USA, type: 195A) was included into the low-pressure viscometer to measure the voltage signal of the position sensor. The readings of the voltage signal were integrated into the measurement reports of each viscosity measurement. The same approach was applied in case of the viscometer-densimeter, where a similar digital multimeter (Prema, Germany, type: 6001) was used.

Improvements to the Temperature-Control and Measurement Systems

As visible in figure 2.1, only one measurement computer was utilized by *El Hawary (2009)* for both apparatuses. This computer also controlled the measuring cell temperature of the viscometer-densimeter. The PID-algorithm to control the measuring cell temperature was integrated into the software developed by *Wöll (2005)*. Thus, downtimes of the software resulted in an interruption of the temperature-control. Waiting to retrieve the set-point temperature was time consuming. Furthermore, the viscosity measurement was often disturbed, because the same measuring card (bmcm, Germany, type: PC20TR) was utilized simultaneously for reading the revolution time using TTL-signals and for

sending the control variable to the power controller of the electrical measuring cell heating.

Against this background, an independent system for controlling the viscometer-densimeter's measuring cell temperature was set up. Parts of the previous system were reused for the new temperature-control system, e.g., the digital multimeter (Prema, Germany, type: 6001) and the thyristor power switch (Juchheim, Germany, type: TYA-110/3). As temperature-control computer, a standard desktop computer was utilized, which was equipped with a GPIB measuring card (Keithley, USA, type: PCI488). The measuring cell temperature is now measured and plotted in real time using a newly developed software in Visual Basic 6 (Microsoft, USA). To control the temperature, a PID-algorithm was implemented into the new software. As actuating variable a voltage signal of (0 to 10) V is delivered to the thyristor power switch, using a standard measuring card (bmcm, Germany, type: PCI Base II MADDA 16).

In addition to setting up a new temperature-control computer, different parts of the temperature-control system were replaced. The previously utilized AC resistance thermometry bridge (ASL, UK, type: F250) was replaced by a more accurate AC resistance thermometry bridge (ASL, UK, type: F17). In addition, the electric heating of the measuring cell of the viscometer-densimeter was renewed.

Further improvements were made to the outer thermostat stage, which consists of a double-wall stainless steel container filled with heat exchanging fluid, as described in section 2.1. Due to wear out of the previous closed dynamic temperature control system, a new system (huber, Germany, 510w) was integrated into the low-pressure viscometer. Furthermore, the fittings of the inflexible tubes connecting the double-wall stainless steel container with the circulation thermostat were not leak tight in case of both apparatuses. These tubes were replaced by flexible metal tubes (Swagelok, USA, type: SS-FJ8TM12TM112-40CM). Thereby, the double-wall stainless steel containers can now be mounted much easier.

3.5 Enhancements of the Low-Pressure Viscometer

Most enhancements of the low-pressure viscometer – e.g., the development of the new time-measurement system, the separation of the two apparatuses or the development of a temperature-controlled gas-dosing system – are described before this section, as these enhancements apply for both apparatuses. However, in addition, the positioning device was improved and the rotating body of the low-pressure viscometer were replaced. The following section deals with these two improvements.

3.5.1 Improvement of the Device for Aligning the Cylinder System

The model function of the low-pressure viscometer is based on a concentric cylinder system. In addition to that, the viscosity is very sensitive to inaccuracies of the centering. Thus, the requirements for the positioning device concerning handling and precision are high.

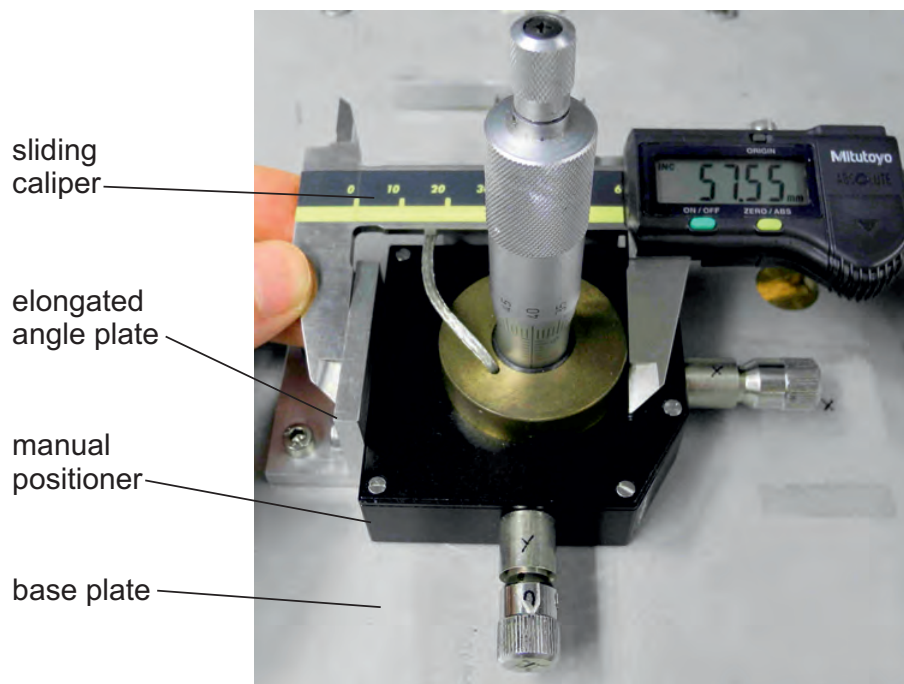


Figure 3.7 Photo of the enhanced positioning device of the low-pressure viscometer. It is shown, how the horizontal x -position of the manual positioner located on top of the base plate is measured using a sliding caliper.

In case of the low-pressure viscometer, the position of the electromagnet was changed in small steps of $30\text{ }\mu\text{m}$ in two horizontal and one vertical axis to center the cylinder system. The damping was measured at each position. The minimum of the damping values is the best estimate for the centric position.

However, it was very challenging to adjust the manual positioner in a reproducible way. *El Hawary (2009)* re-installed the manual positioner (Micos (now Qioptiq), Germany, type: FV-65), which was already used by *Evers (2001)* for the prototype of the low-pressure viscometer. A photo of this manual positioner is shown in figure 3.7. As can be seen, only the vertical micrometer screw has a scale; the two horizontal micrometer screws do not. Thus, it was difficult to determine the exact horizontal position. However, the exact knowledge of the horizontal position is fundamental for centering the cylinder system. As a workaround, the adjustment of the screw was determined by counting the revolutions of the screws. In practice, this has proven to be error-prone.

Against this background, the angle plates connecting the manual positioner to the base plate were rebuilt elongated. With this refinement, the change in the horizontal position of the manual positioner could be determined with a digital caliper, as it is shown in figure 3.7. This simple solution was easy to implement and has proven to be reliable. The technical drawing of the elongated angle plate can be found in this work's appendix, section A.1. The resolution of a common digital caliper is 0.01 mm. For the aligning procedure this resolution is sufficient, as only differences in length have to be determined; not the absolute length. Thus, a common digital caliper can be used.

3.5.2 Rebuild of the Rotating Body of the Low-Pressure Viscometer

The rotating body falls on the bottom of the measuring cell, when the magnetic suspension coupling is switched off. In some cases the rotating body hits the top of the measuring cell instead. The permanent magnet can be damaged severely by these shocks. Consequently, the rotating body, i.e., most likely the permanent magnet, was damaged during the master's thesis of *Schäfer (2009)*. How the rotating body was rebuilt, is subject to this section.

The design of the rotating body of the low-pressure viscometer was first described by *Sauer (2001)*, in whom's student work the set up of the low-pressure viscometer was presented first, in addition to the dissertation of *Evers (2001)*. This design was adopted for the rebuild and was not changed, as the measurement system did work reliably in the past. The technical drawings of the rotating body can be found in *Sauer (2001)* and in *El Hawary (2009)*.

The fluid-dynamic model is based on a concentric cylinder system. Even small uncertainties in geometry, e.g., of 5 μm , result in a significant uncertainty in viscosity, when the viscosity is measured in an absolute way. Thus, the deviations in the outer radius of the rotating body have to be kept minimal, i.e., the radius has to be constant all over the height of the rotating body. Uncertainties can also yield from an inaccurate bearing. Deviations between the magnetic and the geometric symmetry axes have to be minimal.

Against this background, the new permanent magnet was selected very carefully. The permanent magnet is made of samarium cobalt ($\text{Sm}_2\text{Co}_{17}$). The same type of permanent magnet (Arnold Magnetic Technologies, Switzerland, type: Recoma 28) was chosen as it was used by *Evers (2001)*. A number of 50 permanent magnets were fabricated by Arnold Magnetic Technologies and their magnetic fields were scanned by the manufacturer. The angle deviation of the selected permanent magnet was only 0.12° (*Arnold Magnetic Technologies, 2010*); angle deviations of up to 5° are common for this type of permanent magnet. The same materials that were selected by *Evers (2001)* were chosen otherwise. An overview of the different materials is given in section 4.3.3.

The rotating body was assembled by Medizintechnik Quast, Essen, Germany. The geometries of the rotating body were measured using a coordinate-measuring machine. The results are presented in section 4.3.1. Furthermore, the mass of the rotating body was measured by hydrostatic weighing, which is described in section 4.3.2. In addition, the rotating body's axial moment of inertia was calculated, see section 4.3.3.

An outcome of this work is that the uncertainties in viscosity were about 1.70 %, when the viscosity was measured in an absolute way. As stated in sections 4.3.3 and 4.3.5, the uncertainties in viscosity most likely result from uncertainties in geometry and in the magnetic bearing. However, great importance was attached to the geometry's accuracy and the selection of the permanent magnet during the manufacturing process of the rotating body. Concerning the geometries and the magnetic bearing, the limits of accuracy may be reached by now.

3.6 Improvements to the Viscometer-Densimeter

During this work the viscometer-densimeter was commissioned by *Herrndorf (2012b)*. However, severe problems with the viscosity measurement were discovered by *Herrndorf (2012b)*. When the density was measured in between a series of viscosity measurements, large offsets of more than 4 % in viscosity were observed.

How the viscometer-densimeter was enhanced to minimize the scatter, is described in this section. At first, the system developed by *Evers (2001)* and used by *Wöll (2005)* and *El Hawary (2009)* is evaluated. This system was improved in this work, see section 3.6.2. A new positioning device is presented in section 3.6.3. At the end of this section the achievements are evaluated.

3.6.1 Evaluation of the Former Viscosity-Density Measurement System

The special feature of the viscometer-densimeter is the simultaneous measurement of viscosity and density. Therefore, the sinker was utilized as the outer boundary of the cylinder system for the main part of the rotating body. In fact, this design is accompanied by a disadvantage: both, the positions of the sinker and the rotating body are not fixed. However, even a small change in the annulus between the sinker and the rotating body has a large influence on the measured viscosities. To solve this problem, *Docter et al. (1997)* and *Evers (2001)* inserted a centering plate for the sinker at the bottom of the measuring cell. The system of *Evers (2001)* is shown in figure 3.8.

In the system shown in figure 3.8, the sinker was placed onto the centering plate after measuring density and, thus, before measuring the viscosity. Therefore, a small clearance of at least 20 μm between the sinker and the centering plate was necessary. Furthermore, a second clearance was required to position the centering plate inside

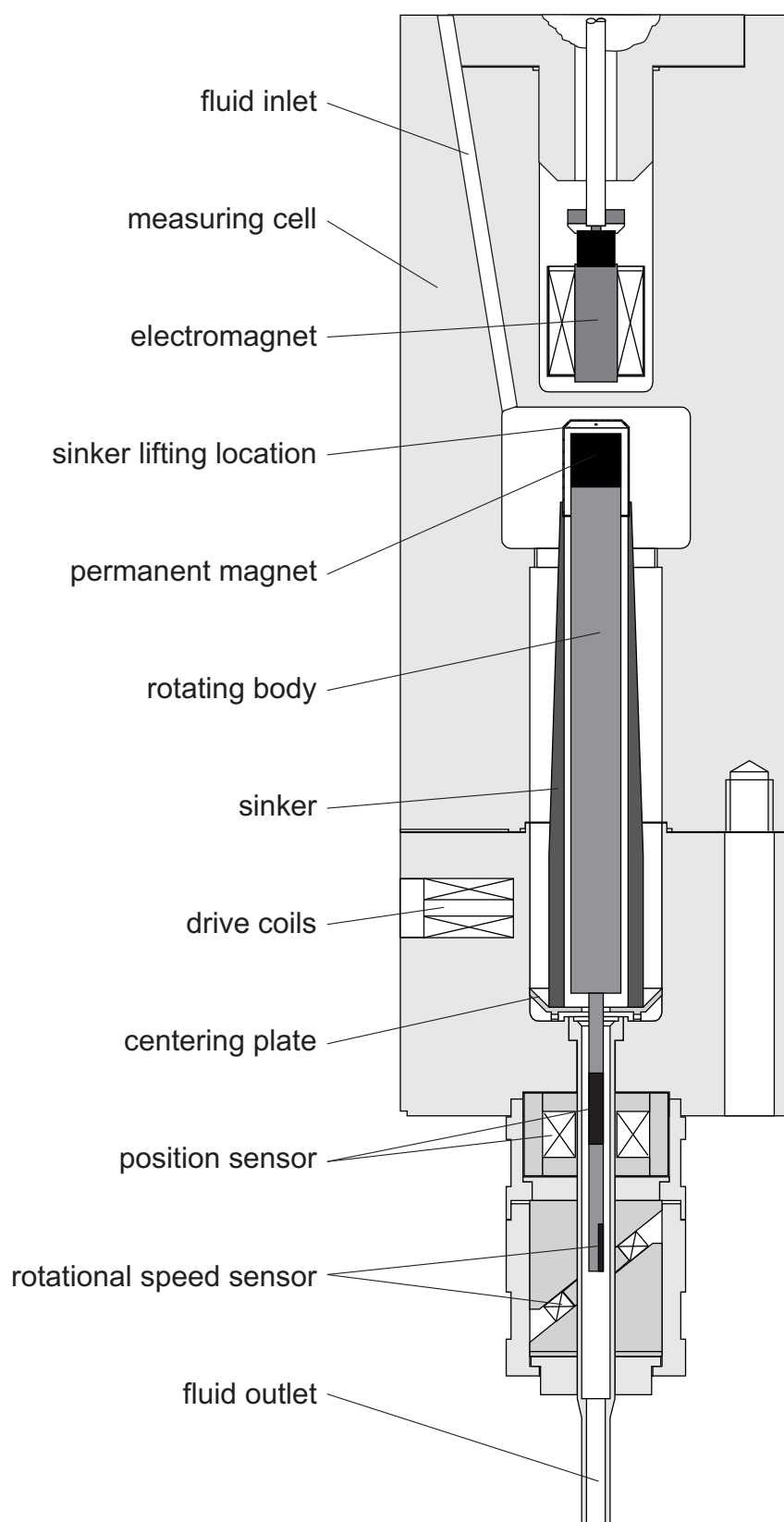


Figure 3.8 Schematic diagram showing the measurement system of the viscometer-densimeter developed by Evers (2001).

the measuring cell. These clearances had to be kept minimal to minimize the scatter in viscosity. On the other hand, the clearances had to be large enough, for that the sinker fitted into the centering plate and the centering plate could be installed inside the measuring cell. All geometries had to be fitted to each other to achieve a low scatter in viscosity.

Wöll (2005) had to rebuild the sinker, because it was destroyed during the measurements. Consequently, he had to rebuild the centering plate, and to rework the measuring cell. Wöll (2005) reported that a clearance of 15 μm between the measuring cell and the centering plate resulted in relative deviations of 0.5 % in viscosity; in combination with a clearance of 25 μm between the sinker and the centering plate yielded relative deviations of 2 % in viscosity. This was way higher than the relative expanded combined uncertainty ($k = 2$) of $U_c(\eta) = 0.25\%$ stated by El Hawary (2009).

After the apparatus - including the sinker and rotating body - was damaged by moist air during the work of Wöll (2005), El Hawary (2009) rebuilt the sinker and the centering plate again. This time, the centering plate was press fitted into the measuring cell. Thus, the clearance between the centering plate and the measuring cell was minimized.

However, at the beginning of this work, a large scatter in viscosity was observed again. An example for the scatter in viscosity using the system of Evers *et al.* (2002) is given in figure 3.9 (Humberg, 2013b). In between the viscosity measurements, the density was measured and thus the sinker was moved. A scatter of up to 2 % in viscosity can be observed. Without lifting the sinker, the viscosity scatter is much lower. Therefore,

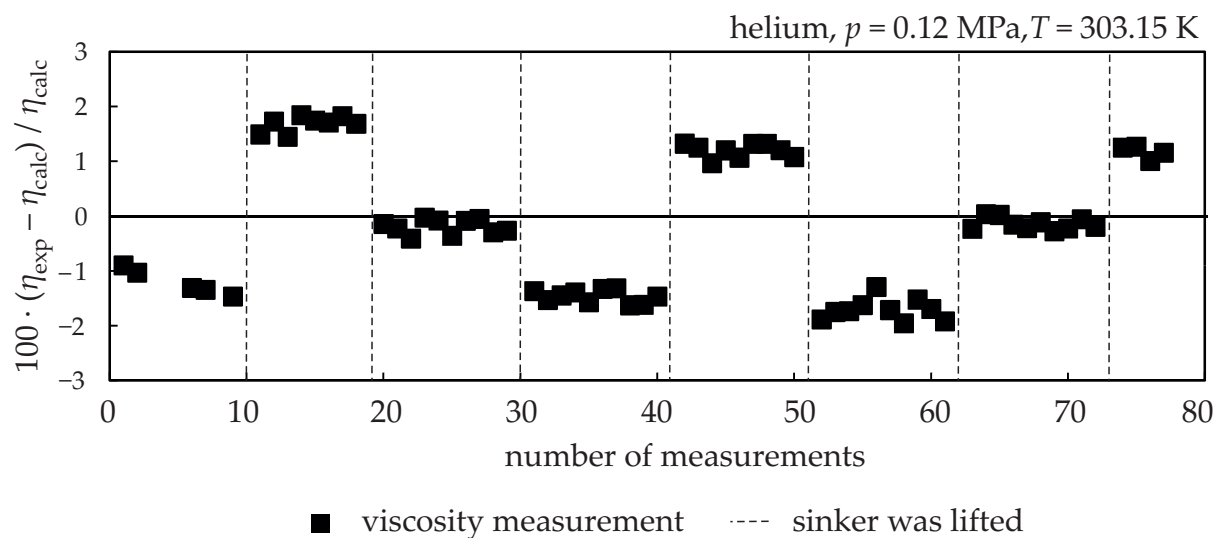


Figure 3.9 Relative deviations of measured viscosities η_{exp} from calculated viscosities η_{calc} . Humberg (2013b) determined η_{exp} using the viscometer-densimeter incorporating the system of Evers *et al.* (2002); see figure 3.8. η_{calc} was calculated with the correlation of Arp *et al.* (1998) (zero line). The dashed lines indicate the density measurements, i.e., movements of the sinker inside the measuring cell.

a worn out clearance between the sinker and the centering plate was a reasonable explanation for the scatter. Thus, the objective was to minimize the clearance.

A solution to reduce the clearance was to insert a new centering plate fitted to El Hawary's sinker. However, this approach was found to be not sustainable. The reasons are:

- Still a clearance was inevitable to place the sinker on the centering plate. Most likely, in practice, the overall clearance was more than 20 μm .
- It was most likely not possible to install a new, fitted centering plate. The inner surface of the measuring cell's lower part was likely damaged by press fitting the centering plate by *El Hawary (2009)*.

In general, utilizing a centering plate was not seen as an optimal solution: A loose or worn out centering plate will cause a scatter in viscosity; press fitting the centering plate could cause the centering plate to be damaged and may thus result in a scatter, too.

3.6.2 A New Viscosity-Density Measurement System

Against this background, a new measurement system for the viscometer-densimeter was developed. The system was manufactured by Medizintechnik Quast, Essen, Germany. A schematic of this system is shown in figure 3.10; a photo of its parts is presented in figure 3.11. The technical drawings of the new system are given in appendix A.4.

The centerpiece of the new system is a flow-guide tube, which surrounds the upper part of the rotating body. Thus, instead of the loose sinker, a fixed flow-guide tube is now functioning as the outer part of the upper cylinder system. This is the essential difference to the system of *Evers (2001)*.

To install the flow-guide tube inside the measuring cell, a ring (called threaded ring in figure 3.11) was laser welded onto the inner wall of the measuring cell's lower part. This ring is threaded half way on the inside. The flow-guide tube can be fixed with a hollow screw inside the measuring cell by means of the thread. The lower part of the ring is not threaded. This part of the ring is used to center the flow-guide tube. El Hawary's press fitted centering plate at the bottom of the measuring cell is utilized as a seat for the flow-guide tube. Therefore, the lower end of the flow-guide tube is designed as a truncated cone to fit into the cone-shaped centering plate. To minimize tensions caused by thermal expansion, the hollow screw, the flow-guide tube, and the threaded ring are all made of the same material as the lower part of the measuring cell, i.e., Inconel 625 (2.4856).

Holes with a diameter of 1 mm are inserted at the bottom and the top of the flow-guide tube, as well as in the ring for fixing it inside the measuring cell. Thereby, the fluid is guided while purging the measuring cell. Furthermore, it is prevented that residual fluid remains in clearance volumes while flushing.

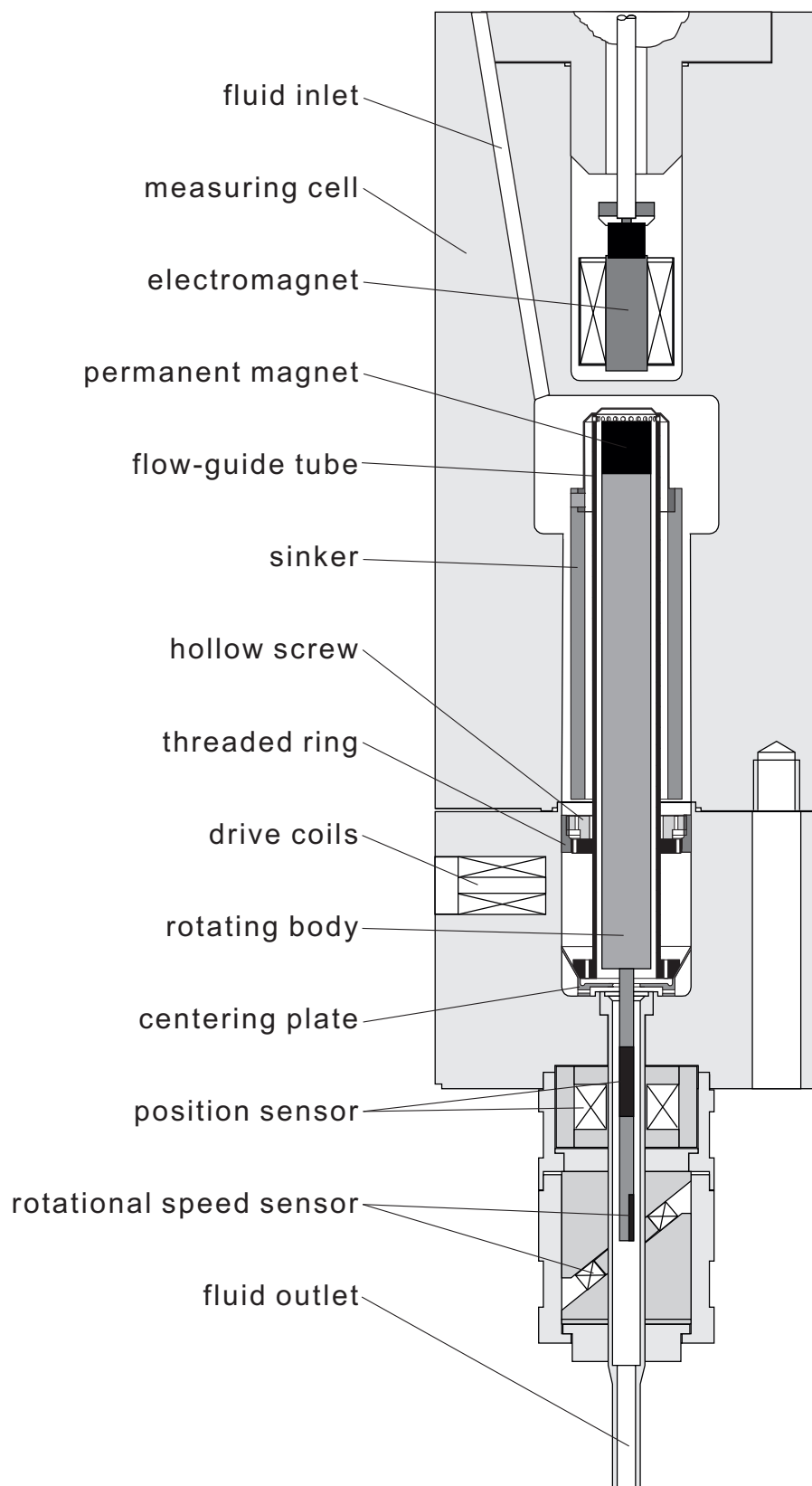


Figure 3.10 Schematic diagram of the new measurement system of the viscometer-densimeter incorporating a flow-guide tube.

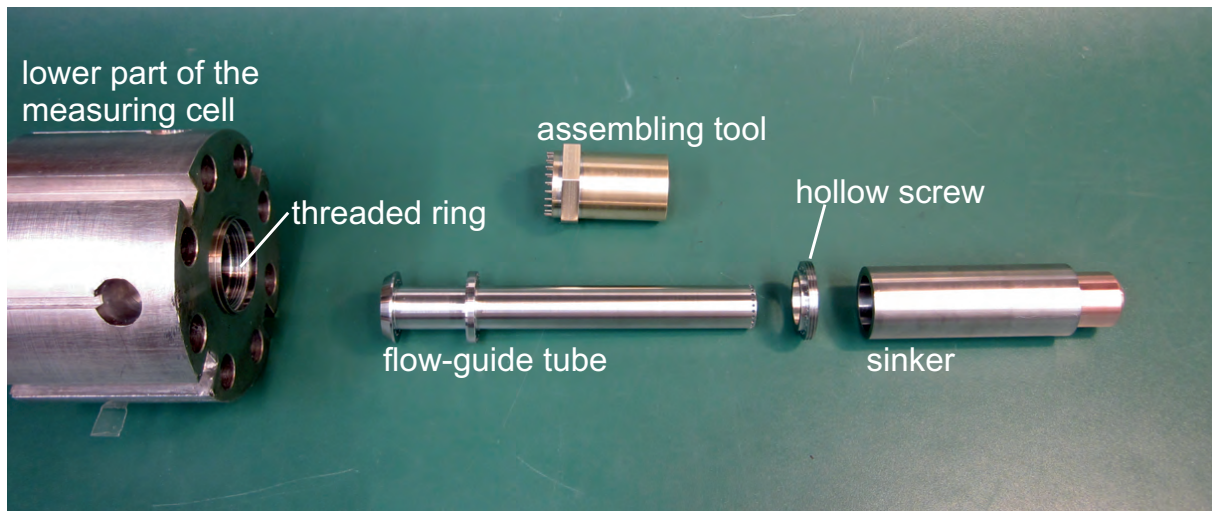


Figure 3.11 Photo of the parts of the new measurement system of the viscometer-densimeter. From left to right, the lower part of the measuring cell with the newly implemented threaded ring, the flow-guide tube, an assembling tool, the hollow screw, and the new sinker can be seen.

The inner surface of the flow-guide tube was honed. To determine the tube's inner radius, it was scanned with a coordinate-measuring machine. The experimental procedures and the uncertainty analysis of the geometry determination are described in section 4.3.1. A high quality of the inner surface of the flow-guide was observed. For the flow-guide tube with a radius of 6.75 mm an expanded uncertainty ($k = 2$) of $4.20 \mu\text{m}$ in the radius was estimated; see table 4.2.

The fluid-guide tube, as well as the screw and the ring have markings. Thereby, the fluid-guide tube can be installed always in the same position. It is recommended to fasten the screw with a torque of 2.5 Nm utilizing the assembling tool.

For testing purposes a second flow-guide tubes was manufactured, which has a nominal radius of 6.5 mm, in contrast to the one with 6.75 mm. A radius of 6.75 mm results in an annulus of 1.45 mm, which corresponds to the annulus of El Hawary's and Evers's system. The annulus is decreased to 1.2 mm, using the 6.5 mm flow-guide tube. The aim behind decreasing the annulus was to increase the measuring range to higher densities with the 6.5 mm flow-guide tube. Due to the small annulus, the formation of Taylor vortices is inhibited. Assuming that the movement of the sinker was the only source of scatter, accuracy and the measuring range could have been improved simultaneously. However, it is recommended to use the 6.75 mm flow-guide tube in favor of a lower scatter.

Development of a Customized Sinker

The design of the sinker was changed to realize the measurement system incorporating the flow-guide tube. In the setup of *Evers et al. (2002)*, *Wöll (2005)* and *El Hawary (2009)*,

the sinker rested on the bottom of the measuring cell. As can be seen in figure 3.10, now it is put over the flow-guide tube resting on top of it.

Basically, the new design of the sinker is in accordance with the sinker design developed by *Evers et al. (2002)*. In contrast to other single-sinker densimeters, in case of the viscometer-densimeter, the sinker is picked up at its top. Thus, the sinker needs a cap, which is made of non-magnetic material to ensure the functionality of the magnetic suspension coupling. Therefore, consistent to *Evers et al. (2002)*, chromium zirconium copper (2.1293) was chosen as material for the cap of the sinker. The cap's wall thickness is 0.25 mm to minimize the force transmission error. The main part of the sinker is made of pure titanium. The same piece of titanium was used as in the work of *Docter et al. (1997)*. Thus, the thermal expansion coefficients determined by *Docter et al. (1997)* can be used. Titanium was chosen, because it has a relatively low density ($\rho_{\text{Ti}} \approx 4.5 \text{ g} \cdot \text{cm}^{-3}$). Thus, a sinker with a large volume ($V_s \approx 12.5 \text{ cm}^3$) and a mass of 60 g can be realized. A sinker's mass of 60 g is required, otherwise the mass of the rotating body, the compensation weights and the settings of the magnetic suspension coupling would have to be changed. Titanium is magnetically almost neutral, it has a low thermal expansion coefficient ($\alpha_{\text{Ti}} = 8.5 \cdot 10^{-6} \text{ K}^{-1}$), and its surface is resistant to corrosion and abrasion.

The cap made of copper chrome zirconium was originally connected by a press fit to the main part of the sinker made of titanium (*Evers, 2001*). However, this connection fell apart due to temperature changes and was replaced by a fine thread by *Wöll (2005)*. *Wöll (2005)* used glue to prevent this connection from separating. This solution was also applied, when *El Hawary (2009)* rebuild the sinker. However, to use glue is not an ideal solution. Sorption effects can be increased and glue can dissolve from the sinker; see *El Hawary (2003)*.

Against this background, the cap was clinched to the main part, made of titanium, with three titanium bolts. These bolts were inserted into three matching holes drilled through the cap and the titanium part of the sinker. After inserting, the titanium bolts were fixed by laser welding in these holes. This all metal connection has proven to be reliable.

The sinker was weighed in water and air to determine its volume V_0 at reference conditions ($T_0 = 293.15 \text{ K}$, $p_0 = 0.1 \text{ MPa}$). The experimental procedures are described by *Docter et al. (1997)*. The experimental setup used in this work is presented in section 4.3.2. During his master's thesis, *Ntontos (2014)* performed the measurements to determine the volume of the new sinker. The volume of the sinker was $V_0(T_0, p_0) = 12.5459 \text{ cm}^3$ with an expanded uncertainty ($k = 2$) of 0.0018 cm^3 (relative expanded uncertainty ($k = 2$) of 0.014 %). The main contributions to this uncertainty were the scatters of the weighings in air (65 %) and water (34 %).

3.6.3 Improved Positioning System of the Viscometer-Densimeter

An eccentric alignment of the cylinder system leads to two severe problems for the viscosity measurement: (1) a systematic offset in viscosity occurs and (2) the scatter in viscosity is increased. Therefore, the demands on the positioning device concerning reproducibility and accuracy are high. This is even more important for the viscometer-densimeter than it is in case of the low-pressure viscometer, because the viscometer-densimeter has a smaller annulus than the low-pressure viscometer. In comparison to the low-pressure viscometer, the positioning device of the viscometer-densimeter is more complex, as is depicted in the following.

As stated in section 2.2, the electromagnet is attached to the underpan weighing hook of the balance. Thus, the entire balance has to be moved in order to center the cylinder system. For this purpose, a manual positioner and a slide bearing were utilized by *Evers et al. (2002)*. A photo of this positioning system is shown in figure 3.12. The slide bearing consisted of two polished steel spheres with two polished steel plates as counter surfaces. A more detailed description of this system is given by *Glos (1999)*.

A low friction of the slide bearing was fundamental for the proper function of the positioning system. However, due to wear out, the friction of this bearing was too high. In consequence, the manual positioner was twisted and damaged. Therefore, the manual positioner was replaced by *El Hawary (2009)*, who furthermore refined the new manual positioner by installing stronger return springs. In addition, the slide bearings

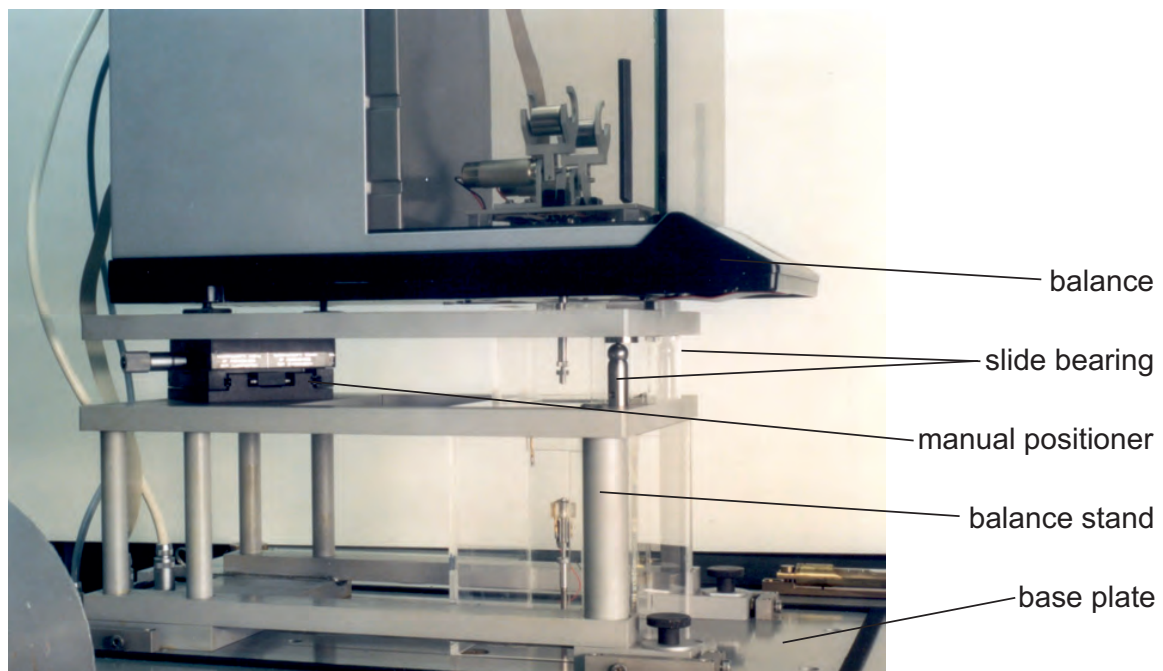


Figure 3.12 Photo of Evers' positioning system of the viscometer-densimeter. (Figure taken from *Evers, 2001*).

were replaced. Unfortunately, the friction was still too high. Thus, the manual positioner was damaged again.

Against this background, a new, larger manual positioner (QioptiQ, Germany, type: XY 20016S) was integrated into the system during this work. This new system is shown in figure 3.13. The balance's center of mass is now above the manual positioner, so there is no need for additional bearings. The new manual positioner is 10 mm higher than the old one. Therefore, the draft shields had to be replaced and the connection between the electromagnet and the underpan weighing hook of the balance was elongated. Technical drawings of the new draft shields can be found in section A.2; technical drawings of the modified balance stand are presented in section A.3. The student work of *Glos (1999)* incorporates the complementary technical drawings. The new system has proven to be reliable and easy to handle. Therefore, the cylinder system can be centered faster and more precise.

Another improvement was made for leveling the balance. The balance stands on two screws in the back and a single stand in the front. The two screws in the back are used to level the balance. These screws were very difficult to access. Thus, two new screws were fabricated. These screws are made of brass, because this material is non-magnetic. A knurled disk of a diameter of 70 mm is soldered to the screw. Therefore, the disk overlaps the underside of the balance. In conclusion, the screws are easy to access and leveling the balance is now easier to handle.

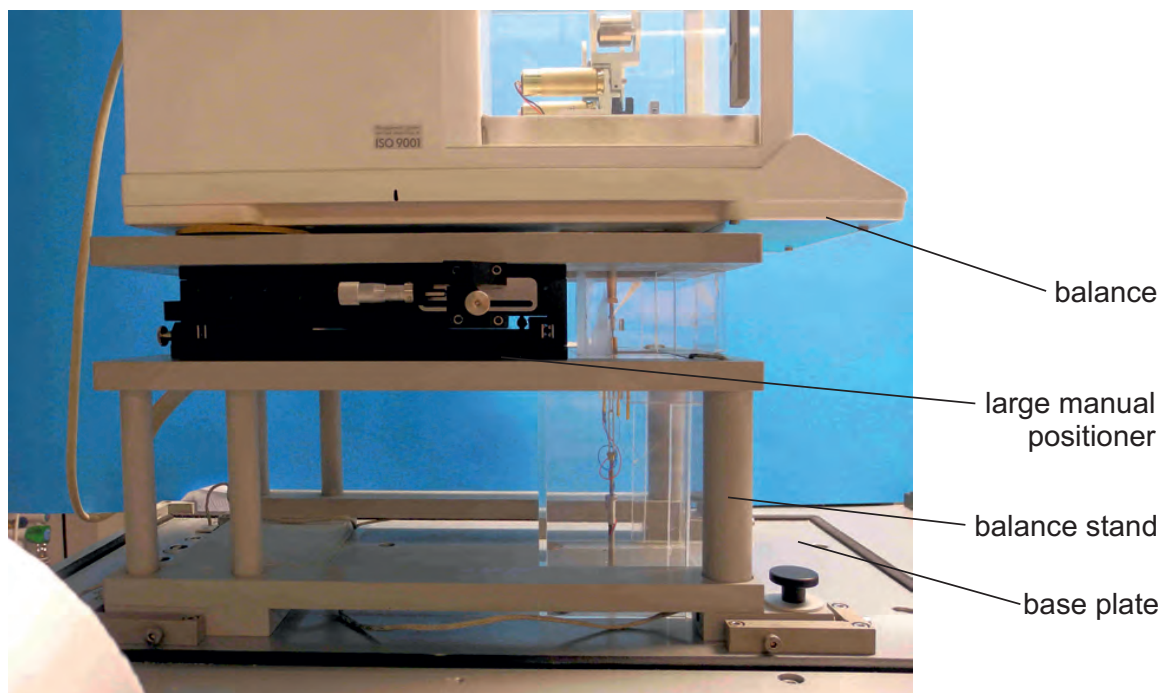


Figure 3.13 Photo of the new positioning system of the viscometer-densimeter, incorporating a larger manual positioner.

3.6.4 Evaluation of the Improved Measurement System

Two major improvements concerning the viscometer-densimeter were presented in the previous sections: (1) A flow-guide tube was integrated into the measuring cell. Thereby, the sinker was replaced as outer boundary of the cylinder system. (2) A larger manual positioner was integrated into the apparatus. Thereby, the positioning device was simplified and improved concerning accuracy. The cylinder system can now be aligned faster and more accurately.

The objective of setting up the new system incorporating a flow-guide tube was to minimize the influence of the sinker position on the viscosity measurement. At the beginning of this work a scatter in viscosity of more than 2 % was observed for the viscosity measurements; see figure 3.9. This scatter could be significantly reduced. However, the influence of the density measurement on the viscosity measurement is still significant. To explain this issue, preliminary results of the new system incorporating the flow-guide tube are shown in figure 3.14. There, viscosities measured without moving the sinker, i.e., without density measurements between the viscosity measurements, on the left are opposed to the viscosity measurements with moving the sinker on the right. As can be seen, in general, the maximum scatter is only 0.2 %, which is a major improvement in comparison to the measurement system used by *Evers et al. (2002)*. However, the scatter with moving the sinker is higher than the scatter without moving the sinker. Furthermore, in average, a systematic positive offset of more than 0.05 % in viscosity can be seen, which is indicated by the dashed line. The results with simultaneous density

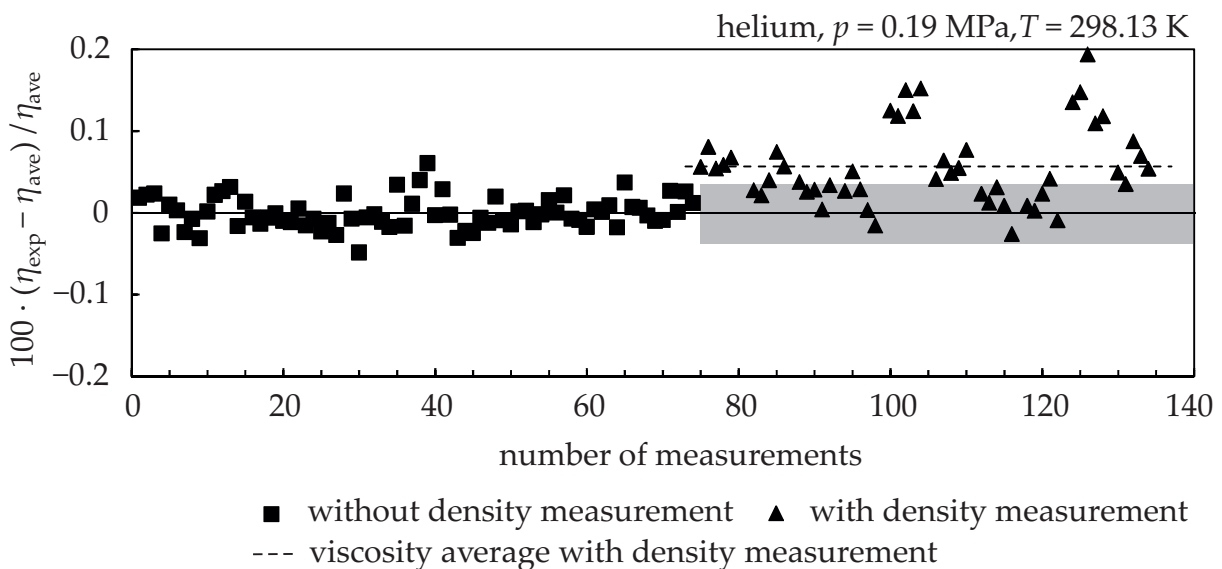


Figure 3.14 Relative deviations of the viscosities η_{exp} from the viscosities η_{ave} . η_{exp} was measured in helium using the viscometer-densimeter incorporating a flow-guide tube with a nominal diameter of 13.5 mm; η_{ave} is the average of the viscosities measured without density measurement.

measurement deviate only in positive direction. Consequently, these deviations result most likely from an eccentricity, which is aroused by the density measurement. In conclusion, the movement of the sinker is not the only reason for the scatter in viscosity. Most likely the position of the rotating body is not fully reproducible after a density measurement. A movement of the rotating body can have different reasons. Due to the combined density measurement, the mounting of the viscometer-densimeter's electromagnet is complex in comparison to the low-pressure viscometer. The electromagnet is connected via an universal joint to the underpan weighing hook of the balance. The underpan weighing hook can move in a horizontal direction. Furthermore, there may be a tolerance in the universal joint.

As can be seen in figure 3.14, the viscosities measured with simultaneous density measurement agree with the other measurements in the lowest quarter. To show this agreement, the lowest quarter of the viscosities measured with simultaneous density measurement is marked gray in figure 3.14. Assuming the eccentricity scatters; then it is likely that the eccentricity was minimal in the lowest quarter. Thus, considering only the viscosities measured in the lowest quarter could be a workaround to compensate for this offset, when determining (η, ρ, T) data sets.

From an experimental point of view it is reasonable to skip the simultaneous density measurement for testing purposes. The balance and even the universal joint would be removed. The electromagnet could be fixed at the manual positioner. Furthermore, it would be possible to align the cylinder system in height, as a vertical manual micrometer screw could be included in the positioning device. This way, the influence of the balance and the universal joint could be investigated.

4 Evaluation of the Viscosity Measurement

During commissioning of the apparatuses several effects were observed, which increased the scatter in viscosity or lead to a low reproducibility. Two effects, i.e., the hysteresis and the influences of sorption and vibration, are presented in the beginning of this chapter in section 4.1. In the second part of this chapter (section 4.2) a viscosity dependent offset is investigated. The third part of this chapter (section 4.3) is about the compensation of a systematic offset in viscosity, which was observed when measuring the viscosity in an absolute way.

4.1 Effects Interfering with the Viscosity Measurement

4.1.1 Hysteresis

The hysteresis of the damping was analyzed in the master's thesis of *Herrndorf (2014)*. For the analysis, the damping of helium was measured in the temperature sequence (253.15; 273.15; 298.15; 323.15; 373.15; 423.15; 473.15) K and again in the temperature sequence (473.15; 423.15; 373.15; 323.15; 298.15; 273.15; 253.15) K, both times with pressures up to 1.6 MPa. Thereafter, all damping values were extrapolated to the limit of zero density.

The effect of the hysteresis on the damping values of helium is shown in figure 4.1. In the left diagram of figure 4.1, the damping $D_{0,\text{He}}$ is plotted versus temperature. As can be seen, the damping is distinctively depending on temperature. The continuous line is a

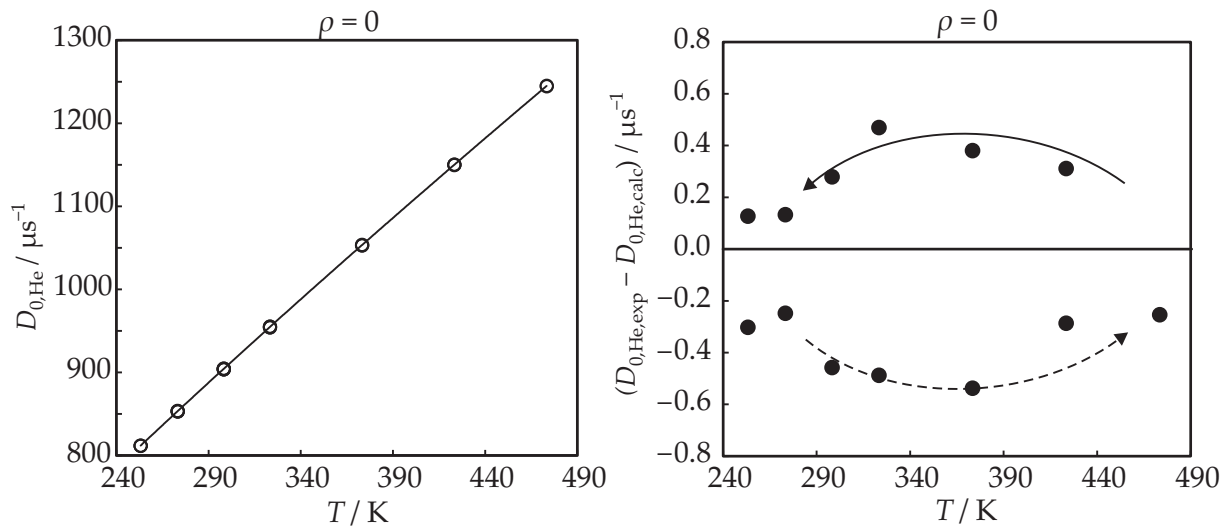


Figure 4.1 Left: Damping values of helium, extrapolated to zero density, plotted versus temperature. The continuous line is a polynomial fit of these values. Right: Deviations of these values to the polynomial fit plotted versus temperature. The arrows indicate the sequence of measurements.

polynomial fit of the damping values. In the right diagram, the absolute deviation of the damping values to their polynomial fit is plotted versus temperature. The arrow with the dashed line represents values measured in the sequence of increasing temperature; the arrow with the continuous line values measured decreasing temperature.

Clearly, the hysteresis effect is superposed by a scatter of the damping values. Nevertheless, it is obvious that the deviations are grouped along the arrows. The hysteresis results in an average deviation of $\Delta D = 0.40 \mu\text{s}^{-1}$. This equals a deviation in viscosity of $\Delta\eta = 0.009 \mu\text{Pa s}$ ($\Delta\eta/\eta \approx 0.05\%$ at $T = 298.15 \text{ K}$).

Throughout the measurement program, isotherms were always changed in the same sequence. This way, the hysteresis was partly compensated. Furthermore, the damping values of all measured gases were affected in a similar way. Thus, according to the *ISO/IEC Guide 98-3 (2008)*, the uncertainty due to hysteresis can be reduced by a factor of 0.29. The average of the deviations resulting from the hysteresis was taken as the best estimate for the uncertainty aroused by the hysteresis. Thus, the expanded uncertainty ($k = \sqrt{3}$) was $U_{\text{hys}}(D) = 0.29 \cdot 0.40 \mu\text{s}^{-1}$.

4.1.2 Effects Generated by Sorption and Vibrations

Sorption effects were first investigated during the bachelor's thesis of *Humberg (2013b)*. To visualize these effects, an example for a long time damping measurement is given in figure 4.2. All data were measured with helium at a pressure of 0.12 MPa and a temperature of 298.15 K without exchanging the sample gas in the measuring cell. As can be seen, the damping was drifting over time to higher values. After purging the measuring cell with helium, the damping values from the start of the measurements could be reproduced. Furthermore, the appearance of the data in figure 4.2 is similar to

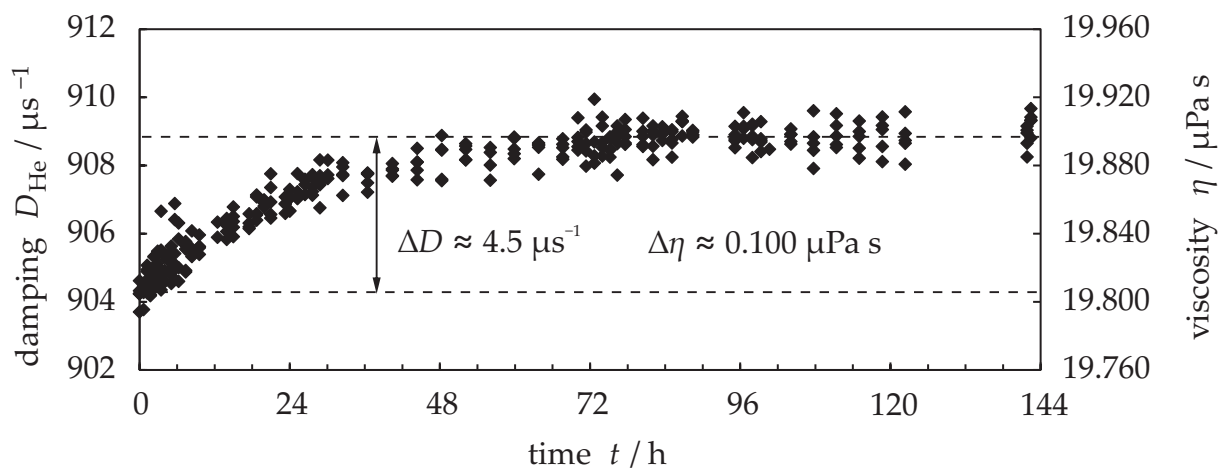


Figure 4.2 Drift of the damping values of helium due to sorption effects; measured at $p = 0.12 \text{ MPa}$ and $T = 298.15 \text{ K}$.

a Langmuir isotherm. Thus, most likely sorption effects caused this drift in the damping values.

A reason for these sorption effects might be diffusion through the measuring cell sealings. These sealings consist of two O-rings made of FKM. A gradient in concentration may yield to diffusion of, e.g., nitrogen into the measuring cell. This effect is commonly known from a two sinker densimeter, which was designed to measure the density of gases at standard conditions with high accuracy (*Richter et al., 2010*). Another reason for the sorption effect can be a plate made of PTFE, which is inserted at the bottom of the measuring cell. Its fundamental function is to minder the shock, when the rotating body drops out of the controlled suspense. Otherwise, the rotating body and - in particular - the permanent magnet inside the rotating body could be damaged irreversibly. Unfortunately, it is likely that small parts of the sample fluid diffuse into the PTFE plate while measuring. After a change of the sample fluid, particles can be released from the PTFE, thus contaminating the new sample fluid.

The sorption effects can cause a positive or negative drift of the damping values, depending on the residual sample gas in the measuring cell. To minimize these effects, the measuring cell can be baked out. An alternative to this is an elaborate flushing procedure, which may take up to three days, if necessary. However, the influence of sorption effects has to be considered in the uncertainty analysis. As can be seen in figure 4.2, sorption effects can have an influence of up to $\Delta\eta \approx 0.1 \mu\text{Pa s}$ ($\Delta\eta/\eta \approx 0.5\%$ at $T = 298.15 \text{ K}$ for helium). For a typical viscosity measurement, the expanded uncertainty ($k = \sqrt{3}$) of the sorption can be estimated to $U_{\text{sorp}}(D) = 0.28 \mu\text{s}^{-1}$. This uncertainty equals the change in the damping of helium observed over the course of 30 min after

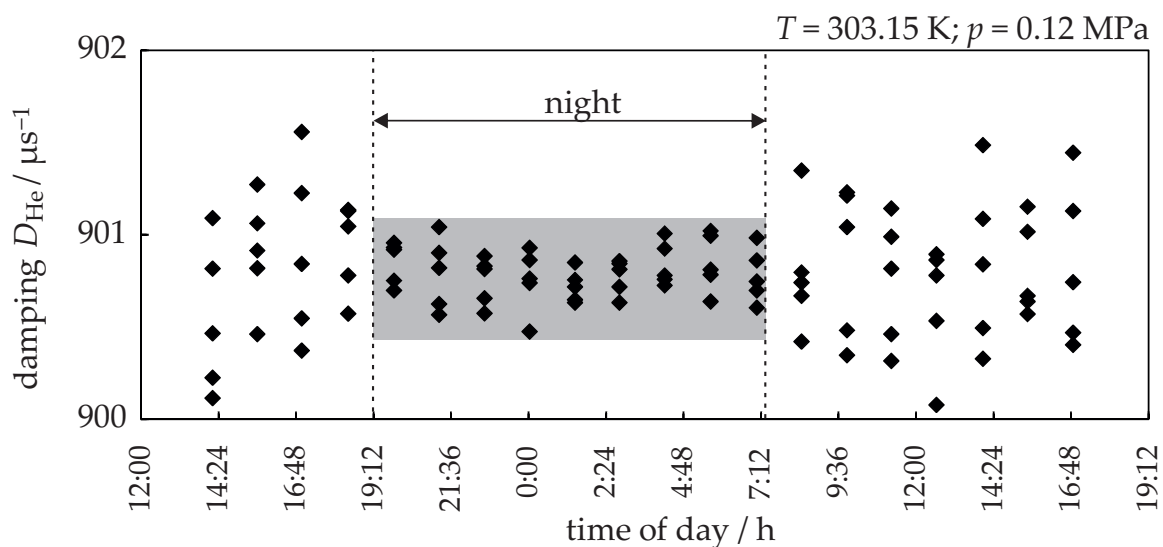


Figure 4.3 Helium damping values measured with the low-pressure viscometer plotted versus time. The damping values measured at night are marked gray. These values scatter less than the daytime values.

measurements on carbon dioxide. The time span of 30 min was chosen to estimate the effect of sorption, as it is common for a viscosity measurement containing at least 3 damping measurements. The expanded uncertainty caused by sorption effects equals a deviation in viscosity of $\Delta\eta \approx 0.006 \mu\text{Pa s}$ ($\Delta\eta/\eta \approx 0.03\%$ at $T = 298.15\text{ K}$ for helium).

In addition to the influence of sorption, yet another effect was discovered by the long-term measurements, see figure 4.3 and 4.4. Like in figure 4.2, the damping values are plotted versus time in these figures. The scatter of the nighttime-values is marked gray. It becomes obvious that the scatter is lower during nighttime. This applies for the low-pressure viscometer (figure 4.3) and the viscometer-densimeter (figure 4.4) in the same way. The most reasonable explanation for this difference in scatter is a reduced amount of vibration during night. Thus, vibrations have to be kept low to minimize the scatter.

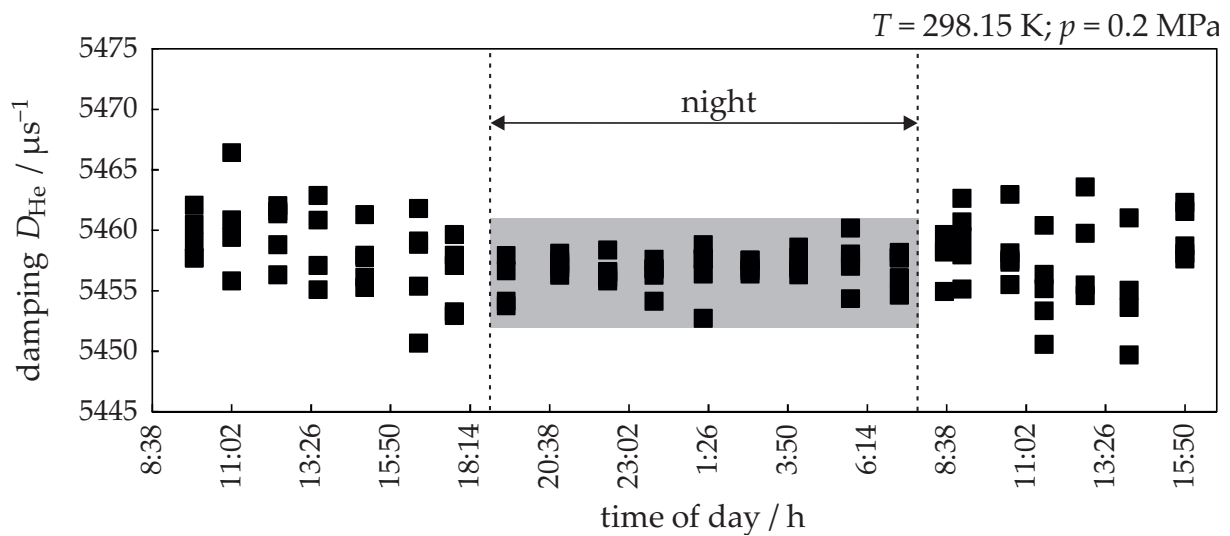


Figure 4.4 Helium damping values measured with the viscometer-densimeter plotted versus time. The data are taken from the bachelor's thesis of *Humberg (2013b)*. The damping values measured at night are marked gray. As in figure 4.3, these values scatter less than the daytime values .

4.2 Compensation of a Viscosity Dependent Offset

After the apparatuses were commissioned, the viscosity of helium, argon and neon was measured for testing purposes with both apparatuses and then compared to reference viscosities. For the low-pressure viscometer, this was done first by *Herrndorf (2014)* at $T = 298.15\text{ K}$ and then by *Ntontos (2014)* over the entire temperature range; for the viscometer-densimeter see *Humberg (2015)*. Noble gases were chosen as reference for two reasons: (1) their viscosity range is relatively high ($\eta_{\text{neon}} \approx 31.7 \mu\text{Pa s}$, $\eta_{\text{helium}} \approx 19.8 \mu\text{Pa s}$) at $T = 298.15\text{ K}$ and (2) *Berg and Moldover (2012)* published recommended viscosities for all three gases. Furthermore, the viscosity of all three gases was calculated

ab initio; see *Bich et al. (2008)*, *Vogel et al. (2010)*, and *Cencek et al. (2012)*. Thus, a validation over a wide viscosity range was possible. For these tests, the relative model function was used; see section 4.3.

Unfortunately, a viscosity dependent offset was observed for both apparatuses. A similar effect had been discovered by *Berg and Moldover (2012)* in the data set published by *Evers et al. (2002)* for measurements with the viscometer-densimeter. To visualize this effect, deviations of the data from *Evers et al. (2002)* from the values published by *Berg and Moldover (2012)* are shown in figure 4.5. The dashed line is a linear fit to the data of *Evers et al. (2002)*. It can be seen that the deviations tend to decrease with increasing viscosity.

Most likely an error of the input parameters of the model function caused the observed offset. Consequently, it was checked, if a systematic offset of any input parameter could cause a viscosity dependent offset. Therefore, a sensitivity analysis was carried out for the parameters of the relative model function. As a result, it was found that only incorrect values of the damping value D could induce this dependence.

The most reasonable explanation for the viscosity dependence was considered to be an offset in the residual damping D_R . This assumption was based on two observations: (1) Due to the sensitivity analysis, only an offset of the damping D could lead to a viscosity dependent offset; the damping D incorporated the fluid damping D_{fluid} and the residual damping D_R . (2) The compensation of the viscosity dependent offset revealed the same offset of the damping D for all measured gases. These gases had a very different viscosity, density and, thus, Reynolds number while measuring. Hence,

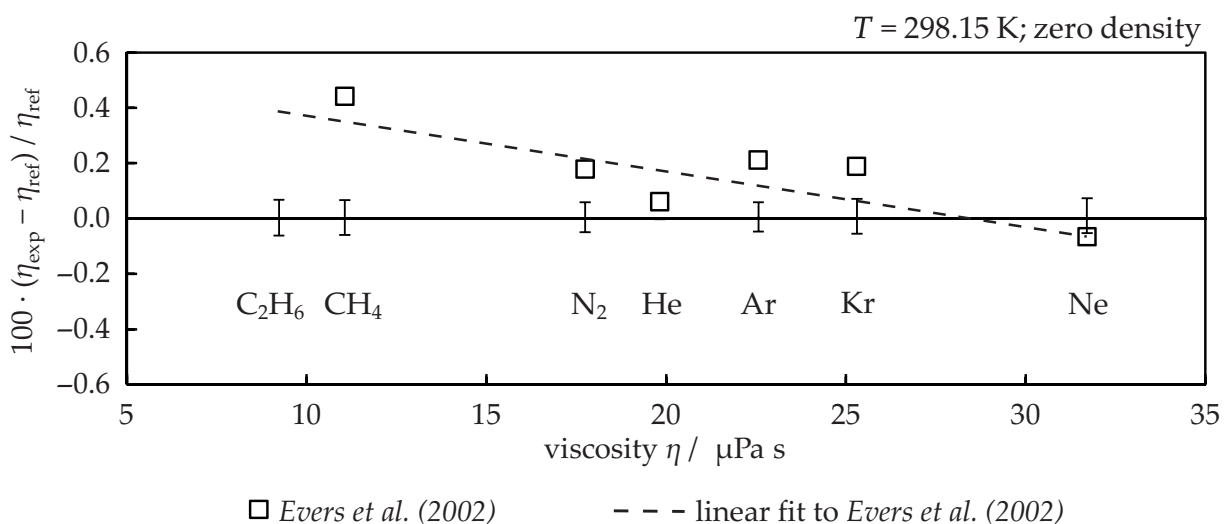


Figure 4.5 Relative deviations of experimental viscosities η_{exp} measured by *Evers et al. (2002)* from reference viscosities η_{ref} (zero line) plotted vs. viscosity. All reference viscosities are taken from *Berg and Moldover (2012)*. The error bars indicate the expanded uncertainty ($k = 2$) reported by *Berg and Moldover (2012)* for the reference values.

the offset of the damping was fluid independent. Consequently the viscosity dependent offset was caused by an offset in the residual damping D_R .

Against this background, the experimental procedures for determining the residual damping by measurement were investigated, which is presented in the following. Thereafter it is shown, how the residual damping can be calibrated using reference viscosities of helium, argon and neon. At the end of this section, both methods are evaluated critically. Most parts of this section are based on the publication of *Schäfer et al. (2015)*.

4.2.1 Determination of the Residual Damping by Vacuum Measurements

The basics of the determination of the residual damping were described in section 2.1. However, the information in section 2.1 does not include the experimental procedures. These procedures were significantly refined during this work. For the sake of documentation, these new findings are described in the following. Furthermore, this section is helpful to understand the critical evaluation of the experimental approach to determine the residual damping.

The basis for an accurate determination of the residual damping is to achieve a low vacuum pressure. Therefore, the vacuum system described in section 3.3 was set up using the metal sealings. Furthermore, the parts of the vacuum system were kept clean; if necessary they were cleaned with Tickopur R 33 (Dr. H. Stamm, Germany) in an ultrasonic bath (Bandelin, Germany, type: Sonorex S 2025FH) to remove residual components like oil.

Before the measurements, the measuring cell was baked out while evacuating to remove residual components which would otherwise limit the vacuum pressure to their vapor pressures. As the residual damping is on average less than 3 % of the damping D , the measuring time was long in order to measure a significant increase in the revolution times. The measurements took 60 min and 30 min (*Ntontos, 2014*) for the low-pressure viscometer and the viscometer-densimeter, respectively. As stated in section 3.3, the vacuum sensors were installed up- and downstream of the measuring cell. The average of both vacuum sensor's readings was taken as the best estimate for the vacuum pressure inside the measuring cell.

Furthermore, all damping values were re-estimated on the basis of the raw data. This procedure was necessary, as the damping determined by the software had a small systematic offset. Using the Solver add-in of the software Excel (Microsoft, USA) for fitting eq. (2.1) to the measurement data yielded a lower sum of deviations and was therefore more accurate than the fitting procedure used in the measurement software.

Typical damping measurements at vacuum pressures are shown in figure 4.6 where damping values measured by *Humberg (2015)* are plotted vs. the vacuum pressure. As

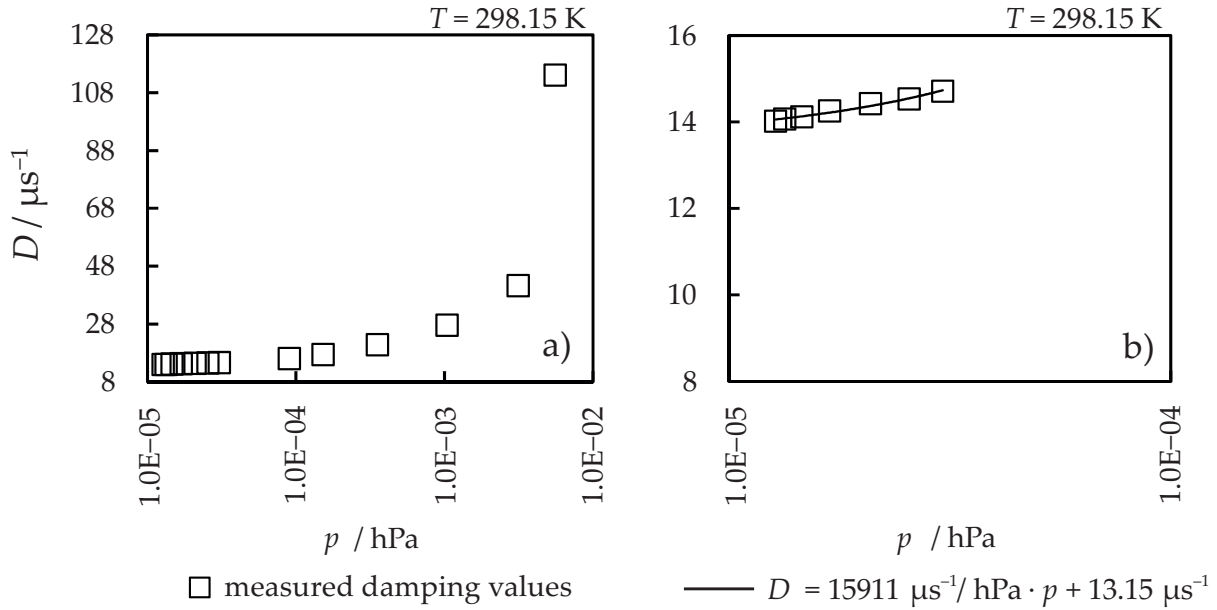


Figure 4.6 Damping values of the low-pressure viscometer plotted vs. the logarithmic vacuum pressure. (Humberg, 2015)

can be seen in figure 4.6 a), the transient section from viscous flow to the molecular flow regime ends at very low pressures of $1 \cdot 10^{-4}$ hPa. Thus, damping measurements at pressures $p < 1 \cdot 10^{-4}$ hPa are required to extrapolate the damping measured at decreasing vacuum pressures to zero density. The damping values measured at the lowest pressures in the molecular-flow regime are depicted in figure 4.6 b). The value of the damping is decreasing with decreasing pressure. Thus, the influence of the residual fluid is significant down to the lowest vacuum pressures. The line in figure 4.6 b) is a linear fit to the data; the equation of the fit is shown below figure 4.6 b). Setting the pressure to zero yields the residual damping, which was $D_R = 13.15 \mu\text{s}^{-1}$.

The experimental procedures applied in the work of *Humberg (2015)* can be refined further. The vacuum sensors incorporate strong permanent magnets. To minimize any influence of these sensors, a distance of 0.5 m between the thermal insulation hood of the apparatuses and the vacuum-pressure sensors is recommended. The same applies for the distance between the apparatuses and the turbo-molecular pump. In addition, the influence of the low heat conduction in vacuum has to be considered. Therefore, it is recommended to fill the measuring cell with fluid during the entire process of changing the temperature. Otherwise, the rotating body might not adapt the new temperature fast enough. The impact of these new refinements has to be investigated elaborately in future. These matters were observed recently and are therefore out of the scope of this work.

However, so far all measured residual damping values resulted in a viscosity dependent offset in relation to reference viscosities. Possible reasons for this are discussed in section 4.2.3, where measured values of the residual damping are compared to calibra-

ted values of the residual damping. The viscosity dependent offset was compensated by a multi-fluid calibration, which is described in the following section.

4.2.2 Multi-Fluid Calibration Method to Determine the Residual Damping

An alternative method to determine the residual damping was developed in this work. In this method, the residual damping was considered an adjustable parameter. This method is called multi-fluid calibration in the following.

A schematic of this method is presented in figure 4.7. For the application of the multi-fluid calibration, helium, argon and neon were measured over the entire temperature range of the apparatuses at low pressures. Then, the measured viscosities were extrapolated to zero density and were compared to the respective reference viscosities. Viscosities calculated ab initio for argon (Vogel *et al.*, 2010) and for neon (Bich *et al.*, 2008) with a standard uncertainty of 0.1 % and for helium (Cencek *et al.*, 2012) with a standard uncertainty of 0.001 % were taken as reference viscosities. At $T = 298.15$ K the recommended reference viscosities published by Berg and Moldover (2012) were used.

Results with a viscosity dependent offset are indicated by the dashed line in the deviation diagram shown in the lower left corner of figure 4.7. There, relative deviations of the viscosity are plotted vs. viscosity. η_{exp} is the experimental viscosity, extrapolated to zero density; η_{ref} (zero line) is the respective reference viscosity. In the iteration procedure applied, the residual damping was varied to minimize the deviations between

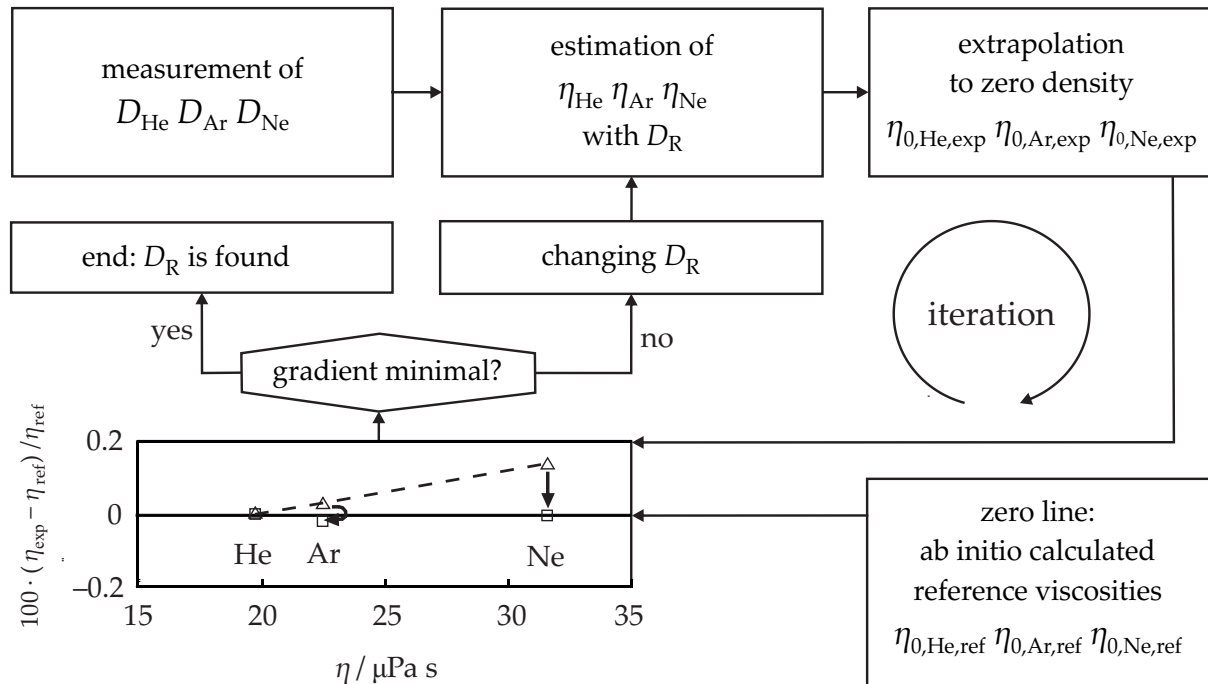


Figure 4.7 Schematic of the multi-fluid calibration method to determine the residual damping.

the experimental and the reference viscosities. The arrows in figure 4.7 indicate, how the deviation was minimized by the iteration. As can be seen, the deviations for all reference fluids are affected by fitting just one parameter: the residual damping.

4.2.3 Evaluation of Measuring and Calibrating the Residual Damping

An overview of the quantitative differences between the two methods to determine the residual damping is given in figure 4.8, in which the low-pressure viscometer's residual damping is plotted vs. temperature. The data in figure 4.8 are taken from the master's thesis of *Humberg (2015)*, who investigated the residual damping of the low-pressure viscometer and the viscometer-densimeter using both methods. The results of the viscometer-densimeter are qualitatively similar to the ones of the low-pressure viscometer. To shorten matters they are not shown here; see *Humberg (2015)* for further detail.

As can be seen in figure 4.8, the measured residual damping has in general a positive offset in comparison to the calibrated residual damping. At $T = 298.15\text{ K}$ the offset was $\Delta D_R \approx 4\mu\text{s}^{-1}$. The impact of such an offset is demonstrated in figure 4.9. This example is based on viscosities measured by *Herrndorf (2014)*, as this data set includes viscosities of ethane, methane and nitrogen, in addition to helium, argon and neon. The data plotted in figure 4.9 were re-evaluated by *Ntontos (2014)* using the relative model function (see section 4.3.6). Therefore, the relative deviations in viscosity for helium are zero.

Two data series based on the measurements of *Herrndorf (2014)* are included in figure 4.9: One data set was evaluated using the calibrated residual damping, for the other data set the calibrated residual damping was set off in positive direction about $\Delta D_R = +3\mu\text{s}^{-1}$, which is similar to the observed offset between the measured residual

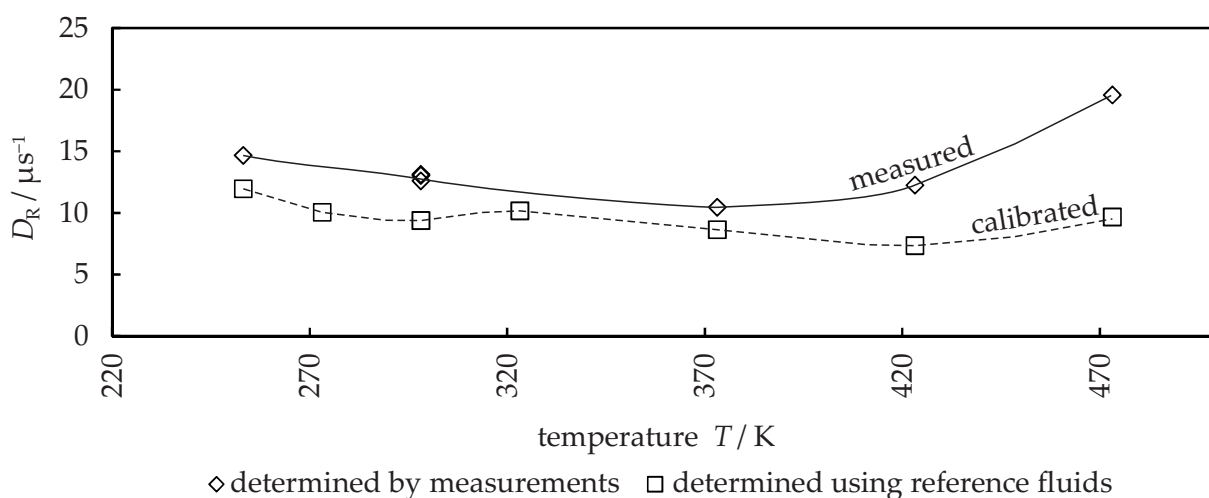


Figure 4.8 The residual damping of the low-pressure viscometer plotted vs. temperature. (*Humberg, 2015*)

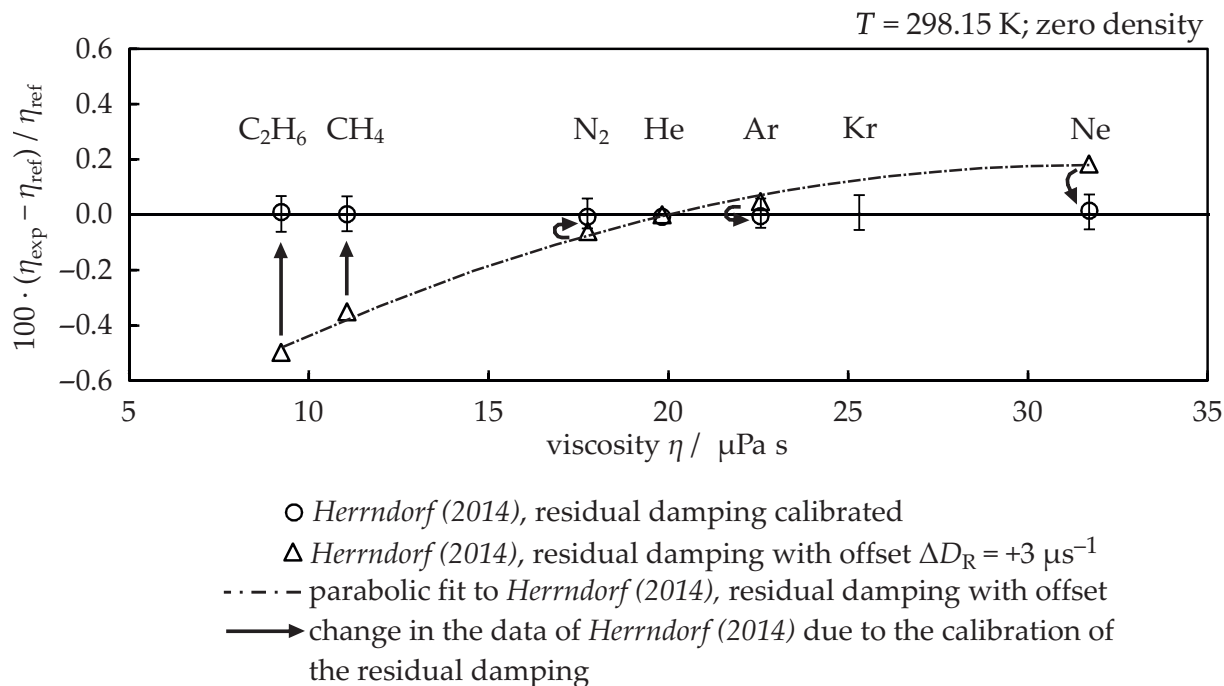


Figure 4.9 Relative deviations of experimental viscosities η_{exp} from reference viscosities η_{ref} plotted vs. viscosity. All viscosities were measured with the low-pressure viscometer. All reference viscosities are taken from *Berg and Moldover (2012)*. The error bars indicate the expanded uncertainty ($k = 2$) given by *Berg and Moldover (2012)* for the reference values.

damping and the calibrated residual damping in figure 4.8. Unfortunately, the residual damping measured by *Herrndorf (2014)* could not be used for this comparison. Reasons for this are a too short measuring time, and, furthermore, broken sensors for determining the vacuum pressure.

However, as can be seen, an offset of $\Delta D_R = +3 \mu\text{s}^{-1}$ results in relative deviations beyond the limits of the expanded uncertainty ($k = 2$) of the reference viscosities, which is indicated by the error bars. Relative deviations to the reference viscosities are 0.19 % for neon and -0.5 % for ethane. After calibrating the residual damping, the data agree excellently with the reference viscosities. A viscosity dependent systematic offset can not be observed. All reference values can be reproduced within their respective expanded uncertainties.

In conclusion, it was assumed that the measured residual damping had a positive offset. Against this background, possible influences on the residual damping D_R were investigated. An analogy to the Spinning Rotor Gauge (SRG) (*Fremerey, 1985*), (*Chang and Abbott, 2007*), (*Isogai, 1993*), (*Jousten, 2003*) was found. This vacuum gauge is used to measure the vacuum pressure by determining the decay rate of a magnetically suspended rotating ball. This ball is slowed down according to the tangential momentum transferred from molecules hitting its surface and according to a residual drag resulting from eddy currents. The SRG can be baked out at $T = 523.15 \text{ K}$ and evacuated to

$p \approx 1 \cdot 10^{-10}$ hPa to measure the residual damping. As mentioned above, the residual damping of the viscometers also mainly results from eddy currents, which are induced in the electrically conductive measuring cell due to inhomogeneities in the magnetic field of the permanent magnet of the magnetic suspension coupling. In contrast to the SRG, for the low-pressure viscometer and the viscometer-densimeter the lowest pressure in the molecular flow regime is $p \approx 1 \cdot 10^{-6}$ hPa. Therefore, the tangential momentum transferred from molecules hitting the surface of the rotating body has a significant influence on the measured vacuum damping, making it dependent on vacuum pressure; see figure 4.6 b). Thus, the vacuum damping depends on the molecular mass and the velocity of the residual molecules and, in addition, on the surface characteristics of the rotating body.

In vacuum, the frequency of the low-pressure viscometer's rotating body is decelerated only by 10 mHz (0.6 rpm) during a measurement run of 60 min. The change in frequency for a typical damping measurement in fluid was however 100 mHz (6 rpm), and the duration was 9 min. The situation is similar for the viscometer-densimeter: in vacuum, the frequency is decreased only by 30 mHz (1.8 rpm) in 30 min; in fluid the decrease is 260 mHz (15.6 rpm) in 3 min. Thus, a source of error for the determination of the residual damping could be that it is not possible to perform the measurements in vacuum in the same frequency range as in the fluid.

Furthermore, due to the relatively long time span to perform a measurement of the damping in vacuum, it was likely that the rotation of the rotating body was disturbed, e.g., by shocks or vibration. Also other long-term effects could have influenced the measurement. There could have been molecules desorbing from the surfaces inside the measuring cell or a change in composition of the residual molecules. A temperature change of the rotating body during a measurement run (resulting from the eddy currents induced when accelerating the body) could also have generated a systematic offset.

Many of the mentioned effects are known from the SRG; see (*Fremerey, 1985*), (*Chang and Abbott, 2007*), (*Isogai, 1993*), (*Jousten, 2003*). To consider these effects in a physically sound way within the apparatuses' entire temperature range is very complex and would probably not improve the accuracy.

Another source of uncertainty of the experimental determination of the residual damping is most likely the influence of temperature. As observable in the data of *Humbert* (2015) it was difficult to achieve low pressures at temperatures $T > 373.15$ K. The consequences are illustrated in figure 4.9: The positive offset of the measured residual damping is increasing in relation to the calibrated one towards higher temperatures. At $T = 473.15$ K, the achievable vacuum pressure was $\geq 1 \cdot 10^{-4}$ hPa. This increased the uncertainty of the extrapolation of the damping values to vacuum. Most likely, the damping values at $T = 423.15$ K and $T = 473.15$ K are too high in relation to the other measured values of the residual damping. Thus, the multi-fluid calibration method is

most likely more accurate than the experimental determination of the residual damping at $T > 423.15 \text{ K}$.

In summary, a significant number of effects was identified, which could disturb the measurement of the residual damping. In addition to that, deviations to other experimental data and to the ab initio calculated viscosities were minimized by using the multi-fluid calibration method. In conclusion, the multi-fluid calibration was considered to be more reliable than the experimental determination of the residual damping. However, in addition to the viscosity dependent offset, furthermore, a systematic offset in viscosity was observed when measuring in an absolute way. This issue is discussed in the next section.

4.3 Compensation of a Systematic Viscosity Offset

Both apparatuses were used by *Evers et al. (2002)*, *Wöll (2005)* and *El Hawary (2009)* to measure the viscosity in an absolute way. To do the same in this work, the input parameters were investigated elaborately. The determination of these parameters is presented in this section. However, a systematic offset in viscosity was observed when measuring in an absolute way. Thus, the uncertainty of the absolute model function was analyzed again on the basis of *ISO/IEC Guide 98-3 (2008)*. Furthermore, the validity of the absolute model function was evaluated critically. An expanded model function was developed and is presented in the end of this section. The systematic offset was compensated using the expanded model function which also resulted in a lower uncertainty.

4.3.1 Determination of the Geometries of the Cylinder Systems

As mentioned before, the model function is very sensitive to the geometries of the cylinder system. Therefore, the geometries have to be determined elaborately to achieve low uncertainties in viscosity. In the work of *Evers et al. (2002)* and *El Hawary (2009)*, the same coordinate measuring machine (Carl Zeiss, Germany, type: UMM 850) was used to determine all geometries. However, this approach is not favorable from a statistical point of view. All estimates could be influenced by the same offset. Thus, in the worst case, the uncertainties could add up. A length related offset in the length measurement of the coordinate-measuring machine (CMM) can possibly cause an offset in viscosity. Consequently, all geometries were measured additionally (3D-Service, Germany, Hattingen) with another CMM (Wenzel Präzision, Germany, type: LH87).

An example of the set-up for the measurement of the geometries is given in figure 4.10. As can be seen, the rotating body of the low-pressure viscometer was clamped by a nonmagnetic fixing device made of PVC. Furthermore, the nonmagnetic stylus and the thermometer are visible in figure 4.10. The diameters were determined by scanning

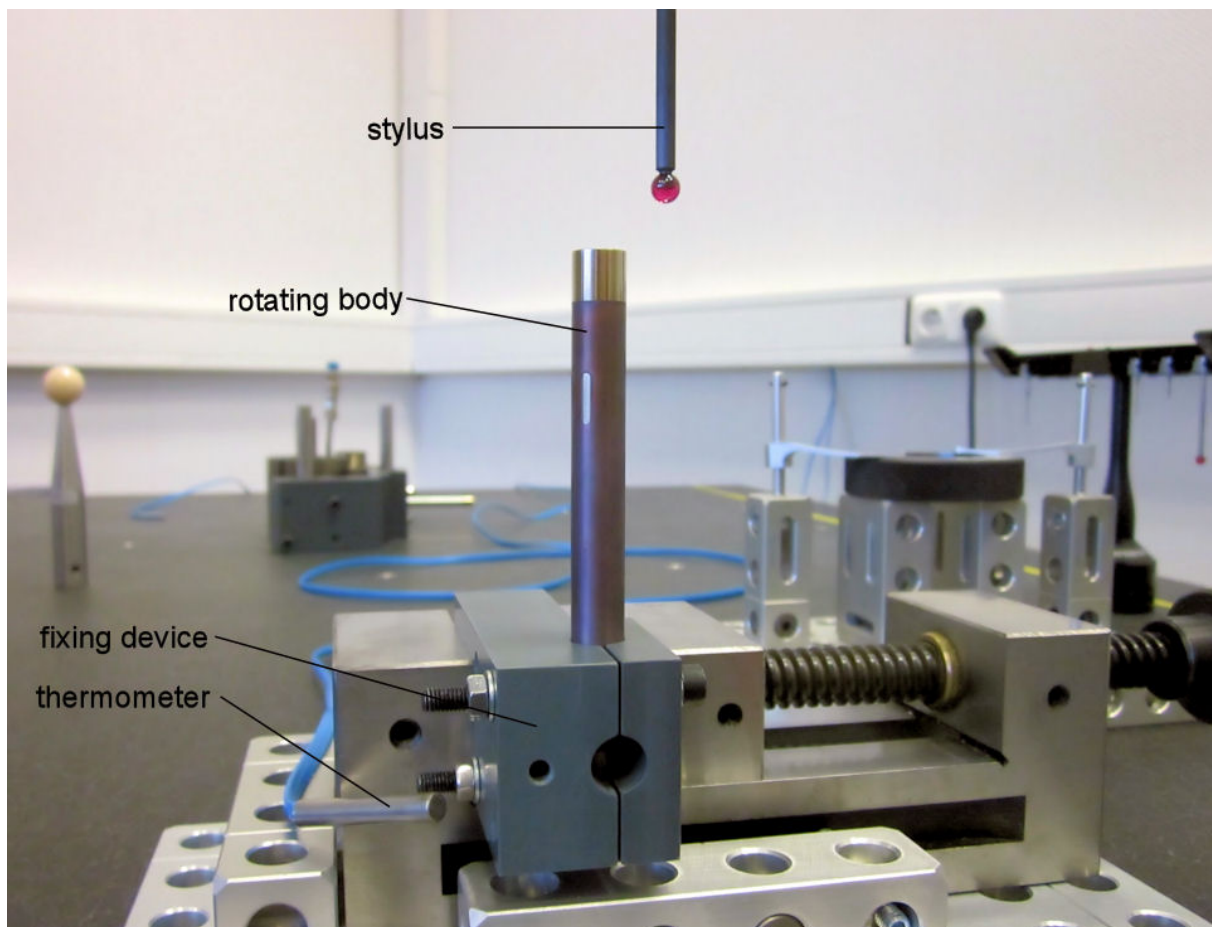


Figure 4.10 Photo of the setup for determining the geometries of the rotating body of the low-pressure viscometer at 3D-Service, Germany.

the surfaces of the items in form of a helix. All parts of the measuring cell and the rotating body were placed inside the air-conditioned laboratory for acclimatization the day before the measurements were started. To minimize an increase in temperature while changing the fixing position, the items were only touched using cotton gloves, which were additionally covered by rubber gloves.

The results of the geometry measurements are listed in tables 4.1 and 4.2 for the low-pressure viscometer and the viscometer-densimeter, respectively. The rotating body and the measuring cell could not be measured over the entire length at once, due to the fixing or the limited stylus length. Therefore, e.g., first the upper and then the lower part of one item was measured. Consequently two diameters were determined. As measurement result the average of both diameters was taken. In addition to the results for the geometries, the expanded uncertainties for the geometries of the low-pressure viscometer and the viscometer-densimeter are presented in table 4.1 and 4.2, respectively.

According to the manufacturers, the standard uncertainties of the coordinate-measuring machines are

$$u_{\text{Wenzel}}(L) = \left(2.9 + \frac{L/\mu\text{m}}{300\,000} \right) \mu\text{m} \text{ and} \quad (4.1)$$

$$u_{\text{Zeiss}}(L) = \left(2.8 + \frac{L/\mu\text{m}}{200\,000} \right) \mu\text{m}, \quad (4.2)$$

where u is the standard uncertainty and L is the measured length in μm . In eqs. (4.1) and (4.2), a basic uncertainty and an uncertainty depending on the measured length L are combined to derive the standard uncertainty $u(L)$ of the geometry measurement. A third source of uncertainty is the scatter of the measurement, which was calculated from the measured coordinates. This value describes the quality of the measured item; e.g., form and roundness deviations.

An exemplary uncertainty budget of a typical geometry determination using the coordinate-measuring machine of the type Wenzel LH87 is given in table 4.3. In this example, the combined uncertainty of the radius of the low-pressure viscometer's rotating body is analyzed. The sensitivity coefficients are 0.5, as the diameter was measured directly and the radius was calculated from the diameter. As can be seen, the expanded uncertainty ($k = 2$) is only $4.20 \mu\text{m}$.

In the following, the results concerning the low-pressure viscometer are discussed and compared. Therefore, the results of both CMMs are included in table 4.1. As can be seen, the deviations between the results of the different CMMs are within their uncertainties. For the measuring cell's radius, the deviation is $1 \mu\text{m}$; for the radius of the rotating body $0.41 \mu\text{m}$. Apparently, the values of the Zeiss UMM 850 CMM are systematically slightly lower than the values determined using the Wenzel LH87 CMM.

More important than this offset is the difference in the expanded uncertainties: the uncertainties of the Zeiss UMM 850 CMM are lower. This difference comes from a lower scatter in the measurements. Assuming that the general uncertainty of both CMMs is

Table 4.1 Values of the geometries of the cylinder system of the low-pressure viscometer. Coverage factor for all expanded uncertainties is $k = 2$.

Input parameter	Zeiss UMM 850		Wenzel LH87 ^a	
	Measured value	Expanded uncertainty	Measured value	Expanded uncertainty
Radius of measuring cell	10.0540 ^b mm	7.76 μm	10.0550 mm	11.39 μm
Radius of rotating body	5.5098 ^c mm	4.07 μm	5.5105 mm	4.20 μm
Height rotating body	–	–	116.2550 mm	6.58 μm

^a Measured by *Hielscher (2014)* at $T = 293.5 \text{ K}$; expanded uncertainty ($k = \sqrt{3}$) $U(T) = 80 \text{ mK}$.

^b Measured by *Buff (2008)*.

^c Measured by *Buff (2012)*.

Table 4.2 Values of the geometries of the cylinder system of the viscometer-densimeter. Coverage factor for all expanded uncertainties is $k = 2$.

Input parameter	Zeiss UMM 850		Wenzel LH87 ^a	
	Measured value	Expanded uncertainty	Measured value	Expanded uncertainty
Radius of flow-guide tube 1	6.5076 ^b mm	3.15 μ m	6.5080 mm	3.11 μ m
Radius of flow-guide tube 2	–	–	6.7545 mm	4.20 μ m
Radius of rotating body	5.2916 ^c mm	3.18 μ m	5.2920 mm	7.59 μ m
Radius of sensor rod	1.4930 ^c mm	3.40 μ m	1.4950 mm	5.79 μ m
Height of rotating body	–	–	118.2270 mm	6.59 μ m
Height of sensor rod	–	–	59.1290 mm	6.19 μ m

^a Measured by *Hielscher (2014)* at $T = 293.5$ K; expanded uncertainty ($k = \sqrt{3}$) $U(T) = 80$ mK.

^b Measured by *Buff (2013)*.

^c Measured by *Buff (2009)*.

equal, there are two possible causes for this difference: (1) Points of high deviation were missed during the measurements of Buff – to achieve a representative value for the scatter, points of relatively large deviation, e.g., the viscosity sensor, have to be included into the measurement – or, (2) the surface of the items had changed. This is discussed further using the inner surface of the measuring cell of the low-pressure viscometer as an example.

A deviation diagram of the measuring cell's diameter is shown in figure 4.11. A cut through the measuring cell is shown on the left side of figure 4.11. The cut is opposed to the deviation plot on the right side. For visualization purposes, the deviations are enlarged by a factor of 50. The region with the largest deviations is the lower part of the measuring cell. The position of the lower part in the deviation diagram is indicated by the dashed lines. As can be seen, the maximum absolute deviations in the lower part are larger than in the upper part. Measuring only in the upper part would lead to an underestimation of the scatter.

A reason for the differences between the upper and the lower part may be the wall thickness. It is only 1 mm in the lower part of the measuring cell to ensure the

Table 4.3 Uncertainty budget for the radius of the rotating body of the low-pressure viscometer. The radius was measured by *Hielscher (2014)* utilizing a coordinate-measuring machine (Wenzel Präzision, Germany, type: LH87).

Source of uncertainty	Uncertainty	Distribution	Coverage factor	Sensitivity coefficient	Standard uncertainty
Coordinate-measuring machine	5.87 μ m	normal	2	0.5	1.47 μ m
Scatter	6 μ m	normal	2	0.5	1.5 μ m
Expanded uncertainty ($k = 2$): 4.20 μ m					

functionality of the position sensor and viscosity-measurement sensor. This part can therefore be bended, when the measuring cell is tightened. The measurements with the Wenzel LH87 CMM were executed in February 2014; the measurements using the Zeiss UMM 850 CMM in 2008. The apparatus was mounted several times in between. In conclusion, a possible cause for the larger scatter of the measurements, which was observed when using the Wenzel LH87 CMM, likely corresponds to a slight damage of the measuring cell. The same may account for the rotating body of the viscometer-densimeter.

The height of the rotating body does not have to be determined with high accuracy. The uncertainty of a sliding caliper is sufficient. Therefore, the height was not determined using the Zeiss UMM 850 CMM in the past. However, during the measurements of *Hielscher (2014)*, the height was included into the measurements, as the measurement of the height of the rotating body is challenging. Due to the strong permanent magnet, the sliding caliper has to be used very carefully to prevent damages to the sliding caliper or the rotating body. Furthermore, the sliding caliper has to be demagnetized after using.

As mentioned above, the measurement results of the viscometer-densimeter's geometries are given in table 4.2. Again, the results of the two CMMs agree within their uncertainties, although the values determined with the Zeiss UMM 850 CMM are

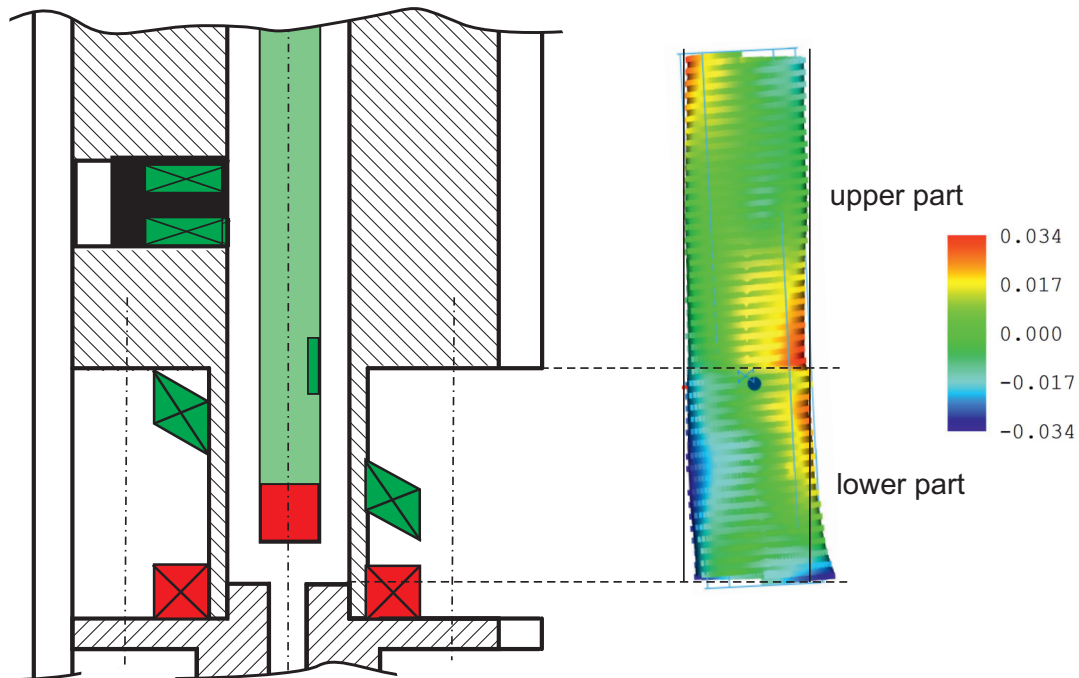


Figure 4.11 Visualization of the quality of the low-pressure viscometer's measuring cell's inner surface, which was examined by *Hielscher (2014)*. Absolute deviations are plotted to the average diameter (green). For visualization purposes the deviations are enlarged by a factor of 50. The unit of the legend is μm .

slightly smaller than the ones measured utilizing the Wenzel LH87 CMM. The largest deviation is 2 μm for the radius of the rotating body's sensor rod.

In conclusion, the results determined with the Zeiss UMM 850 CMM (*Buff, 2008, 2009, 2012 and 2013*) agree with the ones measured with the Wenzel LH87 CMM by *Hielscher (2014)*. Unlike the Wenzel LH87 CMM, the Zeiss UMM 850 CMM can be used free of charge. Thus, it is recommended to use the Zeiss UMM 850 CMM for future measurements.

4.3.2 Mass and Volume Determinations

The mass of a rotating body or a sinker can be determined by weighing it in air. However, the buoyancy force of the air and the calibration characteristics of the balance have to be compensated. The model function for this approach is

$$m = m_{\text{bal},a} \left(1 - \frac{\rho_{a,\text{cal}}}{\rho_{\text{cal}}}\right) \cdot \left(1 - \frac{\rho_a}{\rho}\right)^{-1}, \quad (4.3)$$

where $m_{\text{bal},a}$ is the reading from the balance, $\rho_{a,\text{cal}}$ is the density of air determined while calibrating the balance, ρ_{cal} is the density of the calibration weights, ρ_a is the density of air determined while weighing, and ρ is the density of the rotating body or the sinker. However, this density is not known with high accuracy as both sinker and the rotating bodies are composed of different materials. A low uncertainty can not be achieved with this approach. In the following the rotating body or a sinker is called specimen.

Weighing the specimen in two fluids of known density solves this problem of the unknown density. Water and air were chosen as fluids, as the density of both can be calculated accurately, and it is very different for the two substances at ambient conditions. For determining the density of water the IAPWS formulation (*Wagner and Pruf, 2002*) was used; for moist air the equation of *Davis (1992)* was applied. The specimen's mass

$$m = \left(1 - \frac{\rho_{a,\text{cal}}}{\rho_{\text{cal}}}\right) \left(m_{\text{bal},w} + \rho_w \frac{m_{\text{bal},a} - m_{\text{bal},w}}{\rho_w - \rho_a}\right) \quad (4.4)$$

can be calculated with $m_{\text{bal},w}$ as the reading from the balance while the specimen is immersed in water and with ρ_w as the density of water. To simplify matters, the thermal expansion was neglected in eq. (4.4), see *Ntontos (2014)* for more details. Also neglecting thermal expansion, the volume of a specimen can be determined by

$$V = \left(1 - \frac{\rho_{a,\text{cal}}}{\rho_{\text{cal}}}\right) \left(\frac{m_{\text{bal},a} - m_{\text{bal},w}}{\rho_w - \rho_a}\right). \quad (4.5)$$

An example for the experimental setup for determining mass and volume of a specimen is shown in figure 4.12. See *Ntontos (2014)* for another setup of this kind.

Pressure and temperature have to be measured to calculate the density of water; for moist air, temperature and humidity have to be known. The pressure was measured with a precision barometer (Paroscientific, USA, type: 1650-101) with an expanded uncertainty ($k = \sqrt{3}$) of 0.08 hPa. This reading was corrected for hydrostatic effects in case of water. The temperature of water was determined utilizing a Pt-100 Ω temperature sensor and an AC resistance thermometry bridge (ASL, UK, type: F250). The nominal expanded uncertainty ($k = 2$) in temperature was 10 mK. The air temperature and humidity were determined utilizing a humidity and temperature transmitter (Vaisala, Finland, type: HMT333), which has expanded uncertainties ($k = 2$) of 0.1 K in temperature and 1 % in relative humidity. A balance (Mettler-Toledo, Germany, type: XP205) with a readability of 0.01 mg was used for the measurements. A software was written using Visual Basic 6 (Microsoft, USA). All relevant data like temperature, humidity, barometric pressure, and the reading from the balance could be logged and plotted during the calibration. The user could average the readings over a selectable time span. The data could be exported to a spreadsheet program (Microsoft, USA, type: Excel).

A thin copper wire was attached to the underpan weighing hook connecting it to a cage made of non-magnetic wire. The cage was surrounded by a bowl of glass, which could be filled with water. The sinker and the cage were fully immersed in water when the bowl was filled. A carrier – also made of non-magnetic wire – was placed on the bottom of the bowl.

The bowl rested on a lab jack. Thus, the vertical position of the entire bowl could be varied. When the sinker rested on the carrier, the cage was still immersed fully in



Figure 4.12 Experimental setup for mass and volume calibrations.

water but not in contact with the sinker and the carrier. To weigh the sinker in water, the balance was tared in this position. Then the vertical position of the bowl was lowered, until the sinker was attached solely to the cage. Thereby, the sinker could be weighed in water. This procedure was repeated 10 times to obtain a statistically valid result.

The manufacturer of the used water (sigma aldrich, USA, type: chromasolv Plus) specified the following residual components: chloride (Cl^-): $\leq 0.1 \text{ mg/kg}$, fluoride (F^-): $\leq 0.1 \text{ mg/kg}$, nitrate (NO_3^-): $\leq 0.1 \text{ mg/kg}$, sulfate (SO_4^{2-}): $\leq 0.1 \text{ mg/kg}$. Before the weighings in water, the specimens were cleaned with ethanol and the above mentioned water. The specimen including the cage and the carrier were placed inside the bowl before the bowl was filled with water. After filling the bowl with water, it was closed with a lid made of glass and placed in an ultrasonic bath (Bandelin, Germany, type: Sonorex S 2025FH). The filled bowl was heated to $T = 368.15 \text{ K}$ in the ultrasonic bath and degassed at this temperature. Additionally, all visible residual gas bubbles were removed manually with a wire. The closed, filled bowl was placed for at least 12 h on the lab jack for acclimatization. Thereafter, the temperature stability was checked, residual bubbles were removed and the weighing was started. The front of the setup was covered with a plate to minimize the influence of the draft.

After the weighing in water, the specimen was weighed in air. Before that, the specimen including bowl, carrier and cage were heated to $T = 473.15 \text{ K}$ for 24 h in an oven to remove any residual water. The bowl including specimen carrier and cage were placed on the lab jack. The weighing in air was started after a acclimatization time of at least 12 h.

The procedure of weighing the specimen in water and, thereafter, in air, was applied up to three times. The averages of the respective weighings were taken as best estimate for the weight in water or air. The results of the volume and mass are listed in table 4.4.

Table 4.4 Mass of the rotating bodies; mass and volume of the viscometer-densimeter's sinker. The coverage factor is $k = 2$ for all expanded uncertainties.

	Volume	Expanded uncertainty	Mass	Expanded uncertainty
Low-pressure viscometer's rotating body	–	–	97.2779 g	0.4 mg
Viscometer-densimeter's rotating body	–	–	37.0193 g	0.1 mg
Viscometer-densimeter's sinker ^a	12.5459 cm ³	0.002 cm ³	59.7712 g	1.5 mg

^a Mass and volume determined by *Ntontos (2014)*.

4.3.3 The Axial Moment of Inertia of the Rotating Body

The estimation of the axial moment of inertia J is presented in this section taking the low-pressure viscometer's rotating body as an example. Information concerning the

axial moment of inertia of the viscometer-densimeter's rotating body are given at the end of this section.

An overview of how the axial moment of inertia was estimated, is presented in table 4.5. This table is divided into three columns: (1) In the first column a schematic of the rotating body is shown, (2) in the second column the equations for the estimation of the axial moment of inertia of the low-pressure viscometer's rotating body are given, and (3) the equations for the determination of the mass of the rotating body are listed in the third column.

As can be seen in the schematic, the rotating body was divided into different elements. The axial moment of inertia and the mass were determined separately for each element. For each element the respective equations are listed in table 4.5. The total moment of inertia was estimated by calculating the sum of the single moments of inertia.

Most elements of the rotating body were treated mathematically as filled cylinders. This was for example the case for the permanent magnet (element III). The rotating body's cap, element II, and the position sensor, element X, were treated as hollow cylinders. The viscosity sensor, element VIII, was divided into two parts: a cylinder, element VIIIa, and a rectangular cuboid, element VIIIb. As the center of mass of the viscosity sensor was displaced from the center of rotation, the viscosity sensor's moment of inertia was calculated according to the parallel axis theorem, with c as the perpendicular distance.

For the calculation of the axial moment of inertia, the masses of the different elements have to be known. However, the masses of the different elements were not determined by weighing, since this was technically not possible, as explained in the following. In the manufacturing process, after the rotating body was assembled, its surface was machined by turning to achieve the final dimensions. This procedure was necessary to make sure that the rotating body has the same radius all over its entire length. As a consequence of the machining, the mass of the rotating body was reduced. Thus, the value of a prior mass determination by weighing all elements would have had a significant systematic offset.

As an alternative, the masses of the single elements were calculated using density and volume as input parameters. The respective volume was estimated on the basis of the geometries of the different elements.

In addition to the volume, the densities of the different element's were required to estimate the mass. The densities of the different materials were measured or the density given by the manufacturer of the material was taken as the best estimate. The rotating body consists of four different materials: (1) copper chromium zirconium (CuCrZr), (2) steel (1.4511), (3) a samarium-cobalt magnet ($\text{Sm}_2\text{Co}_{17}$) and (4) two-component glue. The densities of the copper chromium zirconium and the steel elements were determined by weighing samples of the same material; see *Ntontos (2014)* for further details. The

Table 4.5 Overview of the estimation of the axial moment of inertia of the low-pressure viscometer's rotating body. J is the axial moment of inertia; r_o is the rotating body's outer radius; the general symbol for the radius is r ; h is the height; m is the mass and ρ is the density. Geometries concerning the viscosity sensor, i.e., d , c , and l are depicted in the schematic.

Elements of the rotating body	Axial moment of inertia	Mass
I	$J_I = \frac{1}{2} \cdot m_I \cdot r_o^2$	$m_I = \rho_{1.4511} \cdot \pi \cdot r_o^2 \cdot h_I$
II	$J_{II} = \frac{1}{2} \cdot m_{II} \cdot (r_o^2 + r_{i,II}^2)$	$m_{II} = \rho_{1.4511} \cdot \pi \cdot (r_o^2 - r_{i,II}^2) \cdot h_{II}$
III	$J_{III} = \frac{1}{2} \cdot m_{III} \cdot r_{III}^2$	$m_{III} = \rho_{\text{Sm2Co17}} \cdot \pi \cdot r_{III}^2 \cdot h_{III}$
IV	$J_{IV} = \frac{1}{2} \cdot m_{IV} \cdot r_{IV}^2$	$m_{IV} = \rho_{1.4511} \cdot \pi \cdot r_{IV}^2 \cdot h_{IV}$
V	$J_V = \frac{1}{2} \cdot m_V \cdot r_V^2$	$m_V = \rho_{\text{CuCrZr}} \cdot \pi \cdot r_V^2 \cdot h_V$
VI	$J_{VI} = \frac{1}{2} \cdot m_{VI} \cdot r_o^2$	$m_{VI} = \rho_{\text{CuCrZr}} \cdot \pi \cdot r_o^2 \cdot h_{VI}$
	$J_{VIIa} = -m_{VIIa} \cdot [\frac{1}{4}(\frac{d}{2})^2 + \frac{1}{12} \cdot l^2 + c^2]$	$m_{VIIa} = \rho_{\text{CuCrZr}} \cdot \pi \cdot (\frac{d}{2})^2 \cdot l$
	$J_{VIIb} = -m_{VIIb} \cdot [\frac{1}{12} \cdot (l^2 + d^2) + c^2]$	$m_{VIIb} = \rho_{\text{CuCrZr}} \cdot l \cdot d \cdot h_{VIIb}$
VIIIa (VIIa)	$J_{VIIIa} = m_{VIIIa} \cdot [\frac{1}{4} \cdot (\frac{d}{2})^2 + \frac{1}{12} \cdot l^2 + c^2]$	$m_{VIIIa} = \rho_{1.4511} \cdot \pi \cdot (\frac{d}{2})^2 \cdot l$
VIIIb (VIIb)	$J_{VIIIb} = m_{VIIIb} \cdot [\frac{1}{12} \cdot (l^2 + d^2) + c^2]$	$m_{VIIIb} = \rho_{1.4511} \cdot l \cdot d \cdot h_{VIIIb}$
VII	$J_{IX} = \frac{1}{2} \cdot m_{IX} \cdot r_o^2$	$m_{IX} = \rho_{\text{CuCrZr}} \cdot \pi \cdot r_o^2 \cdot h_{IX}$
IX	$J_X = \frac{1}{2} \cdot m_X \cdot (r_o^2 + r_{i,X}^2)$	$m_X = \rho_{1.4511} \cdot \pi \cdot (r_o^2 - r_{i,X}^2) \cdot h_X$
X	$J_{XI} = \frac{1}{2} \cdot m_{XI} \cdot r_{XI}^2$	$m_{XI} = \rho_{\text{CuCrZr}} \cdot \pi \cdot r_{XI}^2 \cdot h_{XI}$
XI		
$\sum_{i=I}^{XI} J_i = J_{\text{calc}}$		$\sum_{i=I}^{XI} m_i = m_{\text{calc}}$

density given by the manufacturer was taken as best estimate for the density of the permanent magnet (*Arnold Magnetic Technologies, 2014*) and the glue (*Kremer, 2015*).

So far, the estimation of the moment of inertia is straight forward. This is mainly because several assumptions were made to simplify the math and some effects were neglected. These issues are discussed in the following. An assumption was that the rotation axis of the rotating body is identical with its geometrical symmetry axis. However, the viscosity sensor, which is made of steel (element VIII), has a lower density than element VII. Furthermore, the viscosity sensor has a perpendicular distance to the symmetry axis of the rotating body. Thus, technically the two axes are not identical. Further influences causing an offset between the axes can be the magnetic bearing of

the rotating body or the sensor coil of the rotational speed sensor. The efforts to quantify these influences, e.g., the influence of the magnetic bearing, are very high. Most likely, the measuring cell would have to be redesigned in order to include a system for the measurement of the position of the rotating body.

Further assumptions were made concerning the geometries of the different elements of the rotating body. An exact experimental determination of the geometries of the different elements would have been challenging, as many elements were notched on the inside or their edges were chamfered during the assembly. In addition, these notches and edges were too small to be measured with a coordinate measuring machine. To simplify matters, it was assumed that the geometry of the elements is identical with the specified values of the technical drawings of the rotating body within an expanded uncertainty ($k = \sqrt{3}$) of $15 \mu\text{m}$.

Also, the influence of the glue was neglected in the analytical approach. This is most likely a plausible simplification, as the density of the glue ($\approx 1050 \text{ kg} \cdot \text{m}^{-3}$) is significantly lower than the density of e.g. CuCrZr ($\approx 8800 \text{ kg} \cdot \text{m}^{-3}$). All gaps between the parts were assumed to be completely filled with glue. Furthermore, it was assumed that the geometry of the gaps is independent of temperature. However, copper expands $17 \mu\text{m}$ from $T = 293.15 \text{ K}$ to $T = 473.15 \text{ K}$, whereas steel expands only by $10 \mu\text{m}$. These changes in geometry due to thermal tensions were neglected.

In summary, compromises had to be made in order to estimate the moment of inertia mathematically. An appropriate measure for the accuracy of the entire estimation was the difference between the experimentally determined and the calculated mass of the rotating body. Unfortunately, the value of the calculated mass was significantly lower than the mass determined by experiment. Relative deviations were $100 \cdot (m_{\text{exp}} - m_{\text{calc}}) / m_{\text{calc}} = +0.32 \%$. Such an offset in mass resulted in a significant viscosity difference of $+0.32 \%$, taking helium at $T = 298.15 \text{ K}$ at $p = 0.1 \text{ MPa}$ as an example.

It was assumed that the rotating body's mass was determined more accurate by experiment than it was calculated. Thus, a corrected axial moment of inertia

$$J_{\text{corr}} = J_{\text{calc}} \cdot \frac{m_{\text{exp}}}{m_{\text{calc}}} \quad (4.6)$$

was taken as the best estimate, with J_{calc} as the calculated axial moment of inertia, J_{corr} as the corrected axial moment of inertia, m_{exp} as the experimentally determined mass of the rotating body and m_{calc} as the mass, which was calculated on the basis of the geometries and densities of the rotating body. The axial moment of inertia was scaled up by $\approx +0.32 \%$.

As this correction was large, the mass and the axial moment of inertia were also determined using a 3D-CAD software (Autodesk, USA, type: Autodesk Inventor) (Heine,

2014). The glue and the chamfered edges and notches were included into this model. This model was also used to estimate the uncertainty of the axial moment of inertia. Therefore, the input parameters, i.e., densities and geometries, were varied within their expanded uncertainties. The observed relative deviation was 0.7 %, which can be taken as an estimate for the expanded uncertainty of the axial moment of inertia. Thus, a relative deviation of 0.32 % in the axial moment of inertia is within its uncertainty. Furthermore, the relative deviation of 0.7 % agreed with an expanded uncertainty ($k = 2$), which was estimated based on *ISO/IEC Guide 98-3 (2008)*. In conclusion, with regard to the estimated expanded uncertainty, the model validated the analytical approach to determine the axial moment of inertia.

Generally, a lower uncertainty of the moment of inertia can be achieved. The largest contribution to the uncertainty in the axial moment of inertia results from the correction, in which the calculated moment of inertia is scaled based on the deviation between the calculated and the experimentally determined mass. An error in the experimental mass determination is a plausible explanation for this deviation and has to be excluded. Therefore, the mass of the rotating body has to be determined again by hydrostatic weighing. In addition, the uncertainty in density of the different materials of the rotating body has to be lowered. However, the required uncertainty can not be achieved by weighing the materials in air and correcting for the buoyancy force. The uncertainty in the geometry of the specimen limits this approach's uncertainty in density to $7 \text{ kg} \cdot \text{m}^{-3}$, even if the geometry of the specimen is determined with a coordinate-measuring machine. Therefore, the density of the materials also has to be determined by hydrostatic weighing.

In summary, from the current point of view, the most suitable solution for the above mentioned problems is to measure the viscosity in a relative way. This matter is discussed in section 4.4.

The Axial Moment of Inertia of the Rotating Body of the Viscometer-Densimeter

The following information is about the determination of the axial moment of inertia of the viscometer-densimeter's rotating body. In principle, the axial moment of inertia of the viscometer-densimeter's rotating body can be determined using the same procedures applied as in case of the low-pressure viscometer. However, the geometries of the viscometer-densimeter's rotating body are more complex than the geometries of the low-pressure viscometer's rotating body. This is observable in the technical drawing of the viscometer-densimeter's rotating body in section A.4. As can be seen, there is a steel plate between the permanent magnet and the main part of the rotating body. This steel plate is similar to element IV of the low-pressure viscometer. In case of the viscometer-densimeter, there is a thread at the bottom of the steel plate. With this thread

the steel plate was screwed into the main part of the rotating body. In addition, this plate was fixed by glue. The sensor rod was connected to the main part of the rotating body in the same way. Most likely this connection incorporates a significant amount of glue, assuming all residual spaces of the threads are filled with it. Estimating the residual spaces has a large uncertainty.

In analogy to the calculations presented above, the density of the different elements is needed to calculate the axial moment of inertia. Samples of the used material are required to determine the corresponding densities. Unfortunately, these samples are missing. Thus, the information about the densities have to be taken from data sheets. This approach has a larger uncertainty than the experimental determination of the densities. In addition, deviations in geometry have to be considered. As can be seen in figure 4.16, the permanent magnet seems to be off-centered to the symmetry axis up to 9 μm . Further deviations in geometry may come from the sensor rod. These two observations are a reasonable cause for a possible deviation between the geometrical axis of symmetry and the axis of rotation.

Against this background the exact determination of the axial moment of inertia is expected to have an insufficient large uncertainty. Most likely, the estimated uncertainty for the axial moment of inertia of the viscometer-densimeter's rotating body will be larger than the estimated uncertainty for the axial moment of inertia of the low-pressure viscometer's rotating body. In summary, it is most likely inevitable to measure the viscosity in a relative way. See section 4.4 for a more detailed conclusion.

4.3.4 Uncertainty Analysis of the Absolute Measurement Principle for the Low-Pressure Viscometer

The uncertainty of measuring the viscosity in an absolute way is analyzed in this section, taking the low-pressure viscometer as an example. The analysis is based on the Guide to the Expression of Uncertainty in Measurement (*ISO/IEC Guide 98-3, 2008*). The theory behind the uncertainty analysis is not reproduced here; see *Schäfer (2009)* for further detail. Measuring in an absolute way is also referred to as absolute measurement principle in the following.

An uncertainty budget of the absolute measurement principle is presented in table 4.6. This uncertainty budget is valid for measuring the viscosity of helium at $T = 298.25\text{ K}$ and $p = 0.1\text{ MPa}$. All known sources of uncertainty are listed in the first column of table 4.6. Most sources of uncertainty are identical with the model function's input parameters, e.g., the geometries of the cylinder system or the damping. How the estimates for the input parameters – and thus their uncertainties – were determined, is described in different parts of this thesis. This information is summarized in the following.

Table 4.6 Uncertainty budget for measuring the viscosity using the low-pressure viscometer in an absolute way. This estimation was made for a typical viscosity measurement of helium at a $T = 298.25$ K and $p = 0.1$ MPa. The uncertainty is underestimated.

Source of uncertainty	Uncertainty	Distribution	Coverage factor	Sensitivity coefficient	Standard uncertainty
Rotating body's radius ^a	4.20 μm	normal	2	$-3243.53 \mu\text{Pa s m}^{-1}$	-6.81 nPa s
Measuring cell's radius ^a	11.39 μm	normal	2	$1674.36 \mu\text{Pa s m}^{-1}$	9.54 nPa s
Rotating body's height ^a	6.58 μm	normal	2	$-168.67 \mu\text{Pa s m}^{-1}$	-0.55 nPa s
Rotating body's mass ^a	0.41 mg	normal	2	$207.26 \mu\text{Pa s m}^{-1}$	0.04 nPa s
Fluid density ^b	0.1 %	normal	2	$2.46 \cdot 10^{-3} \mu\text{Pa s kg}^{-1} \text{ m}^3$	0.00 nPa s
Damping	1.00 s^{-1}	normal	2	$2.25 \cdot 10^{-2} \mu\text{Pa s}$	11.30 nPa s
Residual damping	2.09 s^{-1}	rectangular	$\sqrt{3}$	$-2.25 \cdot 10^{-2} \mu\text{Pa s}$	-27.29 nPa s
Temperature	80 mK	rectangular	$\sqrt{3}$	$4.83 \cdot 10^{-4} \mu\text{Pa s K}^{-1}$	-0.02 nPa s
Thermal exp. coeff. ^c of Cu	5 %	rectangular	$\sqrt{3}$	$-199.43 \mu\text{Pa s m}^{-1} \text{ K}$	-0.10 nPa s
Thermal exp. coeff. ^c of $\text{Ti}_6\text{Al}_4\text{V}$ (3.7165)	3 %	rectangular	$\sqrt{3}$	$80.03 \mu\text{Pa s m}^{-1} \text{ K}$	0.02 nPa s
Thermal exp. coeff. ^d of steel (1.4511)	5 %	rectangular	$\sqrt{3}$	$8.47 \mu\text{Pa s m}^{-1} \text{ K}$	0.00 nPa s
Thermal exp. coeff. ^e of $\text{Sm}_2\text{CO}_{17}$	5 %	rectangular	$\sqrt{3}$	$15.21 \mu\text{Pa s m}^{-1} \text{ K}$	0.01 nPa s
Density ^f of steel (1.4511)	$178 \text{ kg} \cdot \text{m}^{-3}$	normal	2	$5.91 \cdot 10^{-5} \mu\text{Pa s kg}^{-1} \text{ m}^3$	5.22 nPa s
Density ^f of CuCrZr (2.1293)	$39 \text{ kg} \cdot \text{m}^{-3}$	normal	2	$-3.30 \cdot 10^{-5} \mu\text{Pa s kg}^{-1} \text{ m}^3$	-0.63 nPa s
Density ^e of $\text{Sm}_2\text{CO}_{17}$	$173 \text{ kg} \cdot \text{m}^{-3}$	rectangular	$\sqrt{3}$	$-1.95 \cdot 10^{-5} \mu\text{Pa s kg}^{-1} \text{ m}^3$	-1.99 nPa s
Correction of axial moment of inertia	$4.69 \cdot 10^{-9} \text{ kg} \cdot \text{m}^2$	rectangular	$\sqrt{3}$	$1.37 \cdot 10^7 \mu\text{Pa s kg}^{-1} \text{ m}^{-2}$	37.08 nPa s
Further geometries of the rotating body					6.17 nPa s
Expanded combined uncertainty ($k = 2$)					$0.099 \mu\text{Pa s}$
Relative expanded combined uncertainty ($k = 2$)					0.49 %
Viscosity estimated in an absolute way					$20.166 \mu\text{Pa s}$
Ab initio calculated reference viscosity of Cencek et al. (2012), standard uncertainty $0.0002 \mu\text{Pa s}$					$19.8299 \mu\text{Pa s}$
Relative deviation of the absolute experimental viscosity from the ab initio calculated reference viscosity					1.70 %

^a Hielscher (2014)

^b Arp et al. (1998)

^c Touloukian (1975)

^d Deutsche Edelstahlwerke (2008)

^e Arnold Magnetic Technologies (2014)

^f Ntontos (2014)

The geometries of the cylinder system (i.e., radius and height of the rotating body, and the inner radius of the measuring cell) were determined using two different coordinate measuring machines. The respective procedures were described in section 4.3.1. The uncertainties of these geometries result in a significant input to the standard uncertainty in viscosity, which is presented in the last column on the right end of table 4.6. The relative contribution of the cylinder system's geometries to the expanded uncertainty in viscosity is 5.6 %.

The mass of the rotating body of the low-pressure viscometer was determined by weighing it in water and air; see section 4.3.2 for further detail. The mass was used to correct the axial moment of inertia. Due to its low uncertainty, the influence of the uncertainty of the mass is low. The uncertainty of the correction of the axial moment of inertia was listed separately in table 4.6; see below for further detail. The density of the fluid in the measuring cell was calculated using the correlation of *Arp et al. (1998)*. It can be observed that this uncertainty was negligible.

This was different considering the uncertainties of the damping and the residual damping, which had significant relative contributions of 5.2 % and 30.3 % to the expanded uncertainty in viscosity, respectively. The residual damping was determined using the multi-fluid calibration. This method is described in section 4.2.2. The uncertainty of this method depends on the uncertainty of the reference fluids and on the uncertainty of the measurements of helium, argon and neon. Similar to the residual damping, the uncertainty of the damping also depends on the conditions prevailing during the measurements, e.g., the stability of the cylinder system and the scatter. For further details concerning these effects see sections 4.1 and 5.2. Information about the estimation of the dampings' uncertainties can also be found in section 5.2.

The next five sources of uncertainty listed below the dampings are temperature related. However, the uncertainties of temperature and the thermal expansion coefficients were also negligible in this uncertainty analysis.

The residual sources of uncertainty come from the calculation of the axial moment of inertia. The determination of the axial moment of inertia was described in section 4.3.3. As can be seen in table 4.6, the densities of the different materials contribute significantly to the uncertainty in viscosity, holding 1.3 % of the combined standard uncertainty. All geometries of the rotating body other than the outer radius and height are summarized as Further geometries of the rotating body to simplify matters. Table 4.5 gives an overview of these geometries. The contribution of the uncertainties of these geometries on the combined standard uncertainty in viscosity was 1.5 %.

As explained in section 4.3.3, the moment of inertia was scaled on the basis of the difference between the calculated and the experimentally determined mass of the rotating body. This source of uncertainty is called Correction of the axial moment of inertia, and it is the major contribution to the uncertainty in viscosity. About 56 % of

the uncertainty in viscosity results from this correction. However, assuming that the uncertainty of the correction was zero, still the relative expanded combined uncertainty ($k = 2$) in viscosity would be large, i.e., 0.33 %. Although this source of uncertainty is called a correction, it can also be seen as the uncertainty of the present model to calculate the axial moment of inertia. Therefore, it is reasonable to include the uncertainty of this correction.

Finally, the expanded combined uncertainty in viscosity was calculated; it was $0.099 \mu\text{Pa s}$, which equals a relative expanded combined uncertainty ($k = 2$) of 0.49 %. However, the relative deviation between the viscosity determined using the absolute measuring principle to the reference viscosity of helium (Cencek *et al.*, 2012) is 1.70 %, which is presented at the end of table 4.6. This deviation exceeds the estimated uncertainty by far. Assuming all input parameters were determined within their uncertainty and no severe other errors were made, there are two findings based on this observation: (1) The relative expanded combined uncertainty in viscosity of the absolute measurement principle is at least 1.70 %, and (2) there is an unidentified source of uncertainty missing in the uncertainty budget.

The estimated uncertainty in viscosity is contradictory towards previously reported uncertainties. Evers *et al.* (2002) stated a relative combined expanded uncertainty ($k = 2$) of 0.07 % in viscosity for the prototype of the low-pressure viscometer. The uncertainty given by El Hawary (2009) for the low-pressure viscometer was 0.06 % at $T = (253.15 \text{ to } 473.15) \text{ K}$ with pressure up to 2.4 MPa, which is even slightly lower than the uncertainty given by Evers *et al.* (2002). However, in contrast to the uncertainties stated by Evers *et al.* (2002) and El Hawary (2009), Hellmann *et al.* (2014) suggested the uncertainty of El Hawary's data to be at least 1 %, in addition, Hellmann *et al.* (2014) stated that the uncertainty is likely higher at the highest temperatures. This statement confirms the hypothesis of an unidentified source of uncertainty. Against this background, possible sources of uncertainty were considered. Most likely the above mentioned deviations result from the viscous coefficient. This is explained further in the next section.

4.3.5 Evaluation of the Fluid-Dynamic Model

As stated in section 4.3.4, a systematic offset in viscosity was observed, when the viscosity was determined in an absolute way. An uncertainty of the fluid-dynamic model was identified as a possible cause for this offset. Therefore, the assumptions in the derivation of the fluid-dynamic model are evaluated in this section. Furthermore, it is discussed, to what extend an eccentricity is appropriate to compensate the observed offset. First, the fluid-dynamic model is discussed in the following.

The model function incorporates two parameters derived from the fluid-dynamic model: the non-stationary parameter z and the viscous coefficient c_{vis} ; see eq. (2.2).

Basically, two different flow regions are incorporated in the viscous coefficient: the cylindrical flow and the disk flow. The cylindrical flow occurs in the annulus between the rotating body and the measuring cell; the disk flow occurs at the rotating body's top and bottom surfaces. Thus, the viscous coefficient c_{vis} is the sum of the viscous coefficients of the discs c_{disc} and the cylinders c_{cyl} . The viscous coefficient of the cylinder

$$c_{\text{cyl}} = 4\pi \cdot \frac{r_o^2 \cdot r_i^2}{r_o^2 - r_i^2} \cdot h \quad (4.7)$$

depends on the geometries of the cylinder system, which are the radius of the measuring cell or outer radius r_o , the rotating body's radius or inner radius of the cylinder system r_i and the height h of the rotating body. In case of the viscometer-densimeter two cylinder systems have to be considered due to the sensor rod, compare figure 3.10. The viscous coefficient of the disc is

$$c_{\text{disc}} = \frac{32}{6} \cdot r_i^3 \quad \text{for } Re < 30 \quad (4.8)$$

$$\text{or } c_{\text{disc}} = \frac{3.87}{4} \cdot r_i^3 \sqrt{Re} \quad \text{for } Re > 30. \quad (4.9)$$

The first equation, eq. 4.8, can be found in Müller (1932); eq. 4.9 in Schlichting and Gersten (2006). The Reynolds number of the disc flow is defined by

$$Re = \frac{2\pi f r_i^2 \rho}{\eta}, \quad (4.10)$$

with f as the average rotational frequency and ρ as the density of the fluid. In addition to the viscous coefficients, another parameter is obtained from the fluid-dynamic model: the non-stationary parameter

$$z = 4\pi \cdot \frac{r_o^2 \cdot r_i^2}{r_o^2 - r_i^2} \cdot h \cdot \left(\frac{r_o^2 \cdot r_i^2}{2 \cdot (r_o^2 - r_i^2)} \cdot \ln \frac{r_o}{r_i} - \frac{3r_i^2}{8} + \frac{r_i^4}{8r_o^2} \right), \quad (4.11)$$

which depends on the same geometries mentioned above. Again two different non-stationary parameters have to be considered for the viscometer-densimeter due to the sensor rod.

Most input parameters of eqs. (4.7 to 4.11) are geometries, which were measured using a coordinate-measuring machine, as described in section 4.3.1. However, eq. (4.9) incorporates the Reynolds number. Thus, eq. (4.9) depends on the viscosity and the density of the fluid under study and on the rotational frequency of the rotating body. However, eq. (4.9) is used practically only for the model function of the viscometer-densimeter. Therefore, the respective density can be measured. As the viscosity is also

part of the Reynolds number, the model function has to be solved using an iteration, which is, however, mathematically unproblematic.

The fluid-dynamic model was derived on the basis of several assumptions. *Docter et al. (1997)* evaluated all assumptions in their work. Therefore, not all assumptions are discussed here again. A general problem in the evaluation of the assumptions is the lack of experimental observations or arguments supporting or disproving the assumptions. This is the second reason why only selected assumptions are discussed here. Often, the impact of a possible violation of an assumption can not be quantified. Thus, the following evaluation has a subjective component.

A possible disturbance of the flow are temperature gradients, as they can cause convection inside the measuring cell. Temperature gradients can be up to 100 mK for the low-pressure viscometer. Furthermore, when measuring at elevated temperatures, cold fluid can “fall” into the measuring cell coming from the fluid outlet. This problem occurs the other way around when measuring at low temperatures. Both, the disc flow and the cylinder flow can be disturbed by these effects. *Docter et al. (1997)* assumed that the fluid does not move in vertical direction. However, it is likely that this assumption is violated, but the impact of this effect could not be quantified.

Next, the presence of end vortices is discussed. It was assumed that (1) there are no end vortices and (2) the cylinder flow and the disc flow do not interact with each other. These two assumptions depend on each other, as the laminar disc flow at $Re > 30$ most likely leads to end vortices in case of the low-pressure viscometer. This finding is discussed below.

Disc Flow and End Vortices

As mentioned before, the model function is strictly limited to the laminar flow regime. For the cylindrical flow, a critical Taylor number yields the information how to set the limit for the maximum pressure for each isotherm. When the critical Taylor number is not observed, Taylor vortices might develop in the annulus. In this case, the model function is not valid and therefore the viscosity can not be determined with eq. (2.2). However, the disc flow can also change its characteristic: Similar to the Taylor number, a Reynolds number for the disc flow is known. With the help of this Reynolds number, the transition of a laminar Stokes flow to a laminar flow and from laminar to turbulent flow can be predicted. An example of a Stokes flow is given in figure 4.13 a); an example for a laminar flow is shown in figure 4.13 b).

The laminar Stokes flow appears upon a rotating disk, when the Reynolds number is low and thus the inertial forces are small compared to the viscous forces. In this case, the viscous moment of the free disk flow is given by eq. (4.8). This equation is valid,

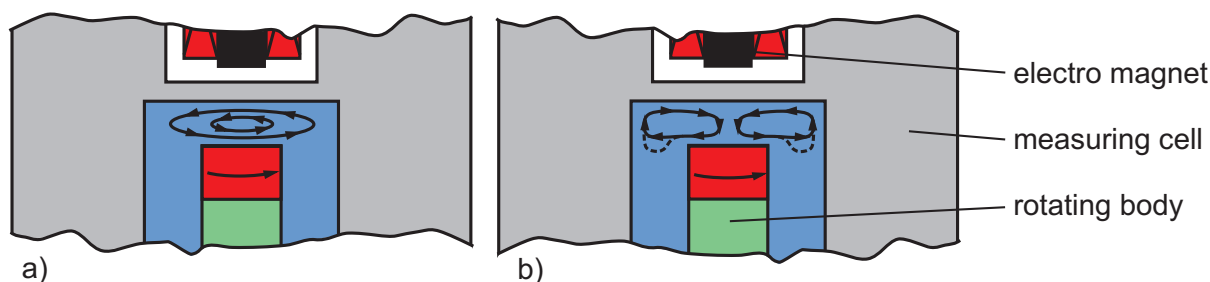


Figure 4.13 Schematic visualizing the possible flow on the top of the rotating body.
a) Laminar Stokes flow.
b) Laminar flow. The dashed line illustrates what is called “end effect” by Kobayashi *et al.* (1991).

when all particles on top and bottom of the rotating body are moving in circular paths parallel to the top and bottom surfaces.

In the laminar disk flow, see figure 4.13 b), the inertial forces are not neglected. Thus, the fluid close to the disk surface is moved to the disk’s rim and beyond, due to its mass inertia. A small pressure gradient arises between the rim and the middle of the disk. In a closed housing, a ring-shaped vortex develops.

It appears that the measuring range of the low-pressure viscometer is limited to a Reynolds number for the disk flow of less than 30. This assumption is discussed in the following on the basis of figure 4.14. In figure 4.14 a), the damping values are plotted vs. the pressure. As can be seen, there is an inflection point in the course of the dampings at approx. $p = 0.8$ MPa. This point may indicate a transition in the flow. To visualize the influence of the changing flow, exemplary only eq. (4.8) was used to describe the moment of the disk flow in the model function. The corresponding results are shown in figure 4.14 b). In figure 4.14 b), the relative deviations of the experimental viscosities η_{exp} for methane from values η_{calc} calculated with the correlation of Quiñones-Cisneros *et al.* (2010) (zero line) were plotted vs. pressure. There is a remarkable offset of 0.4% between the viscosities of pressures up to 0.6 MPa and viscosities at pressures beyond 1.0 MPa. This offset is larger than the uncertainty of the correlation of Quiñones-Cisneros *et al.* (2010), which is 0.3 %.

Only eq. (4.9) was used in the model function to prepare figure 4.14 c). It is obvious that the use of eq. (4.9) gives no reasonable results below pressures of 0.6 MPa at $Re < 30$. However, the data of pressures higher than 1.0 MPa look reasonable. But these data were regarded to have a higher uncertainty than the data measured at $Re < 30$ that were calculated with eq. (4.8). This is explained in the following.

When the fluid-mechanical model was developed by Docter *et al.* (1997), he assumed that the flow at the disk and the flow in the cylinder do not interfere with each other. This is most likely true in the case of the laminar Stokes flow (figure 4.13 a) on the disk

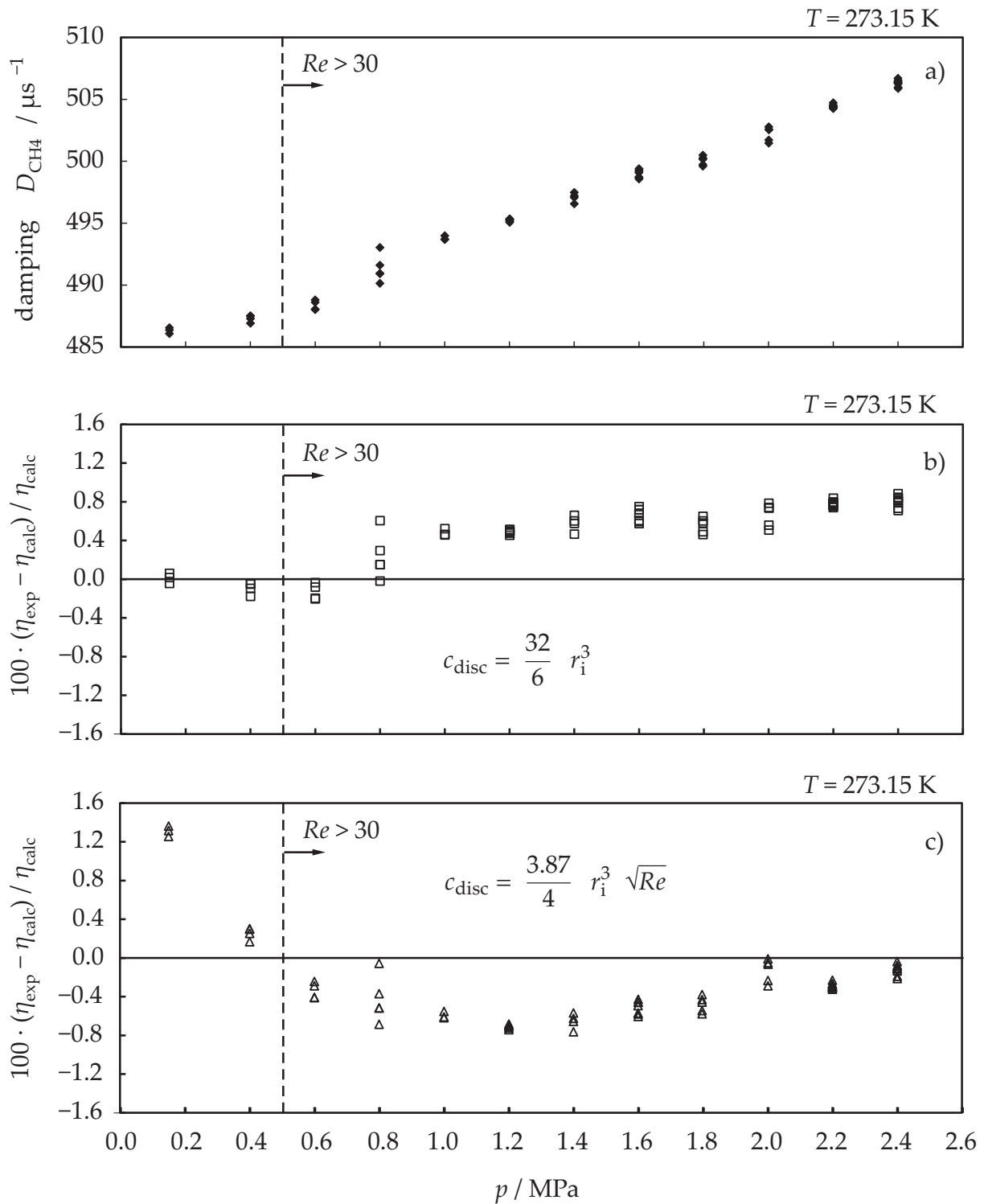


Figure 4.14 Three diagrams that visualize the influence of the Reynolds number of the disk flow. The used methane data were measured at $T = 273.15$ K by Schäfer (2009). The damping D of methane was plotted vs. pressure p in diagram a). In diagrams b) and c), relative deviations of experimental viscosities η_{exp} for methane from values η_{calc} calculated with the correlation of Quiñones-Cisneros *et al.* (2010) (zero line) were plotted vs. pressure. The dashed line marks the state, where $Re \approx 30$.

at $Re < 30$. However, with $Re > 30$ an interference was observed by Kobayashi *et al.* (1991), who studied the “end effect” in a coaxial cylindrical viscometer. A schematic of how the real flow could look like with $Re > 30$, is given in figure 4.13 b). The dashed line illustrates experimental observations of Kobayashi *et al.* (1991). They found out that some fluid, coming from the disk, streams into the annulus at $Re > 30$. Thus, end effects are a reasonable explanation for the shift in the damping values in figure 4.14. Docter’s assumption that the disc flow and the cylinder flow do not interfere is therefore considered to be not valid in case of the low-pressure viscometer at $Re > 30$.

The uncertainty of the measurements at $Re > 30$ depends on the accuracy of the fluid-dynamic model for this region. However, the known fluid-dynamic model is only valid, if the flows do not interfere. Thus, strictly speaking, the fluid-dynamic model is not valid; it most likely describes the real flow with a significant deviation. Therefore, the uncertainty is expected to be high.

In summary, there is a change in the disk flow at $Re \approx 30$, i.e., end effects come into play at $Re > 30$. Thereby, most likely the flow in the annulus is disturbed. The impact of these effects was considered to be not negligible for measurements with the low-pressure viscometer at $Re > 30$. Consequently, the measurement range was limited to $Re < 30$.

The behavior visualized in figure 4.14 was not observed for the viscometer-densimeter, yet. Most likely these effects are smaller in case of the viscometer-densimeter. There are two possible reasons for this: (1) The annulus of the viscometer-densimeter (1.5 mm) is smaller in comparison to the one of the low-pressure viscometer (4.5 mm). Thereby the formation of end vortices is inhibited. (2) The conditions for end vortices are bad at the lower end of the rotating body. Due to the sensor rod, there is no flat disc at the lower end.

Although end vortices are inhibited, there is a disadvantage of the present design of the rotating body of the viscometer-densimeter. As a sensor rod is incorporated, a disc flow does most likely not describe the real flow appropriately. The main part of the rotating body of the viscometer-densimeter has a larger diameter than the sensor rod. Evers *et al.* (2002), however, considered the transition area between the two diameters together with the disc at the end of the sensor rod as one disc. Technically speaking, this is not a valid assumption. The absence of one disc results in an offset in viscosity of +0.7 %. Therefore, this deviation can not be neglected.

In addition to the above listed issues, it was assumed that the disc flow is independent of the suspension height. The variation the vertical position of the low-pressure viscometer’s rotating body is a standard procedure during the alignment of the cylinder system. When the measured damping was plotted vs. height, a parabola-like function was observed. The main origin for this effect was likely a height dependent change in the viscous moment of the disc flow. For the viscometer-densimeter, the influence of the

suspension height was investigated by *Ntontos (2014)*. The observed dependence was also significant.

Unfortunately, it is not possible to investigate the influence of suspension height for just one disc. When the free space above the rotating body is increased, the free space at the bottom of the rotating body is decreased. Only the sum of both viscous moments can be investigated. Therefore, it can not be clarified, if the viscous coefficient is really independent of the suspension height. However, an underestimation of the viscous coefficient of the disc flow, eq. (4.8), is a possible explanation for the positive offset in viscosity.

Other models for the calculation of the viscous coefficient of the disc flow (*Docter, et al. 1997*) were tested. These models described the viscous moment of the disc flow in a closed housing in dependence of the free space above a disc. However, these models resulted in an even larger positive offset of the viscosity. Furthermore, it is very complex to determine the suspension height over the entire temperature range of the apparatuses. Thus, the models were not used.

Viscous Coefficient of the Cylinder Flow

The viscous coefficient of the cylinder flow was derived under the assumption of a concentric cylinder system. The background of this assumption is that if the cylinder system is concentric, the fluid does not move in radial direction. However, in practice this assumption can be violated by an eccentricity, a deviation in geometry or an imprecise magnetic bearing of the rotating body.

An eccentricity can be caused by a parallel offset between the symmetry axis of the rotating body and the symmetry axis of the cylinder system's outer cylinder. In addition, an offset in the angle between the two axes also results in an eccentricity. Both of these deviations are visualized in figure 4.15. The shown system is offset in two ways: (1) The symmetry axis of the rotating body does not agree with the symmetry axis of the measuring cell. This yields an eccentricity as can be seen in cut B - B. (2) There is an angle deviation between the symmetry axes. In cut A - A, the two effects (1) and (2) add up; in cut C - C they compensate each other.

During the commissioning of the apparatuses the eccentricity is minimized by aligning the cylinder system. Therefore, the position of the rotating body inside the measuring cell is varied and the damping values corresponding to the different positions are measured. The position of the rotating body was varied by changing the angle, one vertical and two horizontal axes; see section 5.1 for details. At one position the damping is minimal. This position was used for the measurements, i.e., the cylinder system was considered to be aligned.

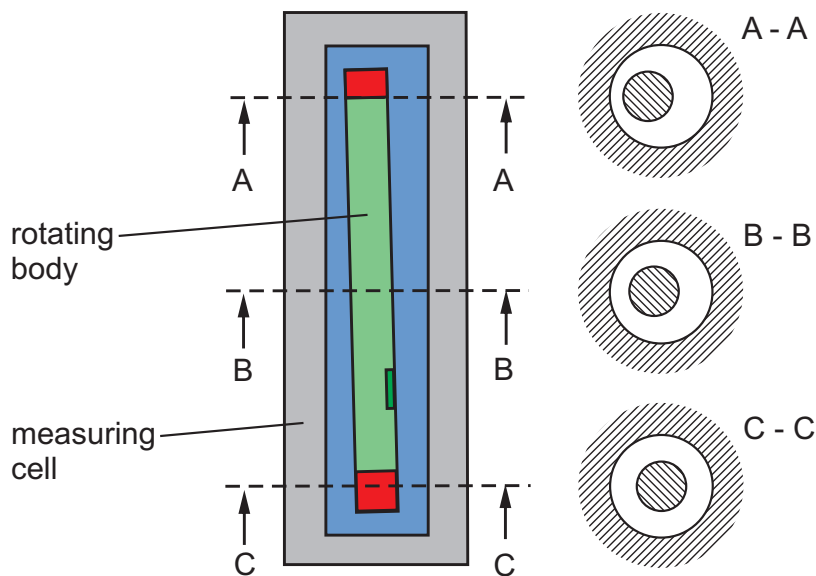


Figure 4.15 Schematic of the measuring cell of the low-pressure viscometer visualizing an eccentricity superposed by an angle deviation.

However, although the cylinder system was aligned elaborately, an eccentricity can recur after changing the temperature. *Ntontos (2014)* observed this for the low-pressure viscometer. Both apparatuses consist of different materials, which have different thermal expansion coefficients. For the low-pressure viscometer, the temperature of the base plate – including the centering device – rises up to 333.15 K, when the measuring cell is heated to $T = 473.15$ K. During the work of *Ntontos (2014)*, this resulted in an inevitable eccentricity; see section 5.2 for further detail. This effect was not investigated for the viscometer-densimeter, yet.

In addition to the eccentricity resulting from thermal issues, there are effects originating from the magnetic bearing. As a magnetic suspension coupling is fundamental for the measurement principle, these effects account for both apparatuses. The rotating body centers itself inside the magnetic field between the permanent magnet and the electromagnet. However, in practice, not all three magnetic axes – (1) the one of the permanent magnet on top of the electromagnet, (2) the one of the electromagnet and (3) the one of the permanent magnet incorporated in the rotating body – are perfectly congruent with the geometric axis of the rotating body and the geometric axis of the outer cylinder. A deviation in angle and a parallel offset of these axes are likely. Due to the imperfection of the magnetic field, the rotating body – and thus the fluid – moves in radial direction inside the measuring cell during one revolution.

Similar effects come from deviations in geometry. The geometries were investigated using a coordinate measuring machine; see section 4.3.1. A plot of the observed deviations is presented in figure 4.16 where a schematic of the viscometer-densimeter's rotating body is shown with a deviation plot of the rotating body's upper part. As can

be seen, the cap of the permanent magnet is off-centered in relation to the residual part of the rotating body. This offset is as large as $9\text{ }\mu\text{m}$ and is probably significant. Although they were not that severe, deviations were also found for the rotating body of the low-pressure viscometer.

An imprecision in the magnetic bearing as well as deviations in geometry yield the dissipation of the rotating body's kinetic energy as the fluid moves in radial direction. This movement is not covered by the fluid-dynamic model. The rotating body slows down too fast and consequently the measured damping is too high. In consequence the measured viscosity is too high. This observation agrees with the positive offset in viscosity.

Compensating the Imperfections of the Cylinder System

A term c_{ecc} can be included into the viscous coefficient c_{vis} of the model function to compensate for the eccentricity. However, the correction used by *Docter et al. (1997)* is based on experimental observations of the behavior of liquid fluids (*DIN 53019-3, 2008*) and not on an analytic solution of the Navier-Stokes equation. Technically speaking, it is not applicable for deviations in geometry or a lack of precision of the magnetic bearing of the rotating bodies.

Assuming the validity of this correction, it is most likely valid for an eccentricity as well as for an angle deviation. Mathematically, it can even compensate all known imperfections of the fluid-dynamic model, i.e., compensate the offset. However, to apply the correction, the exact value of the eccentricity is needed. Unfortunately, there is no way to determine the value of the eccentricity in an absolute way due to the complexity of the observed effects. A reference fluid such as helium could be used to quantify the eccentricity.

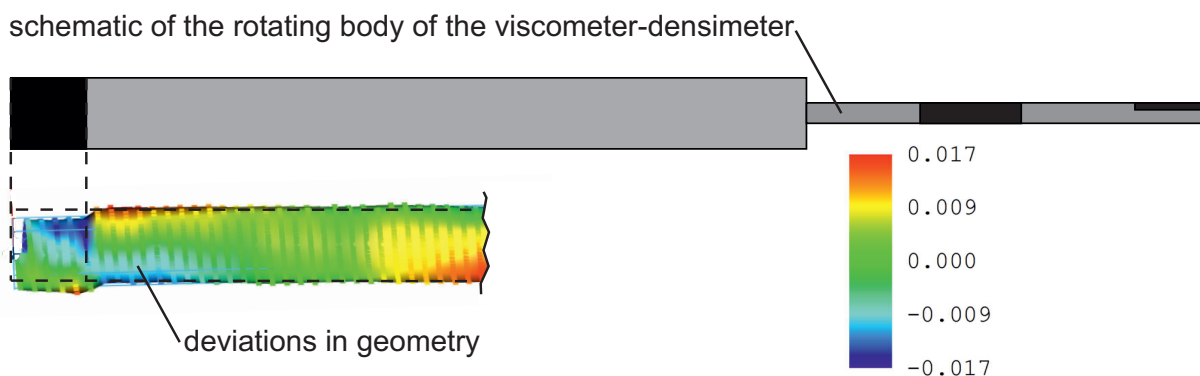


Figure 4.16 Visualization of the quality of the viscometer-densimeter's rotating body, which was examined by *Hielscher (2014)*. Absolute deviations are plotted to the average diameter (green). For visualization purposes the deviations are enlarged by a factor of 50. The unit of the legend is μm .

4.3.6 Measuring the Viscosity Relative to Helium

As mentioned before, the absolute measurement principle had a large uncertainty. In addition, the viscosities determined in an absolute way were off about 1.70 % off in relation to a reference value. Therefore, an alternative method was applied to determine the viscosity. This method is described in the following section.

The fundamental difference to the absolute measurement principle is that in this alternative approach, the viscosity is measured in a relative way, using a reference fluid. This approach is common to measure viscosities; a similar procedure was already used by *Docter et al. (1997)* taking nitrogen as reference. To generally apply this method, the model function given in eq. (2.5) was set into relation to the model function of a reference fluid. This yields a relative model function

$$\eta = \frac{z^* \cdot D - D_R}{z_{\text{ref}}^* \cdot D_{\text{ref}} - D_R} \cdot \eta_{\text{ref}}. \quad (4.12)$$

In comparison to eq. (2.5), additionally a reference damping D_{ref} and a reference viscosity η_{ref} was required to apply eq. (4.12). The non-stationary parameter z^* is defined by eq. (2.4). However, the uncertainty of eq. (4.12) is very sensitive to the uncertainty of the reference viscosity. Therefore, a minimal uncertainty for this reference viscosity was desired. The most appropriate reference fluid was helium in the limit of zero density. These viscosities have a standard uncertainty of only 0.001 % (*Cencek et al., 2012*) over the entire temperature range of the apparatuses. Thus, helium was chosen as reference fluid. As the reference viscosities were only available for zero density, the reference damping D_{ref} was the damping of helium in the limit of zero density $D_{0,\text{He}}$. To determine $D_{0,\text{He}}$, damping values of helium were measured over the entire temperature range at low pressures. Then, these values were extrapolated to zero density at every temperature to obtain $D_{0,\text{He}}(T)$. Per definition, the fluid density is zero in the limit of zero density, thus $z_{\text{ref}}^* = 1$. With this simplification and applied to helium, the relative model function reads:

$$\eta = \frac{z^* \cdot D - D_R}{D_{0,\text{He}} - D_R} \cdot \eta_{0,\text{He}}. \quad (4.13)$$

As can be seen, eq. (4.13) is independent of the viscous coefficient c_{vis} and thus of the geometries incorporated in c_{vis} . The non-stationary parameter z^* depends only weakly on the apparatus constants, e.g., the axial moment of inertia. Thus, practically, eq. (4.13) is also independent from the axial moment of inertia.

In conclusion, input parameters like the geometries of the cylinder system and the axial moment of inertia do not significantly influence the calculation of the viscosity using eq. (4.13). Therefore, the use of eq. (4.13) is accompanied by different benefits. However, in practice, eq. (4.13) is combined with the multi-fluid calibration. The conjunction

was called extended model function. This new approach to measure the viscosity is discussed in the next section.

4.4 Evaluation of the Extended Model Function

During this work, the model function of the viscosity measurement was modified in two ways: (1) it was set into relation to a reference fluid, i.e., helium, and (2) the residual damping was determined using three fluids of different viscosity as reference, i.e., helium, argon and neon. The combination of both is called extended model function in the following. The objective of this section is to summarize the reasons for developing the extended model function. Furthermore, its capability is evaluated.

The main reason for measuring in a relative way, was the large uncertainty of the absolute measurement principle. As described in section 4.3.4, relative deviations of 1.70 % between the viscosities determined in an absolute way and a reference viscosity of helium were observed. Different reasons for this offset were identified, such as deviations in the geometry of the rotating bodies. In addition, it was likely that the magnetic axes were not in agreement with the respective geometric symmetry axes of the rotating bodies. These shortcomings affected both, the axial moment of inertia and the fluid flow in the annulus. In consequence, the calculated moment of inertia had a large uncertainty, and, furthermore, a radial movement of the fluid during measuring was generated. However, any fluid movement in radial direction within the annulus is not covered by the fluid-dynamic model. Another shortcoming of the fluid-dynamic model was that the viscous coefficient of the disc flow was likely not describing the real disc flow with high accuracy.

The above listed observations give sound reasons why it was technically not feasible to measure the viscosity in an absolute way, although the input parameters of the model function were determined using state of the art methods. However, measuring in a relative way did compensate the above listed shortcomings of the absolute model function. The majority of the above mentioned input parameters canceled by setting the absolute model function in relation to a reference fluid. Due to its small uncertainty at zero density, helium was selected as reference. However, using helium as reference is state of the art in viscosity measurement today. The downside of this approach is that the majority of the measurement results is correlated. However, from an experimental point of view, the relative model function was inevitable.

In addition to measuring in a relative way, one parameter of the relative model function, i.e., the residual damping, was calibrated using helium, argon and neon as reference fluids. This multi-fluid calibration was necessary to compensate a viscosity dependent offset. This offset of the residual damping was identified as the only plausible cause for the viscosity dependent offset. Applying the same correction to the residual

damping canceled the viscosity dependence for fluids with very different viscosities. This observation in conjunction with a sensitivity analysis of the model function, and the fact that the correction was fluid independent, were the basis for this conclusion.

Different plausible causes for the offset in residual damping were found, like – in analogy to the spinning rotor gauge – the influences of the rotating body's surface, residual molecules, or the measurement times up to one hour. In contrast to a damping measurement in fluid, the frequency of rotation is slowed down much less during a damping measurement at vacuum pressures. Summarizing the above listed observations, determining the residual damping in an experimental way was error prone due to the complexity of the experimental procedures.

In addition, the multi-fluid calibration has proven to be more than just a valuable alternative to the experimental determination of the residual damping. One of the main advantages of the multi-fluid calibration compared to the experimental determination is the lower uncertainty at temperatures $T > 373.15$ K.

The validity of the extended model function, which is the combination of the relative model function and the multi-fluid calibration, can be evaluated taking the reproducibility of reference viscosities as measure. The damping of helium, argon and neon was measured at low pressures and was then extrapolated to zero density as part of the multi-fluid calibration of the residual damping. When these zero density dampings were inserted into the extended model function, the viscosity at zero density of helium, argon and neon could be re-calculated. The deviations to the reference viscosities at zero density were found to be always within the expanded uncertainty given for the reference viscosities over the entire temperature range from $T = (253.15 \text{ to } 473.15)$ K.

However, most likely the extended model function is applicable for fluids different from the reference fluids, too. The viscosities of the reference fluids ranged from (18 to 40) $\mu\text{Pa s}$ over the entire temperature range of the apparatuses. As stated above, the extended model function was applicable in this wide viscosity and temperature range. Therefore, the extended model function is considered to be applicable for fluids with different – unknown – viscosities.

Moreover, although the extended model function was calibrated just in the limit of zero density, it was successfully used at higher densities. The molar masses of the reference fluids ranged from $4.002 \text{ g} \cdot \text{mol}^{-1}$ (helium) to $39.948 \text{ g} \cdot \text{mol}^{-1}$ (argon). The density of fluids depends on the molar mass at low pressures. As the extended model function is applicable for fluids with very different molar mass, it was considered to be valid beyond the zero density limit.

Schäfer et al. (2015) applied the extended model function to measure the viscosity of carbon dioxide using the low-pressure viscometer. The uncertainty of the extended model function was analyzed using these measurements as an example. All observed sources of uncertainty during the calibration measurements and the carbon dioxide

measurements were taken into account. Relative expanded combined uncertainties ($k = 2$) of (0.20 to 0.41) % were achieved for the low-pressure viscometer. Considering the uncertainty estimated for the absolute measurement principle, this is a major advantage of the extended model function compared to the absolute measurement principle. Using the extended model function, the low-pressure viscometer can be considered to be among the most accurate viscometers in the world. The results of the carbon dioxide measurements and the respective uncertainty analysis are presented in the next chapter.

5 Measurement of the Viscosity of Carbon Dioxide at Low Pressures

The viscosity of carbon dioxide at low pressures was measured in this work, utilizing the enhanced low-pressure viscometer. *Ntontos (2014)* and *Humberg (2015)* did most of the practical work in the laboratory including the data analysis. This work's data were published within the scope of the present doctoral dissertation by *Schäfer et al. (2015)*. Thus – instead of referring to “this work” – it is referred to the corresponding publication of *Schäfer et al. (2015)* in text. This chapter is based on *Schäfer et al. (2015)* to a large extend.

All new equipment described in chapter 3, e.g., the new system for measuring time and controlling the viscosity sequence was available for the measurements of carbon dioxide. Furthermore, the experimental procedures were customized to minimize any effects interfering with the viscosity measurement like hysteresis or sorption. Moreover, the viscosity of carbon dioxide was determined with the extended model function.

The experimental procedures including parts of the commissioning are described in the first section of this chapter. Thereafter, the uncertainty of the measured data is estimated. The results for carbon dioxide are compared to other experimental and literature data in the end of this chapter.

5.1 Experimental Procedures

Before the measurements were started, the apparatus was adjusted to obtain a concentric alignment of the cylindrical system inside the measuring cell. This adjustment was carried out by systematically varying the position of the rotating body inside the measuring cell. As described in section 3.5.1, a device for centering the cylindrical system was placed upon the base plate, to which the electromagnet was connected directly. Thus, contactless motion of the freely suspended rotating body was possible in two orthogonal horizontal directions and in height since the magnetically suspended rotating body centered itself in the electromagnetic field between the electromagnet and the permanent magnet. Therefore, it was sufficient to move the electromagnet and the rotating body followed automatically. The motion on the orthogonal axes was realized in sufficiently small steps of about 30 μm and the damping D was measured in each position. According to the fluid-dynamic model, the damping was minimal once the cylindrical system was set to a concentric position. A similar procedure was applied for the angle alignment and the adjustment of the vertical position of the rotating body inside the measuring cell. The damping measurements required for the alignment procedure were carried out with helium at $T = 298.15\text{ K}$ and a pressure

of 0.1 MPa. Changing the temperature from $T = 473.15$ K down to $T = 253.15$ K and back to $T = 298.15$ K had an influence on the alignment affecting the eccentricity. This enlargement of eccentricity was compensated, and, furthermore, considered in the uncertainty analysis. See section 5.2 for details.

Measurements were carried out along isotherms. The order of the isotherms was always $T = (298.15, 323.15, 373.15, 423.15, 473.15, 253.15, 273.15)$ K and again $T = 298.15$ K. In this way the influence of hysteresis, which is described in section 4.1.1, was minimized. The measuring cell was filled separately for every single state point along an isotherm. The filling procedure was: (1) Reducing the pressure of the remaining fluid down to atmospheric pressure. (2) Refilling the measuring cell to 2 MPa. (3) Reducing to atmospheric pressure and refilling to 2 MPa again. (4) Reducing the pressure to the next measuring point. After adjusting the pressure, the viscosity measurement was started with a delay of 15 min. Thereby, disturbing turbulent flows resulting from the filling procedure and temperature fluctuations were abated. At least three replicates of the damping were measured, and the average value was used as experimental result. Repeated measurements were consistent within $\pm 1.09 \mu\text{s}^{-1}$.

When the fluid of interest was exchanged, the filling procedure was repeated several times. But the pressure was reduced to atmospheric pressure all the way to the new sample cylinder. It was checked for residual fluid by measuring the damping over a long time span of several hours. As the presence of residual fluid was accompanied by sorption effects, a drifting damping was a measure for the residual fluid. A typical drift of the damping coming from sorption effects is depicted in figure 4.2 in section 4.1.2. The filling procedure was repeated until the drift of the damping was negligible.

Measurements were performed only when the laminar disk flow on top and on the bottom of the rotating body and the laminar couette flow in the annulus between the rotating body and the measuring cell were assured. To secure a laminar flow, the Reynolds number for the disk flow and the Taylor number for the flow in the annulus were calculated for every (T, p) state point in dependence of viscosity, density and the maximum rotational frequency f_{max} . The limit for the maximum frequency was set to $f_{\text{max}} = 220$ mHz (13.2 rpm). On this basis, the maximum pressure for each isotherm was calculated.

The same starting frequencies f_{start} were set for all measurements. When starting a damping measurement, the rotating body was accelerated to a frequency of about $f_{\text{max}} = 220$ mHz (13.2 rpm). The scanning of the filtered signal of the viscosity sensor was not started until the frequency had decreased to $f_{\text{start}} = 200$ mHz (12 rpm). Hereby, the formation of the flow in the annulus between the rotating body and the wall of the measuring cell was assured. The duration of a measurement was 9 min.

In order to apply the extended model function, measurements on helium were carried out over the entire temperature range. The helium (Air Liquide, Germany, type: AL-

PHAGAZ 2 He) had a purity of $x_{\text{He}} \geq 0.999999$ [impurities stated by the supplier: $x_{\text{H}_2\text{O}} \leq 0.5 \cdot 10^{-6}$, $x_{\text{O}_2} \leq 0.1 \cdot 10^{-6}$, $x_{\text{CmHn}} \leq 0.1 \cdot 10^{-6}$, $x_{\text{CO}} \leq 0.1 \cdot 10^{-6}$, $x_{\text{CO}_2} \leq 0.1 \cdot 10^{-6}$, $x_{\text{H}_2} \leq 0.1 \cdot 10^{-6}$, where x denotes the mole fraction]. The results were used to determine the temperature dependent damping at zero density of helium $D_{0,\text{He}}(T)$. After that, measurements on argon (Air Liquide, Germany, type: ALPHAGAZ 1 Ar) [purity: $x_{\text{Ar}} \geq 0.99999$, impurities stated by the supplier: $x_{\text{H}_2\text{O}} \leq 3.0 \cdot 10^{-6}$, $x_{\text{O}_2} \leq 2.0 \cdot 10^{-6}$, $x_{\text{CmHn}} \leq 0.5 \cdot 10^{-6}$, where x denotes the mole fraction] and neon (Westfalen, Germany, type: Neon 5.0 T10) [purity: $x_{\text{Ne}} \geq 0.99999$, impurities stated by the supplier: $x_{\text{O}_2} \leq 2 \cdot 10^{-6}$, $x_{\text{N}_2} \leq 5 \cdot 10^{-6}$, $x_{\text{H}_2\text{O}} \leq 2 \cdot 10^{-6}$, where x denotes the mole fraction] were carried out. As described in section 4.2, the residual damping was estimated for each isotherm by the multi-fluid calibration based on these measurements. Finally, the viscosity of carbon dioxide was measured.

5.2 Uncertainty Analysis

This section is based on the uncertainty analysis published by *Schäfer et al. (2015)*. As mentioned before, *Schäfer et al. (2015)* used the extended model function to determine the viscosity of carbon dioxide. Strictly speaking, the uncertainty analysis in this section is only valid for these measurements, because the impact of some effects, e.g., sorption or an eccentricity drift, will be different in future, especially when measuring mixtures of gases. Nevertheless, the results of the uncertainty analysis are a measure for the accuracy of the enhanced low-pressure viscometer and will serve for future uncertainty analyses for this particular instrument. The uncertainty was estimated according to the Guide to the Expression of Uncertainty in Measurement (*ISO/IEC Guide 98-3, 2008*). The practical application of this guide to estimate the uncertainty of the carbon dioxide data is transferable to future measurements, if the viscosity is measured using the same experimental procedures described in section 5.1 and the same kind of calibration.

An uncertainty budget for the carbon dioxide measurements is listed in table 5.1. The expanded uncertainty ($k = 2$) in viscosity was (0.030 to 0.052) $\mu\text{Pa s}$, which corresponds to a relative expanded uncertainty ($k = 2$) of (0.20 to 0.41)%. The main contribution to this uncertainty arose from the damping D , the residual damping D_{R} , and the damping at zero density of helium $D_{0,\text{He}}$. The uncertainties of these input parameters are discussed in further detail below.

As stated in section 4.3.6, the extended model function depends only weakly on the geometry of the cylindrical system inside the measuring cell, the thermal expansion coefficients of the materials, the mass of the rotating body and the density of the fluid. Thus, these input parameters were neglected in table 5.1, since their contribution to the uncertainty was not significant. However, the uncertainty of these input parameters was estimated with state of the art methods, see section 4.3. The term *Rest* in table 5.1

Table 5.1 Budget for the uncertainty^a in viscosity at a temperature of 473.15 K.

Source of uncertainty	Uncertainty	Distribution	Coverage factor	Sensitivity coefficient	Standard uncertainty
Damping	$1.09 \mu\text{s}^{-1}$	Normal	2	0.0222 Pa s^2	$0.0122 \mu\text{Pa s}$
Residual damping	$8.74 \mu\text{s}^{-1}$	Rectangular	$\sqrt{3}$	0.0036 Pa s^2	$0.0181 \mu\text{Pa s}$
Damping at zero density of helium	$1.09 \mu\text{s}^{-1}$	Rectangular	$\sqrt{3}$	0.0186 Pa s^2	$0.0117 \mu\text{Pa s}$
Rest					$0.0022 \mu\text{Pa s}$
Expanded uncertainty ($k = 2$): $0.050 \mu\text{Pa s}$					

^a The expanded uncertainty in viscosity depends on temperature, see table 5.3. For carbon dioxide the relative expanded uncertainty ($k = 2$) ranges from (0.20 to 0.41) %.

represents the collection of further uncertainty contributions such as from the calculation of the viscosity at zero density of helium. To simplify matters, these uncertainties are not further described here.

The uncertainty budget of the expanded combined uncertainty ($k = 2$) in viscosity at $T = 473.15 \text{ K}$ is given in table 5.2. This combined expanded uncertainty may be also called *state-point uncertainty*, as it includes the uncertainties of viscosity, temperature and pressure. The uncertainty in pressure listed in table 5.2 is based on the specifications given by the manufacturer of the utilized pressure transmitter (Paroscientific, USA, type: 1500A-01). This pressure transmitter was calibrated with a gas piston gauge (Fluke Calibration, USA, type: PG-7601) from ambient pressures up to 0.7 MPa. The uncertainty in temperature was estimated based on temperature gradients between the thermometer of the measuring cell and the temperature-control thermometer and temperature oscillations over time.

The viscosity in the low-pressure region depends only weakly on temperature and pressure, thus the expanded combined uncertainty in viscosity was in principle not larger than the expanded uncertainty in viscosity. There are some expanded uncertainties depending on temperature (e.g., uncertainties of the temperature, the residual damping

Table 5.2 Budget for the expanded combined uncertainty^a in viscosity (including uncertainties of temperature and pressure) at a temperature of 473.15 K.

Source of uncertainty	Uncertainty	Distribution	Coverage factor	Sensitivity coefficient	Standard uncertainty
Viscosity	$0.050 \mu\text{Pa s}$	Normal	2	1	$0.025 \mu\text{Pa s}$
Pressure	3.5 hPa	Rectangular	$\sqrt{3}$	0.047 ps	$1 \cdot 10^{-5} \mu\text{Pa s}$
Temperature	109 mK	Rectangular	$\sqrt{3}$	$0.042 \mu\text{Pa s K}^{-1}$	$0.0027 \mu\text{Pa s}$
Expanded combined uncertainty ($k = 2$): $0.050 \mu\text{Pa s}$					

^a The expanded combined uncertainty in viscosity depends on temperature, see U_c in table 5.3. For carbon dioxide the relative expanded combined uncertainty ($k = 2$) ranges from (0.20 to 0.41) %.

and the viscosity), which are presented in table 5.3 to convey an impression about the respective order of magnitude.

Details regarding the uncertainty of the damping D are discussed in the following. The uncertainty budget for the damping D is listed in table 5.4. The uncertainty in the regression of D occurs, because the damping is not measured directly; it is a parameter obtained from a regression. Thus, e.g., the standard deviation of the regression and the uncertainty of the measurement of the revolution time of the rotating body are included in this uncertainty. The expanded uncertainty ($k = 2$) of the regression is $U_{\text{reg}}(D) = 0.02 \mu\text{s}^{-1}$. The scatter of the damping was estimated based on more than 300 single damping values at different temperatures and viscosities. Thereby, it was observed that the uncertainty changes relative to the damping value. The expanded uncertainty ($k = 2$) of the scatter of the damping value is $U_{\text{scat}}(D) = 0.001 \cdot D$. The hysteresis of the damping was analyzed with measurements on helium at different temperatures, see section 4.1.1 for further details. Throughout the measurement program, isotherms were always changed in the same sequence. In this way the hysteresis was partly compensated. The damping values of helium, argon and neon were affected in a similar way like the measured carbon dioxide values. Thus, according to *ISO/IEC Guide 98-3 (2008)*, the uncertainty due to hysteresis was reduced by a factor of 0.29. The expanded uncertainty ($k = \sqrt{3}$) was estimated to be $U_{\text{hys}}(D) = 0.29 \cdot 0.40 \mu\text{s}^{-1}$.

In figure 5.1, helium measurements are shown, which were conducted to observe the long-term reproducibility. Therefore, helium was measured at $T = 298.15 \text{ K}$ at several pressures before and after measuring any fluid. Helium itself, argon, neon and carbon dioxide were measured from $T = (253.15 \text{ to } 473.15) \text{ K}$ between the repeatability checks. The helium viscosities were extrapolated to zero density for comparison. Relative deviations of these viscosities to their initial viscosity are plotted vs. time in figure 5.1. A positive drift of the values can be seen. This drift most likely results from a change in the alignment caused by changing the temperature multiple times while measuring the

Table 5.3 Temperature depending expanded uncertainties U of the temperature T , the residual damping D_R , the viscosity η and the combined uncertainty in viscosity (including uncertainties of temperature and pressure) U_c .

T/K	$U(T)/\text{mK}$ ($k = \sqrt{3}$)	$U(D_R)/\mu\text{s}^{-1}$ ($k = \sqrt{3}$)	$U(\eta)/\mu\text{Pa s}$ ($k = 2$)	$U_c/\mu\text{Pa s}$ ($k = 2$)
253.15	28	6.30	0.052	0.052
273.15	36	6.56	0.052	0.052
298.15	42	2.09	0.030	0.030
323.15	49	7.12	0.051	0.051
373.15	62	7.66	0.050	0.050
423.15	91	8.20	0.049	0.050
473.15	109	8.74	0.050	0.050

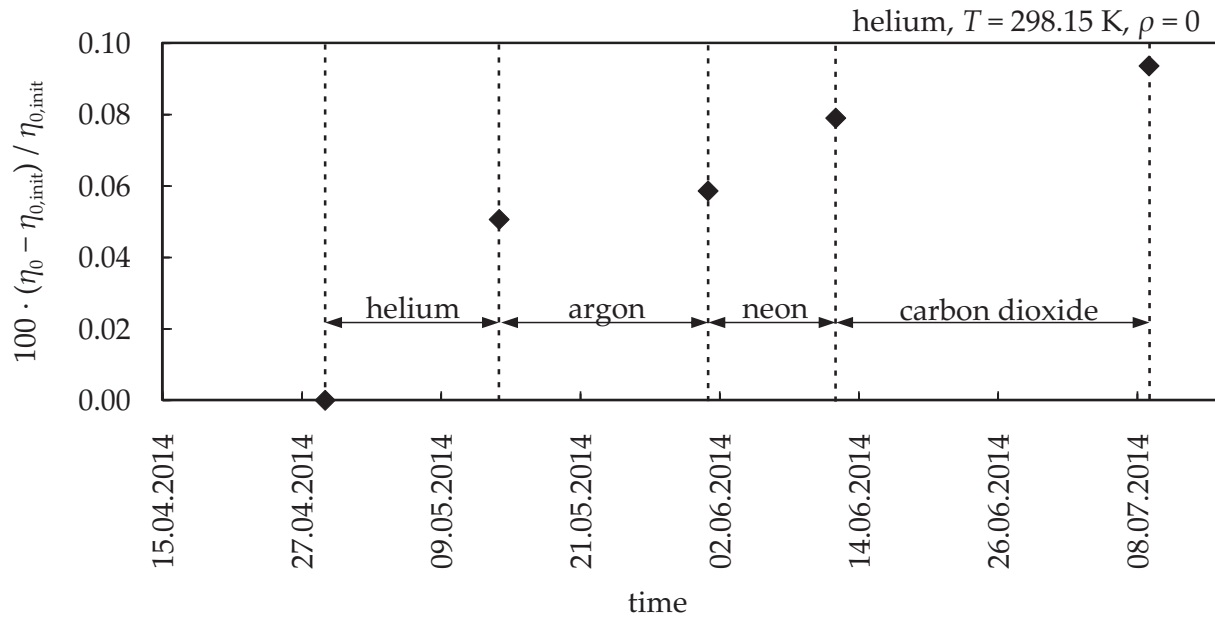


Figure 5.1 Repeatability checks with helium: Relative deviations of viscosities of helium at zero density η_0 to their initial value $\eta_{0,\text{init}}$ at zero density plotted vs. time.

different fluids. The overall observed relative deviation in viscosity is up to 0.1%. Thus, in the calibration and for the measurements itself, the stability of the alignment was a significant source of uncertainty. The respective uncertainties are included in tables 5.4 and 5.5, named *change in eccentricity*.

To compensate the resulting change of the damping of carbon dioxide, the damping at zero density of helium $D_{0,\text{He}}$ was corrected according to the change in eccentricity. The expanded uncertainty ($k = \sqrt{3}$) of this compensation was $U_{\text{ecc}}(D) = 0.29 \cdot 0.12 \mu\text{s}^{-1}$. The factor of 0.29 was applied according to the Guide to the Expression of Uncertainty in Measurement (*ISO/IEC Guide 98-3, 2008*) because the uncertainty of the change in eccentricity was also taken into account in the uncertainty of the damping at zero density of helium $D_{0,\text{He}}$. The expanded uncertainty ($k = 2$) of the damping D was estimated

Table 5.4 Budget for the uncertainty^a of the damping D at a temperature of 473.15 K.

Source of uncertainty	Uncertainty	Distribution	Coverage factor	Sensitivity coefficient	Standard uncertainty
Regression	$0.02 \mu\text{s}^{-1}$	Normal	2	1	$0.01 \mu\text{s}^{-1}$
Scatter	$0.001 \cdot D$	Normal	2	1	$0.52 \mu\text{s}^{-1}$
Hysteresis	$0.29 \cdot 0.40 \mu\text{s}^{-1}$	Rectangular	$\sqrt{3}$	1	$0.07 \mu\text{s}^{-1}$
Sorption	$0.28 \mu\text{s}^{-1}$	Rectangular	$\sqrt{3}$	1	$0.16 \mu\text{s}^{-1}$
Change in eccentricity	$0.29 \cdot 0.12 \mu\text{s}^{-1}$	Rectangular	$\sqrt{3}$	1	$0.02 \mu\text{s}^{-1}$
Expanded uncertainty ($k = 2$): $1.09 \mu\text{s}^{-1}$					

^a The expanded uncertainty of the damping depends on temperature and ranges from (0.68 to 1.09) μs^{-1} .

to be up to $U(D) = 1.09 \mu\text{s}^{-1}$, which was (8 to 32) % of the viscosity's expanded uncertainty.

The uncertainty budget for the damping at zero density of helium $D_{0,\text{He}}$ is given in table 5.5. Partly, the same elements of uncertainty (sorption, hysteresis, change in eccentricity) applied for the damping at zero density of helium $D_{0,\text{He}}$ and for the damping D . Additional uncertainties resulted from the linear extrapolation to obtain $D_{0,\text{He}}$. The estimate for the expanded uncertainty ($k = \sqrt{3}$) of the extrapolation is $U_{\text{ext}}(D_{0,\text{He}}) = 0.61 \mu\text{s}^{-1}$. The scatter of the damping values used for the extrapolation is included in this uncertainty. The expanded uncertainty ($k = \sqrt{3}$) of $D_{0,\text{He}}$ adds up to $U(D_{0,\text{He}}) = 1.09 \mu\text{s}^{-1}$. This was (15 to 49) % of the viscosity's uncertainty.

The uncertainty of the residual damping D_R was mainly depending on the ab initio calculated reference viscosities of helium, argon and neon. The expanded uncertainty ($k = \sqrt{3}$) was estimated to be $U(D_R) = (6.30 \text{ to } 8.74) \mu\text{s}^{-1}$ generally increasing with temperature from $T = (253.15 \text{ to } 473.15) \text{ K}$ as presented in table 5.3. However, the expanded uncertainty ($k = \sqrt{3}$) was $U(D_R) = 2.09 \mu\text{s}^{-1}$ at $T = 298.15 \text{ K}$, where the recommended reference viscosities published by *Berg and Moldover (2012)* were used. The contribution to the uncertainty in viscosity was (53 to 77) %; at $T = 298.15 \text{ K}$ the contribution was only 19 %, due to the low uncertainty of the reference viscosities at this temperature.

Table 5.5 Budget for the uncertainty of the damping at zero density of helium $D_{0,\text{He}}$.

Source of uncertainty	Uncertainty	Distribution	Coverage factor	Sensitivity coefficient	Standard uncertainty
Extrapolation	$0.61 \mu\text{s}^{-1}$	Rectangular	$\sqrt{3}$	1	$0.35 \mu\text{s}^{-1}$
Hysteresis	$0.40 \mu\text{s}^{-1}$	Rectangular	$\sqrt{3}$	1	$0.23 \mu\text{s}^{-1}$
Sorption	$0.28 \mu\text{s}^{-1}$	Rectangular	$\sqrt{3}$	1	$0.16 \mu\text{s}^{-1}$
Change in eccentricity	$0.77 \mu\text{s}^{-1}$	Rectangular	$\sqrt{3}$	1	$0.44 \mu\text{s}^{-1}$
Expanded uncertainty ($k = \sqrt{3}$): $1.09 \mu\text{s}^{-1}$					

5.3 Results of the Measurements on Carbon Dioxide

The viscosity of carbon dioxide was measured at 54 (T, p) state points (including reproducibility checks at $T = 298.15 \text{ K}$) along seven isotherms at $T = (253.15, 273.15, 298.15, 323.15, 373.15, 423.15, 473.15) \text{ K}$ with pressures up to 1.2 MPa. The carbon dioxide (Air Liquide, Germany, type: Kohlendioxid N55) used for the measurements had a purity of $x_{\text{CO}_2} \geq 0.999995$. Air Liquide stated impurities of: $x_{\text{H}_2\text{O}} \leq 2 \cdot 10^{-6}$, $x_{\text{O}_2} \leq 1 \cdot 10^{-6}$, $x_{\text{CmHn}} \leq 0.1 \cdot 10^{-6}$, $x_{\text{N}_2} \leq 2 \cdot 10^{-6}$, $x_{\text{CO}} \leq 0.5 \cdot 10^{-6}$, $x_{\text{NO}_x} \leq 0.1 \cdot 10^{-6}$, where x denotes

the mole fraction. The experimental material was used as received. No further gas analysis was conducted to confirm the purity.

The experimental results for carbon dioxide are listed in appendix B in table B.1. The viscosity value is the average of three succeeding measurements. The measurement of the viscosity took 27 min and the temperature and the pressure in table B.1 are average values of the readings taken over this period of time.

Several authors measured the viscosity of carbon dioxide. *Vogel and Barkow (1986)* as well as *Hendl et al. (1993)* utilized an oscillating disk viscometer. The data were recently re-evaluated by *Vogel (2014)*. For that purpose, Vogel used state of the art ab initio calculated viscosities, e.g., of helium (*Bich et al., 2007*). In addition, Vogel calculated viscosities in the limit of zero density out of the re-evaluated data of *Hendl et al. (1993)* and *Vogel and Barkow (1986)*. The relative standard uncertainties of the re-evaluated data of Vogel and Barkow and Hendl et al. are in general 0.2 % and 0.15 % at room temperature. For the data comparison presented here, only the data re-evaluated by Vogel were used.

Another set of – partly absolute – data was measured by the research group of Kestin, namely by *Kestin et al. (1977)*, *Kestin et al. (1980)*, *Kestin and Leidenfrost (1959)*, *Kestin et al. (1972)* and *Kestin and Whitelaw (1963)* with an oscillating disk viscometer. The lowest relative uncertainty reported by the group of Kestin is 0.05 % in the low-density region.

The data of *Di Pippo et al. (1977)* were measured also utilizing an oscillating disk viscometer with an experimental uncertainty reported to be 0.1 %. The data of *Harris et al. (1979)* were measured with a coiled capillary flow viscometer, and the authors state an uncertainty of 1 %.

Hellmann (2014) recently published data of carbon dioxide calculated ab initio at zero density. As recommended by Hellmann, these data were scaled before plotting by a factor of 1.0055. Hellmann estimated a standard uncertainty of 0.2 % for the scaled values between 300 K and 700 K, increasing to about 1 % towards 150 K and 2000 K.

The viscosity values of *Hunter et al. (1993)* were measured using a coiled capillary flow viscometer with an uncertainty of 0.7 %. *Iwasaki and Takahashi (1981)* published data measured with an oscillating disk viscometer. The authors report an uncertainty of 0.3 %. *Timrot and Traktueva (1975)* achieved an uncertainty of 0.7 % utilizing an oscillating disk viscometer. *Wobser and Müller (1941)* measured the viscosity with a falling sphere viscometer, and the uncertainty was reported to be 0.15 %. *Johnston and McCloskey (1940)* determined the viscosity with an oscillating disk viscometer with experimental uncertainties up to 0.8 %.

The viscosity data obtained during this work – reference *Schäfer et al. (2015)* – and the data of other authors are compared with the viscosity correlation of *Fenghour et al. (1998)* (zero line) in figures 5.2 to 5.3, where relative deviations of experimental values from values calculated with the correlation of *Fenghour et al. (1998)* are plotted vs. density.

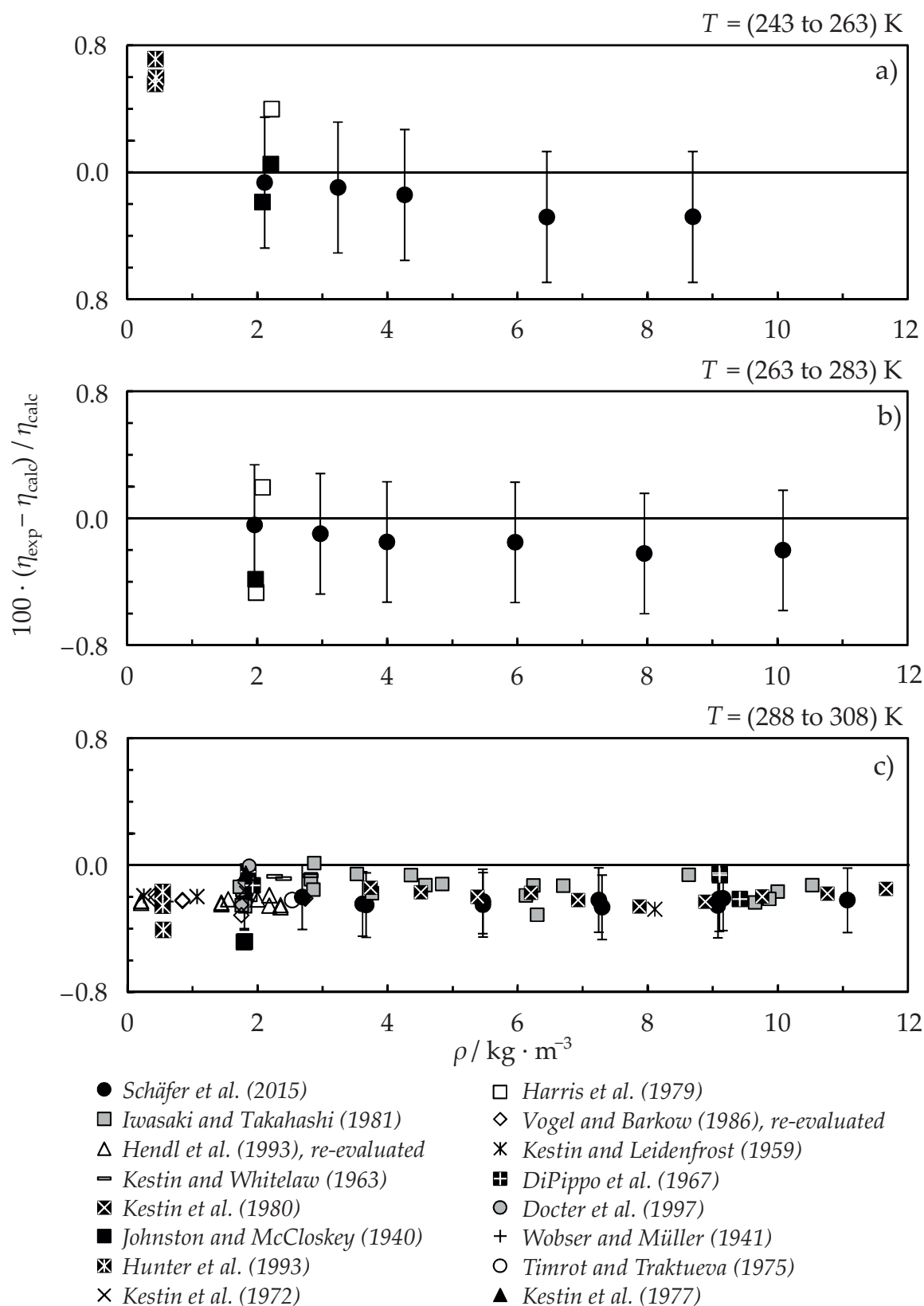


Figure 5.2 Experimental viscosities η_{exp} of carbon dioxide, plotted vs. density ρ as relative deviations from calculated viscosities η_{calc} from the correlation of Fenghour et al. (1998) (zero line). If not given with the experimental data, the density ρ was calculated using the equation of state of Span and Wagner (1996).

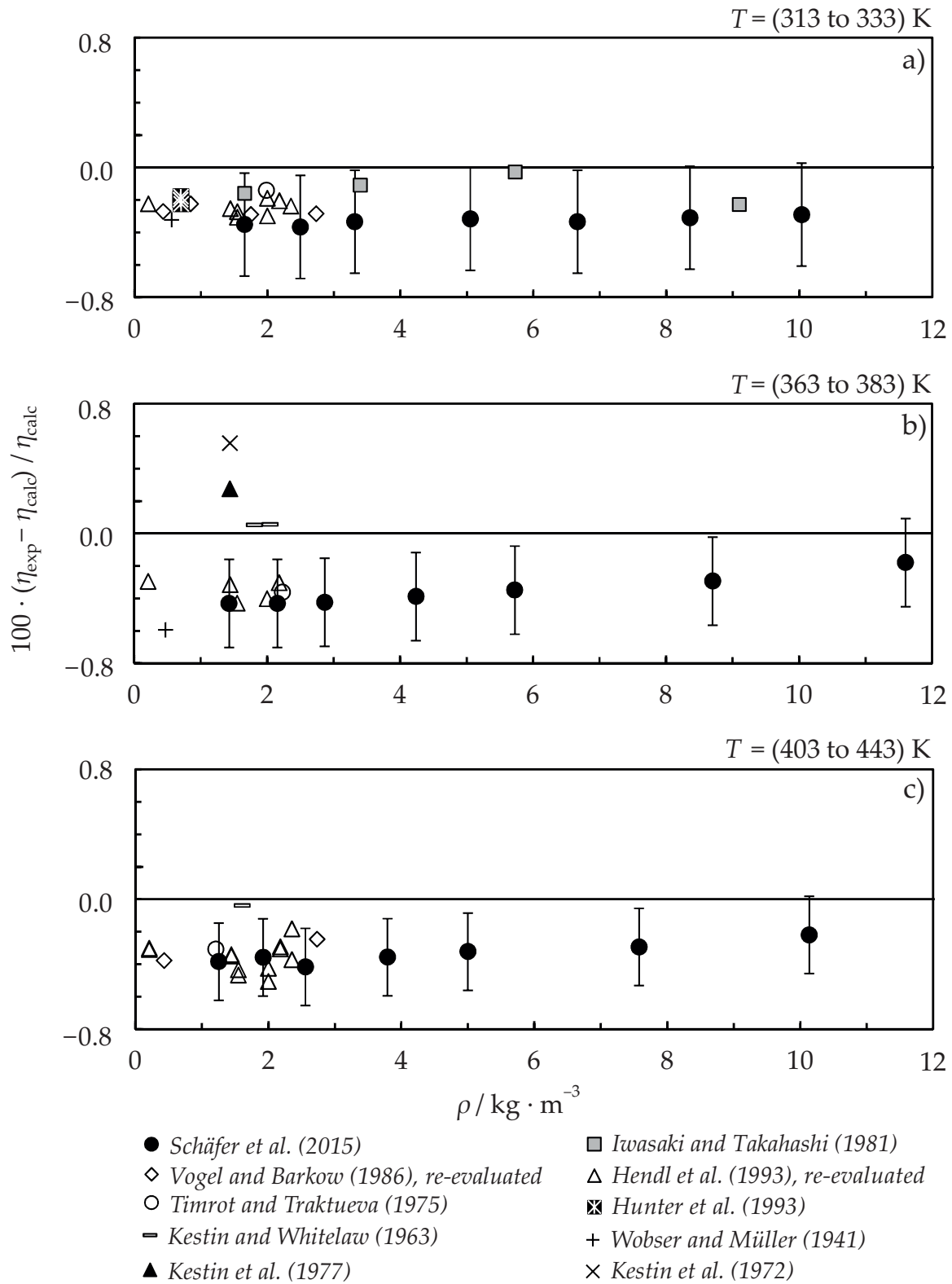


Figure 5.3 Experimental viscosities η_{exp} of carbon dioxide, plotted vs. density ρ as relative deviations from calculated viscosities η_{calc} from the correlation of *Fenghour et al. (1998)* (zero line). If not given with the experimental data, the density ρ was calculated using the equation of state of *Span and Wagner (1996)*.

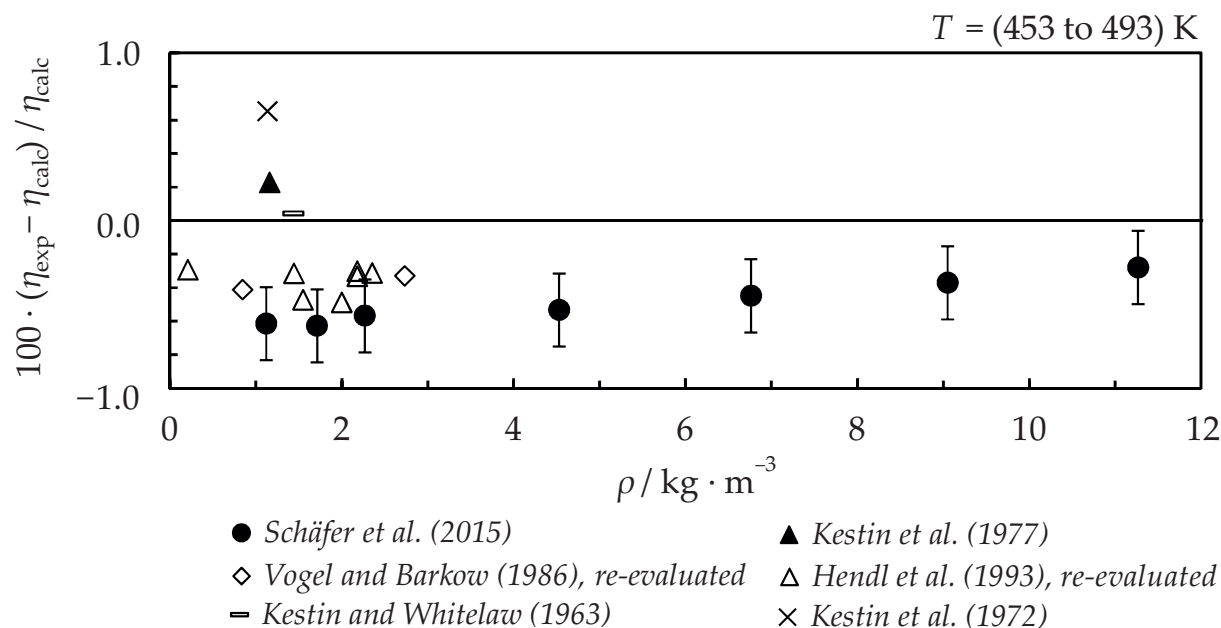


Figure 5.4 Experimental viscosities η_{exp} of carbon dioxide, plotted vs. density ρ as relative deviations from calculated viscosities η_{calc} from the correlation of *Fenghour et al. (1998)* (zero line). If not given with the experimental data, the density ρ was calculated using the equation of state of *Span and Wagner (1996)*.

The uncertainty of the correlation of *Fenghour et al. (1998)* was reported to be 0.3 % in the dilute gas near room temperature increasing up to 5 % at higher pressures. If not included in the published data, the corresponding densities were calculated from the equation of state of *Span and Wagner (1996)* for the purpose of data comparison.

In figure 5.2 a), the data of *Schäfer et al. (2015)* are compared to other literature data at $T = 253.15 \text{ K}$. The relative deviations of the data of *Schäfer et al. (2015)* range from -0.07% at a density of $2 \text{ kg} \cdot \text{m}^{-3}$ to -0.28% with increasing density. The magnitude of the negative trend is slightly smaller at $T = 273.15 \text{ K}$, as shown in figure 5.2 b). At $T = 298.15 \text{ K}$ relative deviations of the present data to the correlation of *Fenghour et al. (1998)* are almost constant with approximately -0.23% . This is within the correlation's uncertainty of 0.3 % at room temperature and low pressures. The present data agree well with the selected literature data at $T = 298.15 \text{ K}$. Relative deviations of the data of *Schäfer et al. (2015)* from the re-evaluated viscosities of Vogel and Barkow are not more than 0.12 % at a density of about $2 \text{ kg} \cdot \text{m}^{-3}$. In the same region, the largest relative deviation from the data of Hendl et al. is only $+0.07 \%$. Thus, the data from *Schäfer et al. (2015)* agree with the re-evaluated viscosities of Vogel and Barkow and of Hendl et al. within the experimental uncertainty discussed in section 5.2.

Generally, the same can be observed for all other selected literature data also considering higher densities at $T = 298.15 \text{ K}$. The maximum relative deviation from the data of *Kestin et al. (1980)* at a density of $3.6 \text{ kg} \cdot \text{m}^{-3}$ is only -0.11% . The relative deviations at higher temperatures (323.15, 373.15, 423.15) K are depicted in figure 5.3 a),

b) and c), respectively. Whereas at a temperature of 323.15 K relative deviations from calculated values are still almost constant, a slightly positive trend can be observed for higher temperatures. For the three mentioned temperatures, the maximum relative deviations from the data of Vogel and Barkow and Hendl et al. are (0.18, 0.14, and 0.24) %. Hence, the data of this work – Schäfer et al. (2015) – agree with the re-evaluated data of Vogel and Barkow and Hendl et al. within their experimental uncertainties. The largest relative deviation of -0.35% from the re-evaluated data of Vogel and Barkow and Hendl et al. occurs at a temperature of 473.15 K, as shown in figure 5.4. Also at $T = 473.15\text{ K}$ the positive trend of the new viscosity values compared to the correlation of Fenghour et al. (1998) is maximal. Relative deviations range from -0.63% at the lowest densities to -0.28% at the highest densities. Taking the entire temperature range into account, there is a significant difference in the initial density dependence of carbon dioxide between the data measured in this work and the correlation of Fenghour et al. (1998). At $T = 253.15\text{ K}$ the relative deviations show a negative slope; the slope changes the sign at approx. $T = 298.15\text{ K}$; at higher temperature the slope becomes positive.

In figure 5.5, viscosity data solely for the low-density region of $(0\text{ to }3)\text{ kg}\cdot\text{m}^{-3}$ are shown. Relative deviations of experimental data from values calculated with the correlation of Fenghour et al. (1998) are plotted vs. temperature. Where possible, zero density viscosities were plotted, i.e., of Vogel (2014) and of Schäfer et al. (2015). This

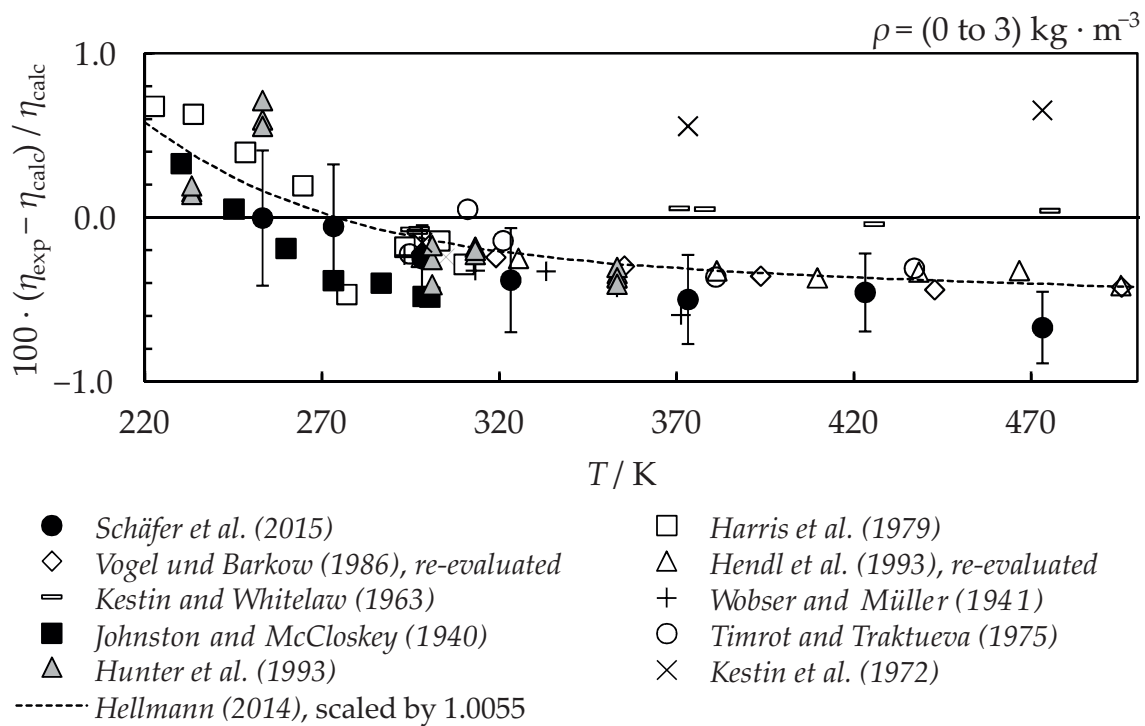


Figure 5.5 Experimental viscosities η_{exp} of carbon dioxide, plotted vs. temperature T as relative deviations from calculated viscosities η_{calc} from the correlation of Fenghour et al. (1998) (zero line).

work's data were linearly extrapolated to the limit of zero density. The data of *Hellmann (2014)* were calculated for the limit of zero density. At zero density, relative deviations of the data of *Schäfer et al. (2015)* from the zero line are almost negligible for a temperature of 253.15 K. Relative deviations increase to -0.67% at $T = 473.15$ K. Thus, there is a temperature depended systematic offset of the data of *Schäfer et al. (2015)* compared to the correlation of *Fenghour et al. (1998)*. At zero density, the relative deviations of this work's data from the re-evaluated data of *Hendl et al.* and *Vogel and Barkow* are only -0.03% for a temperature of 298.15 K. The maximum relative deviation from the data of *Hendl et al.* was -0.35% at $T = 473.15$ K. However, these two data sets still agree within their experimental uncertainties. Apart from that, the data of *Hendl et al.* and *Vogel and Barkow* agree with the data of *Schäfer et al. (2015)* within the experimental uncertainty reported in section 5.2 of this work. Compared with the correlation of *Fenghour et al. (1998)*, the data of *Johnston and McCloskey (1940)* as well as the data of *Wobser and Müller (1941)* show a negative slope with increasing temperature. This tendency somewhat agrees with the trend of the data of *Schäfer et al. (2015)*. The ab initio data of *Hellman* – scaled by a factor of 1.0055, as suggested by *Hellmann (2014)* – represent the temperature dependence in general within our experimental uncertainties.

6 A Simple Apparatus for the Gravimetric Preparation of Gaseous Mixtures

For research on thermophysical properties, the thermodynamic behavior of fluid mixtures is of major interest. As for instance in the field of Carbon Capture and Storage (CCS), the knowledge of thermophysical properties of mixtures with high amounts of carbon dioxide is important. Using the GERG-2008 by *Kunz and Wagner (2012)* or the EOS-CG (Equation of State for Combustion Gases and Combustion Gas-like Mixtures) by *Gernert and Span (2015)* is currently one of the most accurate ways to calculate the thermophysical properties of these mixtures. However, the relative expanded uncertainty in density for the gas phase stated by *Gernert and Span (2015)* is only 0.05 % for a N₂-CO mixture, but 1 %, taking a CO₂-Ar mixture as an example. Thus, technically, the EOS-CG is capable of providing relative expanded uncertainties of remarkable 0.05 %. The weak point, why some mixtures show large uncertainties, is not the model on which the EOS-CG is based in the first place, it is the limited availability of accurate experimental data of mixtures.

When the density of a mixture is measured, the composition of the mixture is a state variable like temperature and pressure. Thus, the combined standard uncertainty for a density measurement of a **binary** fluid mixture can be stated as

$$u_c(\rho) = \sqrt{\underbrace{u^2(\rho)}_{\text{density}} + \underbrace{\left(\frac{\partial \rho}{\partial p}\right)^2 u^2(p)}_{\text{pressure}} + \underbrace{\left(\frac{\partial \rho}{\partial T}\right)^2 u^2(T)}_{\text{temperature}} + \underbrace{\left(\frac{\partial \rho}{\partial x}\right)^2 u^2(x)}_{\text{composition}}}. \quad (6.1)$$

To take full advantage of the high accuracy of a densimeter, e.g., with magnetic suspension coupling, an uncertainty in composition of < 0.1 mol-% is needed. To exploit the measuring range filling pressures up to 20 MPa are favorable. However, commercially available mixtures with a mixture uncertainty less than 0.1 mol-% are very expensive. Furthermore, carbon dioxide- or ethane-rich mixtures with pressures up to 20 MPa are practically not available, as one component has to be filled into the sample cylinder by condensation to achieve high pressures. This procedure is not supported by *DIN EN ISO 6142 (2006)*. However, the preparation of these mixtures is feasible from a thermodynamic point of view. In conclusion, the limited availability and quality of gaseous mixtures hinders mixture measurements.

However, the investigation of the properties of gaseous mixtures is a future goal for the low-pressure viscometer and the viscometer densimeter. This currently also applies for most apparatuses at the chair of thermodynamics at the Ruhr-Universität Bochum.

Against this background *Merken* (2013) and *Schäfer et al.* (2012) developed an apparatus for the gravimetric preparation of gaseous mixtures. The theory of the apparatus is explained in section 6.1, the apparatus itself is described in section 6.2. Towards the end of this chapter in section 6.4, the results of a CO₂-N₂ mixture are presented and compared to measurements with a very accurate two sinker densimeter for standard conditions (*Richter et al.*, 2010).

6.1 Theory of the Gas-Mixture Preparation System

The theory of the gravimetric mixture preparation is described comprehensively in *DIN EN ISO 6142* (2006). Thus, only a brief overview of the theory is given in this work. The following description is mostly application-oriented, taking a CO₂-N₂ mixture as an example.

The molar mixture composition of a gravimetrically prepared mixture can be estimated by

$$x_{N_2} = \frac{m_{N_2}/M_{N_2}}{m_{N_2}/M_{N_2} + m_{CO_2}/M_{CO_2}}, \quad (6.2)$$

where m is the mass and M is the molar mass. The sample cylinder is weighed before and after filling each component. The exact masses of the two components m_{N_2} and m_{CO_2} are calculated taking the readings of the balance recorded while weighing the sample cylinder as input parameters. To yield the masses, first the balance readings are corrected for the balance's weighing characteristics, which result from the ambient conditions while the balance has been calibrated. Furthermore, the buoyancy force acting on the sample cylinder is considered. Using the CO₂-N₂ mixture as an example, the masses are estimated by

$$m_{CO_2} = W_0 - W_1 + \rho_{air,1} V_{cyl,1} - \rho_{air,0} V_{cyl,0} \quad (6.3)$$

$$m_{N_2} = W_2 - W_1 + \rho_{air,2} V_{cyl,2} - \rho_{air,1} V_{cyl,1}, \quad (6.4)$$

where ρ_{air} is the air density and V_{cyl} is the volume of the sample cylinder and W is the determined weight. Two further input parameters are required to calculate the weight W from the reading of the balance m_{bal} : (1) $\rho_{air,cal}$, the air density during the calibration of the balance and (2) ρ_{cal} , the density of the calibration weights. Thus, the weight

$$W = m_{bal} \left(1 - \frac{\rho_{air,cal}}{\rho_{cal}} \right) \quad (6.5)$$

can be calculated. The influence of this correction practically cancels in the calculation of the composition. Thus, it is not further discussed here.

6.2 Description of the Gas-Mixture Preparation System

To give a brief overview of the new simple apparatus, a piping and instrumentation diagram is presented in figure 6.1. In the left, the supply cylinder can be seen, which was used to provide the pure components, e.g., CO₂ and N₂. A gas-dosing system was used to control and supervise the filling procedure.

The gas-dosing system incorporates a bursting disc and a pressure sensor. On the right side of figure 6.1 the sample cylinder is displayed. In figure 6.1 it was placed on a balance to determine its approximate weight, which increased during the filling procedure. Furthermore, a measurement computer, an air temperature and humidity transmitter, and a precision barometer were parts of the apparatus.

In figure 6.2, a photo of the apparatus in the air-conditioned laboratory is shown. In the left part of figure 6.2, a massive weighing table can be seen. The balance with the centermatic is placed thereon. The balance is covered by a wooden draft shield. In the back, the supply cylinder (blue) is visible, which was attached to the gas-dosing system. The sample cylinder is located in the foreground in the middle; behind it, on the table the gas-dosing system and the vacuum pump can be seen. On the right side of the table, the equipment for measuring the ambient pressure, temperature and the humidity is visible. The measurement computer is located at the right side of figure 6.2.

One important step in the design of the apparatus was the choice of a suitable sample cylinder. The sample cylinder has to be weighed multiple times during the filling procedure. Thus, a low weight and small dimensions were favorable. On the other hand, a high inner volume of the cylinders is beneficial. The measuring cells have to be purged multiple times while measuring mixtures to minimize sorption effects. The pressure within a small cylinder is reduced relatively fast by removing fluid. Thus, measurements at high pressures are limited utilizing a small sample cylinder.

Aluminum cylinders (Scott Specialty Gases, Netherlands) with aculife treatment III and IV were chosen. The cylinders have a volume of 20 L. Thus, purging an apparatus, e.g., the viscometer-densimeter is possible multiple times. Furthermore, the amount

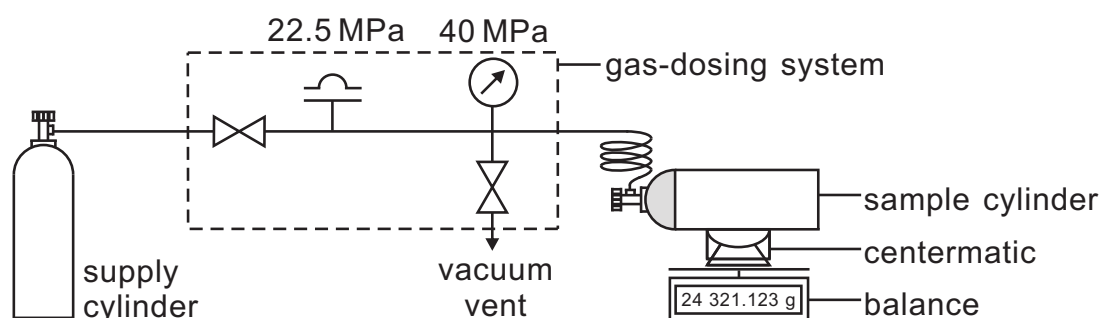


Figure 6.1 Piping and instrumentation diagram of the apparatus for the gravimetric preparation of gaseous mixtures.

of supply cylinders to fill a 20 L cylinder to high pressures is acceptable. The sample cylinder has a nominal weight of 23.6 kg and is easy to handle for two persons.

The quality of the sample cylinder's inner surface is essential for the uncertainty of the mixture composition and the mixture's long-term stability. A rough inner surface or residual traces of water inside the cylinder may lead to sorption effects, which can change the mixture composition (Mysliwicz, 2013). Therefore, as part of the aculife treatment, the inner surface of the cylinder was chemically polished by the manufacturer. After that, the cylinder was baked out, evacuated and filled with nitrogen multiple times to remove residual components, e.g., water.

A photo of the gas-dosing system is shown in figure 6.3 a). The same tested valves (Swagelok, USA, type: SS-4BRG-V51) were used as in the gas-dosing system described in section 3.2. The pressure sensor (WIKA, Germany, type: IS-11) and the specification plate of the bursting disk (Schlesinger, Germany, type: B12,5r250-03L) can be seen. The disk has a nominal bursting pressure of 22.5 MPa.

A mass comparator (Sartorius, Germany, type: CCE60K3) was used to determine the weight of the sample cylinder. The mass comparator consisted of the weighing cell – left in figure 6.3 b) – and the display and control unit; see figure 6.3 b). In figure 6.4, a photo is shown of how a sample cylinder was placed on the weighing cell. The wooden draft shield was removed, so that the centermatic and the adapter for positioning the cylinder on the centermatic (Sartorius, Germany, type: YWP03C) can be

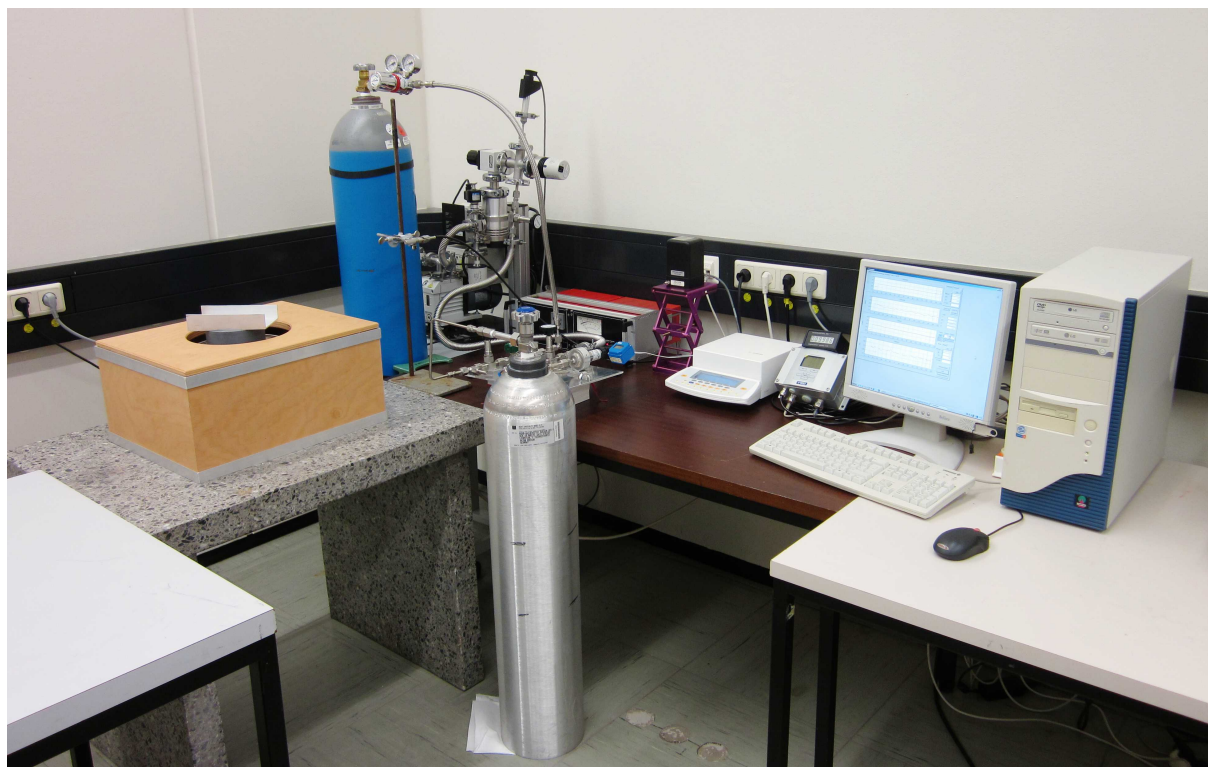


Figure 6.2 Photo of the apparatus for the gravimetric preparation of gaseous mixtures.

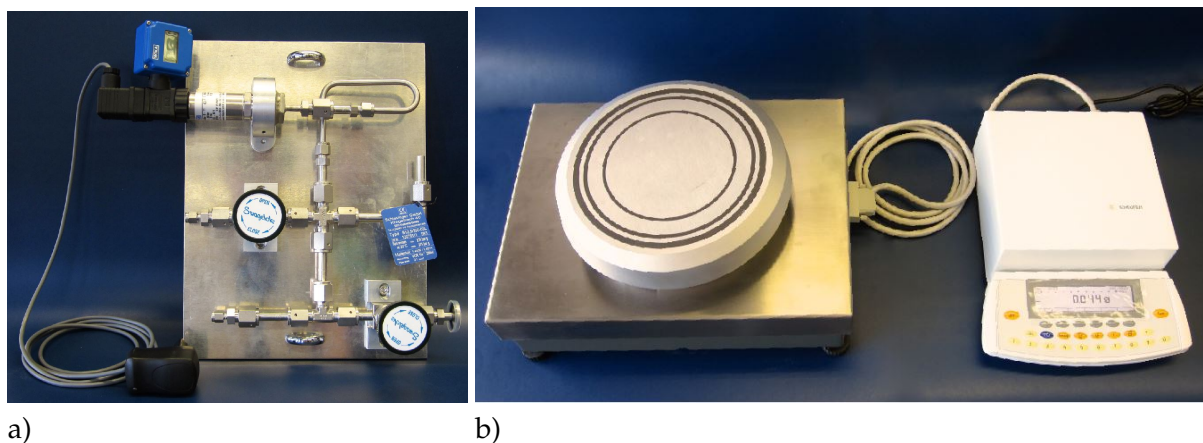


Figure 6.3 Parts of the equipment of the apparatus for the gravimetric preparation of gaseous mixtures:

- a) gas dosing system with the pressure transmitter and valves,
- b) weighing cell with centermatic; display and control unit.

seen. Uncertainties resulting from an off-center placement of the sample cylinder were minimized by the centermatic. The measuring range of the balance was (0 to 64) kg. The expanded uncertainty ($k = \sqrt{3}$) of a weighing was estimated conservatively to be 200 mg, although the nominal uncertainty of the balance was lower. The uncertainty yields partly from the observed scatter during weighing and the linearity of the balance, but it has also experimental reasons. A possible change of the contamination of the outside surface of the sample cylinder, e.g., by removing particles, is covered by this uncertainty. This change can occur in the time between the weighing procedures, e.g., between the evacuation and the first filling. The entire mixture preparation can last up to one week.

The ambient air conditions were determined to compensate for the air buoyancy. The barometric pressure was measured with a precision barometer (Paroscientific, USA, type: 1650-101) with an expanded uncertainty ($k = \sqrt{3}$) of 0.08 hPa. The air

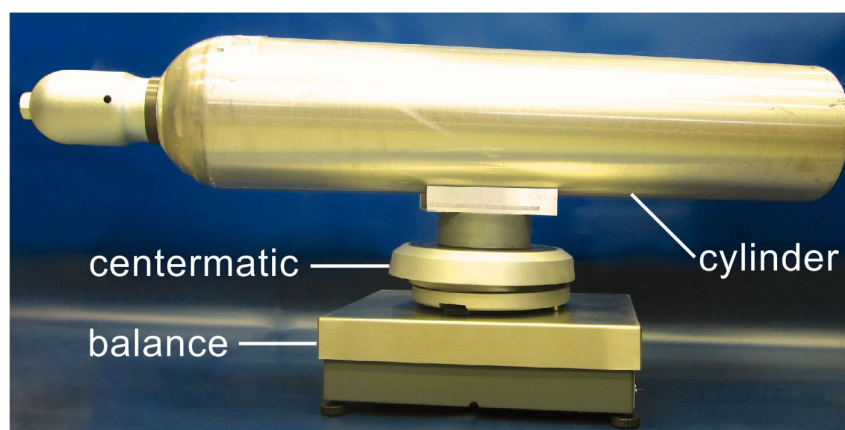


Figure 6.4 Photo of the sample cylinder positioned on the weighing cell. A centermatic is used to place the cylinder always in the same spot.

temperature and humidity were determined utilizing a humidity and temperature transmitter (Vaisala, Finland, type: HMT333), which had an expanded uncertainty ($k = 2$) of 0.1 K in temperature and 1 % in relative humidity.

A software was implemented using Visual Basic 6 (Microsoft, USA). All relevant data like the temperature, humidity, pressure and the reading of the balance were logged and plotted. The user could average the readings over a selectable time span. The data could be exported to a spreadsheet program (Microsoft, USA, type: Excel).

6.3 Experimental Procedures

Condensation of a mixture component inside the sample cylinder changes the mixture composition of the gaseous phase. Thus, the first step in mixture preparation was to check, if the dew-point temperature of the mixture was below ambient temperature up to a pressure of 20 MPa. This requirement was fulfilled in case of the mixture presented here as an example.

After this check, the masses m_{CO_2} and m_{N_2} were determined, that yielded the desired molar composition of the binary mixture, i.e., $x_{\text{CO}_2} = 25 \text{ mol-}\%$ and $x_{\text{N}_2} = 75 \text{ mol-}\%$. Taking nitrogen as an example, the mass was calculated by

$$m_{\text{N}_2} = \frac{x_{\text{N}_2} \cdot M_{\text{N}_2}}{x_{\text{N}_2} \cdot M_{\text{N}_2} + x_{\text{CO}_2} \cdot M_{\text{CO}_2}} \cdot m_{\text{total}}, \quad (6.6)$$

with M as the molar mass and m_{total} as the mass, filled into the sample cylinder in total during the mixture preparation. The total mass was limited by the operating pressure of the cylinder, which was $p_{\text{max}} = 20 \text{ MPa}$ (Luxfer, 2015). Depending on the resulting density of the prepared mixture, a carbon dioxide- or ethane-rich mixture can be incompressible, similar to a liquid fluid. For safety reasons the total mass was limited in a way, that the maximum operating pressure was still satisfied, if the prepared mixture was heated to $T_{\text{max}} = 323.15 \text{ K}$. The total mass was calculated by

$$m_{\text{total}} = \rho_{\text{mix,max}}(T_{\text{max}}, p_{\text{max}}) \cdot V_{\text{cyl}} \quad (6.7)$$

with V_{cyl} as the volume of the sample cylinder. The density $\rho_{\text{mix,max}}$ of the prepared mixture was estimated using the densities of carbon dioxide (Span and Wagner, 1996) and nitrogen (Span et al., 2000) as input parameters for applying the respective mixing rule of Kunz and Wagner (2012).

The estimated masses were $m_{\text{CO}_2} \approx 1.87 \text{ kg}$ and $m_{\text{N}_2} \approx 3.57 \text{ kg}$. The resulting pressure in the sample cylinder was predicted, using the equation of state for carbon dioxide (Span and Wagner, 1996). The filling pressure of carbon dioxide was below its vapor pressure. Thus, carbon dioxide was filled into the sample cylinder using the pressure

difference. Otherwise the supply cylinder can be heated to fill the sample cylinder by condensation. The second component – nitrogen – was also filled by using a pressure difference. For nitrogen a supply cylinder with a volume of 50 L and a filling pressure of 30 MPa was available. The sample cylinder could be filled to a pressure of 20 MPa without changing the supply cylinder. To check if the pressure in the supply cylinder was sufficient, the residual pressure in the supply cylinder was estimated using the equation of state for nitrogen of *Span et al. (2000)*.

The used carbon dioxide (Air Liquide, Germany, type: Kohlendioxid N55) had a purity of $x_{\text{CO}_2} \geq 0.999995$. Air Liquide stated impurities of: $x_{\text{H}_2\text{O}} \leq 2 \cdot 10^{-6}$, $x_{\text{O}_2} \leq 1 \cdot 10^{-6}$, $x_{\text{CmHn}} \leq 0.1 \cdot 10^{-6}$, $x_{\text{N}_2} \leq 2 \cdot 10^{-6}$, $x_{\text{CO}} \leq 0.5 \cdot 10^{-6}$, $x_{\text{NO}_x} \leq 0.1 \cdot 10^{-6}$, where x denotes the mole fraction. The used nitrogen (Air Liquide, Germany, type: Stickstoff N50) had a purity of $x_{\text{N}_2} \geq 0.99995$. Air Liquide stated impurities of: $x_{\text{O}_2} \leq 2 \cdot 10^{-6}$, $x_{\text{H}_2\text{O}} \leq 3 \cdot 10^{-6}$, $x_{\text{CmHn}} \leq 0.2 \cdot 10^{-6}$, where x denotes the mole fraction. The experimental material was used as received. No further gas analysis was conducted to confirm the purity.

Before the components were filled into the sample cylinder, the cylinder was evacuated for 24 h using the vacuum system described in section 3.3. This was necessary, as the sample cylinder was filled with nitrogen by the manufacturer to a pressure of ≈ 0.4 MPa. Thereafter, the balance readings $m_{\text{bal},0}$ of the evacuated sample cylinder were determined; see figure 6.5 a). The weight W_0 was calculated by taking the weighing characteristics of the balance eq. (6.5) into account.

Before weighing the sample cylinder, the balance was tared and the reading of the balance with empty weighing pan was recorded. For recording one reading, a sequence of 10 stable readings of the balance was averaged. Usually, the balance reading was stable after a time of 30 s. Temperature, humidity, and pressure of the air were measured simultaneously and also averaged in the same time period.

After recording the reading of the empty weighing pan, the sample cylinder was placed on the centermatic of the balance, like it is shown in figure 6.4. This was done by two persons, as the cylinder has to be positioned elaborately. An eccentric position causes the centermatic to turn and cant. After the cylinder was positioned appropriately, it took about 30 s for the balance readings to stabilize, then the reading was recorded, and the sample cylinder was removed. The balance reading without sample cylinder was recorded to observe the drift of the balance. Then the sample cylinder was weighed again. The entire procedure was repeated 10 times. For testing purposes, this weighing procedure was executed on three different days to investigate the long term reproducibility of the procedure.

After determining the weight of the evacuated sample cylinder, it was filled with carbon dioxide, see figure 6.5 b). The supply cylinder and the sample cylinder were attached to the gas-dosing system. The apparatus was set up as it is shown in figure 6.1, with the sample cylinder positioned on the balance. The gas-dosing system was

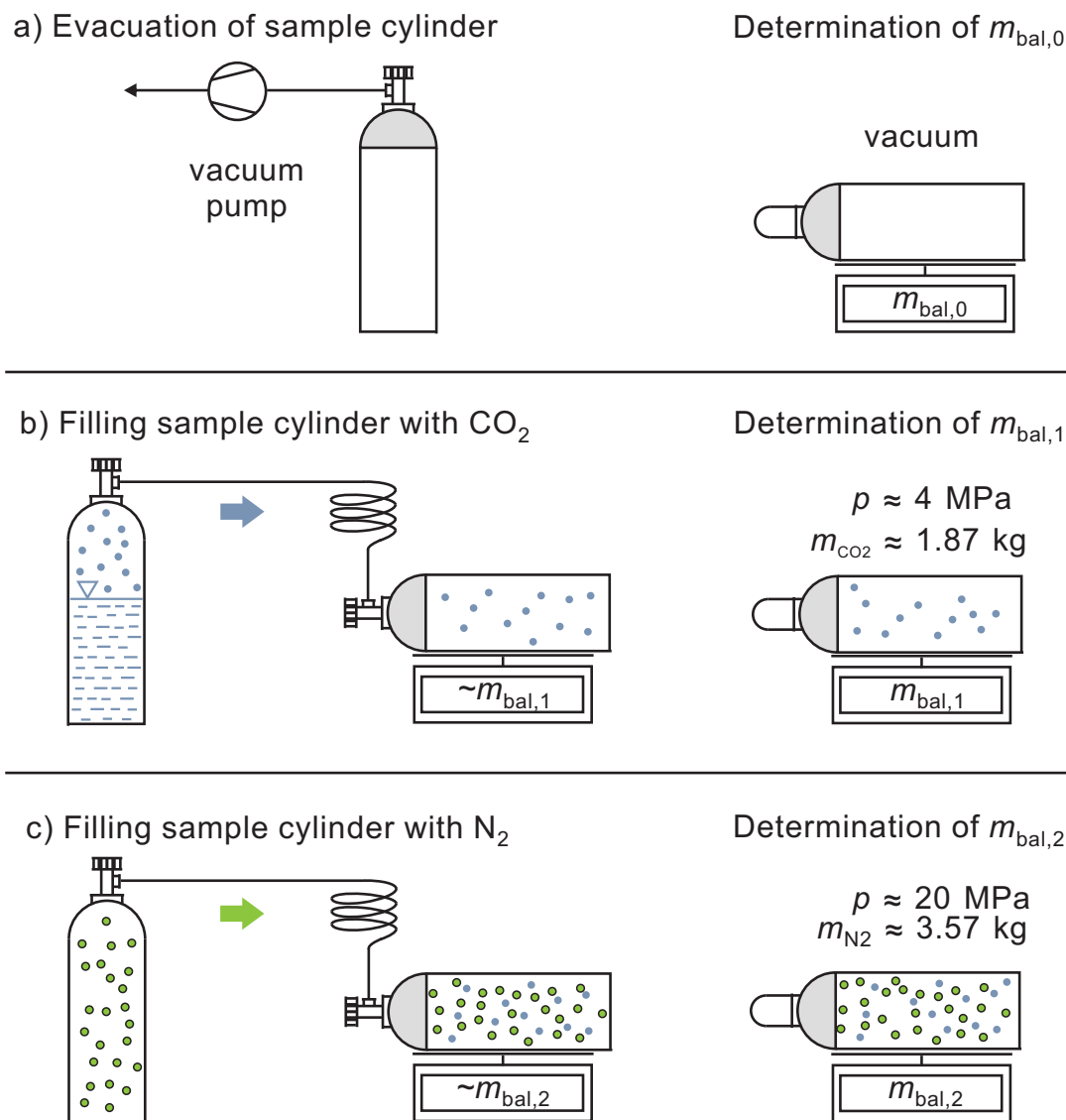


Figure 6.5 Schematic of the mixture preparation procedure.

evacuated for 15 min and purged with carbon dioxide thereafter. This procedure was repeated three times. While the sample cylinder was filled until the desired mass was achieved, it was weighed simultaneously. Thereby, the filled mass was observed. Additionally, the pressure was observed. While the tube for filling the sample cylinder was attached during the filling procedure, the balance readings were systematically set off little (about $\Delta m \approx 1 \text{ g}$). Thus, the exact reading of the balance $m_{\text{bal},1}$ of the sample cylinder including the carbon dioxide filling was determined afterward. However, the sample cylinder was weighed the next day, as the cylinder was cooled down below the dew-point temperature during filling. As applied for the evacuated cylinder, this weighing procedure was executed on three different days. The model function of the composition, eq. (6.2), is very sensitive towards the uncertainty of the second weighing. Therefore, it is favorable when the sample cylinder is weighed on two different days.

As the third step of the mixture preparation, nitrogen was filled into the sample cylinder; see figure 6.5 c). The same procedure was applied as for carbon dioxide, i.e., the cylinders were attached to the gas-dosing system, the filling system was evacuated and purged, and the nitrogen was filled in while mass and pressure were observed. The sample cylinder was heated up to about $T = 333.15$ K due to the compression of the fluid inside the sample cylinder during filling. Thus, the balance reading $m_{\text{bal},2}$ was determined the day after filling and, in addition, at the two following days utilizing the aforementioned procedures.

The masses of the filled in components – carbon dioxide and nitrogen – were estimated by eqs. (6.3) and (6.4). Therefore, the density of air was calculated using the equation of *Davis (1992)*. Input parameters were the air pressure, temperature, and relative humidity. As mentioned above, all three values were recorded during the weighing procedure. The volume of the cylinder was corrected according to the cylinders' filling pressure using the investigations of *Mysliwicz (2015)*, who measured the expansion of an aluminum cylinder (Luxfer, UK). Changes in the outer volume of a sample cylinder due to gas filling were also investigated by *Oh et al. (2013)*.

The volume of the cylinder investigated by *Mysliwicz (2015)* was 10 L. This cylinder was similar to the sample cylinder used in this work, as it was made of the same material by the same manufacturer. As the cylinders used for the present apparatus have a higher volume (20 L), the correction was scaled up. Finally the composition of the mixture was determined by eq. (6.2). The results are discussed in the following section.

6.4 Uncertainty Analysis, Results and their Validation

In table 6.1 the uncertainty in molar composition for the gravimetric preparation of mixtures is analyzed. Table 6.1 is based on the mixture preparation data of *Schäfer et al. (2012)*. To simplify matters, not the balance reading, but the weight W was used in table 6.1. The weight of the sample cylinder was determined: (1) three times when the cylinder was evacuated, (2) three times with CO_2 filled in, (3) three times with $\text{N}_2\text{-CO}_2$ filled in. As stated above, the air conditions (temperature, pressure and humidity) were logged while weighing. These conditions were practically constant during one measurement run of 10 repetitions. As can be seen in table 6.1, e.g., only one air temperature for weighing the evacuated sample cylinder is presented, although the evacuated sample cylinder was weighed three times at different ambient conditions. This approach was chosen here to simplify the uncertainty analysis; its quantitative validity is not affected by it.

Over 60 % of the expanded combined uncertainty results from the uncertainty of the second weighing after the filling of CO_2 . About 38 % of the expanded combined uncertainty results from the uncertainty of the first and last weighing. The uncertainty

Table 6.1 Budget for the expanded combined uncertainty ($k = \sqrt{3}$) in nitrogen composition x_{N_2} of a binary CO_2 - N_2 mixture.^a

Source of uncertainty	Uncertainty	Distribution	Coverage factor	Sensitivity coefficient	Standard uncertainty
Molar mass of nitrogen	0.0002 g mol ⁻¹	normal	2	-0.67 mol-% mol g ⁻¹	-0.067 μmol-%
Molar mass of carbon dioxide	0.001 g mol ⁻¹	normal	2	0.42 mol-% mol g ⁻¹	0.213 μmol-%
1. Weight of evacuated cylinder	200 mg	rectangular	$\sqrt{3}$	3.347 mol-% mg ⁻¹	386.929 μmol-%
2. Weight of evacuated cylinder	200 mg	rectangular	$\sqrt{3}$	3.347 mol-% mg ⁻¹	386.929 μmol-%
3. Weight of evacuated cylinder	200 mg	rectangular	$\sqrt{3}$	3.347 mol-% mg ⁻¹	386.929 μmol-%
1. Weight of CO_2 -filled cylinder	200 mg	rectangular	$\sqrt{3}$	-5.101 mol-% mg ⁻¹	-589.754 μmol-%
2. Weight of CO_2 -filled cylinder	200 mg	rectangular	$\sqrt{3}$	-5.101 mol-% mg ⁻¹	-589.754 μmol-%
3. Weight of CO_2 -filled cylinder	200 mg	rectangular	$\sqrt{3}$	-5.101 mol-% mg ⁻¹	-589.754 μmol-%
1. Weight of CO_2 - N_2 -filled cylinder	200 mg	rectangular	$\sqrt{3}$	1.754 mol-% mg ⁻¹	202.824 μmol-%
2. Weight of CO_2 - N_2 -filled cylinder	200 mg	rectangular	$\sqrt{3}$	1.754 mol-% mg ⁻¹	202.824 μmol-%
3. Weight of CO_2 - N_2 -filled cylinder	200 mg	rectangular	$\sqrt{3}$	1.754 mol-% mg ⁻¹	202.824 μmol-%
Diameter of cylinder	10 mm	rectangular	$\sqrt{3}$	0.12 mol-% mm ⁻¹	70.318 μmol-%
Height of cylinder	10 mm	rectangular	$\sqrt{3}$	0.001 mol-% mm ⁻¹	6.705 μmol-%
Coefficient of pressure expansion	20 %	rectangular	$\sqrt{3}$	52.131 mol-% MPa m ⁻³	14.464 μmol-%
Pressure of empty cylinder	1 %	rectangular	$\sqrt{3}$	0 mol-% bar ⁻¹	0 μmol-%
Pressure of CO_2 -filled cylinder	1 %	rectangular	$\sqrt{3}$	-4.2 10 ⁻⁵ mol-% bar ⁻¹	-0.978 μmol-%
Pressure of CO_2 - N_2 -filled cylinder	1 %	rectangular	$\sqrt{3}$	1.5 10 ⁻⁵ mol-% bar ⁻¹	1.701 μmol-%
Air temperature empty cylinder	0.1 °C	normal	2	-0.001 mol-% °C ⁻¹	-74.657 μmol-%
Air temperature CO_2 -filled cylinder	0.1 °C	normal	2	0.002 mol-% °C ⁻¹	113.792 μmol-%
Air temperature CO_2 - N_2 -filled cylinder	0.1 °C	normal	2	-0.001 mol-% °C ⁻¹	-39.511 μmol-%
Air pressure empty cylinder	0.13 hPa	rectangular	$\sqrt{3}$	0.414 mol-% hPa ⁻¹	30.619 μmol-%
Air pressure CO_2 -filled cylinder	0.13 hPa	rectangular	$\sqrt{3}$	-0.63 mol-% hPa ⁻¹	-46.633 μmol-%
Air pressure CO_2 - N_2 -filled cylinder	0.13 hPa	rectangular	$\sqrt{3}$	0.217 mol-% hPa ⁻¹	16.039 μmol-%
Rel. humidity empty cylinder	1 %	normal	2	-4.3 10 ⁻⁵ mol-% φ ⁻¹	-10.468 μmol-%
Rel. humidity CO_2 -filled cylinder	1 %	normal	2	-6.7 10 ⁻⁵ mol-% φ ⁻¹	-15.605 μmol-%
Rel. humidity CO_2 - N_2 -filled cylinder	1 %	normal	2	-2.3 10 ⁻⁵ mol-% φ ⁻¹	-5.605 μmol-%
Expanded combined uncertainty ($k = \sqrt{3}$): 0.002 mol-%					

^a Most of the information in this table are applicable in an universal way, i.e., not only for the specific mixture taken as example in this work.

of the weighing is dominating with 98 %; the uncertainty of the other input parameters sums up to only 2 %.

The uncertainty of the weighing, which has a rectangular probability distribution, was prevailing in the uncertainty analysis. Consequently, the combined coverage factor corresponded to the one of the weighing. Assuming a rectangular distribution, the combined expanded uncertainty ($k = \sqrt{3}$) in nitrogen composition was 0.002 mol-%.

However, after a mixture was filled into a cylinder, sorption effects can occur. In consequence, the composition of the removed gas can be different from the gravimetrically determined composition. Therefore, the composition of the gravimetrically prepared mixture was validated analytically with a two-sinker densimeter. This densimeter can measure the density at standard conditions with a relative combined expanded uncertainty ($k = 2$) of 0.02 % (Richter *et al.*, 2010). At low pressures, the density of a mixture depends on its molar mass. Knowing the density, the composition can be determined using the GERG-2008 from Kunz and Wagner (2012).

The procedures for determining the mixture composition using the two-sinker densimeter were described comprehensively by Richter *et al.* (2009); see also Neumann (2011). Therefore, they are not further discussed here. In case of the CO₂-N₂ mixture, the sample cylinder was rolled to homogenize the mixture before it was attached to the two-sinker densimeter. In addition, the sample cylinder was heated at its bottom before and while removing fluid. Thereby, convection was triggered inside the cylinder, also to homogenize the mixture.

The analytically determined composition – utilizing the two-sinker densimeter – was $x_{\text{N}_2} = 75.00$ mol-%; $U(x_{\text{N}_2}) = 0.04$ mol-% ($k = 2$) and the gravimetrically determined composition was $x_{\text{N}_2} = 74.981$ mol-%; $U(x_{\text{N}_2}) = 0.002$ mol-% ($k = \sqrt{3}$). Thus, the analytical and gravimetric results agreed within the expanded uncertainty of the analytical determination of the mixture composition. Thereby, the functionality of the apparatus for the gravimetric preparation of gaseous mixtures was validated. In conclusion, it is now possible to prepare mixtures with an expanded combined uncertainty ($k = \sqrt{3}$) in composition of 0.002 mol-%. Very accurate density measurements are thereby enabled in a wide pressure range, as filling pressures up to 20 MPa are possible. This apparatus is fundamental for further mixture measurements. As shown by first results of a two-sinker densimeter (Yang *et al.*, 2015), the data situation of mixtures can be improved significantly.

The apparatus for the gravimetric preparation of gaseous mixtures is advantageous especially for such mixtures, where the molar masses of the components are similar, e.g., argon and carbon dioxide. Thus, for an Ar-CO₂ mixture, the expanded combined uncertainty ($k = 2$) in composition can be up to 0.21 mol-%, when the uncertainty is determined utilizing the two-sinker densimeter.

7 Summary and Conclusion

During this work, a low-pressure viscometer and a viscometer-densimeter were improved and prepared for the measurement of binary gaseous mixtures containing carbon dioxide. An apparatus for the gravimetric preparation of gaseous mixtures was developed to provide exactly the required mixtures. A flow-guide tube was integrated into the measuring cell of the viscometer-densimeter to reduce a scatter in viscosity. Furthermore, the viscosity-measurement principle was evaluated, its uncertainty was re-estimated, and an extended model function was developed to compensate offsets in viscosity and to reduce the uncertainty in viscosity. Using this extended model function, the viscosity of carbon dioxide was measured with the low-pressure viscometer.

In the beginning of this work, a time efficient independent simultaneous operation of both apparatuses was hindered by the absence of a second system for automating the viscosity measurement. In addition, due to an age-related deterioration of electronic components, the existing automation system was unreliable. Thus, a new system for automating the viscosity measurement was developed and integrated into both apparatuses. The basis for an economic operation of both apparatuses was thereby provided.

The apparatuses were equipped with a temperature-controlled gas-dosing system. The temperature of all parts in contact with the sample fluid can be kept at $T = 323.15$ K. The condensation of mixture components – and thus a change in mixture composition distorting the measured viscosity – is thereby largely prevented.

It was found out that carbon dioxide-rich mixtures with filling pressures up to 20 MPa and an uncertainty in mixture composition of 0.1 mol-% were not available commercially or, if available, were very expensive. Consequently, an apparatus for the gravimetric preparation of gaseous mixtures was developed. Gaseous mixtures including carbon dioxide-rich mixtures with pressures up to 20 MPa can now be prepared. The expanded uncertainty ($k = \sqrt{3}$) in composition of a gravimetrically prepared CO₂-N₂ mixture was estimated to be 0.002 mol-%. This gravimetrically determined composition was validated analytically using a two-sinker densimeter for standard conditions (*Richter et al.*, 2010). In summary, a cost efficient supply of mixtures with high filling pressures and a low uncertainty in mixture composition was set up.

In case of the viscometer-densimeter, the positioning device for aligning the cylinder system was re-designed to enable a reproducible and accurate alignment of the cylinder system. Therefore, a larger manual positioner was implemented into the positioning device, which was thereby simplified and improved essentially concerning handling, reproducibility and accuracy. However, the measured viscosities scattered about 2 %. The simultaneous density measurement was identified as the most reasonable cause for

the scatter. Thus, the measurement principle of the viscometer-densimeter was refined by integrating a flow-guide tube into the measuring cell. The scatter in viscosity was reduced by a factor of 10, namely to 0.2 %. However, the scatter in viscosity was lower than 0.2 %, when the density was not measured simultaneously. In conclusion, the movable outer boundary of the cylinder system, i.e., the sinker, was not the only reason for the scatter aroused by the simultaneous density measurement. As a scatter lower than 0.2 % is desired, this issue has to be investigated further in future.

When the first viscosities were measured with the low-pressure viscometer, two different offsets to reference viscosities were observed: (1) a systematic offset in viscosity, and (2) a viscosity dependent offset, i.e., an offset in viscosity decreasing with increasing viscosity. Similar offsets were observed for the viscometer-densimeter, too. Both offsets were larger than previously reported expanded combined uncertainties in viscosity for the apparatuses. It was shown that multiple sources of uncertainty were responsible for the systematic offset. Some of the disturbing effects were found to be inevitable, e.g., inaccuracies in the fluid-dynamic model or an eccentricity of the cylinder system. However, the impact of the disturbing effects was practically canceled in of the model function by setting it into relation to a reference fluid, i.e., helium. The model function became practically independent of the uncertainties of the apparatus constants (e.g., the geometries of the cylinder system and the eccentricity) and even from inaccuracies of the fluid-dynamic model.

The viscosity dependent offset resulted from an offset of an input parameter of the model function called residual damping. This conclusion was drawn because a fluid independent correction of the residual damping canceled the viscosity dependent offset. Furthermore, this explanation was supported by a sensitivity analysis of the model function and an evaluation of the experimental methods, with which the residual damping was determined. Against this background, a new method to determine the residual damping was developed, in which the residual damping is calibrated using reference viscosities of fluids with different viscosity, i.e., helium, argon, and neon. As reference, experimental reference viscosities and reference viscosities calculated ab initio can be used. This method was called multi-fluid calibration method, because multiple reference fluids are required to apply the calibration. For the multi-fluid calibration method a lower uncertainty was estimated as for the experimental determination of the residual damping in vacuum. The viscosity dependent offset was not observed when the calibrated residual damping was used. Thus, the multi-fluid calibration can be considered as a reasonable replacement of the experimental determination of the residual damping.

The combination of measuring in a relative way and determining the residual damping with the multi-fluid calibration was called extended model function. In case of the low-pressure viscometer, the viscosity of carbon dioxide was measured using the exten-

ded model function. Measurements ranged from $T = (253.15 \text{ to } 473.15) \text{ K}$ with pressures up to 1.2 MPa. A relative expanded combined uncertainty ($k = 2$) of (0.20 to 0.41) % was estimated (Schäfer *et al.*, 2015). Thus, previously reported expanded uncertainties ($k = 2$) of 0.06 % (El Hawary, 2009) were corrected by a factor more than 3. The experimental results agreed within the given uncertainties with re-evaluated (Vogel, 2014) viscosities of Hendl *et al.* (1993) and Vogel and Barkow (1986). The measurements are considered as a valuable description of the initial density dependence of the viscosity of carbon dioxide.

8 References

- Arnold Magnetic Technologies* (2014): RECOMA. The Complete Range of SmCo_5 and $\text{Sm}_2\text{Co}_{17}$ alloys. Data Sheet. Available at: http://www.arnoldmagnetics.com/uploadedFiles/Products/Samarium_Cobalt/Recoma_Grade_pdfs/Recoma%20Combined%20-%20140527.pdf [Accessed: 07.07.2015]
- Arnold Magnetic Technologies* (2010): Inspection Certificate. Record No. 2100506/5 1568, Lupfig, 2010.
- Arp, V. D.; McCarty, R. D.; Friend, D. G.* (1998): Thermophysical Properties of Helium-4 from 0.8 to 1500 K with Pressures to 2000 MPa, NIST Technical Note 1334 (revised), 1998.
- Berg, R. F.; Moldover, M. R.* (2012): Recommended Viscosities of 11 Dilute Gases at 25 °C. *J. Phys. Chem. Ref. Data* 41 (2012), 043104.
- Bich, E.; Hellmann, R.; Vogel, E.* (2007): Ab Initio Potential Energy Curve for the Helium Atom Pair and Thermophysical Properties of the Dilute Helium Gas. II. Thermophysical Standard Values for Low-Density Helium. *Mol. Phys.* 105 (2007), 3035–3049.
- Bich, E.; Hellmann, R.; Vogel, E.* (2008): Ab Initio Potential Energy Curve for the Neon Atom Pair and Thermophysical Properties of the Dilute Neon Gas. II. Thermophysical Properties For Low-Density Neon. *Mol. Phys.* 106 (2008), 813–825.
- Böcker, M.* (2011): Discussion about the Safety Factor of Swagelok Valves. Personal Communication, 2011.
- Brachthäuser, K.; Kleinrahm, R.; Lösch, H. W.; Wagner, W.* (1993): Entwicklung eines neuen Dichtemeßverfahrens und Aufbau einer Hochtemperatur-Hochdruck- Dichtemeßanlage. *VDI Fortschritt-Berichte, Reihe 8, Nr. 371*, VDI-Verlag, Düsseldorf, 1993.
- Buff, B.* (2008): Measurement Record of the Low-Pressure Viscometer's Measuring Cell. Record: Messzelle ND 12-06-2008. Coordinate-Measuring Machine: Zeiss UMM 850. Chair of Production Systems, Ruhr-Universität Bochum, Bochum, 2008.
- Buff, B.* (2009): Measurement Record of the Viscometer-Densimeter's Rotating Body. Record: Viskositaetskoerper 28-05-2009. Coordinate-Measuring Machine: Zeiss UMM 850. Chair of Production Systems, Ruhr-Universität Bochum, Bochum, 2009.
- Buff, B.* (2012): Measurement Record of the Low-Pressure Viscometer's Rotating Body. Record: Viskositaetskoerper ND 14.02.2012. Coordinate-Measuring Machine: Zeiss UMM 850. Chair of Production Systems, Ruhr-Universität Bochum, Bochum, 2012.

- Buff, B. (2013):* Measurement Record of the Viscometer-Densimeter's Flow-Guide Tube. Record: Leitrohr VDMA 2013-04-06 $v=0.5\text{mm/s}$. Coordinate-Measuring Machine: Zeiss UMM 850. Chair of Production Systems, Ruhr-Universität Bochum, Bochum, 2013.
- Cencek, W.; Przybytek, M.; Komasa, J.; Mehl, J. B.; Jeziorski, B.; Szalewicz, K. (2012):* Effects of Adiabatic, Relativistic, and Quantum Electrodynamics Interactions on the Pair Potential and Thermophysical Properties of Helium. *J. Chem. Phys.* 136 (2012), 224303.
- Chang, R. F.; Abbott, P. J. (2007):* Factors Affecting the Reproducibility of the Accommodation Coefficient of the Spinning Rotor Gauge. *J. Vac. Sci. Technol. A* 25 (2007), 1567–1576.
- Daun, F. (2012):* Belastungstests von Ventilen. Semesterarbeit, Chair of Thermodynamics, Ruhr-Universität Bochum, Bochum, 2012.
- Davis, R. S. (1992):* Equation for the Determination of the Density of Moist Air (1981/91). *Metrologia* 29 (1992), 67–70.
- Deutsche Edelstahlwerke (2008):* Data Sheet on the Properties of Steel X3CrNb17 (1.4511). Witten, Germany. Available at: <http://www.dew-stahl.com/service/technischebibliothekbroschueren/werkstoffdatenblaetter/rsh-staehle/> [Accessed: 07.07.2015]
- Di Pippo, R.; Dorfman, J. R.; Kestin, J.; Khalifa, H. E.; Mason, E. A. (1977):* Composition Dependence of the Viscosity of Dense Gas Mixtures. *Physica A* 86 (1977), 205–223.
- DIN 53019-3 (2008):* Viskosimetrie – Messung von Viskositäten und Fließkurven mit Rotationsviskosimetern – Teil 3: Messabweichungen und Korrekturen. Beuth Verlag, Berlin, 2008.
- DIN EN ISO 6143 (2006):* Gas analysis – Comparison Methods for Determining and Checking the Composition of Calibration Gas Mixtures (ISO 6143:2001). European Committee for Standardization, Brussels, 2006.
- Docter, A. (1992):* Projektierung und Konstruktion des Druckmeßkreises und der Füllleinrichtung einer neuen Präzisionsdichtemessanlage. Diploma Thesis, Chair of Thermodynamics, Ruhr-Universität Bochum, Bochum, 1992.
- Docter, A.; Lösch, H. W.; Wagner, W. (1997):* Entwicklung und Aufbau einer Anlage zur simultanen Messung der Viskosität und der Dichte fluider Stoffe. VDI Fortschritt-Berichte, Reihe 3, Nr. 494, VDI-Verlag, Düsseldorf, 1997.
- Docter, A.; Lösch, H. W.; Wagner, W. (1999):* A New Apparatus for Combined Measurements of the Viscosity and Density of Fluids for Temperatures from 233 to 523 K at Pressures up to 30 MPa. *Int. J. Thermophys.* 20 (1999), 485–505.

- El Hawary, T. (2003):* Messung der dynamischen Viskosität und der Dichte von vier Erdgasgemischen für Drücke bis 15 MPa und Temperaturen bis 373 K in einer kombinierten Viskositäts-Dichte-Messanlage. Studienarbeit, Chair of Thermodynamics, Ruhr-Universität Bochum, Bochum, 2003.
- El Hawary, T. (2009):* Messung der Dichte und Viskosität in der Gasphase von Methan, Stickstoff und Methan-Stickstoff-Gemischen mit einer weiterentwickelten kombinierten Viskositäts-Dichte-Messanlage und einer neuen Viskositätsmessanlage für geringe Gasdichten. Dissertation, Chair of Thermodynamics, Ruhr-Universität Bochum, Bochum, 2009.
- Evers, C. (2001):* Weiterentwicklung einer kombinierten Viskositäts-Dichte-Messanlage und Messung der dynamischen Viskosität von Stickstoff, Argon, Methan, Helium, Neon und Krypton in Abhängigkeit von Dichte und Temperatur. Dissertation, Chair of Thermodynamics, Ruhr-Universität Bochum, Bochum, 2001.
- Evers, C.; Lösch, H. W.; Wagner, W. (2002):* An Absolute Viscometer-Densimeter and Measurements of the Viscosity of Nitrogen, Methane, Helium, Neon, Argon, and Krypton over a Wide Range of Density and Temperature. *Int. J. Thermophys.* 23 (2002), 1411–1439.
- Fenghour, A.; Wakeham, W. A.; Vesovic, V. (1998):* The Viscosity of Carbon Dioxide. *J. Phys. Chem. Ref. Data* 27 (1998), 31–44.
- Frank, R. (1982):* Molekularpumpen. In: Wutz, M.; Adam, H.; Walcher, W. (eds.), *Theorie und Praxis der Vakuumtechnik*. Friedr. Vieweg & Sohn, Braunschweig, 1982.
- Fremerey, J. K. (1985):* The Spinning Rotor Gauge. *J. Vac. Sci. Technol. A* 3 (1985), 1715–1720.
- Friend, D. G. (1990):* Viscosity Surface for Mixtures of Methane and Ethane. *Cryogenics* 30 (1990), 105–112.
- Gernert, J.; Span, R. (2015):* EOS-CG: A Helmholtz Energy Mixture Model for Humid Gases and CCS Mixtures. *J. Chem. Thermodyn.* In press.
- Glos, S. (1999):* Entwicklung eines horizontalen Positioniersystems zur Minimierung des Exzentrizitätsfehlers bei einer Viskositäts-Dichte-Meßanlage. Konstruktiver Entwurf, Chair of Thermodynamics, Ruhr-Universität Bochum, Bochum, 1999.
- Harris, E. J.; Hope, G. C.; Gough, D. W.; Smith, E. B. (1979):* Viscosity of Gaseous Carbon Dioxide, Sulphur Hexafluoride and Nitrous Oxide at Low Temperatures. *J. Chem. Soc., Faraday Trans. 1* 75 (1979), 892–897.
- Heine, M. (2014):* Modeling the Axial Moment of Inertia of the Low-pressure Viscometer's Rotating Body using Autodesk Inventor. Personal Communication, 2014.

- Hellmann, R. (2014):* Ab Initio Potential Energy Surface for the Carbon Dioxide Molecule Pair and Thermophysical Properties of Dilute Carbon Dioxide Gas. *Chem. Phys. Lett.* 613 (2014), 133–138.
- Hellmann, R.; Bich, E.; Vogel, E.; Vesovic, V. (2014):* Intermolecular potential energy surface and thermophysical properties of the CH₄-N₂ system. *J. Chem. Phys.* 141 (2014), 224301.
- Hendl, S.; Neumann, A.-K.; Vogel, E. (1993):* The Viscosity of Carbon Dioxide and Its Initial Density Dependence. *High Temp. - High Pressures* 25 (1993), 503–511.
- Herrndorf, M.-A. (2012a):* Entwurf und Aufbau einer thermostatisierten Gasdosierung. Semesterarbeit, Chair of Thermodynamics, Ruhr-Universität Bochum, Bochum, 2012.
- Herrndorf, M.-A. (2012b):* Inbetriebnahme einer Anlage zur Messung der Viskosität und Dichte von Gasen. Bachelor's Thesis, Chair of Thermodynamics, Ruhr-Universität Bochum, Bochum, 2012.
- Herrndorf, M.-A. (2014):* Kalibrierung einer Niederdruck-Viskositäts-Messanlage und Messung der Viskosität von Kohlendioxid. Master's Thesis, Chair of Thermodynamics, Ruhr-Universität Bochum, Bochum, 2014.
- Hielscher, R. (2014):* Measurement Records of the Low-Pressure Viscometer's and the Viscometer-Densimeter's Geometries. Coordinate-Measuring Machine: Wenzel LH87. 3D-Service Koordinatenmesstechnik, Hattingen, 2014.
- Humberg, K. (2013a):* Konzeption und Aufbau eines Automatisierten Viskositätsmesssystems. Semesterarbeit, Chair of Thermodynamics, Ruhr-Universität Bochum, Bochum, 2013.
- Humberg, K. (2013b):* Inbetriebnahme zweier Anlagen zu Messung der Viskosität von Gasen. Bachelor's Thesis, Chair of Thermodynamics, Ruhr-Universität Bochum, Bochum, 2013.
- Humberg, K. (2015):* Untersuchung von Einflüssen auf die Messdatenerfassung eines Rotationsviskosimeters. Master's Thesis, Chair of Thermodynamics, Ruhr-Universität Bochum, Bochum, 2015.
- Hunter, I. N.; Marsh, G.; Matthews, G. P.; Smith, E. B. (1993):* Argon+Carbon Dioxide Gaseous Mixture Viscosities and Anisotropic Pair Potential Energy Functions. *Int. J. Thermophys.* 14 (1993), 819–833.
- ISO/IEC Guide 98-3 (2008):* Uncertainty of measurement - Part 3: Guide to the Expression of Uncertainty in Measurement (GUM:1995). International Organization for Standardization, Geneva, 2008.

- Isogai, H. (1993): Analysis of Thermal Influence on the Accuracy of a Spinning Rotor Gauge. Vacuum 44 (1993), 1181–1187.*
- Iwasaki, H.; Takahashi, M. (1981): Viscosity of Carbon Dioxide and Ethane. J. Chem. Phys. 74 (1981), 1930–1943.*
- Johnston, H. L.; McCloskey, K. E. (1940): Viscosities of Several Common Gases Between 90°K and Room Temperature. J. Phys. Chem. 44 (1940), 1038–1058.*
- Jousten, K. (2003): Is the Effective Accommodation Coefficient of the Spinning Rotor Gauge Temperature Dependent? J. Vac. Sci. Technol. A 21 (2003), 318–324.*
- Kestin, J.; Khalifa, H. E.; Ro, S. T.; Wakeham, W. A. (1977): The Viscosity and Diffusion Coefficients of Eighteen Binary Gaseous Systems. Physica A: Statistical Mechanics and its Applications 88 (1977), 242–260.*
- Kestin, J.; Korfali, Ö.; Sengers, J. V. (1980): Density Expansion of the Viscosity of Carbon Dioxide Near the Critical Temperature. Physica A: Statistical Mechanics and its Applications 100 (1980), 335–348.*
- Kestin, J.; Leidenfrost, W. (1959): An Absolute Determination of the Viscosity of Eleven Gases over a Range of Pressures. Physica 25 (1959), 1033–1062.*
- Kestin, J.; Ro, S. T.; Wakeham, W. A. (1972): Viscosity of Carbon Dioxide in the Temperature Range 25–700°C. J. Chem. Phys. 56 (1972), 4114–4118.*
- Kestin, J.; Whitelaw, J. H. (1963): A Relative Determination of the Viscosity of Several Gases by the Oscillating Disk Method. Physica 29 (1963), 335–356.*
- Kobayashi, H.; Nashima, T.; Okamoto, Y.; Kaminaga, F. (1991): End Effect in a Coaxial Cylindrical Viscometer. Rev. Sci. Instrum. 62 (11) (1991), 2748–2750.*
- Kremer, G. (2015): Araldit AW 106 /HV 953 U [Online]. Available at: <http://www.kremer-pigmente.com/de/mal---binde--und-klebmittel/araldit-aw-106-hv-953-u-1-pack-97940.html> [Accessed: 04.08.2015]*
- Kunz, O.; Wagner, W. (2012): The GERG-2008 Wide-Range Equation of State for Natural Gases and Other Mixtures: An Expansion of GERG-2004. J. Chem. Eng. Data 57 (2012), 3032–3091.*
- Luxfer (2015): L6X Aluminium Cylinder Specifications [Online]. UK. Available at: <http://www.luxfercylinders.com/products/industrial-specialty-gas-cylinders/493-l6x-aluminum-cylinder-specifications> [Accessed: 27.05.2015]*
- Merkens, M. E. (2013): Aufbau einer Apparatur zur gravimetrischen Herstellung von Gasgemischen. Bachelor's Thesis, Chair of Thermodynamics, Ruhr-Universität Bochum, Bochum, 2013.*

- Millat, J.; Dymond, J. H.; Nieto de Castro, C. A. (1996): Part one: General. Introduction. In: Millat, J.; Dymond, J. H.; Nieto de Castro, C. A. (eds.), Transport Properties of Fluids. Their Correlation, Prediction and Estimation. Cambridge Univ. Press, Cambridge, 1996.
- Müller, W. (1932): Einführung in die Theorie der zähen Flüssigkeiten. In: Artin E. and Kowalewski G. (eds.) Mathematik in Monographien und Lehrbüchern. Band 10. Akademische Verlagsgesellschaft M.B.H., Leipzig, 1932.
- Mysliwietz, B. (2013): Discussion about the Gravimetric Preparation of Gaseous Mixtures. Personal Communication. Chair of Thermodynamics, Ruhr-Universität Bochum, Bochum, 2013.
- Mysliwietz, B. (2015): Dehnt sich eine Gasflasche wie ein Ballon aus? Available at: http://www.labortechniker.de/Ballongas_mal_anders/Ballongas.html [Accessed: 28.05.2015]
- Neumann, A.-C. (2011): Messung der Normdichte von reinen Gasen und erdgasähnlichen Gemischen sowie Bestimmung der Zusammensetzung binärer Gemische. Studienarbeit, Chair of Thermodynamics, Ruhr-Universität Bochum, Bochum, 2011.
- Nieto de Castro, C. A.; Wakeham, W. A. (1996): Part one: General. Methodology. In: Millat, J.; Dymond, J. H.; Nieto de Castro, C. A. (eds.), Transport Properties of Fluids. Their Correlation, Prediction and Estimation. Cambridge Univ. Press, Cambridge, 1996.
- Ntontos, G. (2014): Kalibrierarbeiten zur Inbetriebnahme zweier Viskositätsmessanlagen. Master's Thesis, Chair of Thermodynamics, Ruhr-Universität Bochum, Bochum, 2014.
- Oh, S. H.; Kim, B. M.; Kang, N. (2013): Evaluation of Changes in Cylinder Volume Due to Gas Filling and Subsequent Release. Metrologia 50 (2013), 318–324.
- Quiñones-Cisneros, S. E.; Huber, M. L.; Deiters, U. K. (2010): REFPROP Reference Fluid Thermodynamic and Transport Properties. NIST Standard Reference Data Base 23, Version 9.0, 2010.
- Rainwater, J. C.; Friend, D. G. (1987): Second Viscosity and Thermal-Conductivity Virial Coefficients of Gases: Extension to Low Reduced Temperatures. Phys. Rev., A 36 (1987), 4062–4066.
- Richter, M.; Kleinrahm, R.; Glos, S.; Span, R. (2009): Normdichtemessgerät für Erdgase - Bedienungsanleitung und Dokumentation. Chair of Thermodynamics, Ruhr-Universität Bochum, Bochum, 2009.

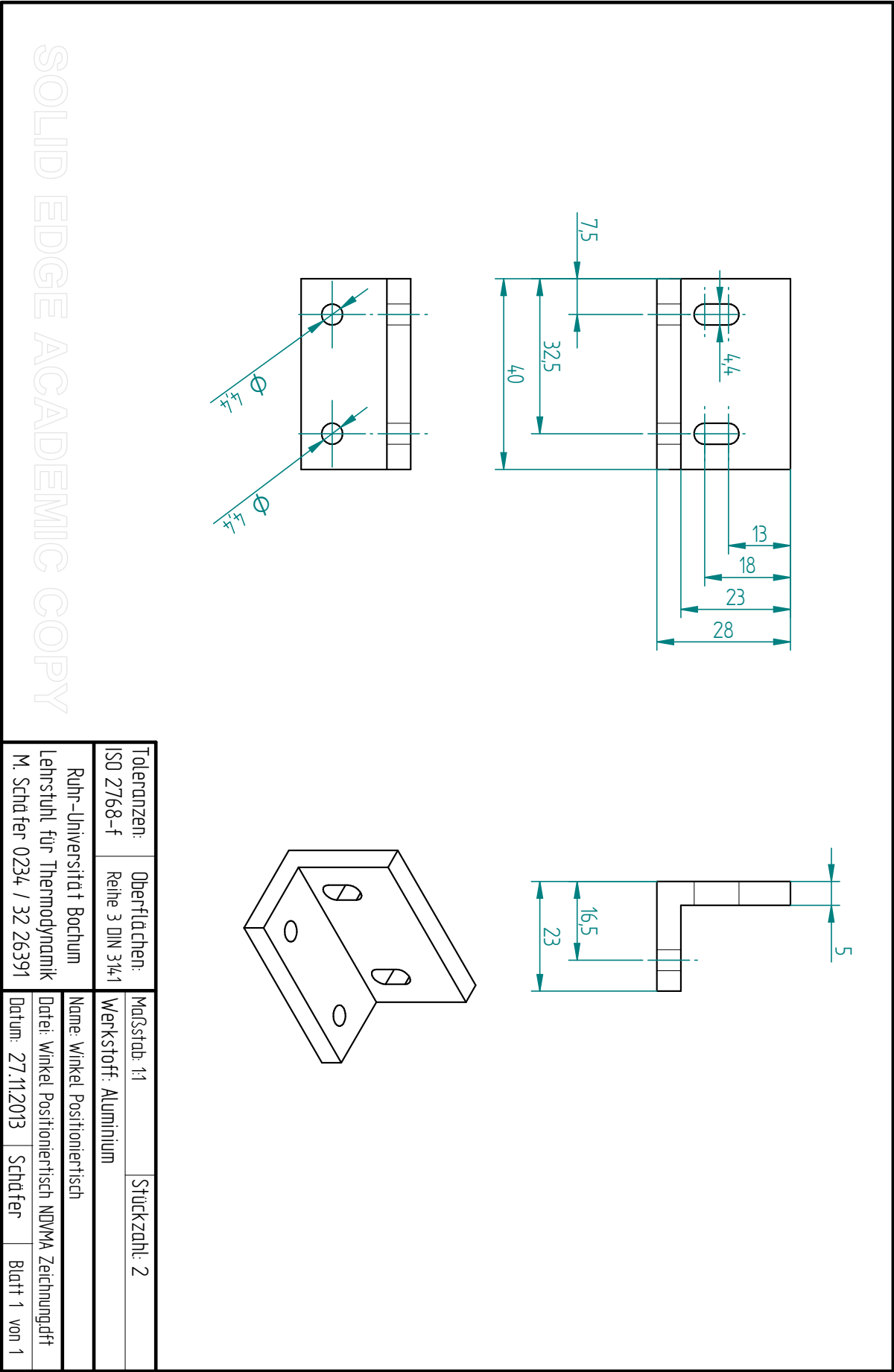
- Richter, M.; Kleinrahm, R.; Glos, S.; Wagner, W.; Span, R.; Schley, P.; Uhrig, M. (2010): A Two-Sinker Densimeter for Accurate Measurements of the Density of Natural Gases at Standard Conditions. Int. J. Thermophys. 31 (2010), 680–697.*
- Richter, M.; Kleinrahm, R.; Lentner, R.; Span, R. (2015): Development of a Special Single-Sinker Densimeter for Cryogenic Liquid Mixtures and First Results for a Liquefied Natural Gas (LNG). J. Chem. Thermodyn. (2015), <http://dx.doi.org/10.1016/j.jct.2015.09.034>.*
- Sauer, M. (2001): Konstruktion einer Messapparatur für Viskositätsmessungen bei niedrigen Gasdichten. Konstruktiver Entwurf, Chair of Thermodynamics, Ruhr-Universität Bochum, Bochum, 2001.*
- Schäfer, M. (2009): Messung der dynamischen Viskosität von Methan, Ethan und binären Methan-Ethan-Gemischen in der Gasphase mit einer Viskositäts-Apparatur für geringe Gasdichten. Diploma Thesis, Chair of Thermodynamics, Ruhr-Universität Bochum, Bochum, 2009.*
- Schäfer, M.; Wegge, R.; Richter, M.; Span, R. (2012): An Apparatus for the Gravimetric Preparation of Gas Mixtures. Poster presentation, Thermodynamik-Kolloquium, Potsdam, 2012.*
- Schäfer, M.; Richter, M.; Span, R. (2015): Measurements of the Viscosity of Carbon Dioxide at Temperatures from (253.15 to 473.15) K with Pressures up to 1.2 MPa. J. Chem. Thermodyn. 89 (2015), 7–15.*
- Schlichting, H.; Gersten, K. (2006): Grenzschicht-Theorie. 10th rev. edn., Springer-Verlag, Berlin, 2006.*
- Span, R.; Lemmon, E. W.; Jacobsen, R. T.; Wagner W.; Yokozeki A. (2000): A Reference Equation of State for the Thermodynamic Properties of Nitrogen for Temperatures from 63.151 to 1000 K and Pressures to 2200 MPa. J. Phys. Chem. Ref. Data 29 (2000), 1361–1433.*
- Span, R.; Wagner, W. (1996): A New Equation of State for Carbon Dioxide Covering the Fluid Region from the Triple-point Temperature to 1100 K at Pressures up to 800 MPa. J. Phys. Chem. Ref. Data 25 (1996), 1509–1596.*
- Swagelok (2011): Produkt Katalog. Swagelok Company, 2011.*
- Timrot, D. L.; Traktueva, S. A. (1975): Dependence of the Viscosity of CO₂ and SF₆ on Temperature at Moderate Densities. Therm. Eng. 22 (1975), 105–108.*
- Touloukian, Y. S. (1975): Thermal Expansion. Metallic Elements and Alloys. Thermophysical Properties of Matter. Volume 12. IFI/Plenum, New York, 1975.*

- Vogel, E. (2014): Korrigierte Viskositätsdaten bei kleinen Dichten und im Limit von Null-dichte für Kohlendioxid. Personal Communication, 2014.
- Vogel, E.; Barkow, L. (1986): Precision-Measurements of the Viscosity Coefficient of Carbon-Dioxide Between Room Temperature and 650 K. *Zeitschrift für physikalische Chemie-Leipzig* 267 (1986), 1038–1043.
- Vogel, E.; Jäger, B.; Hellmann, R.; Bich, E. (2010): Ab Initio Pair Potential Energy Curve for the Argon Atom Pair and Thermophysical Properties for the Dilute Argon Gas. II. Thermophysical Properties for Low-Density Argon. *Mol. Phys.* 108 (2010), 3335–3352.
- Wagner, W.; Kleinrahm, R. (2004): Densimeters for Very Accurate Density Measurements of Fluids over Large Ranges of Temperature, Pressure, and Density. *Metrologia* 41 (2) SI (2004), 24–39, PII S0026-1394(04)72412-3.
- Wagner, W.; Pruß, A. (2002): The IAPWS Formulation 1995 for the Thermodynamic Properties of Ordinary Water Substance for General and Scientific Use. *J. Phys. Chem. Ref. Data*, 31 (2) (2002), 387–535.
- Wobser, R.; Müller, F. (1941): Die innere Reibung von Gasen und Dämpfen und ihre Messung im Höppler-Viskosimeter. *Kolloid-Beihefte* 52 (1941), 165–276.
- Wöll, O. (2005): Messung der dynamischen Viskosität und der Dichte von trockener und feuchter Luft und Weiterentwicklung einer kombinierten Viskositäts-Dichte-Messanlage. Dissertation, Chair of Thermodynamics, Ruhr-Universität Bochum, Bochum, 2005.
- Yang, X.; Ben Souissi, M. A.; Richter, M.; Kleinrahm, R.; Span, R. (2015): Vapor-Phase (p, ρ, T, x) Behavior and Virial Coefficients for the Binary Mixture (0.05 Argon + 0.095 Carbon Dioxide) over the Temperature Range from (273.15 to 323.15) K with Pressures up to 9 MPa. To be submitted to *J. Chem. Eng. Data*.

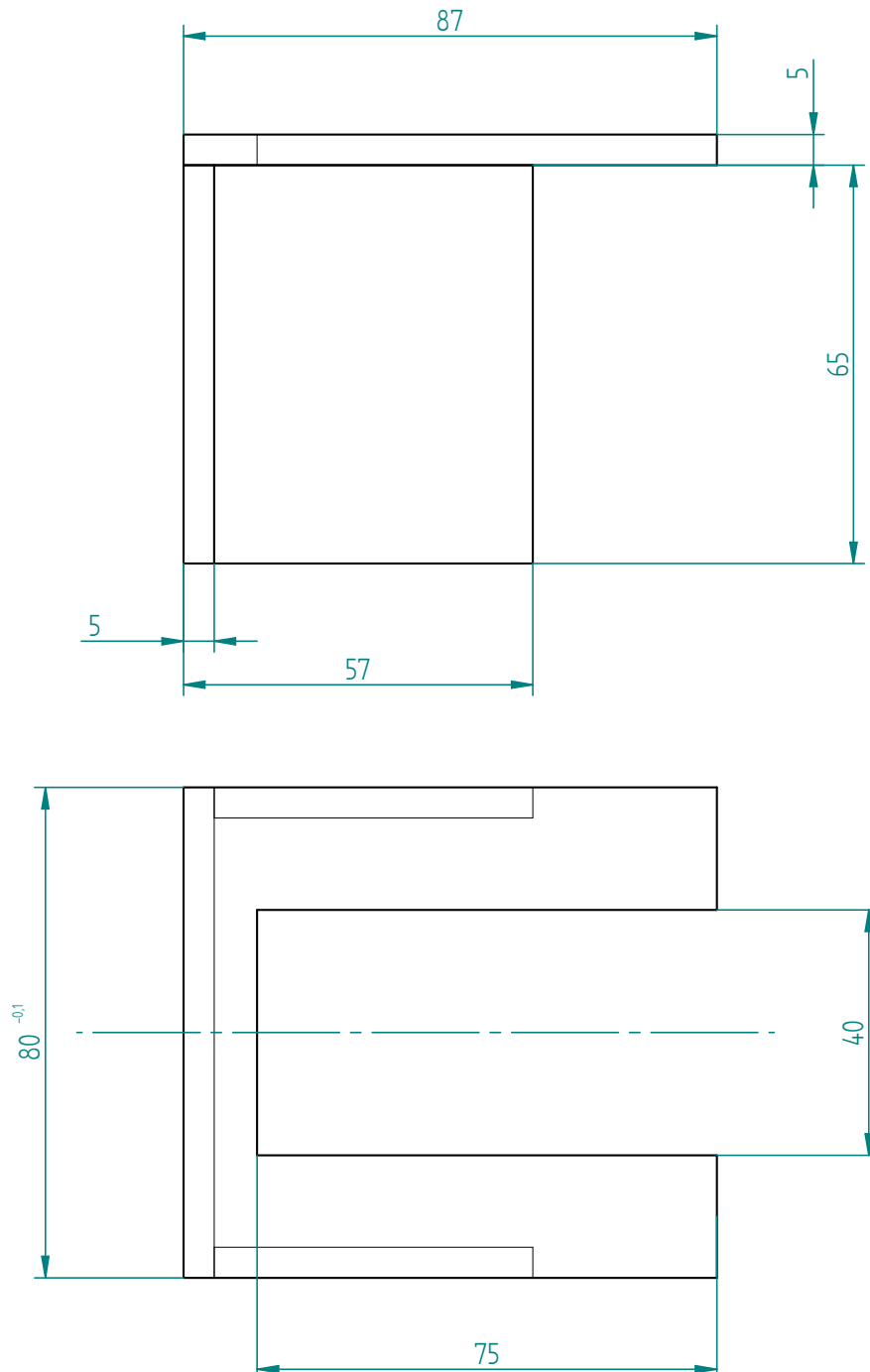
A Technical Drawings

This appendix contains technical drawings of both apparatuses. Please note that the drawings are not true to scaled here. The technical drawings included in this appendix are: in section A.1 the angle plate to fix the low-pressure viscometer's manual positioner, in section A.2 the draft shield for the viscometer-densimeter's balance, in section A.3 modifications to the stand for the viscometer-densimeter's balance, and in section A.4 the viscometer-densimeter's flow-guide tube.

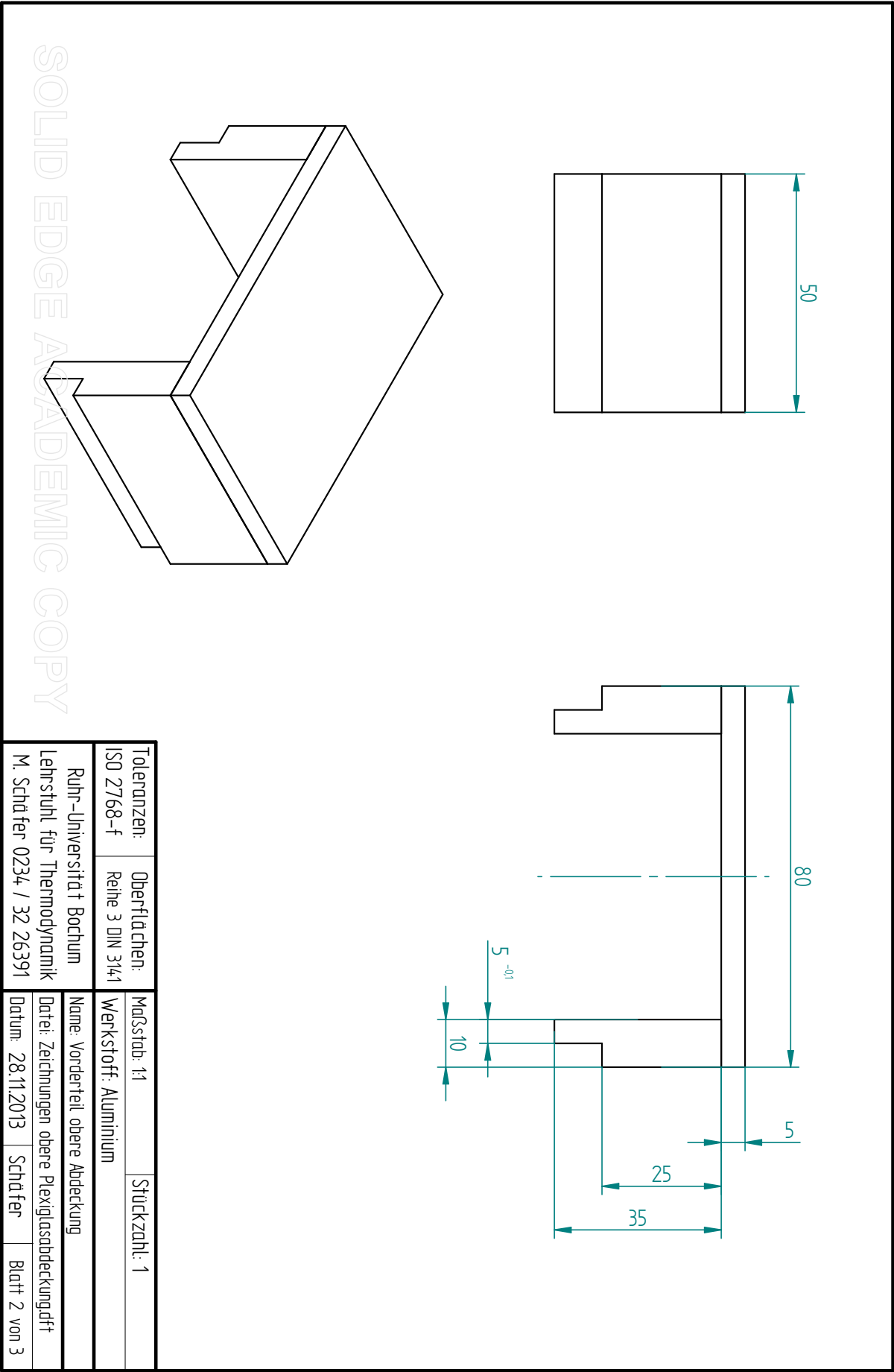
A.1 Angle Plate to Fix the Manual Positioner of the Low-Pressure Viscometer

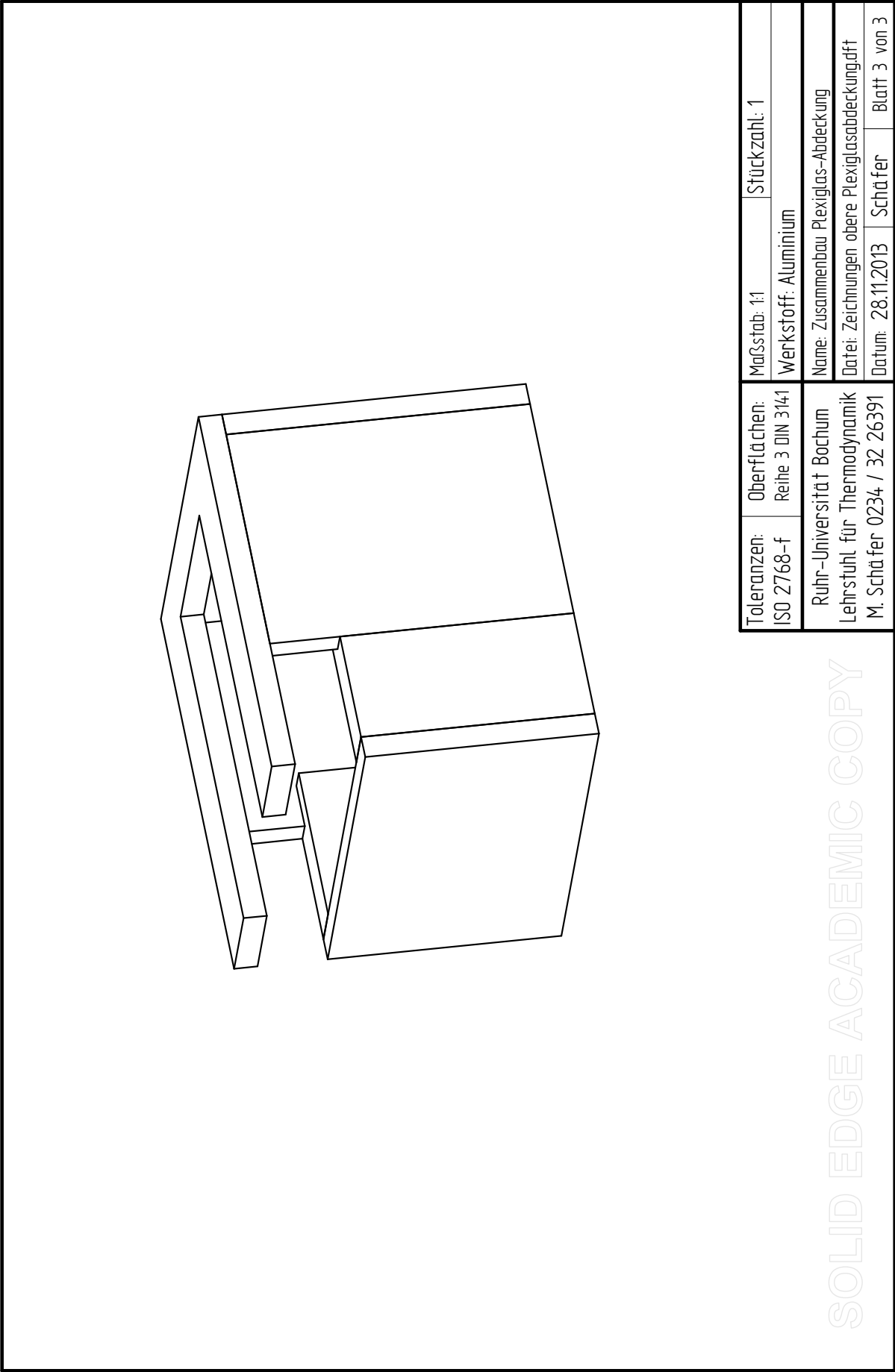


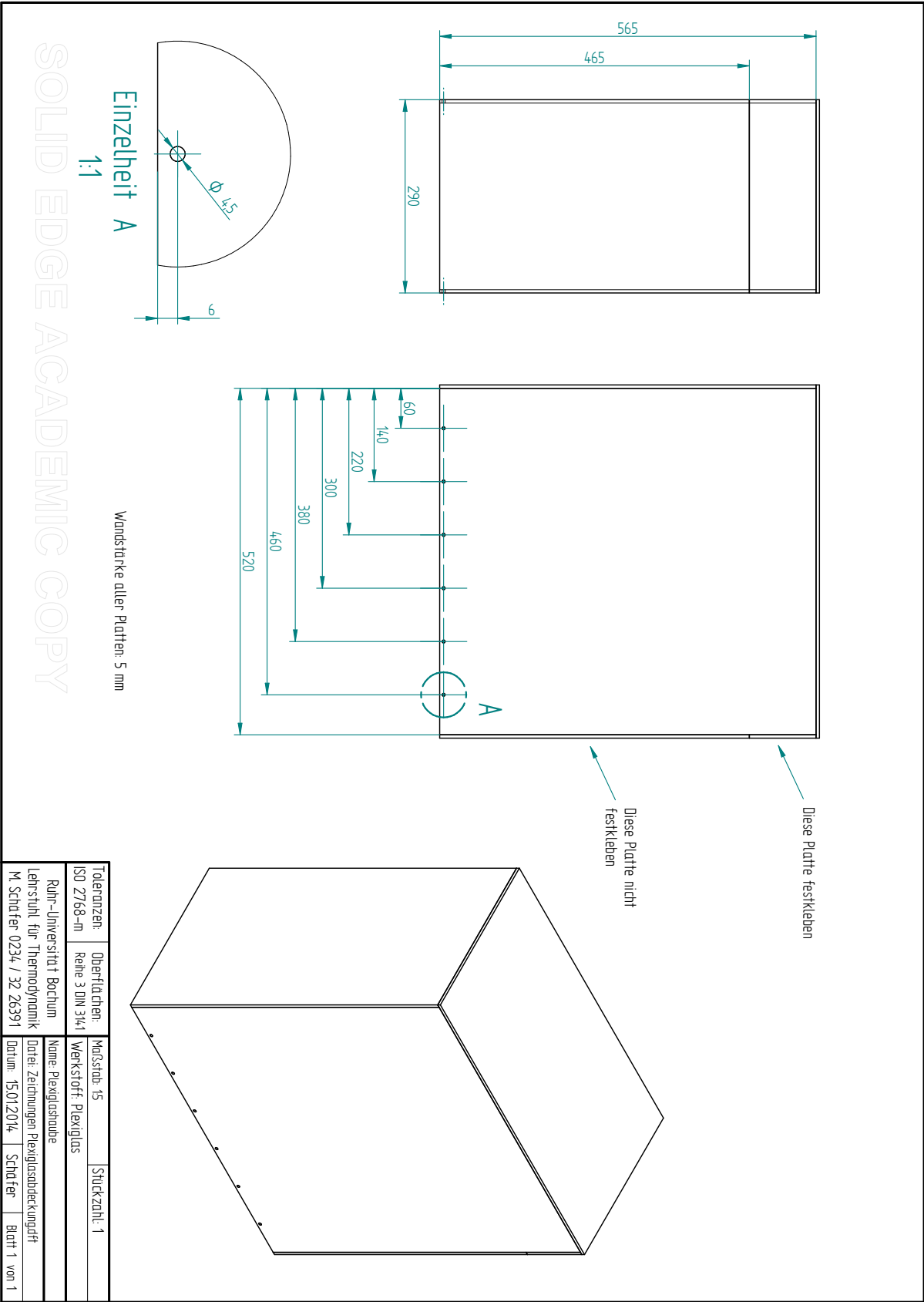
A.2 Draft Shield of the Viscometer-Densimeter's Balance



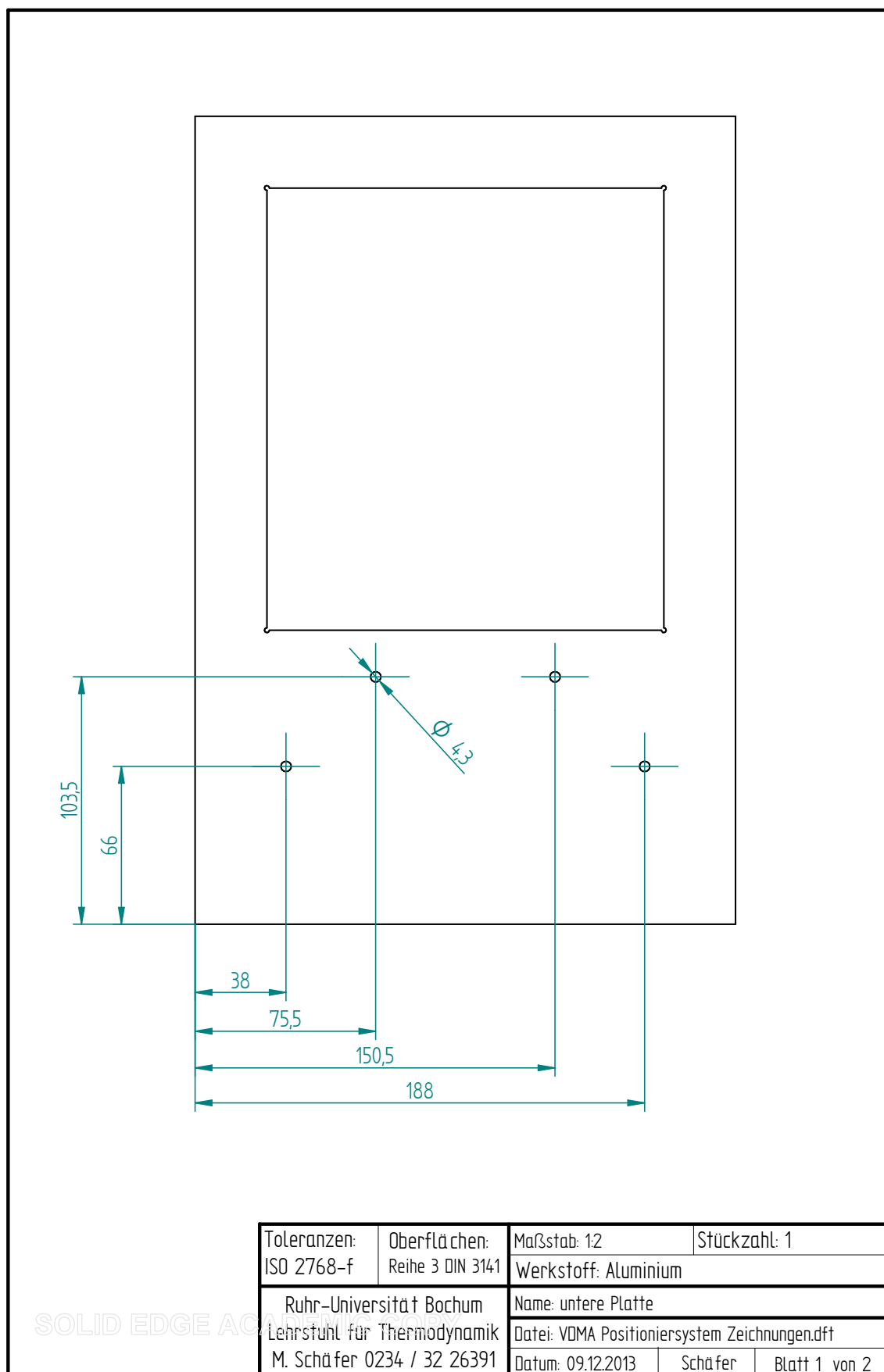
Toleranzen: ISO 2768-f	Oberflächen: Reihe 3 DIN 3141	Maßstab: 1:1	Stückzahl: 1
Ruhr-Universität Bochum Lehrstuhl für Thermodynamik M. Schäfer 0234 / 32 26391		Werkstoff: Plexiglas	
		Name: Hinterteil obere Abdeckung	
		Datei: Zeichnungen obere Plexiglasabdeckung.dft	
		Datum: 09.12.2013	Schäfer Blatt 1 von 3

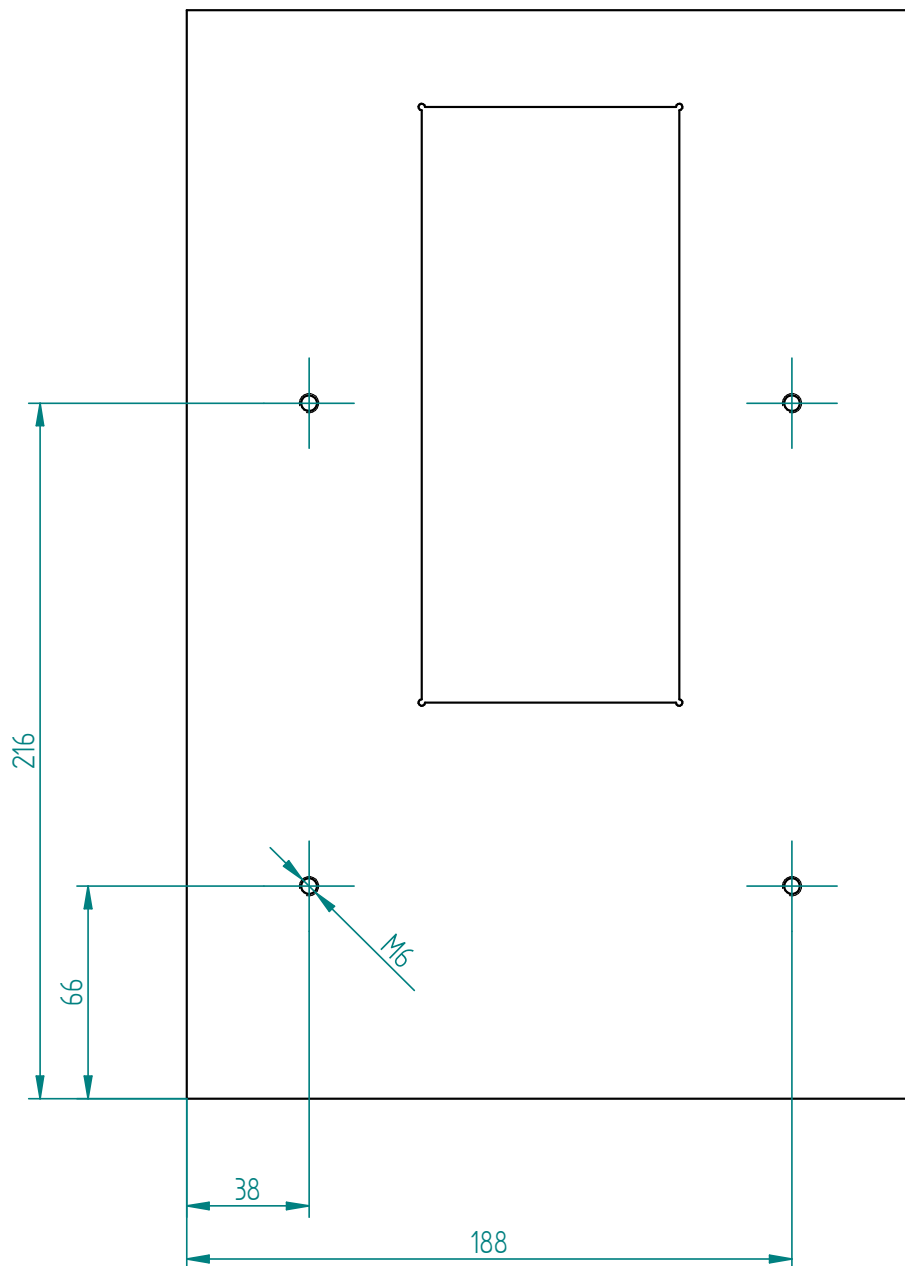






A.3 Modifications to the Stand for the Viscometer-Densimeter's Balance

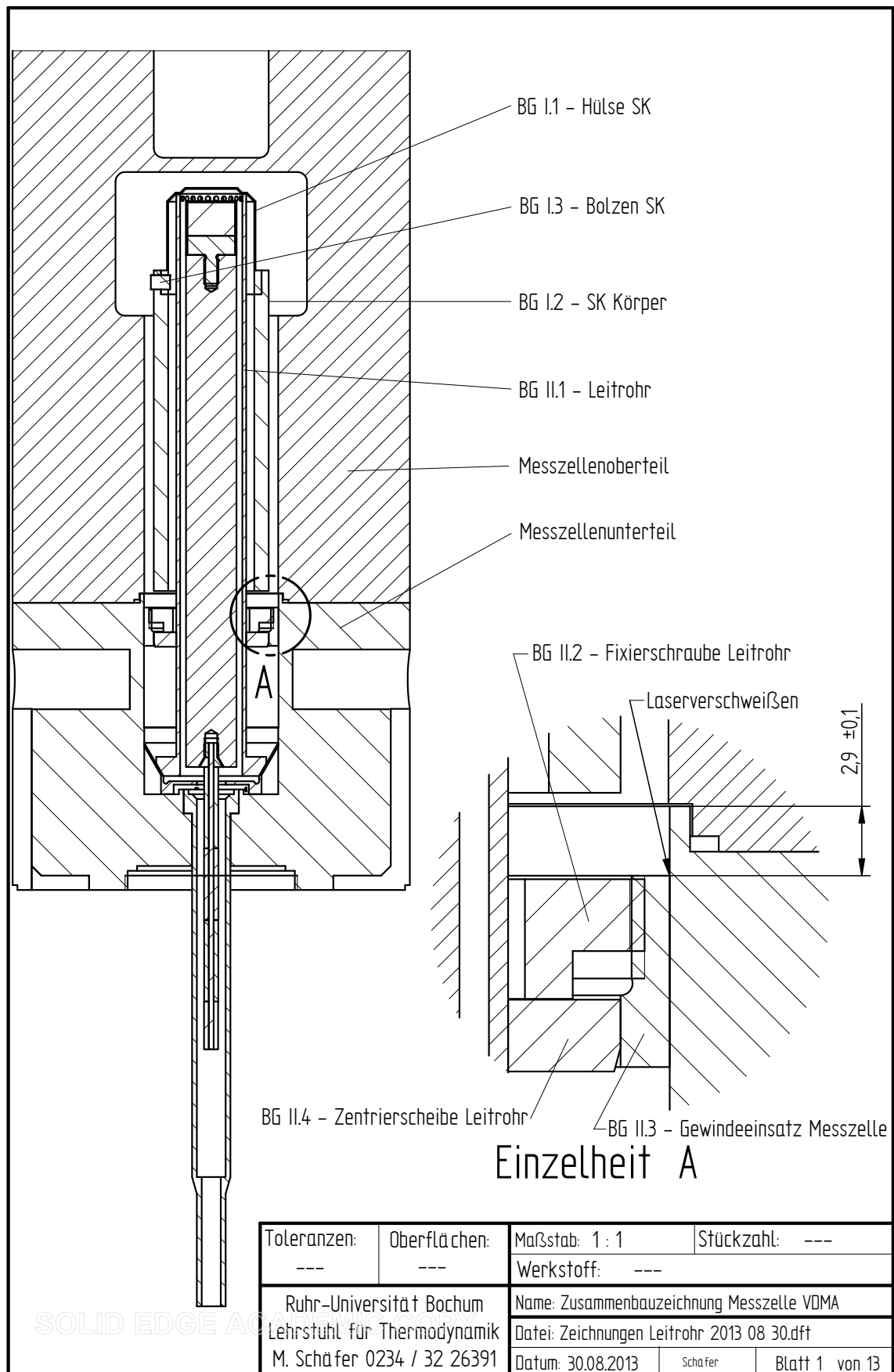


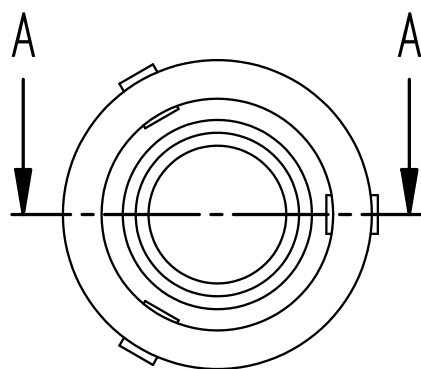


Toleranzen: ISO 2768-f	Oberflächen: Reihe 3 DIN 3141	Maßstab: 1:2	Stückzahl: 1
Werkstoff: Aluminium		Name: obere Platte	
Ruhr-Universität Bochum Lehrstuhl für Thermodynamik M. Schäfer 0234 / 32 26391		Datei: VDMA Positioniersystem Zeichnungen.dft	
Datum: 09.12.2013		Schäfer	Blatt 2 von 2

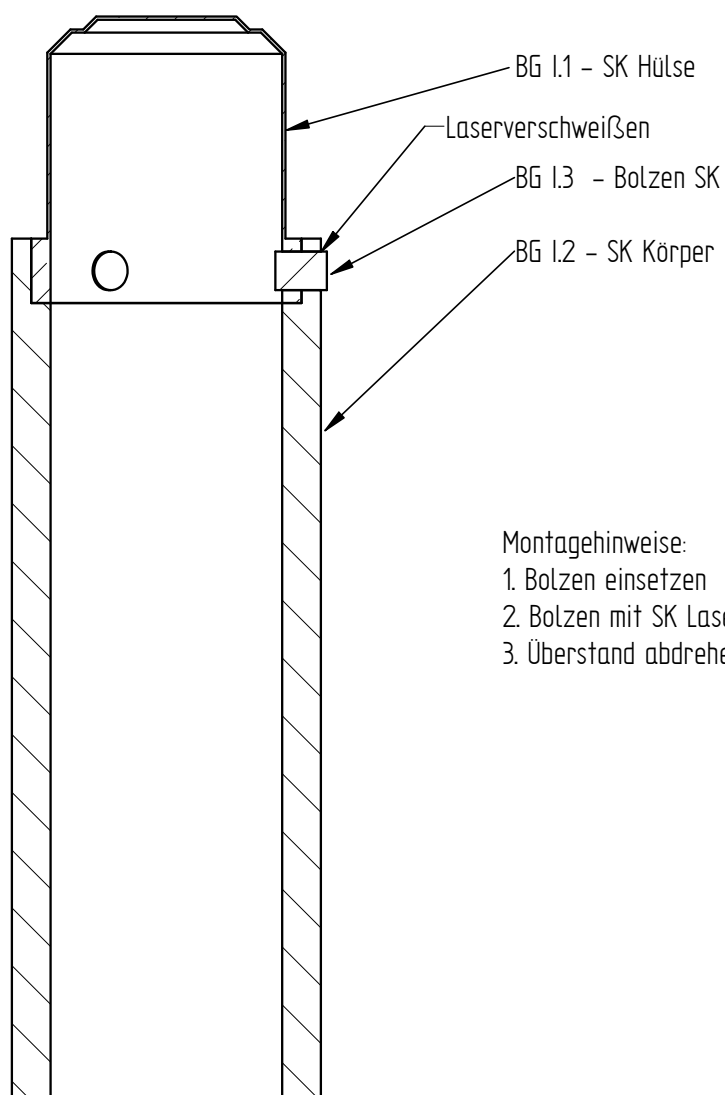
SOLID EDGE ACADEMIC COPY

A.4 The Viscometer-Densimeter's Flow-Guide Tube





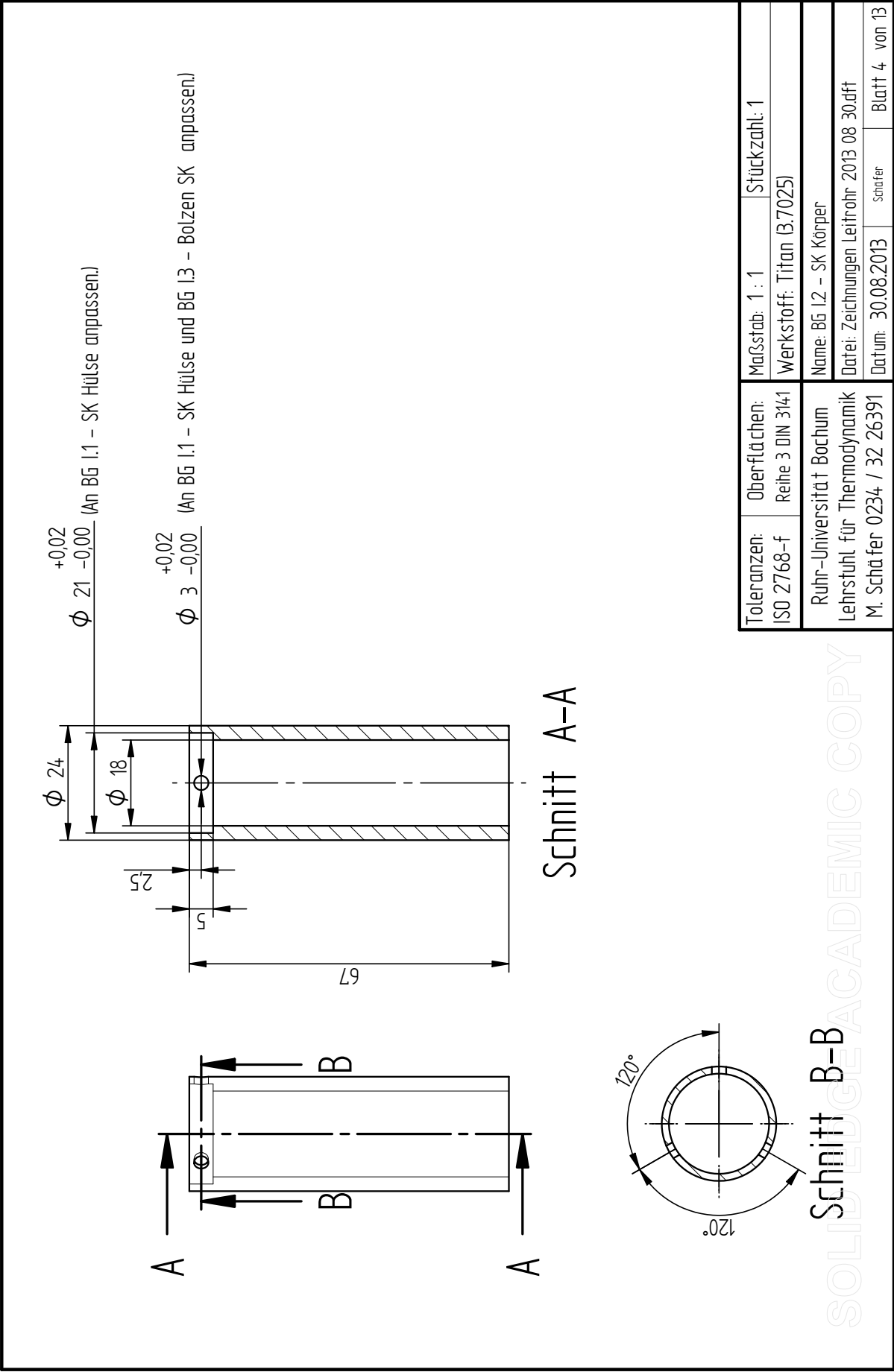
Schnitt A-A

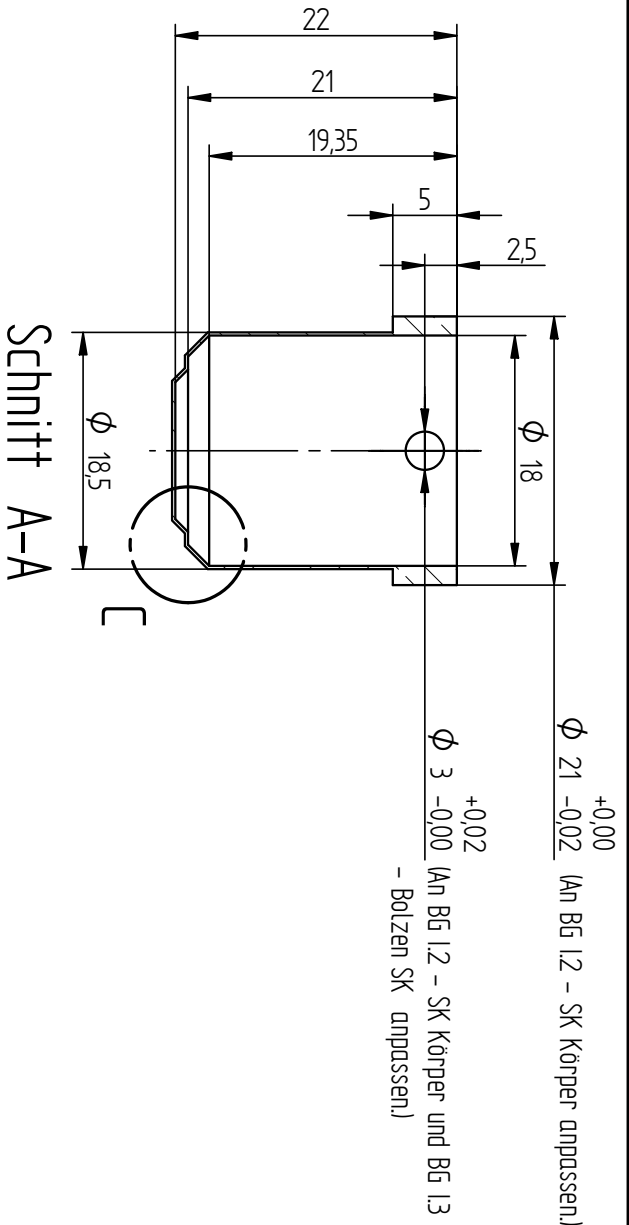


Montagehinweise:

1. Bolzen einsetzen
2. Bolzen mit SK Laserverschweißen
3. Überstand abdrehen

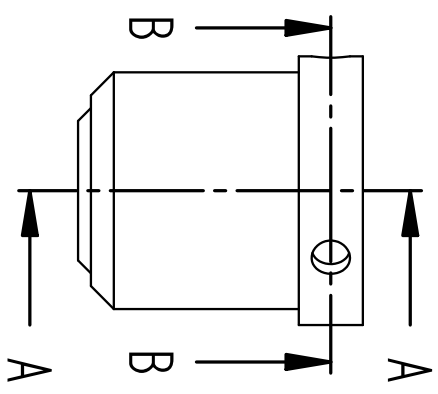
Toleranzen:	Oberflächen:	Maßstab: 2 : 1	Stückzahl: ---
---	---	Werkstoff: ---	
Ruhr-Universität Bochum		Name: BG I Zusammenbauzeichnung SK	
Lehrstuhl für Thermodynamik		Datei: Zeichnungen Leitrohr 2013 08 30.dft	
M. Schäfer 0234 / 32 26391		Datum: 30.08.2013	Schäfer Blatt 2 von 13



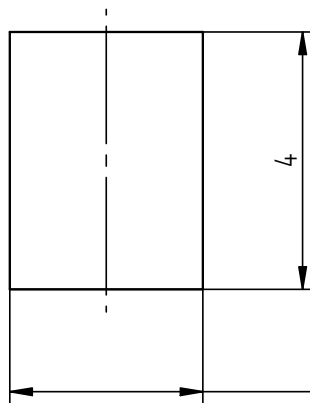
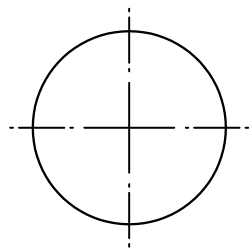


SOLO EDUACADEMIC COPY

Einzelheit C

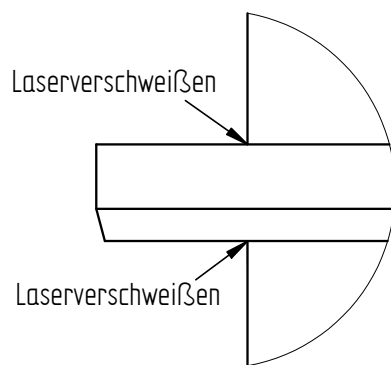
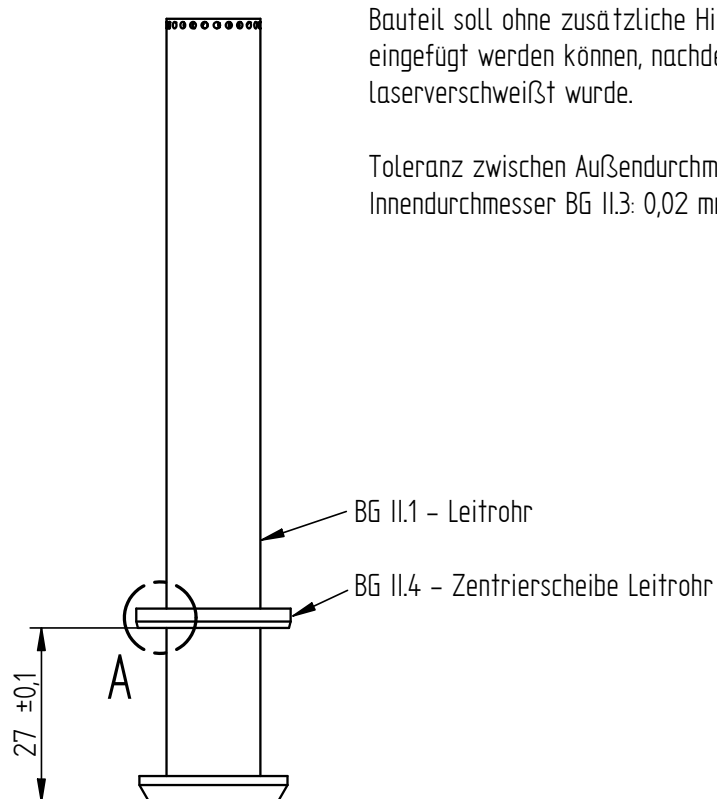


Toleranzen: ISO 2768-f	Oberflächen: Reine 3 DIN 3141	Maßstab: 2 : 1	Stückzahl: 1
Ruhr-Universität Bochum Lehrstuhl für Thermodynamik M. Schäfer 0234 / 32 26391		Werkstoff: CuCrZr (2.1293)	Name: BG 1.1 - SK Hülse
Datum: 30.08.2013		Zeichnungen Lehrstuhl 2013 08 30.dft	Blatt 3 von 13

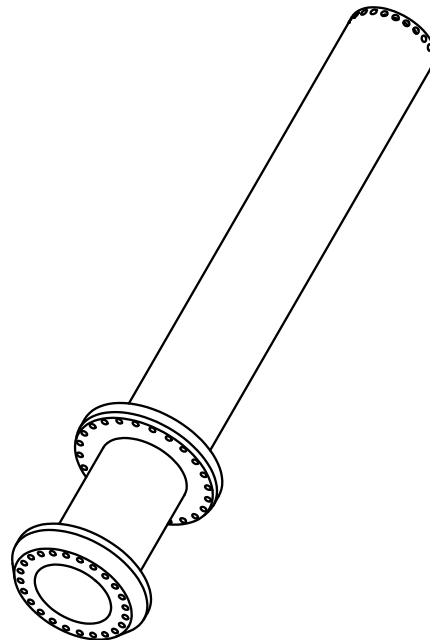


$\phi \begin{matrix} +0,00 \\ 3 \\ -0,02 \end{matrix}$ (An BG I.2 (SK Körper) und BG I.1 (SK Hülse) anpassen.)

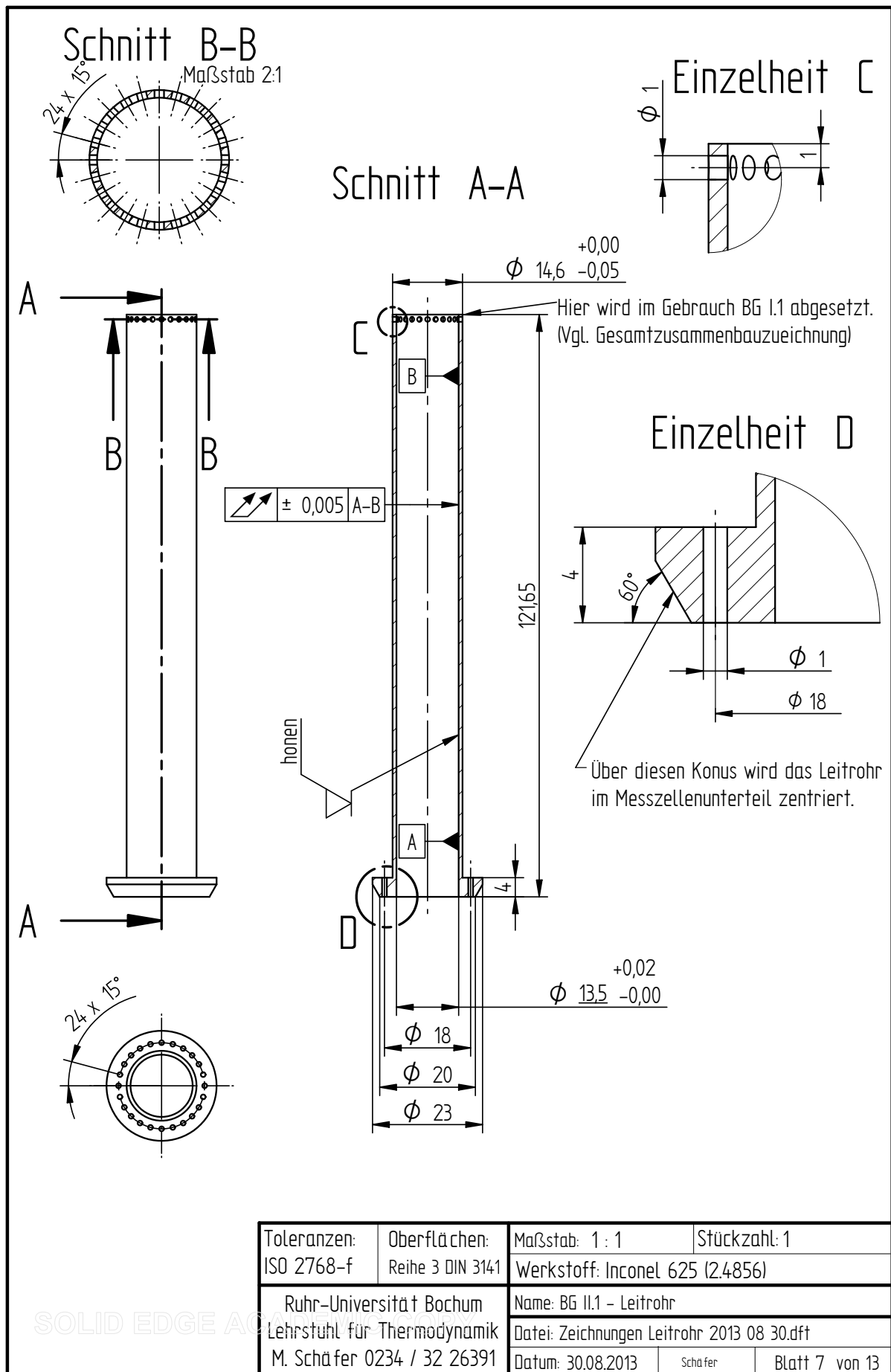
Toleranzen: ISO 2768-f	Oberflächen: Reihe 3 DIN 3141	Maßstab: 10 : 1	Stückzahl: 3
Werkstoff: Titan (3.7025)		Name: BG I.3 – Bolzen SK	
Ruhr-Universität Bochum Lehrstuhl für Thermodynamik M. Schäfer 0234 / 32 26391		Datei: Zeichnungen Leitrohr 2013 08 30.dft	
Datum: 30.08.2013		Schäfer	Blatt 5 von 13

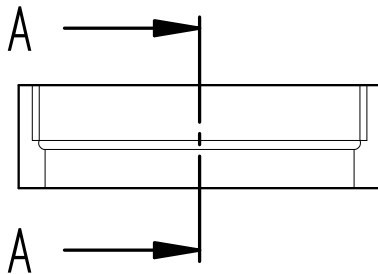


Einzelheit A



Toleranzen: ---	Oberflächen: ---	Maßstab: 1 : 1	Stückzahl: ---
Ruhr-Universität Bochum Lehrstuhl für Thermodynamik M. Schäfer 0234 / 32 26391		Werkstoff: Inconel 625 (2.4856)	
		Name: BG II Zusammenbauzeichnung Leitrohr	
		Datei: Zeichnungen Leitrohr 2013 08 30.dft	
		Datum: 30.08.2013	Schäfer Blatt 6 von 13

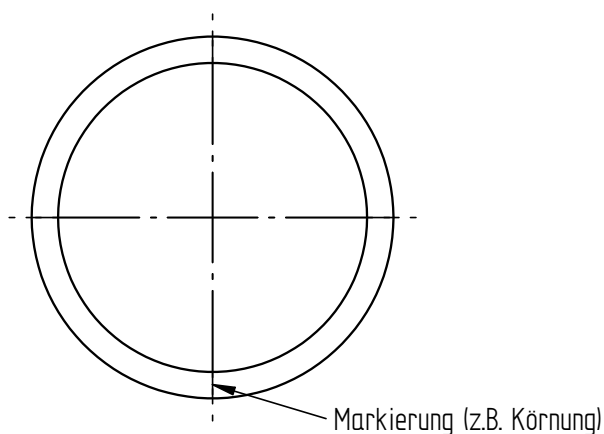
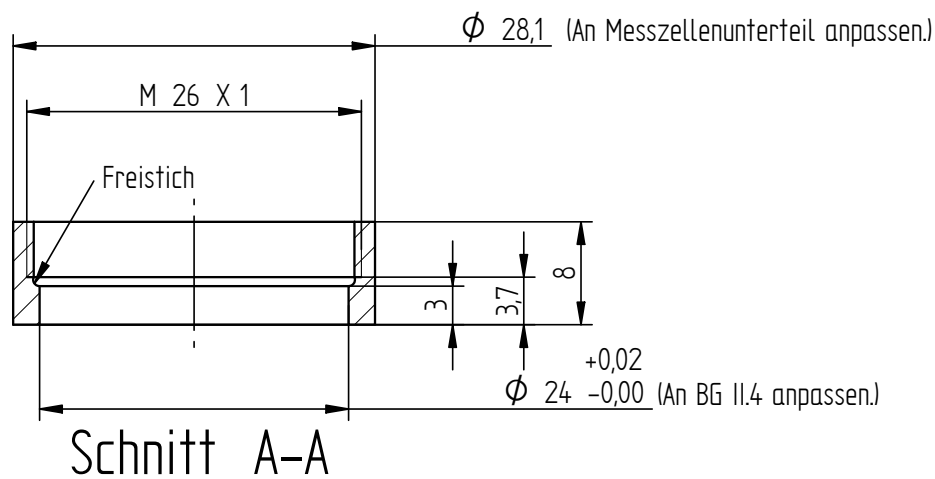




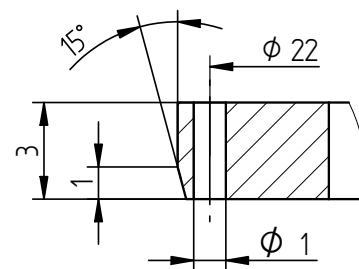
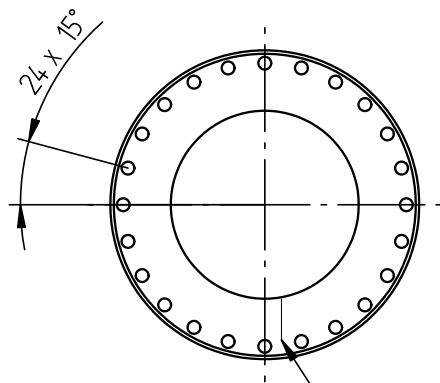
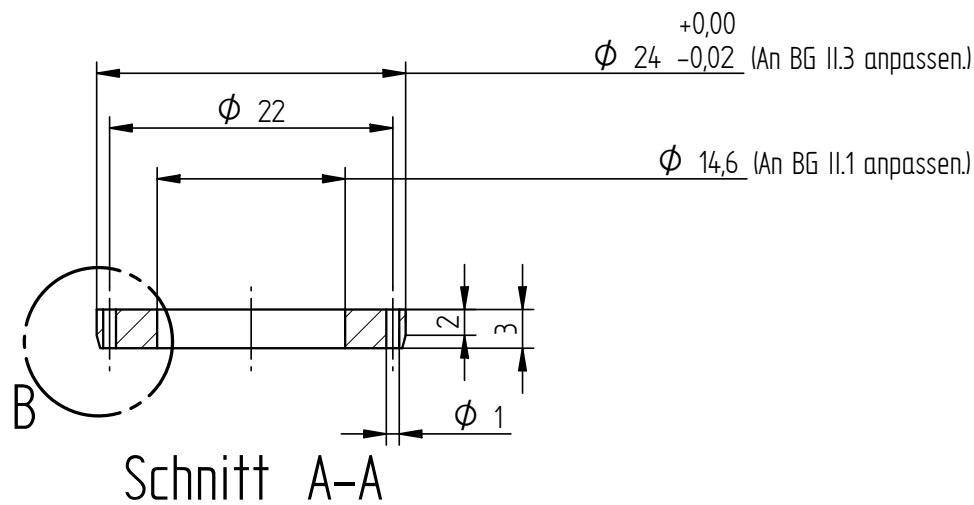
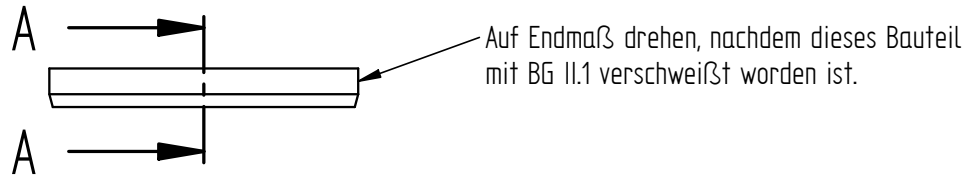
Bei Bedarf Messzellenunterteil nachbearbeiten, um dieses Bauteil in der richtigen Höhe (siehe Blatt 1) im Messzellenunterteil positionieren zu können.

Bauteil im Messzellenunterteil drehen, sodass die Markierungen am Bauteil und am Messzellenunterteil übereinstimmen.

Bauteil mit Messzellenunterteil Laserverschweißen, dann Innendurchmesser $\varnothing 24$ auf Endmaß drehen.



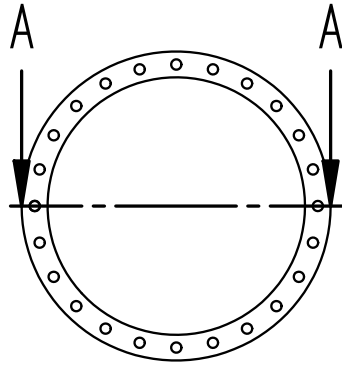
Toleranzen: ISO 2768-f	Oberflächen: Reihe 3 DIN 3141	Maßstab: 2 : 1	Stückzahl: 1
Ruhr-Universität Bochum Lehrstuhl für Thermodynamik M. Schäfer 0234 / 32 26391		Werkstoff: Inconel 625 (2.4856)	
		Name: BG II.3 – Gewindeinsatz Messzellenunterteil	
		Datei: Zeichnungen Leitrohr 2013 08 30.dft	
		Datum: 30.08.2013	Schäfer Blatt 9 von 13



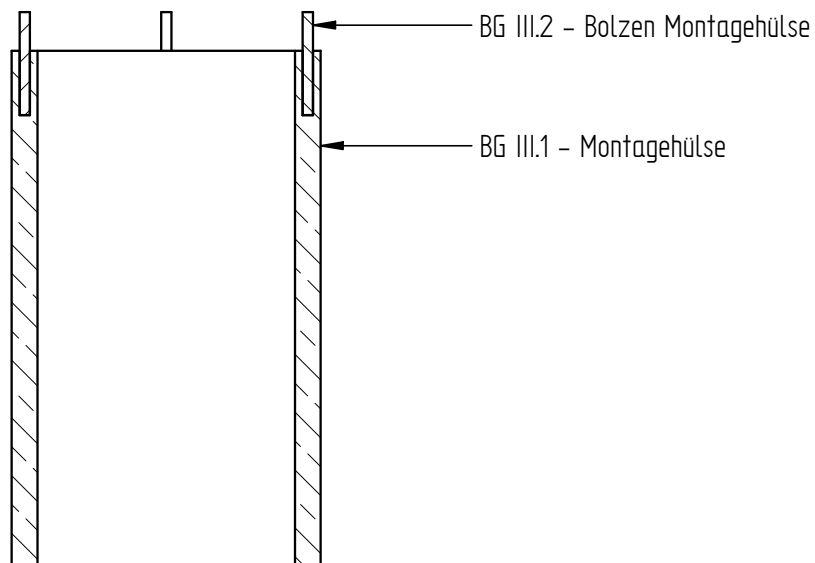
Einzelheit B

Markierung (z.B. Phase an Bohrung)

Toleranzen: ISO 2768-f	Oberflächen: Reihe 3 DIN 3141	Maßstab: 2 : 1	Stückzahl: 1
Ruhr-Universität Bochum Lehrstuhl für Thermodynamik M. Schäfer 0234 / 32 26391		Werkstoff: Inconel 625 (2.4856)	
		Name: BG II.4 Zentrierscheibe Leitrohr	
		Datei: Zeichnungen Leitrohr 2013 08 30.dft	
		Datum: 30.08.2013	Schäfer Blatt 10 von 13

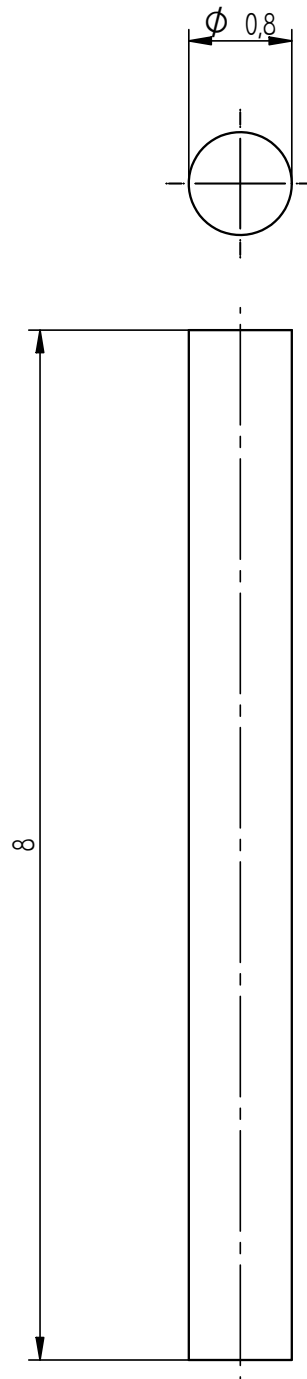


BG III.2 soll mit dem Hammer in BG III.1 eingeschlagen werden.



Schnitt A-A

Toleranzen: ---	Oberflächen: ---	Maßstab: 2 : 1	Stückzahl: ---
Werkstoff: ---		Name: BG III Zusammenbauzeichnung Montagehilfe	
Ruhr-Universität Bochum Lehrstuhl für Thermodynamik M. Schäfer 0234 / 32 26391		Datei: Zeichnungen Leitrohr 2013 08 30.dft	
Datum: 30.08.2013		Schäfer	Blatt 11 von 13



Toleranzen: ISO 2768-f	Oberflächen: Reihe 3 DIN 3141	Maßstab: 20 : 1	Stückzahl: 24
Ruhr-Universität Bochum Lehrstuhl für Thermodynamik M. Schäfer 0234 / 32 26391		Werkstoff: unmagnetischer Stahl o.Ä.	
		Name: BG III.2 - Bolzen Montagehülse	
		Datei: Zeichnungen Leitrohr 2013 08 30.dft	
		Datum: 30.08.2013	Schäfer Blatt 13 von 13

B Experimental Carbon Dioxide Data

Table B.1 Experimental (η , p , T) data for carbon dioxide, published in *Schäfer et al. (2015)*. From left to right, the temperature^a T (ITS-90), the pressure^b p , a calculated density ρ_{calc} (*Span and Wagner, 1996*), the viscosity^c η and the expanded combined uncertainty ($k = 2$) in viscosity U_c (including uncertainties of temperature and pressure) are listed in the sequence measured.

T / K	p / MPa	$\rho_{\text{calc}} / \text{kg} \cdot \text{m}^{-3}$	$\eta / \mu\text{Pa s}$	$U_c / \mu\text{Pa s}$
298.153	0.6045	11.072	14.945	0.030
298.151	0.4985	9.078	14.929	0.030
298.151	0.4029	7.300	14.918	0.030
298.152	0.3033	5.467	14.911	0.030
298.152	0.2046	3.670	14.903	0.030
298.151	0.1008	1.799	14.901	0.030
323.159	0.5987	10.037	16.128	0.051
323.160	0.5004	8.356	16.116	0.051
323.159	0.4007	6.665	16.104	0.051
323.160	0.3049	5.053	16.099	0.051
323.159	0.2009	3.316	16.088	0.051
323.159	0.1516	2.497	16.079	0.051
323.160	0.1008	1.657	16.078	0.051
373.159	0.8026	11.603	18.493	0.050
373.161	0.6049	8.703	18.456	0.050
373.159	0.3999	5.725	18.431	0.050
373.160	0.2968	4.240	18.416	0.050
373.159	0.2011	2.867	18.403	0.050
373.159	0.1514	2.155	18.399	0.050
373.160	0.1004	1.428	18.396	0.050
423.143	0.9989	12.681	20.768	0.050
423.143	0.8008	10.137	20.725	0.050
423.142	0.6004	7.578	20.696	0.050
423.141	0.3976	5.003	20.677	0.050
423.143	0.3020	3.794	20.665	0.050
423.141	0.2041	2.560	20.647	0.050
423.143	0.1533	1.921	20.656	0.050
423.142	0.1002	1.255	20.648	0.050

Table B.1 (continued)

T / K	p / MPa	$\rho_{\text{calc}} / \text{kg} \cdot \text{m}^{-3}$	$\eta / \mu\text{Pa s}$	$U_c / \mu\text{Pa s}$
473.154	1.2009	13.586	22.899	0.050
473.154	0.9978	11.267	22.878	0.050
473.154	0.8030	9.051	22.844	0.050
473.155	0.6011	6.763	22.815	0.050
473.154	0.4035	4.531	22.785	0.050
473.154	0.2025	2.269	22.766	0.050
473.155	0.1530	1.714	22.751	0.050
473.164	0.1001	1.121	22.751	0.050
253.146	0.4014	8.699	12.717	0.052
253.146	0.3005	6.451	12.706	0.052
253.146	0.2005	4.266	12.713	0.052
253.146	0.1530	3.241	12.714	0.052
253.146	0.1002	2.113	12.713	0.052
273.168	0.5028	10.086	13.724	0.052
273.170	0.3994	7.954	13.710	0.052
273.167	0.3017	5.967	13.709	0.052
273.169	0.2034	3.996	13.700	0.052
273.169	0.1518	2.972	13.703	0.052
273.168	0.1004	1.959	13.706	0.052
reproducibility checks				
298.150	0.5028	9.158	14.936	0.030
298.150	0.4000	7.247	14.925	0.030
298.150	0.3032	5.466	14.914	0.030
298.150	0.2016	3.616	14.903	0.030
298.150	0.1504	2.690	14.906	0.030
298.150	0.1008	1.799	14.902	0.030
298.151	0.4997	9.100	14.935	0.030

^a The expanded uncertainties ($k = \sqrt{3}$) of the temperature at $T = (253.15, 273.15, 298.15, 323.15, 373.15, 423.15, 473.15) \text{ K}$ are $U(T) = (28, 36, 42, 49, 62, 91, 109) \text{ mK}$, respectively.

^b The expanded uncertainty ($k = \sqrt{3}$) of the pressure in $U(p) = 3.5 \text{ hPa}$.

^c The expanded uncertainties ($k = 2$) in viscosity at $T = (253.15, 273.15, 298.15, 323.15, 373.15, 423.15, 473.15) \text{ K}$ are $U(\eta) = (52, 52, 30, 51, 50, 49, 50) \text{ mK}$, respectively.

Lebenslauf

Michael Schäfer,
geboren am 27. Dezember 1983 in Essen,
ledig.

Ausbildung

Schule	08.1990 bis 07.1994	Grundschule, Hattingen
	08.1994 bis 06.2003	Gymnasium, Velbert-Langenberg Abschluss: Abitur
Praktika	08.2003 bis 09.2003	Helmut Mauell, Velbert-Neviges
	11.2008 bis 04.2009	Stork Turbo Service, Essen
Studium	09.2003 bis 08.2004	Elektrotechnik an der Fachhochschule Gelsenkirchen
	11.2007 bis 01.2008	Mechanical Engineering an der Chal- mers University of Technology, Göte- borg, Schweden
	10.2004 bis 12.2009	Allgemeiner Maschinenbau an der Ruhr-Universität Bochum Abschluss: Diplom Ingenieur

Berufliche Tätigkeit

studentische Hilfskraft	05.2007 bis 10.2007 04.2008 bis 09.2008	Institut für Thermo- und Fluiddyna- mik, Ruhr-Universität Bochum, Lehr- stuhl für Thermodynamik, Prof. Dr.- Ing. R. Span
wissenschaftl. Mitarbeiter	seit 02.2010	Institut für Thermo- und Fluiddyna- mik, Ruhr-Universität Bochum, Lehr- stuhl für Thermodynamik, Prof. Dr.- Ing. R. Span